UNIVERSITY OF TURIN

PhD School in Life and Health Sciences

Molecular Medicine

XXIX Cycle

Academic Years: 2014-2017

P140CAP MODULATES SYNAPTIC PLASTICITY THROUGH ITS

INTERACTION WITH THE NMDA RECEPTOR

Tutor: Prof.ssa Paola Defilippi   Candidate: Costanza Angelini

Co-tutor: Prof.ssa Mirella Giovarelli

Coordinator: Prof. Francesco Novelli

TABLE OF CONTENTS

ABSTRACT

p140Cap is a scaffold protein of the post synaptic density involved in the stabilization of mature dendritic spine. Previous works demonstrated that p140Cap KO mice display defects in memory consolidation and impaired long-term potentiation (LTP) and long-term depression (LTD). These events are mediated by the N-methyl-D-aspartate receptor (NMDAR) which plays a crucial role for synaptic efficacy strengthening and contributes to learning and memory processes. Proteomic analysis of p140Cap interactors in synaptosomes revealed that the NMDAR subunit GluN2A and GluN2B are potentially high-fidelity interactors of p140Cap. In this study, we investigate the involvement of p140Cap in synaptic plasticity events mediated by the NMDA receptor.

Here we show that p140Cap selectively associates the GluN2A subunit of the NMDAR and that the interaction occurs mainly through the first proline-rich region of p140Cap and the GluN2A C-terminal region between residues 1349 and 1464. Upon specific activation, the NMDAR complex triggers a cellular signaling cascade through the interaction with scaffold and signaling molecules, which favours NMDAR stabilization and full activation. Among the scaffold molecules involved, PSD95 has been recognized as a major player. Our data show that in p140Cap KO hippocampal neurons the percentage of co-localization of GluN2A and PSD95 is significantly decreased. Consistently, GluN2A is less associated with PSD95 in p140Cap KO crude synaptosomes than in WT synaptosomes. Similarly, also the lipid raft marker Flotilin-1 and the GTPase Rac1 come out to be less associated with GluN2A. In addition, Rac1 results less active in p140Cap KO synaptosomes compared to the WT ones. These data suggest that p140Cap can influence the composition of the molecular complex associated to the NMDAR. Recent studies demonstrated that NMDAR trafficking to lipid rafts, as signaling platforms, is dynamically enhanced during synaptic plasticity process as memory formation. Here we show that p140Cap is present at the cell membrane both associated to synaptic lipid raft and to soluble postsynaptic membranes. We hypothesized that p140Cap can positively influence the composition of the molecular complex associated to the NMDAR, modulating the recruitment of specific components to the lipid rafts. Indeed, by analysing the amount of specific constituents of the synaptic lipid rafts, we demonstrate that both GluN2A and PSD95 are significantly and specifically less recruited in lipid raft domains of p140Cap KO mice, without grossly affecting raft composition.

The reduced localization of NMDARs in the synaptic lipid rafts of p140Cap KO mice could explain the impaired LTP and LTD, and the defects in memory and learning observed in these animals.

Overall, our data provide evidence that p140Cap may facilitate the functional association of GluN2A and PSD95, and their selective recruitment in membrane domains enriched of signaling molecules, thus improving the efficiency of synaptic signal transduction.

1 NMDA RECEPTOR AND SYNAPTIC PLASTICITY

1.1 MICROANATOMY OF THE EXCITATORY SYNAPSE

The billions of neurons in the mammalian brain communicate with each other via specialized junctions called synapses. The ability of the synapse to alter its strength and structure (synaptic plasticity), is crucial for all aspects of nervous system function and critical for regular development of the central nervous system (CNS). Short-term alterations in synaptic strength are assumed to be converted to long-lasting memories that are embedded in stable morphological changes (Sala & Segal, 2014).

The vast majority of these synapses occur at contacts between presynaptic axons and postsynaptic dendrites, and they use glutamate as the excitatory neurotransmitter (Sheng & Hoogenraad, 2007). The presynaptic active zone and the post synapse are separated by a gap of 20–25 nm, and a wide variety of cell adhesion molecules hold pre- and postsynaptic membranes together in register and at the appropriate separation (Figure 1). Presynaptic specialization is a cluster of synaptic vesicles (~40 nm diameter), some of which are closely associated ("docked") with a thickening of the presynaptic plasma membrane (the active zone), where vesicle exocytosis occurs. Directly opposed to the active zone is the post synaptic density (PSD), a thick electron-dense membrane-associated protein complex specialized for postsynaptic signaling and plasticity (Dosemeci, Weinberg, Reese, & Tao-Cheng, 2016). The PSD is housed on dendritic spines, specialized structures which represent the locus of neuroexcitatory transmission and plasticity (Sala & Segal, 2014).

Normal synaptic transmission depends on the proper localization and arrangement of specific proteins on both sides of the synapse. Synaptic plasticity is mediated by changes in the molecular composition of synapses and in chemical modification of synaptic proteins. Pathological synapse development and/or function almost certainly contribute to many neuropsychiatric disorders (e.g. schizophrenia, autism, mental retardation) and common neurodegenerative diseases (e.g. Alzheimer's disease) and stroke (Nimchinsky, Sabatini, & Svoboda, 2002).
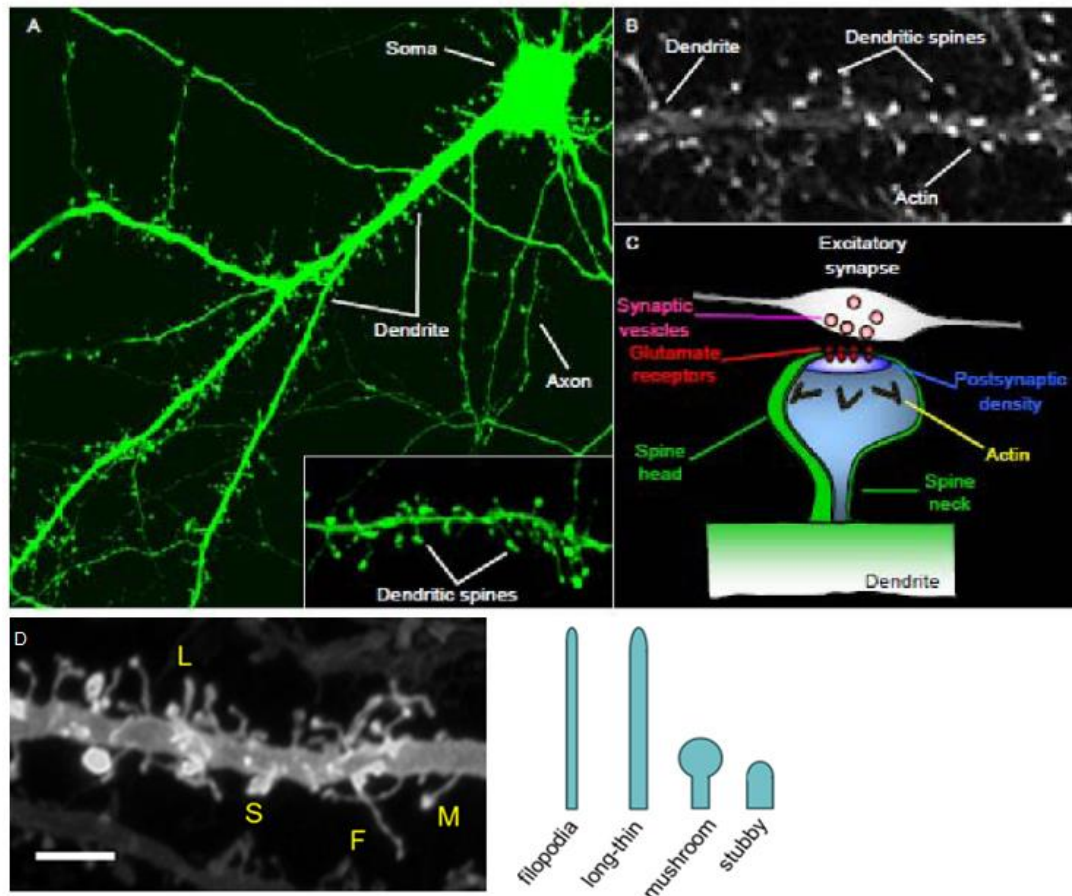
1.2   THE DENDRITIC SPINE

Spines are actin-rich membranous protrusions from the neuronal surface (Figure 1A and 1B). They consist of a head (volume ~ 0.001–1 μm^3) connected to the neuron by a thin (diameter <0.1 µm) spine neck. They may arise from the soma, dendrites, or even the axon hillock, and they are found in various neuronal populations in all vertebrates and some invertebrates. More than 90% of excitatory synapses terminate on spines; the human brain thus contains $>10^{13}$ spines (Nimchinsky et al., 2002). The "normal" dendritic spine density ranges from 0.2 to 3.5 spines per 1 µm of dendrite (the latter is a count in human post-mortem cortex). Obviously, this number is dependent on age, cell type, and position along the dendrite (Sala & Segal, 2014).

Typical spines have a bulbous head (receiving a single synapse) connected to the parent dendrite through a thin spine neck. Because the neck hinders diffusion of molecules to and from the parent dendritic shaft, spines serve as microcompartments in which biochemical changes in one individual synapse can be isolated from other synapses on the same neuron. The geometry of the spine neck determines calcium efflux into the dendrite shaft and hence the degree of calcium elevation in the spine head following ionotropic glutamate receptors activation (Sheng & Hoogenraad, 2007). Dendritic spines are highly heterogeneous structures that show dynamic motility, especially during development. Their number, size, and shape undergo plastic changes correlated with long-term modifications of synaptic strength and interneuronal connectivity. Spine shape has been categorized as "mushroom," "filopodia," or "stubby," but electron microscopy studies show a continuum between these categories (figure 1D). There is growing evidence that different spine shapes and sizes reflect different developmental stages and/or altered strength of synapses (Sheng & Hoogenraad, 2007).

Spines with large heads, "mushrooms", are generally stable, express large numbers of AMPA (α-amino-3-hydroxy-5-methyl-4-isoxazolepropionic acid) receptors, and contribute to strong synaptic connections. By contrast, spines with small heads, "filopodia," or "stubby," are more motile, less stable, and contribute to weak synaptic connections (Sheng & Hoogenraad, 2007). The size, shape, motility, and stability of dendritic spines depend largely on actin, the primary cytoskeleton within spines. A complex network of regulatory proteins, including the Rho family GTPases, controls actin arrangement and spine morphogenesis (Schubert & Dotti, 2007).

The cytoskeleton of dendritic spines is composed mainly of filamentous (F)-actin that forms parallel filaments in the neck of the spines and lattice and twisted filaments in the spine head. Thus, it is not surprising that all the molecules that regulate growth and shrinkage of dendritic spines will eventually modify positively or negatively actin polymerization, and even the overexpression of actin alone in neurons could increase dendritic spine density (Sala & Segal, 2014).

Figure 1: Dendritic spines are small protrusions along dendrites that contain postsynaptic densities. A: Example of a cortical neuron expressing green fluorescent protein. The main dendrite is branched and has dendritic spines along its length. The inset shows a high magnification image of dendritic spines. B: Dendrite of a cortical neuron immunofluorescence staining for phalloidin, a marker of endogenous β-actin. Note the enrichment of β-actin in the dendritic spines. C: Schematic of excitatory synapse. D: Immunofluorescence and schematic representation of dendritic spines with different shape. (Modified from "Epac2-mediated dendritic spine remodelling: implications for disease" Peter Penzes et al., Mol Cell Neurosci. 2011 February; 46(2): 368–380).

1.3 THE POST SYNAPTIC DENSITY

The PSD is typically located on the dilated tip ("head") of the dendritic spine. The PSD is a dense sub membranous disk-like proteinaceous structure, ∼200–800 nm wide and ∼30–50 nm thick. This structure contains an array of molecules important for synaptic transmission and plasticity. Indeed in the PSD are localized the glutamate receptors that

are activated by the glutamate neurotransmitter released from the presynaptic terminal, as well as a host of associated signaling and structural molecules (adhesion molecules, cytoplasmic signaling enzymes, and cytoskeletal elements) (Sheng & Kim, 2011).

The dimensions of the spine head are highly correlated with the size of the PSD and associated active zone, as well as synaptic strength. Indeed, the postsynaptic membrane can be divided into the PSD itself, as well as peri-synaptic membrane (within 100 nm of the PSD), and extrasynaptic regions, set at greater distances from the PSD. Extrasynaptic regions have specialized postsynaptic functions and are enriched for a distinctive set of proteins, such as metabotropic glutamate receptors (mGluRs) and proteins involved in endocytosis (Sheng & Hoogenraad, 2007).

Recently, thanks to immuno-electron microscopy, a distinct layer µ50 nm thick was uncovered immediately adjacent and deep to the PSD. Because this part of the PSD comprises different proteins and displays a more labile organization than the core layer lining the synaptic membrane, this separate structural and functional layer of the PSD was named as its "pallium" or "mantle" (Dosemeci et al., 2016).

The core layer of the PSD contains 300–400 copies of PSD-95 (in the rodent forebrain) and related membrane-associated guanylate kinase (MAGUK) molecules. PSD-95 is the most abundant scaffold protein of the PSD. PSD-95 is oriented with its N-terminus near the plane of the postsynaptic membrane and its C-terminus deep in the spine. This close apposition to the membrane puts PSD-95 able to bind ionotropic glutamate receptors as N-Methyl-D-aspartic acid receptors (NMDARs) and AMPA receptors. Guanylate kinase-associated protein (GKAP) instead, can bind PSD-95 near its C-terminal (Kim et al., 1997). GKAP is in the PSD at a ratio of approximately one GKAP for two PSD-95s so a layer of GKAP cross-linked with PSD-95 could provide an interface between the core layer and the "pallium" of the PSD. Thus, the dense matrix of PSD-95/MAGUK filaments capped by GKAPs provides a stable platform for the subjacent "pallium" (Dosemeci et al., 2016).

This second layer term the "pallium", is likely pegged to the PSD core through GKAPs, which can simultaneously associate with PSD-95 and Shanks. A network containing Shanks and Homer are likely to form an extended scaffold continuous sandwiched between the electron-dense PSD core and the actin "spinoskeleton" and it is highly dynamic, exhibiting striking changes during synaptic activity. Under conditions of strong excitation, the "pallium" becomes electron-dense, with the addition of Ca^{2+}/calmodulin

dependent protein kinase (CaMKII) and several other proteins. Accumulating evidence on the movements of individual proteins suggests a mechanism for concerted insertion of receptors (AMPARs) to the PSD and re-organization of the actin spinoskeleton, both mediated by CaMKII.

1.4 N-METHYL-D-ASPARTATE RECEPTORS AND SYNAPTIC PLASTICITY

Spine morphology is profoundly influenced by the activity of ionotropic glutamate receptors (iGluRs). Within the large family of iGluRs, N-methyl-D-aspartate receptors (NMDARs) constitute a subfamily identified by specific molecular composition and unique pharmacological and functional properties (Paoletti & Neyton, 2007).

The NMDAR protein complex can be regarded as a core subset of the PSD. When activated, NMDARs allow the influx of calcium into the spine contributing to fast synaptic transmission. For this reason, NMDARs are essential mediators of brain plasticity because are capable of converting specific patterns of neuronal activity into long-term changes in synapse structure and function that are thought to underlie higher cognitive functions. NMDAR dysfunctions are also involved in various neurological and psychiatric disorders including stroke, pathological pain, neurodegenerative diseases and schizophrenia (Paoletti, Bellone, & Zhou, 2013).

NMDA receptors are trigger for the induction of two major forms of synaptic plasticity: long-term potentiation (LTP) and long-term depression (LTD), which are respectively characterized by long lasting enhancement and reduction of synaptic transmission between two adjacent neurons after repetitive stimulation (Fan, Jin, & Wang, 2014).

1.4.1 LTP MECHANISM

NMDARs are heterotetrametric plasma membrane channels composed of two obligatory GluN1 and two modulatory GluN2 (A-D) subunits (Cull-Candy, Brickley, & Farrant, 2001), although sometimes the GluN2 subunits are replaced by GluN3(A-B) subunits (Ulbrich & Isacoff, 2008) (Figure2). NMDARs form a heteromeric channel when the two GluN2 subunits are identical, or a triheteromeric channel when two different GluN2 subunits co-assemble with two identical GluN1 subunits (Fan et al., 2014).

GluN1 and GluN3 subunits represent the binding site for channel co-agonist glycine or d-serine, instead channel agonist, glutamate, binds to GluN2 subunits.

During low-frequency synaptic transmission, glutamate released from the presynaptic terminal binds to both NMDA-type and AMPA/kainate-type glutamate receptors. If the postsynaptic neuron is at its normal resting membrane potential, the pore of the NMDA receptor channel will be blocked by Mg^{2+} ions and no current will flow. Under such conditions, the excitatory postsynaptic potential (EPSP) will be mediated entirely by the AMPA receptors. Because blockade of the NMDA receptor by Mg^{2+} is voltage-dependent, the function of the synapse changes markedly when the postsynaptic cell is depolarized. Thus, high-frequency stimulation will cause summation of EPSPs, leading to a prolonged depolarization that expels Mg^{2+} from the NMDA channel pore. Removal of Mg^{2+} allows Ca^{2+} and Na to enter the postsynaptic neuron. The increase in Ca^{2+} concentration within the dendritic spines of the postsynaptic cell serves as a second messenger signal that turns out to be the trigger for LTP. In the early phase of LTP, (approximately the first 30–60 minutes), Ca^{2+} leads to activation of protein kinases: Ca^{2+}/calmodulin dependent protein kinase (CaMKII) and protein kinase C (PKC). CaMKII activation (the enzyme can be auto-phosphorylated at T286 on the alpha subunits and T287 on the beta subunits), mediates the phosphorylation on the AMPAR auxiliary protein Stargazing and allows the receptors to bind to PSD-95. In this way, extra-synaptic AMPA receptors translocate to synaptic region to increase AMPAR conductance. Moreover, the increase in AMPAR conductance that is observed during the initial stages of LTP is also due to S831 phosphorylation of GluR1 subunit of AMPAR by PKC or CaMKII. The second mechanism leading to enhancement of AMPAR-mediated currents during the early phases of LTP is exocytosis of AMPAR-containing vesicles into the plasma membrane, thereby supplying a pool of receptors that could be inserted into the synapse (Lisman, Yasuda, & Raghavachari, 2012).

 LTP late phase depends on changes of gene expression and the synthesis of new proteins. This phase appears to be initiated by protein kinase A (PKA) which activates transcriptional factors as CREB, which stimulates the expression of other proteins as transcriptional regulators, protein kinases, AMPARs and proteins involved in the constitution of new synaptic contacts that serve essentially to strengthening pre-post synaptic contacts and spine actin cytoskeleton enlargement. In particular, LTP induction shifts the G-actin/F-actin ratio toward F-actin (rise in spine actin filaments) and increases spine volume, whereas long-term depression (LTD) induction shifts the ratio toward G-actin (decrease in spine actin filaments) and results in spine shrinkage (Hotulainen &

Hoogenraad, 2010). The major signaling hot spots in actin cytoskeleton regulation are small Rho and Ras GTPases (Tada & Sheng, 2006). Rho GTPases, including RhoA, Rac, and Cdc42 have been extensively studied in neurons and have profound influence on dendritic spine morphogenesis. In dendritic spines, RhoA activation has been shown to be necessary for expression of LTP via cofilin inactivation. Rac and Cdc42 instead, regulate spine head formation, mainly by activating Arp2/3 complex–induced nucleation and inhibiting actin depolymerization via cofilin (Hotulainen & Hoogenraad, 2010).

1.4.2 NMDARs AND LTP

NMDA receptors properties can account for many of the characteristics of LTP:

- LTP requires paired activation in both presynaptic and postsynaptic neurons tightly linked in time. Such a requirement is the central postulate of a theory of learning devised by Donald Hebb in 1949 (Brown & Milner, 2003). Hebb proposed that coordinated activity of a presynaptic terminal and a postsynaptic neuron would strengthen the synaptic connection between them, precisely as is observed for LTP. This indicates the involvement of a **coincidence detector** that allows LTP to occur only when both presynaptic and postsynaptic neurons are active.

  NMDA receptor behaves like a molecular coincidence detector because the channel of this receptor opens (to induce LTP) only when two events occur simultaneously: glutamate is bound to the receptor, and the postsynaptic cell is depolarized. Thus, at resting membrane potential, the pore of the NMDAR channel is blocked by physiological levels of extracellular Mg^{2+}. NMDAR activation requires postsynaptic depolarization (to relieve the voltage dependent Mg^{2+} block) that coincides with presynaptic release of glutamate that binds to GluN2 subunits. A third element is required for NMDAR activation: the presence of glycine or D-serine occupying a binding site present in the GluN1 subunit (Sanz-Clemente, Nicoll, & Roche, 2013). Therefore, Ca^{2+} and Na ion influx into the cell through NMDARs only occurs when both presynaptic and postsynaptic neurons are stimulated at the same time.

- LTP is **input-specific**. Thus, it is restricted to activated synapses rather than to all synapses on a given cells. This feature of LTP is consistent with its involvement in memory formation allowing the selective storage of information at synapses.

The specificity of LTP can be explained by the fact that NMDA channels will be opened only at synaptic inputs that are active and releasing glutamate, thereby confining LTP to these sites even though EPSPs generated at active synapses depolarize the postsynaptic neuron.

- Another important feature of LTP is **associativity**. If one pathway is weakly activated while a neighbouring pathway onto the same cell is strongly activated, both synaptic pathways undergo LTP. This selective enhancement of conjointly activated sets of synaptic inputs is often considered a cellular analogous of associative learning, where two stimuli are required for learning to take place.

For what concerns associativity, a weakly stimulated input releases glutamate but cannot sufficiently depolarize the postsynaptic cell to relieve the Mg^{2+} block from NMDARs. If adjacent postsynaptic cells inputs are strongly stimulated, however, they provide the "associative" depolarization necessary to relieve the block.

1.5 MOLECULAR STRUCTURE OF NMDA RECEPTOR SUBUNITS

NMDA receptor subunits are modular structures that contain four discrete semiautonomous domains: the N-terminal domain (NTD), the agonist binding domain (ABD), both located in the extracellular region; then a membrane domain made of several transmembrane segments which form the ion channel; and an intracellular C-terminal tail (Figure 2).

In the extracellular region, there is a tandem of large globular domains which includes the N-terminal domain (NTD), encompassing the first 380 amino acids, and is involved in subunit assembly. Thanks to crystallographic studies, high-resolution structures of several isolated domains of NMDARs are now available (Paoletti, 2011). NTD shows sequence homology with the bacterial protein leucine/isoleucine/valine-binding protein (LIVBP). This domain plays a significant role in subunit assembly. In GluN2A and GluN2B, the NTD also contains binding sites for allosteric inhibitors such as Zn2+ and ifenprodil (Paoletti & Neyton, 2007).

The agonist-binding domain (ABD;~ 300 amino acids) consist of the S1 segment preceding the trans membrane segment M1 and the S2 segment sandwiched between the trans membrane segments M3 and M4. The isolated ABD, consisting of the S1 and S2 domains connected by a short peptide linker, retained the pharmacology of the full-length receptor, binding antagonists and agonists with normal affinity (Blanke & VanDongen,

2009; Paoletti, 2011). Numerous structures of ABDs have been solved, including those of GluN1, GluN3 and GluN2A subunits complexed with their natural ligand (glycine or d-serine for GluN1 and GluN3, glutamate for GluN2A). As expected, these structures show the typical bilobate (or clamshell-like) fold with the ligand bound in the central interlobe cleft (Paoletti, 2011).

TM domain is made of three transmembrane segments (M1, M3 and M4) plus a short re-entrant loop (P loop or M2). In addition to forming the ion pore, the TM series has signalling sequences that participate in subunit assembly, and N-glycosylation sites in the extracellular loop domain that confer either constitutive or activity-dependent synaptic delivery (Sanders et al., 2013). Both ABD and TM series show (low) sequence homology with bacterial proteins of known structure resembling an inverted KcsA potassium channel.

Finally, C-terminal domain (CTD) is highly variable in length depending upon the subunit, and is involved in receptor trafficking, anchoring and coupling to signalling complexes (see paragraph "*NMDA Receptor C-terminal tail and NMDAR associated molecular complex*") (Paoletti, 2011).
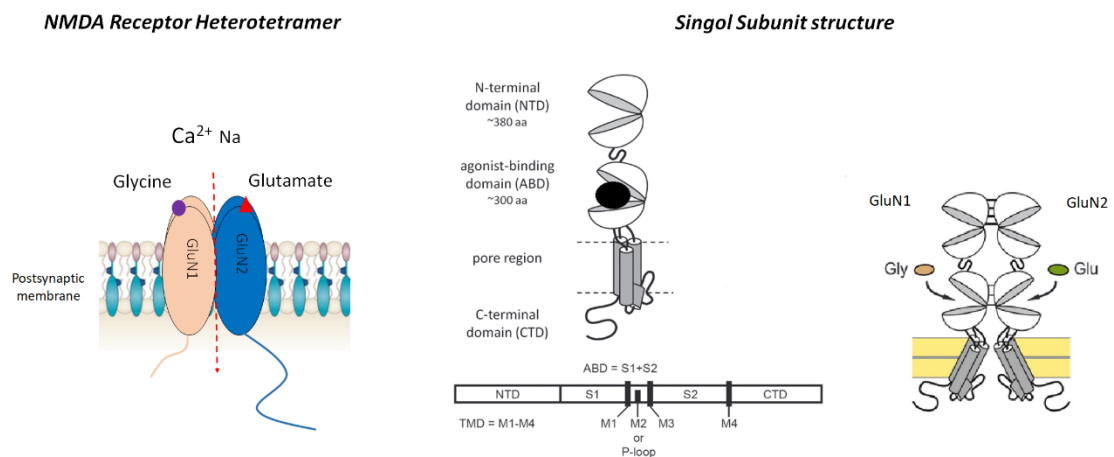
Figure 2: Schematic representation of the structure of NMDA glutamate receptor. Domain organization of an individual subunit (modified from "Molecular basis of NMDA receptor functional diversity" Pierre Paoletti European Journal of Neuroscience, Vol. 33, pp. 1351–1365, 2011).

1.6 NMDARs Subunits Properties

1.6.1 The GluN1 Subunit

The obligatory GluN1 subunit is ubiquitously expressed in the CNS, both embryonic and adult. However, there are developmental and regional variations depending on the type of GluN1 isoform (Paoletti, 2011). The GluN1 subunit is encoded by a single gene but has eight distinct isoforms (GluN1-1a to 4a and GluN1-1b to 4b) owing to alternative splicing (Ewald & Cline, 2009).

In the adult rat brain GluN1-2 subunits are widely and abundantly distributed throughout the brain. The GluN1-1 and GluN1-4 subunits have a quite complementary distribution pattern, the former being concentrated in the most rostral structures (including the cortex and hippocampus) while the latter is principally expressed in more caudal structures such as the thalamus and cerebellum. The GluN1-3 variants are expressed at only very low levels. Finally, the GluN1-a vs. GluN1-b variants have largely overlapping expression patterns but the 'a' forms outnumber the 'b' forms in most, but not all, brain regions (expression level ratio 5:1 in the forebrain but 1:5 in the cerebellum) (Figure 3). Notably, in the hippocampus, while the GluN1-a isoforms are expressed at high levels in all principal cell layers (dentate gyrus granule cells, CA1-3 layers), the GluN1-b isoforms are largely restricted to the CA3 layer (Paoletti, 2011).

The genetic elimination of GluN1 is lethal in neonatal stages, and studies using conditional GluN1 knock-out mice revealed an absence of functional NMDARs as the GluN2 subunits are retained in the ER. In addition, GluN1 influences some characteristics of NMDARs such as their inhibition by protons or zinc and their potentiation by polyamines. Finally, the GluN1 C-terminus contains several motifs that regulate receptor trafficking and binding to many proteins, including calmodulin, CaMKII, yotiao, alpha-actinin, tubulin, neurofilaments and DREAM (Sanz-Clemente et al., 2013).

1.6.2 The GluN2 Subunit

GluN2 subunits are encoded by four different genes GluN2A-D. The four GluN2 subunits, which are major determinants of the receptor's functional heterogeneity, show expression patterns that differ strikingly in both time (during development) and space (from one brain region to the other) (Paoletti et al., 2013)(Figure3).

In the embryonic brain, only GluN2B and GluN2D subunits are expressed, and the latter is mostly found in caudal regions. Major changes in the expression patterns of the GluN2 subunits occur during the first 2 postnatal weeks. GluN2A expression starts shortly after birth and rises steadily to become widely and abundantly expressed in virtually every CNS area in the adult. Concomitant to this progressive rise in GluN2A expression, GluN2D expression drops markedly, and in the adult, it is expressed at low levels mostly in the diencephalon and mesencephalon. In sharp contrast to GluN2D expression, GluN2B expression is maintained at high levels following birth, peaks around the first postnatal week and becomes progressively restricted to the forebrain areas (cortex, hippocampus, striatum, olfactory bulb), where it remains expressed at quite high levels (Paoletti, 2011).

Lastly, expression of GluN2C appears late in development (postnatal day 10 (P10)), and its expression is mainly confined to the cerebellum and the olfactory bulb.

GluN2A and GluN2B also differ for subcellular localization. Before recruitment to a synapse, NMDARs can cycle in and out of the plasma membranes of dendrites via exo- and endocytosis. More than 65% of synaptic NMDARs can shuttle between synaptic and extra synaptic sites. While nascent synapses are populated predominantly by GLUN2B-containing receptors before supplementation with GLUN2A-containing receptors, extra synaptic NMDARs are predominantly GLUN2B-containing receptors as shown by recordings from hippocampal, cortical, and cerebellar granule cell neurons (Ewald & Cline, 2009).

It follows that NMDARs with GluN2A are directly beneath transmitter release sites while NMDARs with GluN2B appear more concentrated perisynaptically (Sanders et al., 2013). GluN2B enrichment in extrasynaptic domains would fit with the idea that extrasynaptic NMDARs constitute a distinct population, serving a specific function. This idea is also quite satisfying when one considers that GluN2B-NMDARs have a higher affinity for glutamate, whose concentration is lower in the extrasynaptic space.

Developmental replacement of GluN2B by GluN2A at hippocampal synapses may also depend on the match between the cytoplasmatic carboxy terminal domain of GluN2 and the predominant MAGUK expressed at a given post-natal age. For instance, during early post-natal development, immature hippocampal synapses contain SAP102 and NMDARs with GluN2B. During maturation, as SAP102 is replaced by PSD95 and NMDARs with GluN2A replace NMDARs with GluN2B (Sanders et al., 2013). Interestingly, the shift

GluN2B-to-GluN2A does not occurs in knockout mice that do not express PSD95. Since biochemical assays show that SAP102 and PSD95 can both interact with GluN2A and GluN2B, it appears likely that pre-assembled GluN2A-PSD95 is preferentially inserted directly beneath transmitter release sites of more mature animals (Besshoh, Chen, Brown, & Gurd, 2007; Sans et al., 2003). However, the replacement of GluN2B- with GluN2A-NMDARs at synapses is not ubiquitous and complete, and GluN2B-NMDARs still represent a major portion of synaptic NMDARs in many other regions of the adult central nervous system (CNS). Therefore, even though it is broadly accepted, the idea that extra synaptic receptors are essentially GluN2B-NMDARs, or are at least enriched in GluN2B-NMDARs compared with their synaptic counterpart, is still open for debate (Papouin & Oliet, 2014).
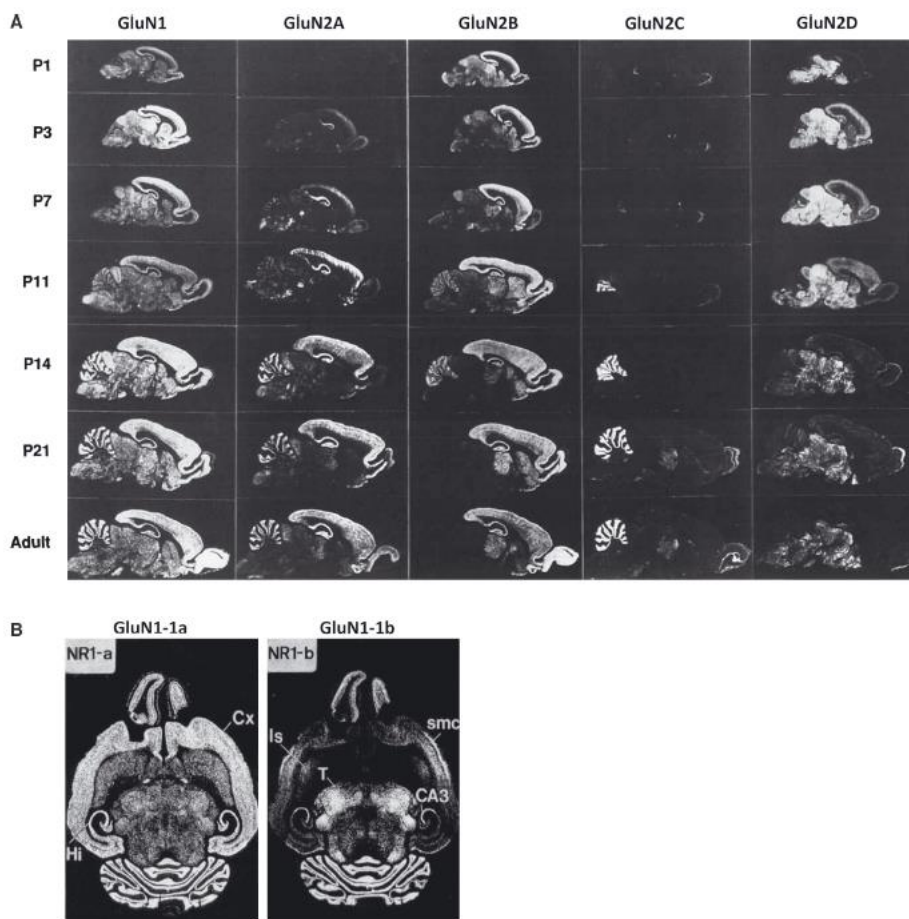
*Figure 3: Distribution of NMDAR subunit mRNAs in the rat brain. In situ hybridizations. **A**: Postnatal developmental change in the expression of GluN1 and GluN2A–D mRNAs. Sagittal sections. **B**: Expression of the two GluN1 splice variants GluN1-1a and GluN1-1b (containing the extracellular N1 cassette) at P12. Horizontal sections (from "Molecular basis of NMDA receptor functional diversity" Pierre Paoletti European Journal of Neuroscience, Vol. 33, pp. 1351–1365, 2011).*

1.6.3 THE GLUN3 SUBUNIT

Although considerably less attention has been dedicated to the GluN3 subunits, it is known that they also have unique properties. For example, unlike GluN2 subunits, GluN3 binds to glycine and not to glutamate. Therefore, NMDARs containing exclusively GluN1/GluN3 subunits can act as excitatory glycine receptors, which are impermeable to calcium. Tri-heteromers containing GluN2 and GluN3 subunits, however, are sensitive to glutamate, but they show a decrease in open probability, calcium permeability and magnesium sensitivity in comparison with GluN1/GluN2 NMDARs (Henson, Roberts, Perez-Otano, & Philpot, 2010). Therefore, the early onset of GluN3A expression and unique channel properties suggest that it may play a role during development and synaptic maturation by attenuating NMDAR function (Sanz-Clemente et al., 2013).

The GluN3A and GluN3B subunits also display differential ontogenetic profiles. GluN3A expression peaks in early postnatal life and then declines progressively. Conversely, GluN3B expression slowly increases throughout development, and in the adult, it is expressed at high levels in motor neurons and possibly other regions (Paoletti et al., 2013).

1.7 THE NMDA RECEPTOR C-TERMINAL TAIL AND THE NMDAR ASSOCIATED MOLECULAR COMPLEX

Among ionotropic glutamate receptor subunits, NMDAR subunits appear to be the longest, with the total number of amino acids per subunit in the range of 900–1500 amino acids (GluN1 being the shortest and GluN2B the longest). This difference in subunit size between AMPA, kainate and NMDA receptors is almost entirely accounted for by differences in the length of the intracellular carboxyterminal that is involved in receptor trafficking and couples receptors to signalling cascades (Paoletti et al., 2013).

As a matter of fact, NMDA receptor intracellular tail associates a range of molecules which form the NMDA receptor complex (Figure 4). Ca^{2+} ions entering the neuron through the NMDAR are privileged, because they are able to act locally on large signal transduction complexes associated with synaptic NMDARs, which consist of calcium-dependent enzymes, second messengers, protein kinases and phosphatases, scaffolding proteins, cytoskeletal elements, GTP binding proteins and their regulators, and adhesion molecules. NMDAR-mediated calcium influx activates these complexes, generating signal transduction cascades that produce long-lasting changes in synaptic function and structure (Blanke & VanDongen, 2009).

The intracellular carboxy terminus of NMDAR subunits contains various sequences that act as sites for interaction with anchoring and signaling proteins in the PSD. Well-described signaling domains in the carboxy terminus include binding and phosphorylation sites for αCaMKII, a mediator of LTP and LTD of synaptic efficacy (Gardoni et al., 1998; Merrill, Chen, Strack, & Hell, 2005); phosphorylation sites for the tyrosine kinases, Src and Fyn, that regulate channel function (Chen & Roche, 2007); an adaptor protein 2 (AP-2) binding site that regulates receptor internalization (Prybylowski et al., 2005); and a proximal ESDV sequence that permits anchoring at PDZ domains of scaffolding proteins in the PSD (Sanders et al., 2013; Sheng, 2001).
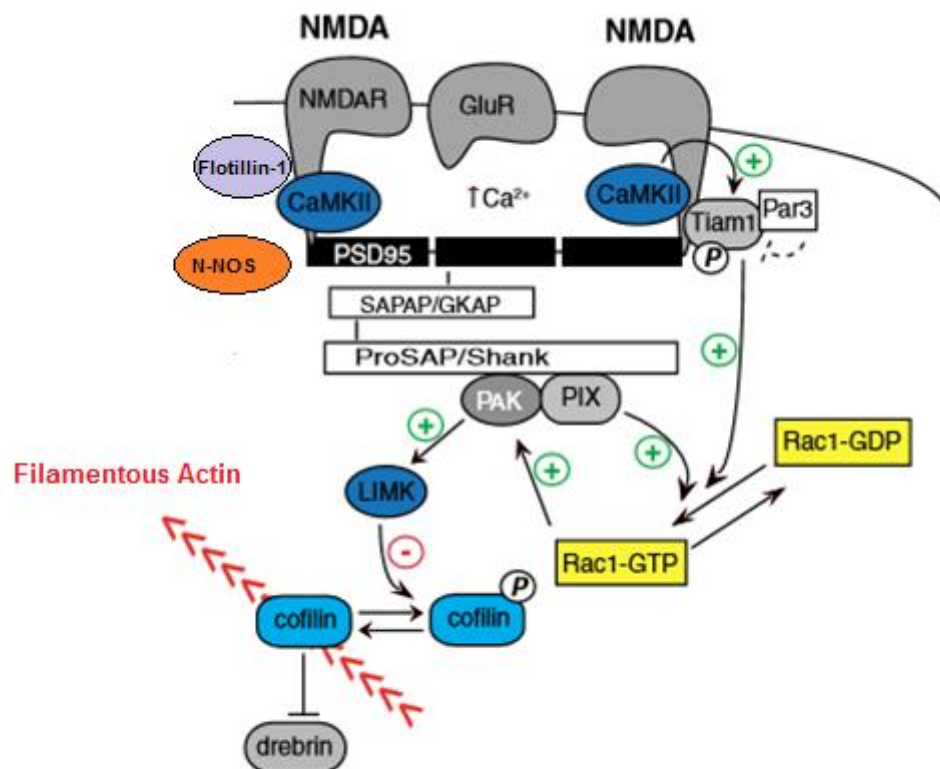
Figure 4: *NMDA receptor complex and actin-regulatory pathways controlled by NMDA receptors (modified from "Transmitting on actin: synaptic control of dendritic architecture" Vanessa Schubert and Carlos G. Dotti Journal of Cell Science 120, 205-212, 2007).*

The Rho-GTPase Rac1 has been reported to be part of the NMDA receptor complex as determined by proteomic analysis of the NMDA receptor complex (Husi & Grant, 2001). Tejada-Simon et al., also demonstrated that hippocampal slices stimulation with NMDA

Despite the cytosolic tails of NR2A and NR2B subunits are highly homologous, the sites of their interaction with CaMKII as well as the regulation of this binding differ. In particular, CaMKII dependent phosphorylation of PSD-95 serine 73 causes GluN2A dissociation from PSD-95, while it does not interfere with GluN2B binding to PSD-95 (Gardoni, Polli, Cattabeni, & Di Luca, 2006).

GluN2A and GluN2B share some common binding partners (such as postsynaptic density protein 95 (PSD-95), (Sheng & Kim, 2011), they bind differentially to some other proteins. For example, GluN2A-NMDARs interact with Homer and β-Catenin (Al-Hallaq, Conrads, Veenstra, & Wenthold, 2007), whereas GluN2B-NMDARs bind synaptic Ras GTPase activating protein (SynGAP)(Zhou & Sheng, 2013).

induced Rac1 activation and translocation to the membrane. Interestingly, they also demonstrated that NMDA-induced activation of Rac1 results in a physical association of Rac1 with the NMDA receptor complex (Tejada-Simon, Villasana, Serrano, & Klann, 2006).

NMDA receptor complex can also associate synaptic lipid raft. In fact, different GluN2 subunits could be segregated via interaction with lipid rafts. Consistent with this idea are data showing that both GluN2A and GluN2B interact with the lipid raft associated protein Flotillin-1 (Swanwick, Shapiro, Yi, Chang, & Wenthold, 2009). Additionally, GluN2A is divided evenly between the postsynaptic density and rafts, whereas GluN2B is relatively depleted from rafts (Fetterolf & Foster, 2011). These data are all consistent with a model in which lipid rafts constitute an integral structural component of the postsynaptic apparatus and supports the suggestion that they are involved in the regulation of postsynaptic structure and function (Delint-Ramirez et al., 2010).

1.8   NMDARs and Lipid Raft

1.8.1   the Lipid Raft Structure: Flotillin microdomains as signalling platforms

Lipid rafts are specialized structures that form an organized portion of the membrane with concentrated signaling molecules and link to the cytoskeleton (Simons & Sampaio, 2011). These membrane domains and their unique protein and lipid content are critical for many cellular functions. The localization of receptors and signalling molecules into lipid raft partially depends upon binding with lipid-raft associated proteins such as Flotillins.

Hippocampal NMDARs interact with lipid raft associated protein Flotillin-1 and 2, this interaction has been observed using a two-yeast hybrid screening, while looking for new NMDARs interactors (Swanwick et al., 2009).

The Flotillin family is composed of two highly homologous proteins, Flotillin 1 and Flotillin 2 that share ~50% amino acid sequence identity. They form part of a larger family of proteins that are characterised by the presence of a prohibitin homology (PHB) domain (Browman, Hoegg, & Robbins, 2007). PHB domain containing proteins have distinct functions in varied organisms, tissues and cellular locations, but share the common feature of behaving as integral membrane proteins that oligomerise to form microdomains. These microdomains demonstrate insolubility in cold non-ionic detergents and buoyancy on sucrose density gradients, both of which are classical hallmarks of membrane rafts. The PHB domain confers membrane association through the presence of acylation sites and putative hydrophobic hairpins that are thought to insert into the inner leaflet of the membrane. Flotillin-2 is myristoylated on Gly2, and its major palmitoylation site is found at Cys4 (Neumann-Giesen et al., 2004). By contrast, Flotillin-1 is not myristoylated but is palmitoylated on Cys34 (Otto & Nichols, 2011).

Flotillin microdomains represent assembly sites for active signalling platforms that typically involve the activity of Src family kinases. In hippocampal neurons, Flotillin-1 promotes formation of glutamatergic synapses and interacts with synaptic adhesion-like molecules (SALMs) to regulate neurite outgrowth by coordinating adhesion, exocytosis and actin cytoskeleton dynamics (Swanwick, Shapiro, Vicini, & Wenthold, 2010).

1.8.2 NMDAR AND LIPID RAFT: A DYNAMIC ASSOCIATION

Neurons are polarized cells whose function depends on the segregation of proteins to specific microdomains of the membrane (Hering, Lin, & Sheng, 2003). The synapses, both the presynaptic and postsynaptic sites, are highly enriched in lipid rafts. Indeed, lipid rafts not only contribute to neurotransmitter exocytosis in presynaptic terminals, but also in the post synapse modulate neuronal signaling through clustering of neurotransmitter receptors, ion channels and components of downstream effectors (Fan et al., 2014).

Numerous PSD proteins such as NMDA receptors (GluN1, GluN2A and GluN2B), AMPA receptors (GluR1 and GluR2), metabotropic glutamate receptors (mGluRs), PSD-93/95, CaMKII, and cadherin, are associated with synaptic lipid rafts. The association of the PSD with lipid rafts might be important in signal integration and synaptic function.

Accumulating evidence has indicated that precise localization of neurotransmitter receptors, transporters, ion channels and other synaptic proteins in lipid rafts can be regulated by cholesterol and this regulation is critical for synaptic plasticity. In addition, lipid raft disruption leads to depletion of excitatory and inhibitory synapses, loss of dendritic spines, and instability of surface AMPA receptors (Hering et al., 2003).

The level of interaction between NMDARs and lipid raft may be dynamically enhanced under certain conditions, such as high amounts of glutamate due to increased neuronal activity (Swanwick et al., 2009).

Recent studies describe that NMDARs trafficking to lipid rafts, is dynamically enhanced during synaptic plasticity process as memory formation. In particular, Delint-Ramirez and co-workers analysed the recruitment of NMDARs to synaptic lipid rafts in the hippocampus and they found that spatial training induces the selective recruitment of GluN1 and GluN2A subunits (Delint-Ramirez et al., 2010; Delint-Ramirez, Salcedo-Tello, & Bermudez-Rattoni, 2008).

Moreover, movement of NMDAR from lipid rafts to PSDs was reported following ischemia and this was correlated with increased tyrosine phosphorylation of GluN2A and GluN2B subunits in rafts (Besshoh, Bawa, Teves, Wallace, & Gurd, 2005).

The findings are consistent with a close structural and functional relationship between lipid rafts and PSDs and support a role for synaptic lipid raft in the modulation of synaptic signaling.

2 P140CAP

2.1 DISCOVERY, EXPRESSION AND FUNCTIONS

p140Cap is a scaffold protein of 140kDa mainly expressed in brain, testis and epithelial-rich tissues such as mammary gland (Di Stefano et al., 2011).

In neurons, p140Cap is localized in the excitatory synapse both in the pre- and post-synaptic compartments (Ito et al., 2008), and its silencing leads to a decreased number of mature mushroom spines. These observations provided evidence that p140Cap has a key role in the control of synaptic remodelling and in the regulation of dendritic spine morphology (Hayashi et al., 2011; Jaworski et al., 2009).

p140Cap discovery dates back to 2000 when Lian Li et al. where looking for SNAP-25 interacting proteins in rat brain (Chin, Nugent, Raynor, Vavalle, & Li, 2000). From this investigation, they originally identified and characterized a 145kDa protein called SNIP (SNAP-25b-Interacting Protein) that specifically interacts with the N-terminal domain of SNAP25 and is involved in vesicular trafficking, likely by anchoring SNAP-25 to the membrane cytoskeleton. Afterwards, the human KIAA1684 protein, with a molecular mass of 140kDa, was discovered as the human orthologue of mouse p140Cap and rat SNIP proteins. Based on its identification in our lab as a partner of p130Cas, we named this protein p140Cap (p130Cas-associated protein)(Di Stefano et al., 2004).

In 2007, p140Cap was characterized as a novel Src-binding protein, which negatively regulates Src activation via C-terminal Src kinase (Csk) in non-neuronal cells (Di Stefano et al., 2007). In breast cancer cells, p140Cap negatively regulates cell spreading, motility, growth and invasion, affecting tumour cell properties (Damiano et al., 2012; Di Stefano et al., 2004; Di Stefano et al., 2007).

2.1.1 GENOMIC ORGANIZATION OF P140CAP

p140Cap is coded by the Src Kinase Signaling Inhibitor 1 gene (*Srcin1*), which is highly conserved in mouse, rat, dog, cow, zebrafish and in humans (Di Stefano et al., 2011). *Srcin1* maps on chromosome 11 in mouse with a coding sequence spanning on 22 exons (Di Stefano et al., 2004). The first two exons, 1a and 1b, are subjected to alternative splicing on exon 2 resulting in mRNA isoforms coding for two proteins that differ in their N-terminal portion. In human the *Srcin1* gene maps on Chromosome 17q21.1. and it counts 27 exons.

2.2 P140CAP: STRUCTURE, DOMAINS ORGANIZATION AND INTRINSIC DISORDER
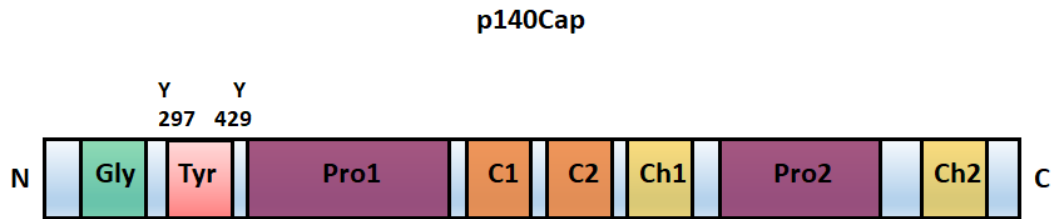
p140Cap

Figure 5: Schematic representation of the structure of p140 Cas-associated protein (p140Cap) also known as SRCIN1.

p140Cap is an adaptor protein which interacts with many partners involved in cell polarity, cell–cell adhesion and synaptic signal transduction.

p140Cap is a highly hydrophilic protein and contains neither a signal sequence nor a putative trans-membrane domain. However, p140Cap contains a putative N-terminal myristylation site, a tyrosine-rich domain, two proline-rich regions, a coiled-coil domain, two charged amino acid rich regions near the C-terminus and a putative actin-binding site (Di Stefano et al., 2011) (Figure 5).

- The analysis of p140Cap amino acidic sequence through in silico myristoylation prediction tool for glycine myristoylation MYRbase (http://mendel.imp.ac.at/myristate/myrbase/) revealed a reliable myristylation site in p140Cap N-terminal sequence (GNAPSQDPERSSPPMLS). The myristate moiety is important for protein subcellular localization by facilitating protein-membrane as well as protein–protein interactions (Martin, Beauchamp, & Berthiaume, 2011).

- p140Cap is tyrosine phosphorylated in epithelial cells upon integrin mediated adhesion and EGF receptor activation (Di Stefano et al., 2004). Two tyrosines contained in the sequences "EPLYA" (Tyr 264) and "EGLYA" (Tyr 396) were identified as the major residues responsible for p140Cap tyrosine phosphorylation and they play a crucial role for p140Cap binding to Csk kinase (Repetto et al., 2013).

- p140Cap contains two proline-rich regions with multiple PPXY and PXXP. The proline-containing motifs PPXY and PXXP are involved in protein-protein interactions with the WW domain (two signature tryptophan residues that are spaced 20-23 amino acids apart and the SH3 domain, respectively (Chin et al., 2000). In particular, the terminal proline-rich domain of p140Cap has been found to associate the SH3 domains of Src kinase (Di Stefano et al., 2007) and of

Vinexin (Ito et al., 2008). A short 92 amino acid C-terminal region (aa 1124–1216) in the proline-rich 2 of p140Cap also directly associates with all members of the microtubule (MT) plus end tracking protein EB family (Jaworski et al., 2009). Finally, p140Cap has also been shown to pull-down with Cortactin, a Src kinase substrate and F-actin binding protein (Damiano et al., 2012).

- In p140Cap amino acidic sequence two regions with high probability of forming a coiled-coil were identified (Chin et al., 2000). The coiled-coil feature of these regions was supported by their sequence similarity to the coiled-coil regions of various filamentous cytoskeleton-associated proteins such as myosin heavy chains and tropomyosin (Chin et al., 2000).

2.2.1 P140CAP SECONDARY STRUCTURE AND INTRINSIC DISORDER

Despite the widely accepted protein paradigm "sequence-to-structure-to-function", intrinsically flexible but biologically active proteins have been repeatedly observed during the modern history of protein science. In fact, naturally flexible proteins, instead of being just rare exceptions, represent a unique and very broad class of proteins. The accepted meaning of the "intrinsic disorder proteins" (IDPs) is based on notion that a corresponding protein (or protein region) is biologically active, yet exists as collapsed or extended, dynamically mobile conformational ensemble, either at the level of secondary or tertiary structure (Uversky, 2015).

We run the analysis of secondary structure and disorder prediction of p140Cap by Phyre2 (Protein Homology/analogY Recognition Engine V 2.0) database revealed that 28% is alpha helix, 2% is beta strand and 75-77% of the protein is disordered (Angelini and Menchise, unpublished). Furthermore, the analysis of p140Cap amino acidic sequence, performed using the DisEMBL Intrinsic Protein Disorder Prediction web server, confirmed a high grade of disorder. In particular, DisEMBL computational tool makes use of three different criteria to define the disorder level of protein residues:

- 1-Loops/coils. Even though loops/coils are not necessarily disordered; protein disorder is only found within loops. It follows that loop assignment can be used as a necessary but not sufficient requirement for disorder.

- 2-Hot loops. They constitute a subset of loop having a high degree of mobility as determined from C-alpha temperature (B-)factors. It follows that highly dynamic loops should be considered protein disorder.

- 3-Missing coordinates. Non-assigned electron densities in X-ray 3D structures most often reflect intrinsic disorder, and can been used in disorder prediction (Figure 6). p140Cap disorder prediction confirmed a high percentage of disorder especially in the C-terminal region according to all the criteria. Region between residues 300 and 600 also presents a high disorder degree regarding the loop content.
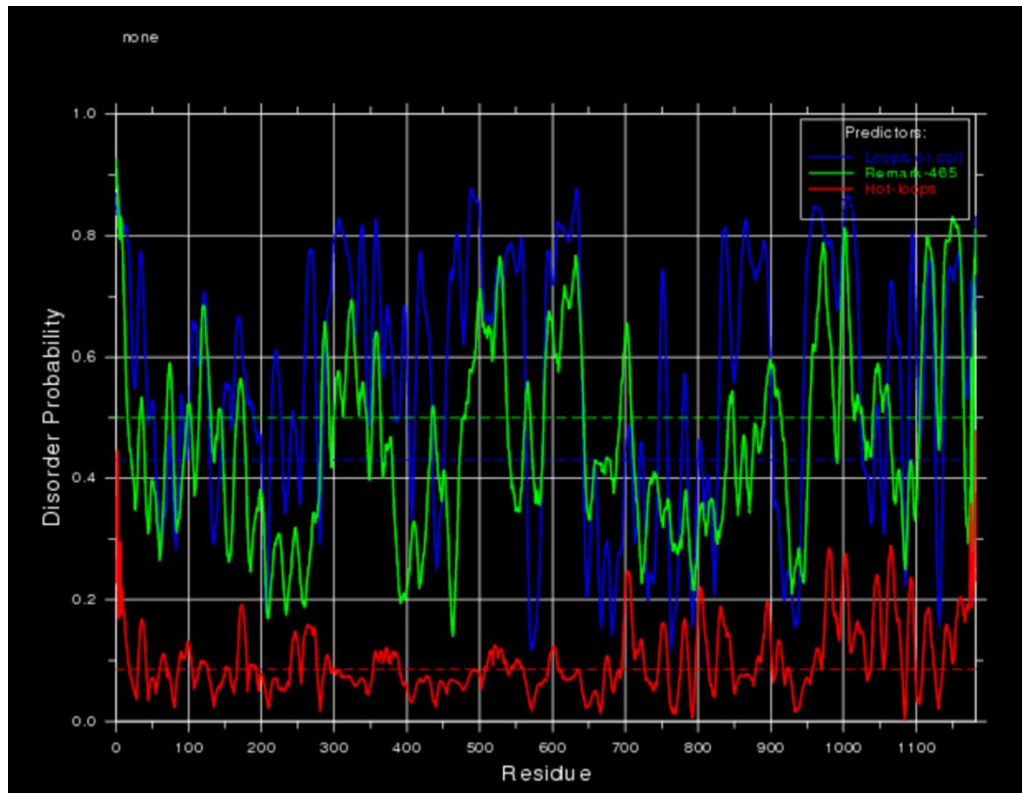
Figure 6: *p140Cap disorder probability calculated on human amino acidic sequence with DisEMBL. Predictions are shown according to each of the three definitions (see text). The predicted probabilities are shown as curves along the sequence and scores should be compared to the corresponding random expectation value (dotted lines).*

A further indication of the IDPs character of p140Cap could be found in its amino acid composition. In fact, the analysis of ProtParam (ExPASy.org) revealed that p140Cap is significantly depleted in so-called "order promoting amino acids" such as Ile, Val, Trp, Tyr, Phe, Cys, and Asn and is substantially enriched in "disorder promoting amino acids" (Ala, Arg, Gly, Gln, Ser, Glu, Lys, Pro) (Uversky, 2015).

Scaffold proteins exploit several intrinsic disorder facilitated mechanisms to enhance function so that they get more functionality from less structure (Cortese, Uversky, & Dunker, 2008). IDPs or intrinsically disordered regions (IDRs) within proteins are present in a large fraction of the human proteome and are important for the assembly by phase

transition of membrane-less organelles and other cytoplasmic or nucleoplasmic structures. The low complexity of IDRs provides the structural flexibility enabling the interaction with distinct partners and favors the formation of large assemblies driven by phase transition (Astron & de Curtis, 2015).

In this context, p140Cap mainly disordered structure may represent an important feature for its scaffold role. In fact, it could undergo a disorder-to-order transition upon interaction with specific binding partners, acting as a modulator of alternative pathways by promoting specific interactions among signaling proteins.

2.3   P140CAP IN THE EXCITATORY SYNAPSE

p140Cap is strongly expressed in the brain. The dissection of 13 region of rat brain showed a relative abundance of p140Cap in the cerebellum and telencephalon, including the hippocampus, neocortex, entorhinal cortex, and visual cortex (Ito et al., 2008). The analysis of protein expression level in rat brain during embryonic and postnatal developmental stages revealed that p140Cap is expressed from embryonic day 12.5, although its expression dramatically increased between embryonic days E14.5 and E18.5, suggesting an involvement of the protein in neuronal development (Ito et al., 2008). For what concern p140Cap subcellular localization, biochemical fractionation and immunoblotting showed that PSD-95 and p140Cap are enriched in both mouse and rat synaptic plasma membrane fraction (Alfieri et al., 2017). Moreover, electron microscopy analyses revealed that p140Cap is located mainly at post-synapses but also at pre-synapses (Ito et al., 2008) (Tacchetti, Raimondi and Alfieri, unpublished). p140Cap localization at pre-synapses is consistent with the previous report of p140Cap interaction with the SNARE protein SNAP-25 (Chin et al., 2000), and with synaptophysin (Ito et al., 2008), which may underline a role for p140Cap in the regulation of neurotransmitter release.

For what concerns p140Cap accumulation at dendritic spines, in primary hippocampal neurons, its localization is mainly at the post-synaptic density (PSD), where it plays a role in the regulation of dendritic spines morphology (Jaworski et al., 2009). In fact, although polymerized actin is still the main component of the spine cytoskeleton, recent evidence suggests that microtubules actively participate in the shaping of dendritic spine morphology. p140Cap has been shown to associate with EB3, a microtubule tip-tracking protein, and to favour EB3 entry into spines, to modulates spine morphology. Thus,

p140Cap promotes EB3-labeled growing microtubule ends recruitments to spines, as well as it modulates cortactin function and dendritic spine actin dynamics. Since p140Cap is an inhibitor of c-Src (Di Stefano et al., 2007) and it localizes at the PSD with Cortactin, which is one of the main Src substrate, it was proposed that dynamic microtubules may affect actin polymerization through p140Cap-mediated Src regulation (Jaworski et al., 2009).

2.4 P140CAP KO MICE MODEL CHARACTERIZATION

p140Cap knockdown *in vitro* in primary hippocampal neurons both by siRNA (Tomasoni et al., 2013), and by shRNA (Jaworski et al., 2009) lowers the number of mushroom spines (mature spines) and proportionally increases the number of dendritic filopodia (immature spine). Moreover, it also decreases the number of PSD95 positive puncta (Tomasoni et al., 2013).

Dynamic changes in spine morphology and number play a fundamental role in cognitive functions. Indeed, several neurological disorders such as autism spectrum disorders, schizophrenia and Alzheimer's disease are linked to aberrant shape and number of dendritic spines.

p140Cap *in vivo* relevance was investigated by using a total knock-out mouse model (Repetto et al., 2014). The characterization of these mice revealed that p140Cap is a key element for both cognitive functions and synaptic plasticity. Indeed, p140Cap KO mice are impaired in object recognition test, as well as in LTP and in LTD measurements. Moreover, primary neurons obtained from p140CapKO mice show a strong reduction in the number of mushroom spines and an abnormal organization of synapse-associated F-actin. Indeed F-actin clusters display an abnormally elongated morphology, running parallel to the dendritic shaft membrane rather than protruding from it.

These phenotypes are most likely caused by a local reduction of the inhibitory control of RhoA and of cortactin toward the actin-depolymerizing factor cofilin. Indeed, p140Cap may control the levels of active RhoA in synaptosomes by decreasing Src-dependent tyrosine phosphorylation of the RhoA-specific GTPase-activating protein p190RhoGAP. Moreover, p140Cap may also affect the local recruitment of active RhoA through Citron-N, a scaffold protein required for spine maintenance which associates p140Cap (Repetto et al., 2014). However, it is possible that the memory defects and electrophysiological phenotypes are not only related to actin dynamics but rather depend on other processes,

such as the glutamate ionotropic receptors turnover which is closely correlated with the dynamic changes of DSs (Repetto et al., 2014).
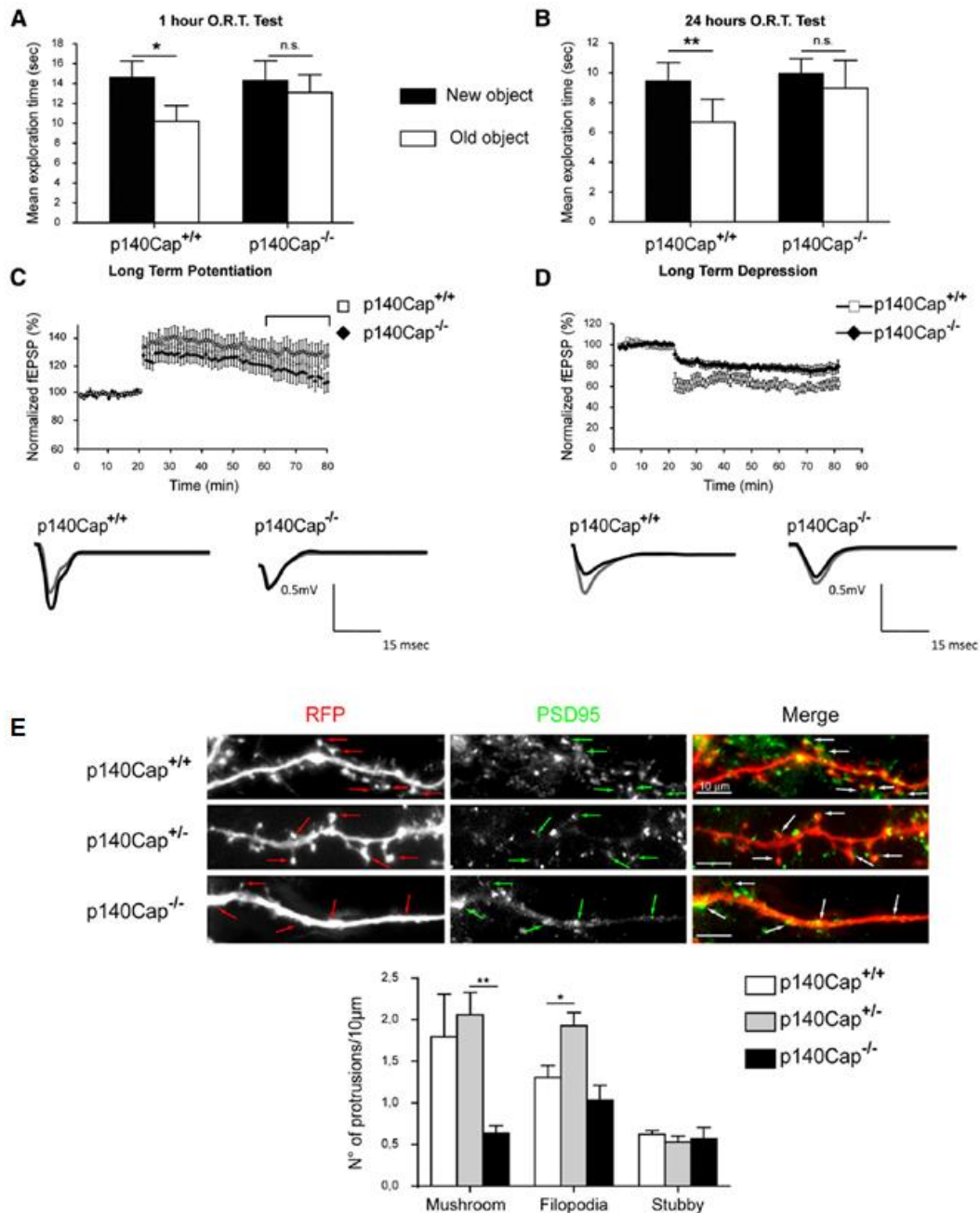
Figure 7: p140Cap KO mice display reduced memory consolidation and impaired synaptic plasticity. A, B, p140Cap KO mice display impairment in visual object recognition test ORT. C, D, p140Cap is important for synaptic plasticity both of the LTD and of the LTP type. LTP and LTD measurements on perirhinal cortex of p140Cap KO and control mice. E: Primary hippocampal neurons from mice of the indicated genotypes were transfected with p-mRFP for indications of protrusions filling ("p140Cap Regulates Memory and Synaptic Plasticity through Src-Mediated and Citron-N-Mediated Actin Reorganization" Repetto D et al., The Journal of Neuroscience, January 22, 2014 • 34(4):1542–1553)

2.5 p140Cap SYNAPTIC INTERACTOME

To deeply understand the molecular complexes and pathways underlying p140Cap function, a quantitative proteomic and bioinformatic analysis of p140Cap immunoprecipitation from mouse crude synaptosomes preparations was performed (Alfieri et al., 2017). The results of this proteomic study show that p140Cap localization is mainly, but not exclusively, in the PSD. Indeed, an exceptionally high enrichment of p140Cap identified interactors overlaps with published PSD proteomic datasets (Alfieri et al., 2017). Moreover, in immunoprecipitation studies p140Cap was detected in complexes with postsynaptic molecules as PSD95 (Dosemeci et al., 2007) and mGluR5 (Farr et al., 2004), and was initially identified as an interactor of SNAP-25 in a two-hybrid screen (Chin et al., 2000). Subsequent studies have shown that this interaction takes place in the PSD, involving also PSD95, and is required for spine morphogenesis (Tomasoni et al., 2013).

The bioinformatic analysis of p140Cap synaptic interactors allowed classifying proteins into functionally related modules. In particular, correlation between the experimentally measured protein abundances and the Reactome pathway terms for the interacting proteins allowed the classification of p140Cap interactors into 3 modules: module 1 for interactors involved in pathways related to receptors trafficking and chemical signaling through the synapse; module 2 for interactors involved in adhesion and junction; module 3 for interactors involved in axon guidance functions (Figure 8). In particular in module 1 NMDAR subunits GluN2A and GluN2B were identified as high fidelity interactors of p140Cap.

Taken together, the functional enrichment analysis from these three distinct sources (GO, Reactome and KEGG) indicate that the p140Cap interactors exhibit functions relevant to synaptic structure, synaptic transmission and plasticity.
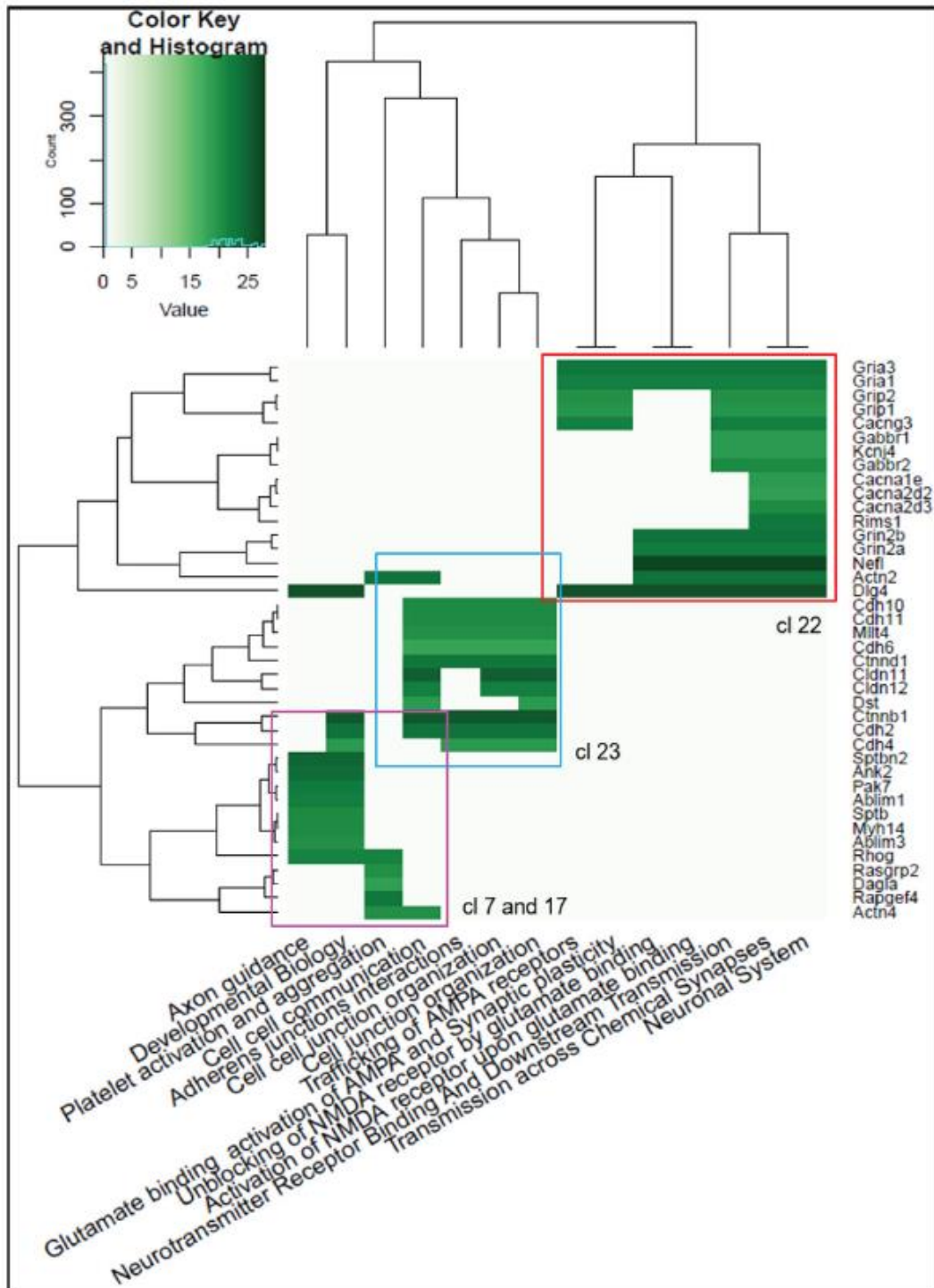
Figure 8*: Heatmap of the Reactome Pathway enrichment analysis clustering. Intensity is based on the average relative protein abundance in mass spectrometry. Three main modules are observed: upper right, Module 1; centre, Module 2; and, bottom left, Module 3 (Synaptic Interactome Mining Reveals p140Cap as a New Hub for PSD Proteins Involved in Psychiatric and Neurological Disorders. Alfieri et al., Front. Mol. Neurosci. 10:212. 2017).*

2.6 P140CAP AND LIPID RAFT ASSOCIATION

p140Cap sub cellular localization in neurons was described by brain homogenates fractionation experiments. The analysis of p140Cap and SNAP-25 co-distribution in synaptosomal fractions of rat brain homogenates revealed that p140Cap co-fractionates with SNAP25 on plasma membrane but not on synaptic vesicles (Chin et al., 2000). Further characterization of p140Cap sub localization showed that PSD95 and p140Cap are enriched in the synaptic plasma membrane fraction of brain homogenates (Jaworski et al., 2009). All together, these data revealed p140Cap enrichment both in the pre- and in the postsynaptic membrane, describing its possible role as a membrane-cytoskeleton linker protein. Moreover, p140Cap membrane association is consistent with its putative reliable N-terminal myristylation sequence.

For what concerns p140Cap association with membrane lipid raft, RaftProt (http://lipid-raft-database.di.uq.edu.au/), a database of mammalian lipid raft-associated proteins as reported in high-throughput mass spectrometry studies, revealed p140Cap presence in detergent resistant membrane (DRM) fraction in two independent lipid raft proteomic analysis both performed on rat brain (Jia et al., 2006; Suzuki et al., 2011).

In particular, in the paper of Suzuki et al., liquid chromatography coupled with tandem mass spectrometry (LC/MS/MS) was performed on postsynaptic membrane rafts and p140Cap was found to be significantly associated with the detergent resistant membrane of the post synapse (p=2,16E-05).

3 AIM OF THE RESEARCH

p140Cap is a scaffold protein involved in the regulation of dendritic spines morphology. p140Cap knockout (KO) mice neurons show reduced number of mushroom spines and a proportional increase in the number of dendritic filopodia (Repetto et al., 2014). Consistently, p140Cap KO mice display defective long-term potentiation (LTP) and reduced long-term depression (LTD), two forms of synaptic plasticity necessary for learning and memory. Indeed, p140Cap KO mice have impaired memory consolidation. These defects could be due to an improper functioning and/or localization of NMDARs, which play a crucial role in LTP induction. However, p140Cap involvement in NMDAR mediated synaptic plasticity has not yet been investigated.

p140Cap involvement in excitatory transmission mediated by NMDARs has also been suggested by the proteomic analysis of p140Cap interactome in synaptosomes. This analysis revealed that NMDAR subunits GluN2A and GluN2B are potentially high-fidelity interactors of p140Cap (Alfieri et al., 2017).

The aim of this project was to assess whether p140Cap plays any role in synaptic plasticity events mediated by the NMDAR. To reach this goal, we plan to dissect the molecular interaction between p140Cap and the NMDA receptor subunits and to generate a model of interaction. Moreover, we plan to analyse if p140Cap may influence either NMDA receptor localization and/or the molecular composition of NMDA receptor associated complexes, thus impairing LTP/LTD induction and dendritic spine architecture.

4 EXPERIMENTAL PROCEDURES

4.1 ANIMALS

Mixed 129Sv × C57BL/6J p140Cap heterozygous mice were generated as described in Repetto et al., 2014. All experiments were approved and performed in accordance with the Italian law (authorization D.M. n°279/95B 27/11/1995) and dispositions of "D.L. n°116, 27/1/1992 in relation to animal use and protection in scientific research." Male, 3-4-month-old wild-type and p140Cap knockout littermates were used for synaptosomes preparations. Animals were sacrificed by cervical dislocation.

4.2 CELL CULTURES

Human HEK293 epithelial cells and COS-7 cells were obtained from American Type Culture Collection. Cells were cultured in DMEM medium supplemented with 10% heat-inactivated fetal bovine serum (FBS) and penicillin/streptomycin (100 U/mL and100 g/mL, respectively) at 37°C in a 5% CO2 atmosphere and 95% of humidity.

4.3 PRIMARY HIPPOCAMPAL NEURONS CULTURE

Mouse hippocampal neurons were established from the hippocampus of E16–E17 pups derived from breeding of heterozygous mice, or p140Cap+/- female with p140Cap+/-male. Isolated hippocampus was washed with ice cold HBSS (Gibco) and then incubated with 0.25% trypsin for 15 minutes at 37°C. The tissue pellet was washed two times with prewarmed HBSS at 37 °C for 10 minutes. Neurons dissociation was achieved by gently triturating the tissue with p1000 pipette and then with a p200 pipette. The dissociated cells were plated onto 20mm glass coverslips coated with poly-L lysine (Sigma) at the density of 8×10^4 cells/coverslip and maintained in Neurobasal (Invitrogen) with B27 supplement and antibiotics, 2mM glutamine and 2mM glutamate. Mature neurons (day in vitro DIV 16-17) were fixed in paraformaldehyde (PFA) 4% and sucrose 4% (Sigma Aldrich) for 8min at room temperature or with pre-cooled methanol for 10 minutes at -20°C.

4.4 DNA CONSTRUCTS

For expression in mammalian cells, full-length mouse p140Cap cDNA was cloned into the BamHI site of pCDNA3.1/Myc-Hys expression vector (Invitrogen) and sequenced. Full length mouse p140Cap cDNA was cloned into the EcoRI-KpnI sites of pEGFP-N2 vector (BD Biosciences Clontech, Palo Alto, CA) and sequenced (Di Stefano et al., 2004). Constructs expressing p140Cap domains were cloned as described: full-length p140Cap cDNA was digested with XhoI. A DNA fragment of 2310 bp and a fragment of 1100 bp, corresponding to p140Cap aa 1-770 and aa 770-1140 respectively were obtained and cloned into the XhoI site of pCDNA3.1/Myc-Hys expression vector.

p140Cap aa 219-477 was obtained by full-length p140Cap digestion with PSTI and cloned into the PSTI site of pCDNA3.1/Myc-Hys.

p140Cap aa 351-691 was obtained by site specific mutagenesis from full-length mouse p140Cap. Forward primer was designed to incorporate a restriction site for NHEI (1158 bp) (primer sequence: GCTGGCTAGCTGCAATGGACTCCCCGCCT), reverse primer was designed to incorporate a restriction site for HINDIII (2175 bp) (primer sequence: GCAGAAGCTTGACAGCAGTGGGCTG). The amplified region was cloned into pCDNA3.1/Myc-Hys expression vector (Invitrogen).

p140Cap aa 667-866 was obtained by site specific mutagenesis from full-length mouse p140Cap. Forward primer was designed to incorporate a restriction site for XbaI (primer sequence: AGATCTCCTCGGCCAGCAGCACCCCTGCA), reverse primer was designed to incorporate a restriction site for HINDIII (primer sequence: AAGCTTCTAACCCTCATCCACTTGCCTTCG) the amplified DNA was cloned into XbaI/HindIII sites of pCDNA3.1/Myc-Hys expression vector from the p-GEM vector.

P140Cap aa 770-1217 was cloned into Nhe site of pCDNA3.1/Myc-Hys expression vector.

pEGFP-GLUN2A was a gift from Stefano Vicini (Addgene plasmid # 17924), pEGFP-GluN2B was a gift from Stefano Vicini (Addgene plasmid # 17925). PSD-95 FLAG was a gift from Wei-dong Yao (Addgene plasmid # 15463). GST-GluN2A (1049-1464), GST-GluN2A (1349-1464) and GST-GluN2A (1244-1389) C-terminal tail constructs were kindly provided by Professor Gardoni (Gardoni et al., 1999).

4.5   CELL TRANSFECTION

4.5.1   CALCIUM-PHOSPHATE TRANSFECTION

HEK293 cells were transfected by calcium phosphate precipitation. Up to 15 µg of DNA can be used for one 10 cm plate. If more than one plasmid was used for transfecting the same plate, DNA amounts was equalized among different plates by adding control vector plasmid DNA, so that the total amount of plasmids used for each plate is the same. Cell density was 50-80% confluent on the day of transfection. For transfection DNA was mixed with sterilized milliQ water and 50µL of $CaCl_2$ 2M to a final volume of 500 µL. The mix was slowly dropwise added to 500 µL of HBS while aerating the mix by gently vortex. The solution was incubated 15 minutes at room temperature and then was mixed with complete medium and dropped around the plate. 24 hours after transfection, the medium was gently aspirated and prewarmed fresh medium was added to the plates. The following day, the cells were harvested, and proteins were extracted.

4.5.2   LIPOFECTAMINE LTX TRANSFECTION

Lipofectamine LTX (Invitrogen) was used for COS-7 cells and primary neurons transfection. The day before transfection, COS-7 cells were plated at the density of $5x10^4$/cells for coverslips in a 24 well plate. For each coverslip, 0.5 µg of DNA (GluN2A-eGFP, GuN2B-eGFP, RFP-p140Cap full length, myc-p140Cap full-length, myc-p140Cap (aa 1-770), myc-p140Cap (aa 728-1217), flag-PSD95) were diluted into 100 µl of DMEM antibiotic and serum free. PLUS™ Reagent was directly added to the diluted DNA (a 1:1 ratio to DNA) and incubated for 5 minutes at room temperature. 2µl of Lipofectamine LTX was added into the above diluted DNA solution and incubate for 25 minutes at room temperature to form DNA-Lipofectamine LTX complexes. The solution was directly added to each well mixed gently by rocking the plate back and forth. The cells were incubated at 37°C in a CO2 incubator for 36 hours and then were fixed with ice-cold 100% methanol for 15 minutes at -20°C for immunostaining experiments.

Primary hippocampal neurons were transfected at 14–16 DIV with Lipofectamine LTX using 1µg of cDNA plasmid myc-p140Cap (aa 1-770) or control myc-empty vector. Neurons were fixed 48 hours after transfection with 4% Paraformaldehyde (PFA) 4% Sucrose for 8 minutes at room temperature.

4.6 IMMUNOFLUORESCENCE

All the procedures were performed at room temperature. Fixed cells on coverslips were washed 3 times with PBS for 10 minutes. Only cells fixed with PFA were permeabilized with PBS 0.1% Triton X-100 for 3-5 minutes. Coverslips were washed again for three times with PBS and then were then incubate for 30 min with blocking solution (PBS 5% BSA). Coverslips were incubated with primary antibodies diluted in PBS (α p140Cap monoclonal antibody Mab 1:500, α myc homemade mouse polyclonal 1:200, α GFP Mab 1:1000 Abcam, αGluN2A rabbit polyclonal 1:300 Thermo Scientific, α PSD95 Mab 1:1000 Abcam, α Flotillin-1 rabbit polyclonal 1:500 Santa Cruz) for 1 hour. Coverslips were washed 3 times for 10 minutes with PBS and then incubated with Alexa Fluor Dye secondary antibodies (dilution 1:2500, Invitrogen) for 1 h protected from light. In some experiments the coverslips were incubated with DAPI staining solution for 5 minutes to perform nucleus staining. The samples were rinsed several times in PBS and mounted on glass slides with Mowiol (for neurons only) or with ProLong (Invitrogen) mounting mediums. Samples were examined using Nikon ViCo Video Confocal Microscope equipped with a triple bandpass filter set (FITC, TRITC, DAPI). For each coverslip, at least 5 images were analysed.

4.7 SYNAPTOSOMES PREPARATION

All procedures were done at 4°C using precooled reagents. Synaptosomes were prepared from the telencephalon of WT and p140Cap KO mice. The tissues were immediately transferred in 8 mL of ice cold synaptosomes buffer (0.32 M sucrose, 4 mM HEPES pH 7,3, 1mM EGTA) containing a freshly added protease inhibitors (Roche) and phosphatase inhibitor cocktail (1mM PMSF, 1mM NaOv3, 1mM NaF and 2mM DTT). The tissue was homogenized with a Dounce glass homogenizer and glass pestle (Sigma Aldrich) and centrifuged at 1000 g at 4°C for 10 minutes to remove the pelleted nuclear fraction (P1). The resulting supernatant (S1) was centrifuged at 12.500 g for 20 min at 4°C (JA 25.50 Beckman rotor, Sorvall) to yield the crude synaptosomal pellet (P2). S2 was discharged and P2 was resuspended in 10 mL of synaptosomes buffer and centrifuged again at 12.500 g for another 20 min to yield the washed crude synaptosomal fraction. P2 was then resuspended in 2mL of ice-cold lysis buffer (150mM NaCl, 50mM Tris pH 7, 5% Glycerol, 1% NP-40, 1mM MgCl2, Roche protease inhibitors 25X, 1mM Sodium

Orthovanadate, 1mM DTT, phenylmethylsulphonyl fluoride, 1mM sodium fluoride) and immediately processed for immunoprecipitation.

4.8 PROTEINS EXTRACTION AND QUANTIFICATION

Protein extraction was performed at 4°C. HEK293 cells and DIV 3, 7, 10, 14, 17, 21 hippocampal WT and p140Cap KO neurons for time course experiments were lysed with lysis buffer (150mM NaCl, 50mM Tris pH 7, 5% Glycerol, 1% NP-40, 1mM MgCl2), supplemented with Roche protease inhibitors 25X and phosphatase inhibitors (1mM Sodium Orthovanadate, 1mM DTT, phenylmethylsulphonyl fluoride, 1mM sodium fluoride). The cell culture dish was put on ice and washed with ice-cold PBS. Then the PBS was aspirated, and ice-cold lysis buffer was added. Lysis buffer was incubated for 10 minutes under constant agitation at 4°C. Adherent cells were scraped off the dish using a cold plastic cell scraper, and were gently transferred into a pre-cooled microcentrifuge tube. Cell extract was centrifuged for 10 minutes at 13.000g 4°C and the supernatant was aspirated and placed in a fresh tube kept on ice.

Preparation of telencephalon lysate for time-course experiments was performed on ice. The tissue was quickly collected, placed in Eppendorf tubes and immerse in liquid nitrogen to snap freeze. The samples were stored at -80°C for later use or keep on ice for immediate homogenization. For 1 telencephalon, 1 mL of RIPA buffer (150 mM NaCl, 1.0% NP-40, 0.5% sodium deoxycholate, 0.1% SDS (sodium dodecyl sulfate), 50 mM Tris, pH 8.0, 5mM EGTA) supplemented with protease and phosphatase inhibitors was added and the tissue was homogenized with an electric homogenizer. The homogenates were centrifuged for 45 min at 13,000 rpm at 4°C in a microcentrifuge. The supernatant was aspirated and placed in a fresh tube kept on ice.

Protein concentration was determined using the Bio-Rad protein assay method (Biorad, Hercules, CA, USA).

4.9 WESTERN BLOT

Western blots were performed with Mini-PROTEANR TGX™ Precast Gradient 4–15% Gels from Bio-Rad (California 94547 USA). Samples were mixed with Laemmli buffer (4X solution: SDS 8%, Glicerol 40%, Tris-HCl pH 6,8, 0,625M, phenol blue, 5% β-Mercaptoethanol), boiled for 10 minutes at 95°C and subjected to SDS–PAGE using Running Buffer (10X solution: Tris 250mM, Glycine 1,92M, SDS 1%). Electrophoresis

was carried out initially at 100mV to allow samples to enter in the stacking gel, then at 250 mV for about 30 minutes. Gels were transferred on Nitrocellulose blotting membrane (GE Healthcare Life Sciences) using cold Towbin buffer (25mM Tris, 192mM Glycine, 20% Methanol). The transfer tank was placed in ice and the transfer was performed at 120mV for 60 minutes. The membranes were stained with Ponceau S solution (Glacial Trichloroacetic acid 6%, Ponceau Red 0,2%) to check the transfer quality. Then the Ponceau S stain was rinsed off with three washes with Tris-buffered saline TBS (50mM Tris p < h 7–150mM NaCl) 0,03% Tween-20 and the membrane was blocked with TBS 5% milk for 1 h at room temperature. Membrane were washed three times with TBS 0,03% Tween-20 and incubated overnight at 4°C with primary antibody diluted in TBS 1% BSA (α-p140Cap monoclonal antibody Mab (clone 2A8) produced at the MBC, University of Turin) α-GluN2A rabbit polyclonal (PA5-35377 Thermo Scientific), α-GluN2B Mab (Neuromab), α-GluN1 rabbit polyclonal (Thermo Scientific), α-PSD95 Mab (Abcam), α-Flotillin-1 rabbit polyclonal antibody (H-104 Santa Cruz), α-Gria2 rabbit polyclonal antibody (Abcam), α-Camk2β rabbit polyclonal antibody (Abcam), α-Src rabbit polyclonal antibody (Cell Signaling), α-Gfap Mab (Dako-Agilent Technologies), α-transferrin receptor 1-CD71 Mab (H68.4 Thermo Scientific), α-Rac1 Mab (clone 23A8 Millipore), α-CDC42 rabbit polyclonal antibody (Cell Signaling), α-Tubulin Mab (T5168 Sigma-Aldrich Co, Italy), α GAPDH Mab (Millipore). The blots were rinsed 3 times for 10 minutes with TBS 0,03% Tween-20 and incubated in the HRP-conjugated secondary antibody anti-mouse and anti-rabbit (dilution 1:10.000, purchased from Sigma Aldrich) solution for 1 hr at room temperature protected from light. Membranes were rinsed 5 times for 10 minutes with TBS 0,03% Tween-20 and then developed with Bio-Rad's Clarity ECL on ChemiDoc Touch Imaging System (Biorad).

4.10 IMMUNOPRECIPITATION

Immunoprecipitation (IP) was performed form HEK293 cells extracted using lysis buffer (see above) and P2 WT and p140Cap KO crude synaptosomes. For each IP, 0,2mg Dynabeads protein G (30mg Dynabeads R /mL Invitrogen, Carlsbad, CA, USA) coupled with 1µg of antibody (α GFP rabbit polyclonal, α p140Cap, α GluN2A) was considered for 1mg of cell extract. Beads were washed with PBS 1X 0.05% Tween-20, then were incubated with the antibody diluted in the same buffer for 15 minutes at room temperature under gentle rotation. Antibody-coupled Dynabeads were then washed twice with PBS

1X 0.05% Tween-20 and then incubated with 1mg of extracts for 2 h at 4°C under gentle rotation. Beads were washed five times with cold lysis buffer, then resuspended in 10μl of 2X Leammli buffer in reducing conditions, incubated at 95°C for 10 minutes and analysed by western blot.

4.11 GST PULL-DOWN ASSAY

Overnight cultures from single colonies of E. coli transformed with the plasmid of GluN2A C-terminal tail (aa 1049-1464, aa 1349-1464, aa 1244-1389) were grown over night in 50 mL of Luria-Bertani medium containing 100 Wg/mL ampicillin (Sigma, St.Louis, MO, USA) at 37°C. Bacterial suspension was diluted 1:10 with Luria-Bertani medium containing 100 Wg/mL ampicillin and incubated under the same conditions for 2h. Synthesis of recombinant proteins was induced by 0.1mM isopropyl-L-D-thiogalactopyranoside (Sigma, St. Louis, MO,USA). The bacteria were grown for another 4 h and harvested by centrifugation. Bacterial pellets were resuspended with ice-cold PBS containing 5 mM dithiothreitol (DTT), 100 Wg/mL lysozyme, 0.1mM PMSF and incubated on ice for 15 min. Lysis was achieved by the addition of 1.5% N-laurylsarcosine (sarkosyl) from a 10% stock in PBS. Bacteria were sonicated on ice for 1 min and the lysate was clarified by centrifuging at 10.000g (5 min, 4°C) in a JA 25.50 Beckman rotor (Sorvall). For pull-down assays, supernatants were incubated with glutathione sepharose 4B (GE) resin for 1 h at 4°C. To evaluate the interaction with endogenous synaptosomal p140Cap, resin bound proteins were washed 5 times with lysis buffer, and then were incubated with 1mg of crude synaptosomes for 2h at 4°C. After incubation the resin was washed 10 times with lysis buffer plus 0,5% Triton X-100 and resuspended in Laemmli buffer.

4.12 RAC GTPASES ACTIVITY ASSAY

P2 crude ynaptosomes were resuspended in buffer (100 mM NaCl, 10% glycerol, 1% NP40, 10 mM MgCl2, 50mM Tris, supplemented with protease inhibitor cocktail). Glutathione-coupled Sepharose 4B beads were bound to recombinant GST-PAK CRIB domain fusion proteins and were incubated with synaptosomes at 4 °C for 30 min. Glutathione-coupled Sepharose 4B beads were washed three times and eluted in Laemmli buffer. The presence of Rac1was analysed by western blot.

4.13 LIPID RAFT ISOLATION FROM TOTAL BRAIN

Lipid raft were prepared as previously described (Delint-Ramirez et al., 2008) with some modifications. Briefly, the telencephalon was mixed and homogenized in buffer (0.5 mL of 150 mM NaCl, 25 mM Tris-Cl buffer, pH 7.5, containing 50 mM NaF, 10 mM NaP2O7, 1 mM Sodium orthovanadate, complete protease inhibitors cocktail) and 1% Triton X-100. 2 mg of triton X-100 extracts were incubated for 30 min at 4°C and centrifuged (13 000 g, 4°C, 10 min.) to separate the detergent-insoluble pellet. Triton X-100-insoluble pellet was resuspended in 1 mL of lysis buffer and mixed with 2M sucrose (2 mL), overlaid with 1 M (4 mL) and 0.2 M (3 mL) sucrose, and centrifuged for 18 h at 200 000 g (SW40 Ti; Beckman) at 4°C. After centrifugation, 1 mL fractions were collected from the top to the bottom of the gradient. Equal volumes of each fraction were subjected to Western Blot analysis.

4.14 SYNAPTIC LIPID RAFT ISOLATION

Synaptic lipid rafts were prepared from crude synaptosomal pellet (P2). All procedures were done at 4°C using precooled reagents. P2 was resuspended in synaptosomes buffer and quantified. 4mg of P2 were collected and washed again with synaptosomes buffer. The pellet was resuspended with 1 mL of buffer (150 mM NaCl, 25 mM Tris-Cl buffer, pH 7.5, containing 50 mM NaF, 10 mM NaP2O7, 1 mM Sodium orthovanadate, complete protease inhibitors cocktail) containing 1% Triton X-100 and incubated for 30 minutes at 4°C. Lipid raft isolation is based on their characteristic insolubility in non-ionic detergents as Triton X-100. However, Triton X-100-insoluble parts of the synaptic junctions include both lipid rafts (detergent resistant membrane, DRMs) and PSDs. Both subcellular compartments are characterized by distinct different densities and can therefore be separated by an additional sucrose step.

To this end, after the incubation with triton containing buffer, the suspension was placed beneath a discontinuous sucrose gradient in a 14 mL ultracentrifuge tube (Thinwall Polypropylene Tubes 14 mL, 14 x 95 mm, Beckman Coulter). The suspension was placed at the bottom of the tube and mixed with sucrose 90% to achieve a final sucrose percentage of 45%. Then it was overlaid with 4mL of sucrose 35% and 4 mL of sucrose 5% and centrifuged at 200.000g for 18 hours at 4°C (SW 40 Ti; Beckman). After centrifugation, 1mL fractions were collected from the top to the bottom of the gradient. Equal volumes of each fraction were subjected to Western blot analysis.

4.15 STATISTICAL ANALYSIS

For quantification, statistical significative differences were evaluated using unpaired t-tests. Error bar: s.e.m. using the Student's t-test.

5 RESULTS

5.1 P140CAP IS A NEW INTERACTOR OF NMDA RECEPTOR SUBUNIT GLUN2A

p140Cap KO mice display reduced memory consolidation and impaired synaptic plasticity (Repetto et al., 2014). Since the NMDAR plays a crucial role in these events, we investigated the involvement of p140Cap in NMDAR-dependent plasticity processes. p140Cap immunoprecipitation from P2 crude synaptosome fraction obtained from WT and p140Cap KO mice were analysed in western blotting with specific antibodies, revealing that p140Cap specifically associates with the GluN2A subunit, while the association with GluN1 and GluN2B was mainly aspecific (Figure 9A). p140Cap association with the NMDAR subunits was also validated by co-immunoprecipitation experiments in heterologous cells. For this purpose, HEK293 cells were co-transfected with myc-tagged p140Cap cDNA in combination with GFP-tagged GluN1, GluN2A and GluN2B subunit constructs. Cell extracts were immunoprecipitated with anti-p140Cap antibody and analysed in western blot with anti-GFP antibody to reveal association with specific subunits. The results confirmed that p140Cap specifically associates with the GluN2A subunit. Conversely, the association was weaker with GluN2B and totally absent with GluN1 (Figure 9B). To further confirming the association of p140Cap with GluN2A, immunofluorescence co-clustering analysis of p140Cap and GluN2 subunits were performed in heterologous COS-7 cells. The results showed that p140Cap specifically co-localizes with GluN2A, while no co-localization was present with GluN2B (Figure 9C). This interaction was also confirmed by reverse immunoprecipitation of GluN2A from synaptosomes (Figure 9D). Moreover, GluN2A and p140Cap co-localize along dendrites of WT mature primary hippocampal neurons, as shown in double immunostaining experiments (Figure 9E). Overall, these results provide the evidence that p140Cap mainly associates the GluN2A subunit of NMDAR.

Figure 9:**A**: *p140Cap immunoprecipitation from WT and p140Cap KO P2 crude synaptosome fraction (1mg) were blotted with the indicated antibodies.* **B**: *immunoprecipitation of myc-tagged p140Cap from HEK293 cells co-transfected with GFP-tagged NMDAR subunit GluN1, GluN2A, and GluN2B (1mg). Immunoprecipitation experiments were performed with anti-p140Cap antibody followed by blotting with the anti-GFP antibody.* **C**: *confocal imaging of COS-7 cells co-transfected with RFP-p140Cap (red) in combination with GFP-GluN2A (green) or GFP-GluN2B (green). Scale bar 12µm.* **D**: *reverse immunoprecipitation of GluN2A from WT and p140Cap KO synaptosomes (1mg). Mock rabbit IgG was used in WT synaptosomes as negative control for IP.* **E**: *GluN2A and p140Cap immunofluorescent detection of primary WT hippocampal neurons (Scale bar 12µm and 5µm).*

D

E

DIV 16 Hippocampal neurons WT
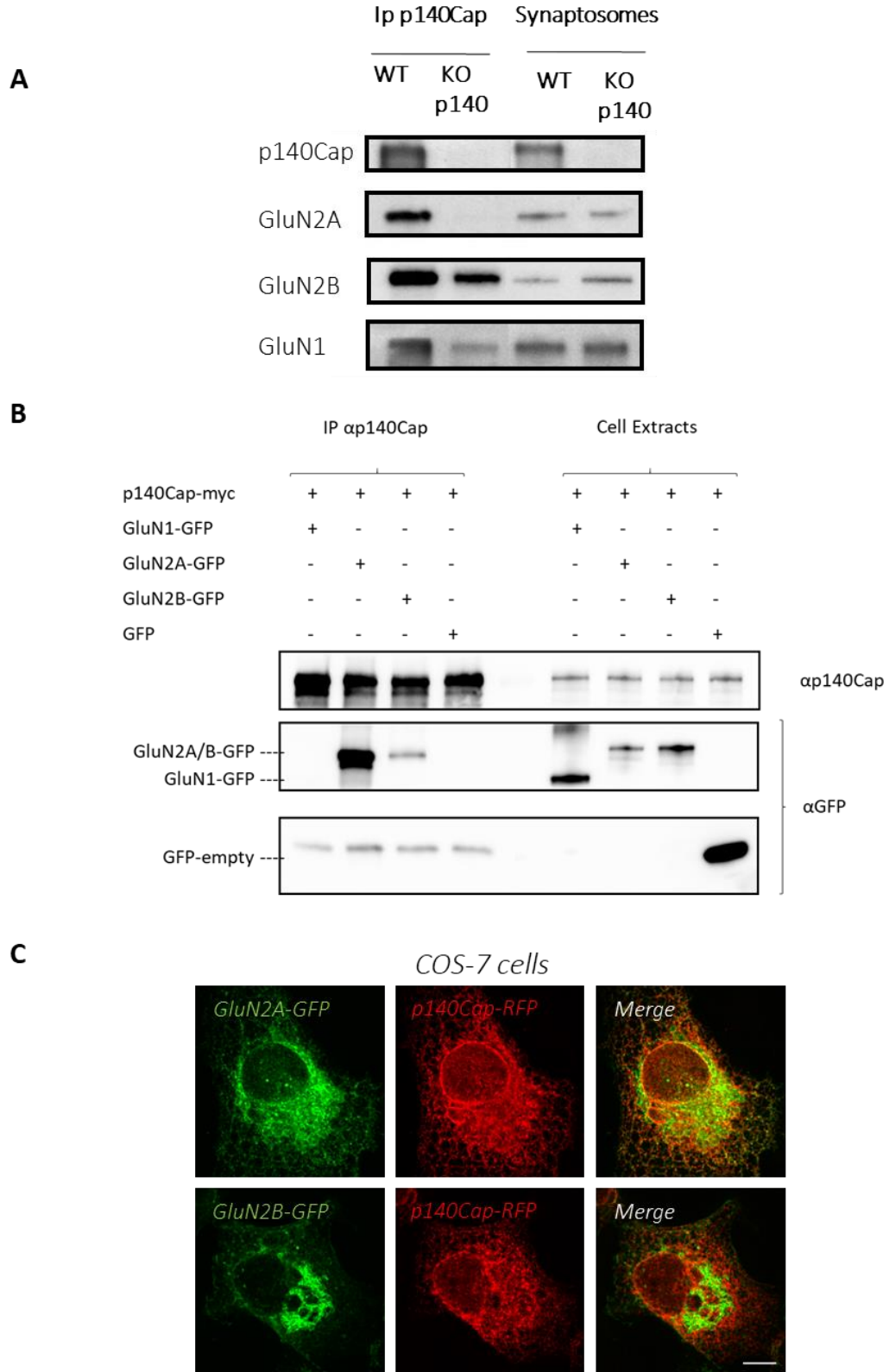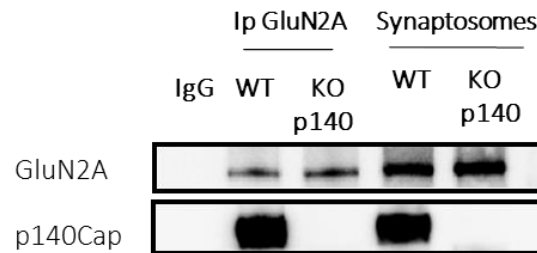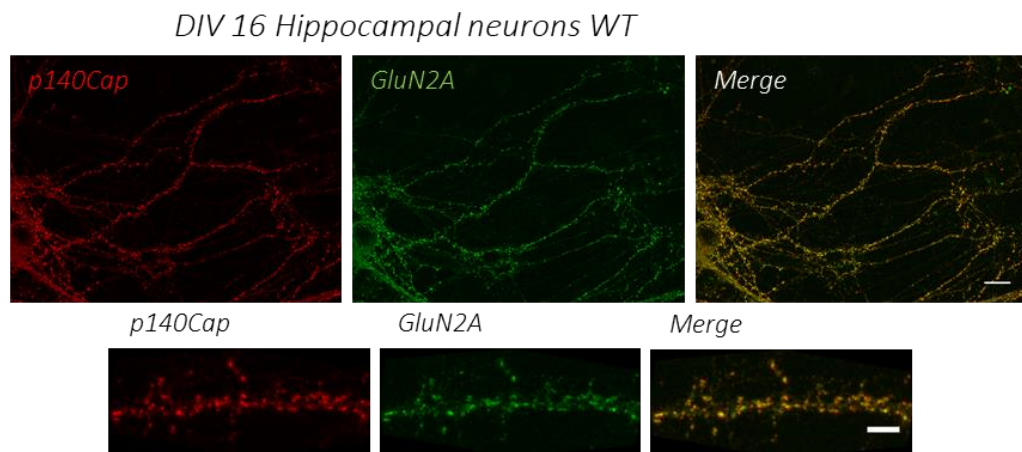
5.2 P140CAP PROLINE-RICH DOMAIN 1 IS REQUIRED FOR THE ASSOCIATION WITH GLUN2A

Protein-protein interaction assays were performed to validate the association between p140Cap and GluN2A. Immunoprecipitation experiments were performed to characterize the domains of p140Cap involved in the association with GluN2A. To this end, HEK293 cells were co-transfected with a GFP-GluN2A construct and with myc-tagged p140Cap constructs for the full-length protein or its shorter mutants (Figure 10A). Cell extracts were immunoprecipitated with anti-GFP antibody and blotted with anti-p140Cap antibody.

The result pointed out that p140Cap associates the GluN2A subunit through its N-terminal region (aa 1-770), and in particular through the subdomain 351-691 which includes p140Cap proline-rich region 1 (Figure 10B).

Consistently, immunofluorescence experiments in COS-7 cells upon transfection of myc-tagged p140Cap full length protein or mutant forms with GFP-tagged GluN2A demonstrated a significantly higher co-localization of GluN2A with both the p140Cap N-

terminal part (aa 1-770) and the aa 351-691 region, than with the p140Cap C-terminal region (aa 728-1217) (Figure 10C and 10D). Notably, the colocalization of GluN2A with the p140Cap region that includes the proline-rich 1, is lower than that with the entire N-terminal portion. This last result suggests that the full p140Cap N-terminal portion may reach the optimal conformation for the interaction with GluN2A.

Figure 10: A: schematic representation of myc-tagged p140Cap fragments. B: HEK293 cells co-transfected with constructs encoding myc-tagged p140Cap fragments and GFP-GluN2A were extracted and immunoprecipitated with anti-GFP antibody C: p140Cap full-length, p140 aa 1-770, 351-691 and 728-1217 all myc –tagged where co-expressed with GFP-GluN2A in COS-7 cells (scale bar 12 µ.m). D: Co-localization was quantified with Manders' coefficient M1 (RFP-GluN2A co-localization). At least 5 images were examined for each co-transfection * p<0.05, ** p<0.005.
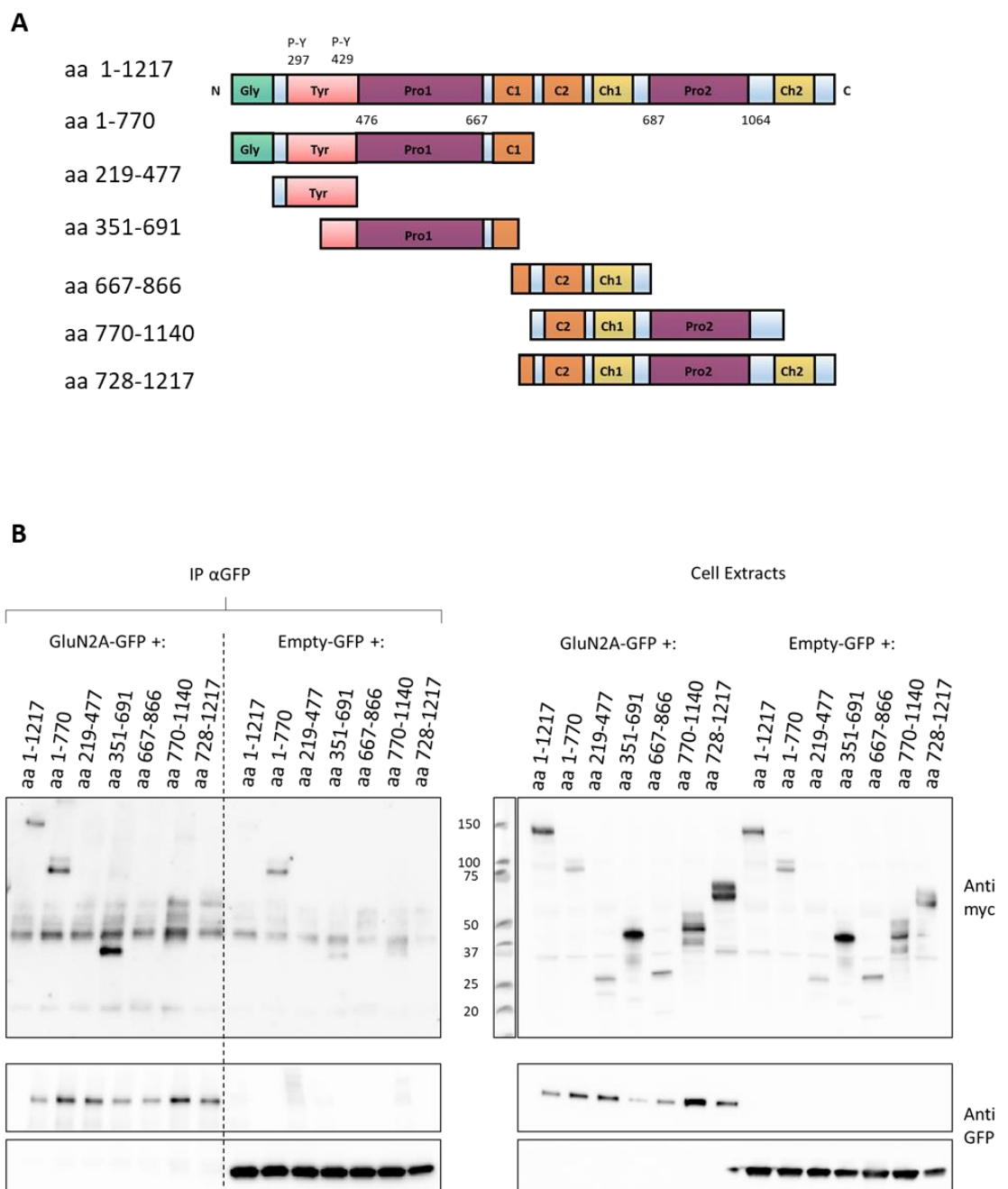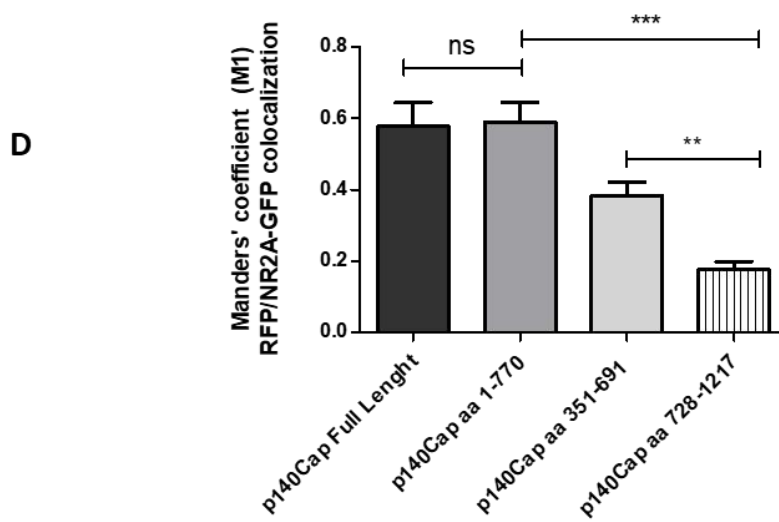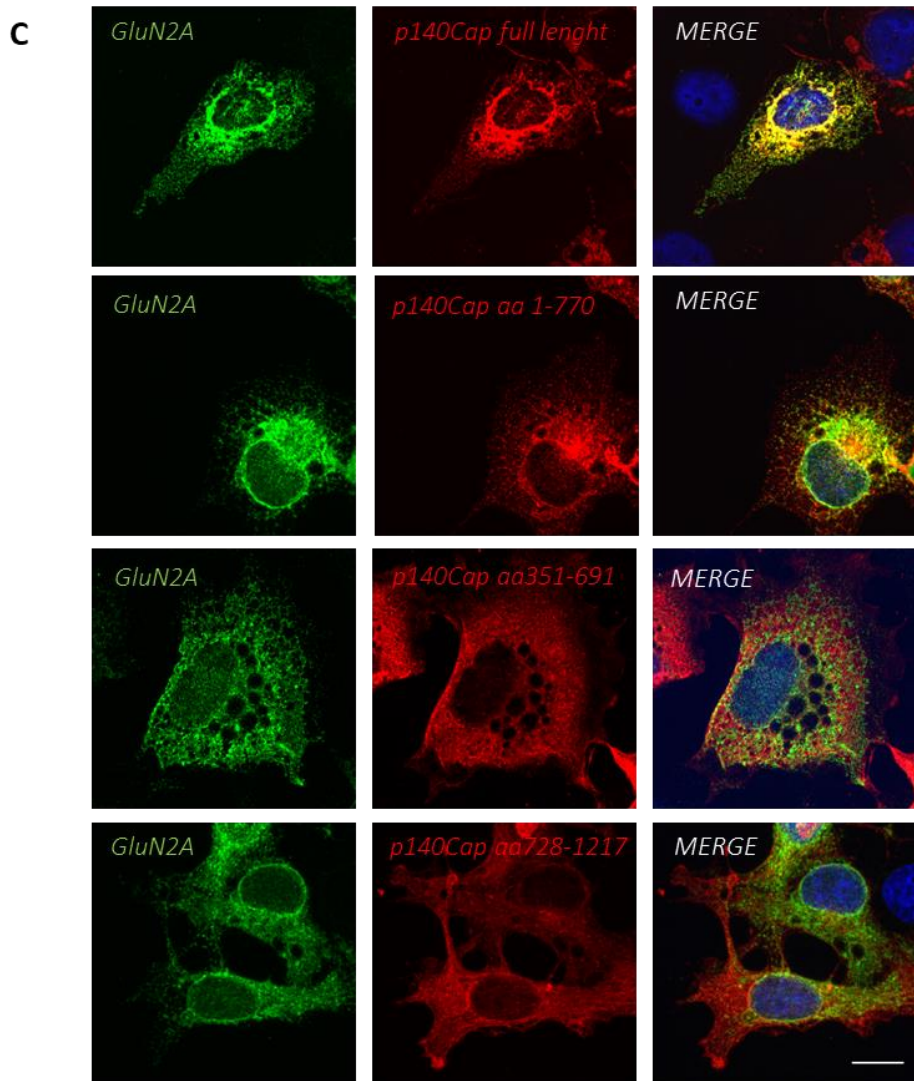
5.3 THE GLUN2A SUBUNIT ASSOCIATES P140CAP THROUGH THE CARBOXY-TERMINAL REGION 1349-1464

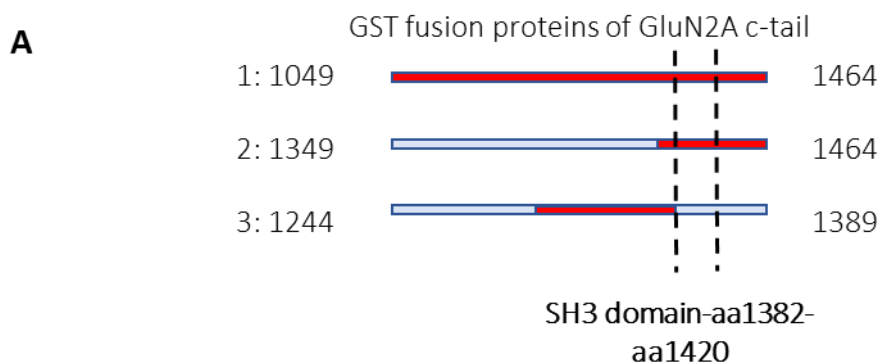Glutathione S-transferase (GST) pull-down assay with recombinant bacterial fusion proteins of the GluN2A C-terminal tail was used to identify the region responsible for the interaction with p140Cap. In particular, GST fusion proteins for GluN2A full intracellular domain (amino acid 1049 to 1464), and for two enclosed regions (1349 to 1461 and 1244 to 1389) were immobilized on Glutathione Sepharose 4B beads (Figure 11A).

GST pull-down assay was performed on HEK293 cells extracts stably expressing p140Cap (Figure 11B) and on WT synaptosomes extracts (Figure11C). The assay allowed to identify the GluN2A region comprised between amino acid 1349 and 1464 as the one responsible for the interaction with p140Cap. However, as shown in Figure 11B and C, the binding of the small fragment 1349-1464 is weaker than that obtained with the large fragment 1049-1464, suggesting that the entire C terminal tail of GluN2A owns the optimal conformation for the interaction with p140Cap.

The GluN2A domain responsible for the association with p140Cap contains an SH3-like region from residue 1382 to 1420 (Ladepeche, Dupuis, & Groc, 2014; Sanders et al., 2013). Since the p140Cap domain involved in the interaction with GluN2A is a proline-rich region, we hypothesize a model of association between p140Cap and GluN2A based on a proline-rich/SH3 domain interaction (Figure12).

Figure 11: A: schematic representation of GST fusion proteins of GluN2A C-tail mutants used to identify the region responsible for the interaction with p140Cap. B and C: GST pull-down assay of GST-GluN2A fragments with cell lysates of HEK293 stably expressing RFP-p140Cap (1mg) or with WT synaptosomes (1mg).

B

Blot anti
p140Cap

ponceau

Pull-Down HEK293 stably expressing
p140Cap-RFP

C

Blot anti
p140Cap

ponceau

Pull-Down WT synaptosomes
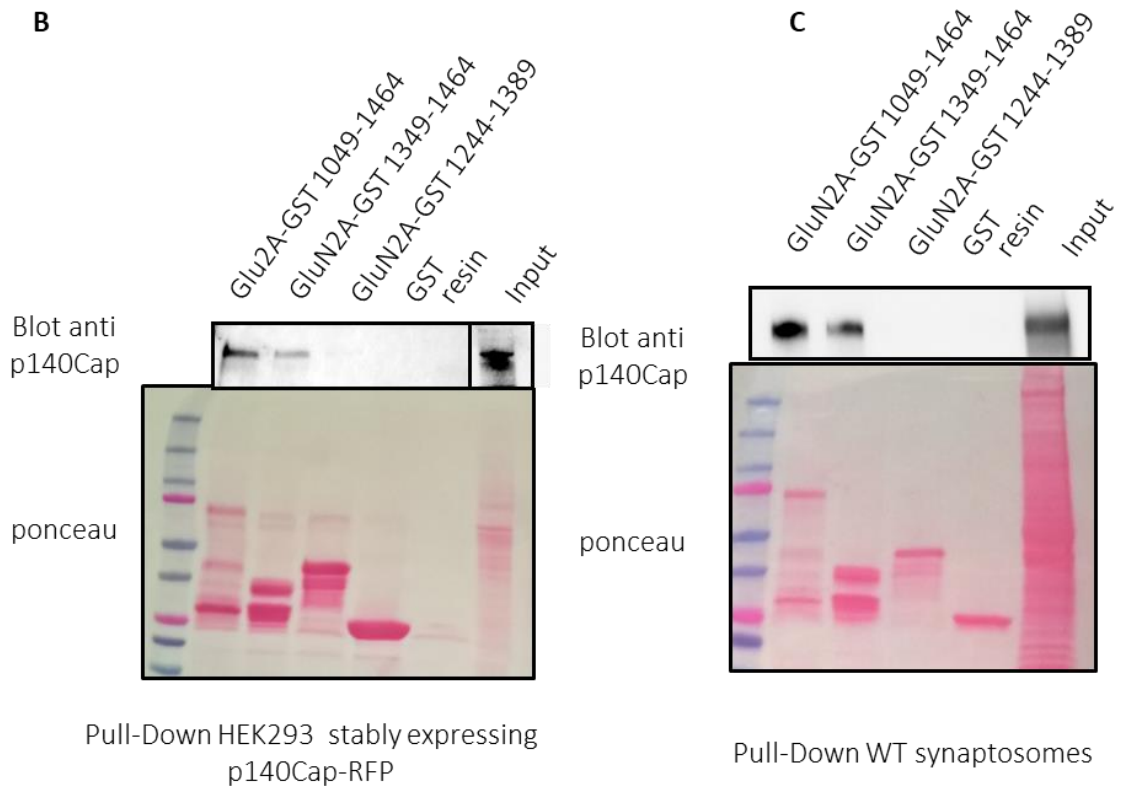
Figure 12: *Hypothetical model for interaction between p140Cap and GluN2A.*
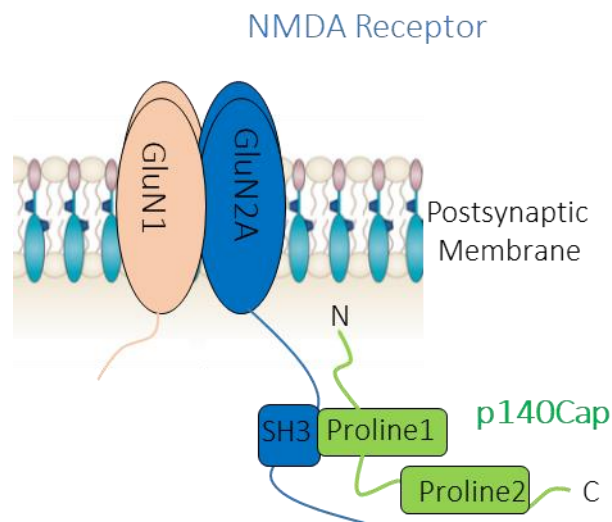
NMDA Receptor

5.4 P140CAP DOES NOT INFLUENCE GLUN2B-GLUN2A SWITCH DURING BRAIN DEVELOPMENT AND IN VITRO MATURATION

In many neurological diseases, the switch of expression of GluN2B/GluN2A subunit of NMDA receptor during development is delayed or altered. For instance, in a mouse model of Rett Syndrome (MeCP2 KO animals) GluN2B-to-GluN2A subunit switching, which regulates the channel kinetics and the biophysical properties of excitatory synapses in the developing brain, shows a delayed postnatal maturation and may be responsible for the molecular pathology of synaptic defects in RTT (Asaka, Jugloff, Zhang, Eubanks, & Fitzsimonds, 2006). Since p140Cap associates the GluN2A subunit, the dynamic of temporal expression of NMDA receptor subunits was investigated in WT and p140Cap KO hippocampal neurons at different Days in Vitro (DIV). To assess if p140Cap could delay GluN2A expression, cell extracts from WT and p140Cap KO neurons at different DIV (3, 7, 10, 14, 17 and 21) were analysed in western blot with anti-GluN2A and anti GluN2B antibodies. The results show that the expression of both NMDA receptor subunits was comparable between p140Cap KO and WT during in vitro maturation of primary hippocampal neurons (Figure 13A, B and C).

This result is consistent with the biochemical investigation of GluN2B-to-GluN2A subunit switch in WT and p140Cap KO mouse telencephalon, at different post natal days. Indeed, the analysis revealed the same kinetics of GluN2A expression between p140Cap KO and their littermates WT during post-natal development (Figure 13D, E and F). Moreover, PSD95 and glial marker GFAP (Glial fibrillary acidic protein) expression were also unchanged. Interestingly, blotting the same extracts with antibody to p140Cap confirmed that p140Cap is expressed very early (at P0); these data are consistent with previous works (Ito et al., 2008). All together these results underlie that p140Cap does not grossly alters GluN2A temporal expression or protein level.

Figure 13: **A**: *total protein extracts (20µg) were obtained from WT and p140Cap KO hippocampal neurons at 3, 7, 10, 14, 17 and 21 DIV (days in vitro) and immunoblotted with antibodies against GluN2B, GluN2A and tubulin.* **B** *and* **C**: *GluN2A and GluN2B expression were normalized against tubulin.* **D**: *protein extract from WT and p140Cap KO telencephalon (30µg) of different post-natal days (P0, P7, P14, P60) were immunoblotted with the indicated antibodies.* **E** *and* **F**: *GluN2A and GluN2B expression were normalized against tubulin.*
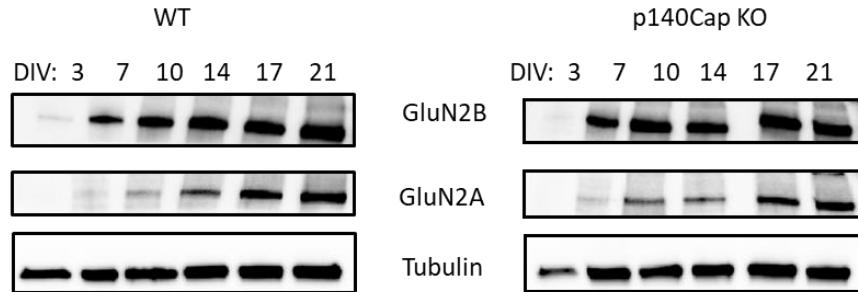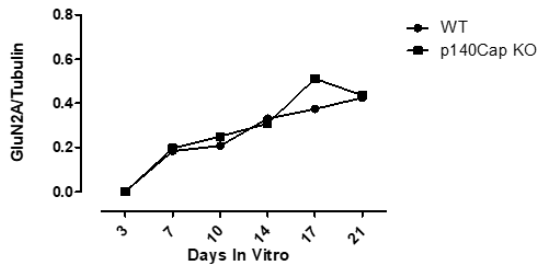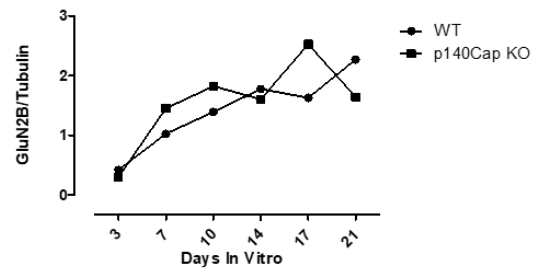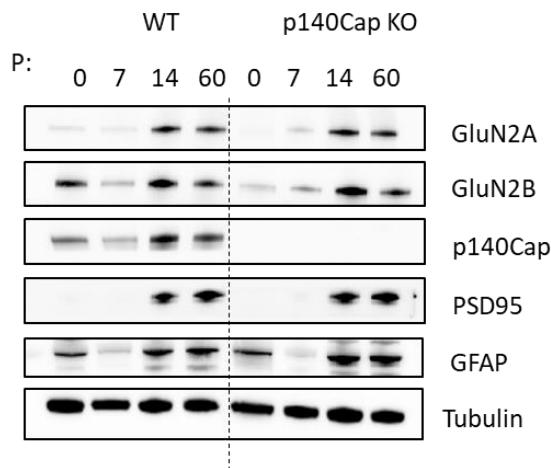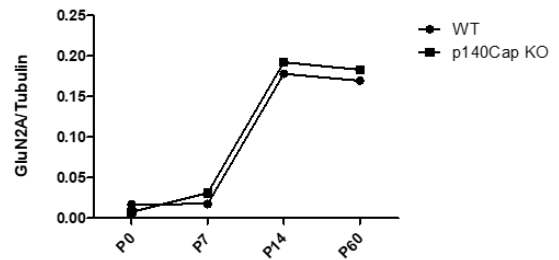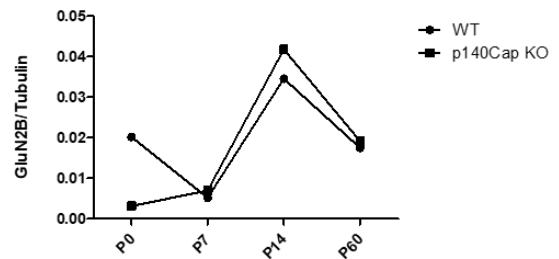
5.5 P140CAP AFFECTS THE COMPOSITION OF THE MOLECULAR COMPLEX ASSOCIATED TO GLUN2A CONTAINING NMDARS

A specific set of signaling molecules bind to the C-terminal region of NR2 subunit of NMDA receptor forming a large multi-protein complex, which includes scaffold and signaling proteins. All these molecules execute their functions in an organized way within complexes to facilitate synaptic transmission and plasticity at excitatory synapse (Frank & Grant, 2017). Therefore, we investigated if p140Cap could influence the composition of molecular complex associated to GluN2A-containing NMDAR. To this purpose, GluN2A immunoprecipitation from WT and p140Cap KO synaptosomes was performed. The results showed that, while in total extracts protein levels is unaffected, in p140Cap KO synaptosomes, GluN2A was significantly less associated to the scaffold protein PSD95, to the lipid raft associated protein Flotillin-1, and to the Rho-GTPase molecule Rac1 (Figure 14A, B, C and D) than in WT synaptosomes. These alterations could potentially alter the threshold for induction of NMDAR-dependent LTP, the same phenotype which was recently observed in p140Cap KO mice (Repetto et al., 2014).

Indeed, PSD95 plays a crucial role in assembling NMDAR-associated protein complex, thereby facilitating the functional coupling of NMDAR with downstream signaling molecules in the PSD (Sheng & Kim, 2011). Moreover, NMDA-induced activation of Rac1 results in a physical association with the NMDAR complex. This means the existence of a native NMDAR complex that, when activated, recruits Rac1 (Tejada-Simon et al., 2006).

p140Cap association with PSD95, Rac1 and Flotillin-1 was also validated by immunoprecipitating p140Cap from WT P2 synaptosomes. Interestingly no association was found with Cdc42, another Rho GTPase protein, supporting a specific role of p140Cap in association with Rac1 (Figure 14E). All together, these data reveal that p140Cap takes part to the GluN2A containing NMDAR complex and influences its molecular composition.

Figure 14: A: GluN2A was immunoprecipitated from p140Cap KO and WT P2 synaptosomes. Mock rabbit IgG was used in WT synaptosomes as negative control for IP. B, C, D: quantification of the co-immunoprecipitation. The values are the result of the ration of co-IP protein normalized on the corresponding input (synaptosomes) and the IP protein (GluN2A) * p<0.05, **p<0.005. Images are representative of n=5 mice per experimental group. E: p140Cap immunoprecipitation from P2 crude synaptosomes revealed p140Cap association with molecules involved in the large NMDA multi-protein complex (PSD95, Rac-1, Cdc42, Flotillin-1). p140Cap KO synaptosomes were used as negative control for the IP.
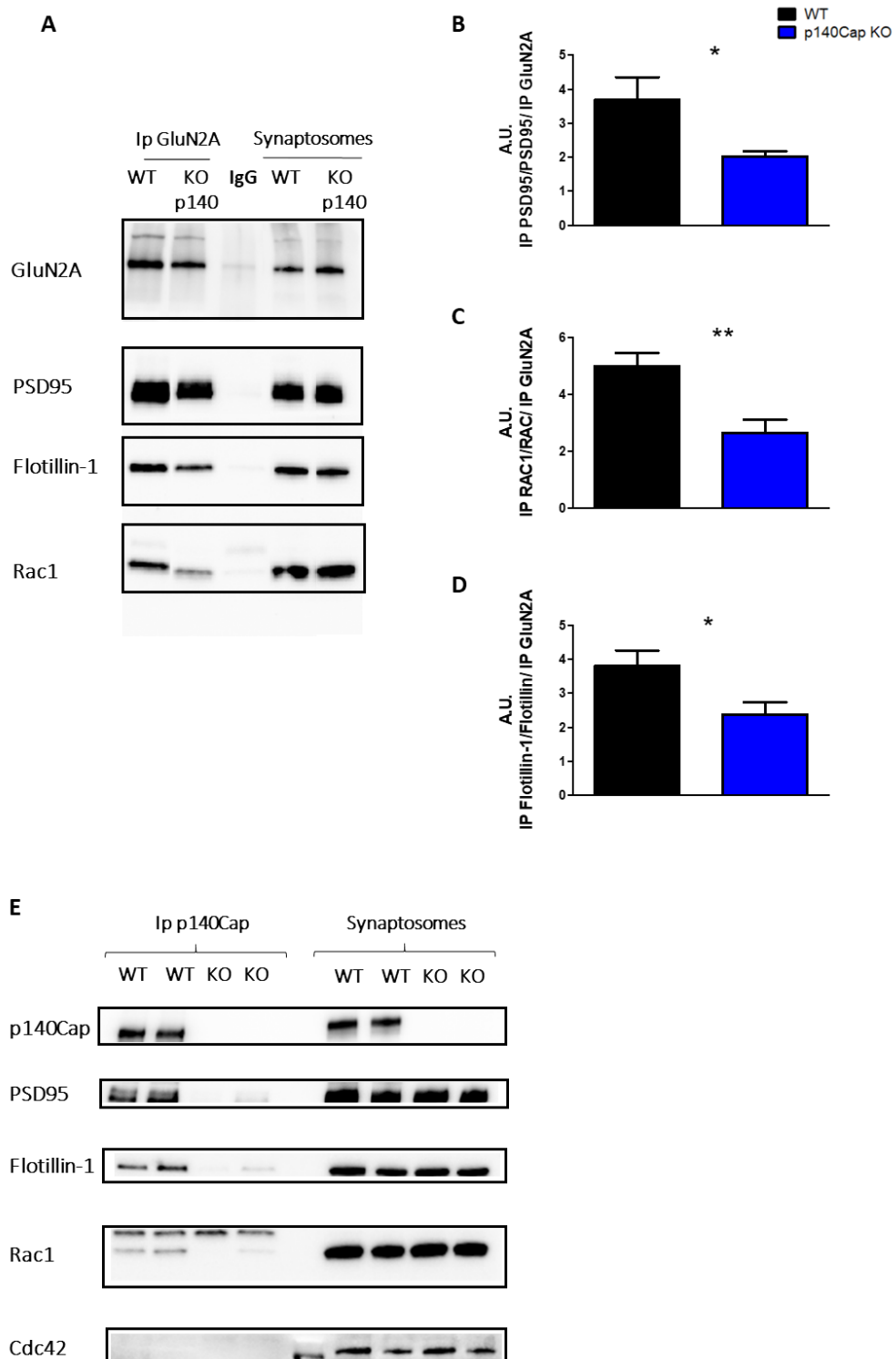
5.6   P140CAP POTENTIATES THE ASSOCIATION BETWEEN PSD95 AND GLUN2A

PSD95 is the most abundant scaffold protein of the Post Synaptic Density. PDZ2 domain of PSD95 binds to the last four amino acids (ESDV) of NR2 subunits of NMDA receptor providing a physical link between receptors and intracellular molecules (Gold, 2012). Moreover, PSD95 is essential to enhance NMDAR clustering at synapses (Kim, Cho, Rothschild, & Sheng, 1996), to inhibit GluN2-mediated internalization (Lavezzari, McCallum, Dewey, & Roche, 2004) and to increase the number of functional channels at the cell surface (Lin, Skeberdis, Francesconi, Bennett, & Zukin, 2004). PSD95 also appears to stabilize NMDAR at the cell surface and to cluster GluN2 subunits in heterologous cells (Niethammer, Kim, & Sheng, 1996; Sheng & Kim, 2011).

Biochemical data from our lab (Alfieri A, unpublished), obtained from immunoprecipitation experiments in HEK293, revealed that p140Cap can associate PSD95, independently from GluN2A (Figure 15A). Since biochemical data in Figure 14 A, B, revealed a reduction of GluN2A association to PSD95 in KO synaptosomes, we investigated if p140Cap could influence PSD95 and GluN2A clustering in heterologous COS-7 cells (Figure 15B). Co-expression of PSD95 with GluN2A induced plaque-like clusters as already described (Kim et al., 1996). In cells triple-transfected with GluN2A, PSD95 and p140Cap, the formation of GluN2A-PSD95 clusters significantly increased. Moreover, the three proteins co-localize, suggesting that p140Cap may take part of a ternary complex, including PSD95 and GluN2A, likely potentiating the association of PSD95 with GluN2A (Figure 15C).

To validate whether p140Cap can play any role in stabilizing GluN2A and PSD95 association, immunostaining experiments of GluN2A in combination with PSD95 were performed both in primary mature WT and p140Cap KO hippocampal neurons (Figure 16A). Although p140Cap KO neurons already showed reduced density of PSD95 puncta (as described in Tomasoni et al., 2013), here we found that also the percentage of punctae containing both GluN2A and PSD95 was significantly reduced in p140Cap KO neurons (Figure 16B and C). Overall, these results demonstrate that p140Cap is important for stabilizing GluN2A containing NMDARs at the post synaptic density membrane, forming a ternary complex with GluN2A and PSD95.

To further proving whether p140Cap can influence GluN2A synaptic localization, preliminary rescue experiments were performed by transfecting p140Cap KO hippocampal neurons with a cDNA construct encoding for the p140Cap N-terminal

region (aa1-770) involved in GluN2A binding (see above). The results revealed that p140Cap aa1-770 can restore dendritic spines morphology and GluN2A synaptic localization, as shown by the co-localization between phalloidin actin staining and GluN2A (Figure 16D).

*Figure 15: A: HEK293 were co-transfected with myc-p140Cap and GFP-GluN2A or flag-PSD95 or both. Empty-GFP was used as negative control for the IP. p140Cap was immunoprecipitated with anti-p140 antibody from all the conditions. B: Clustering assay in COS-7 cells transfected with flag-PSD95, GFP-GluN2A with or without RFP-p140Cap. Scale bar 12μm. C: Co-localization between PSD95 and GluN2A was quantified with Manders' coefficient * p<0.05. At least 5 images were analysed for each condition.*
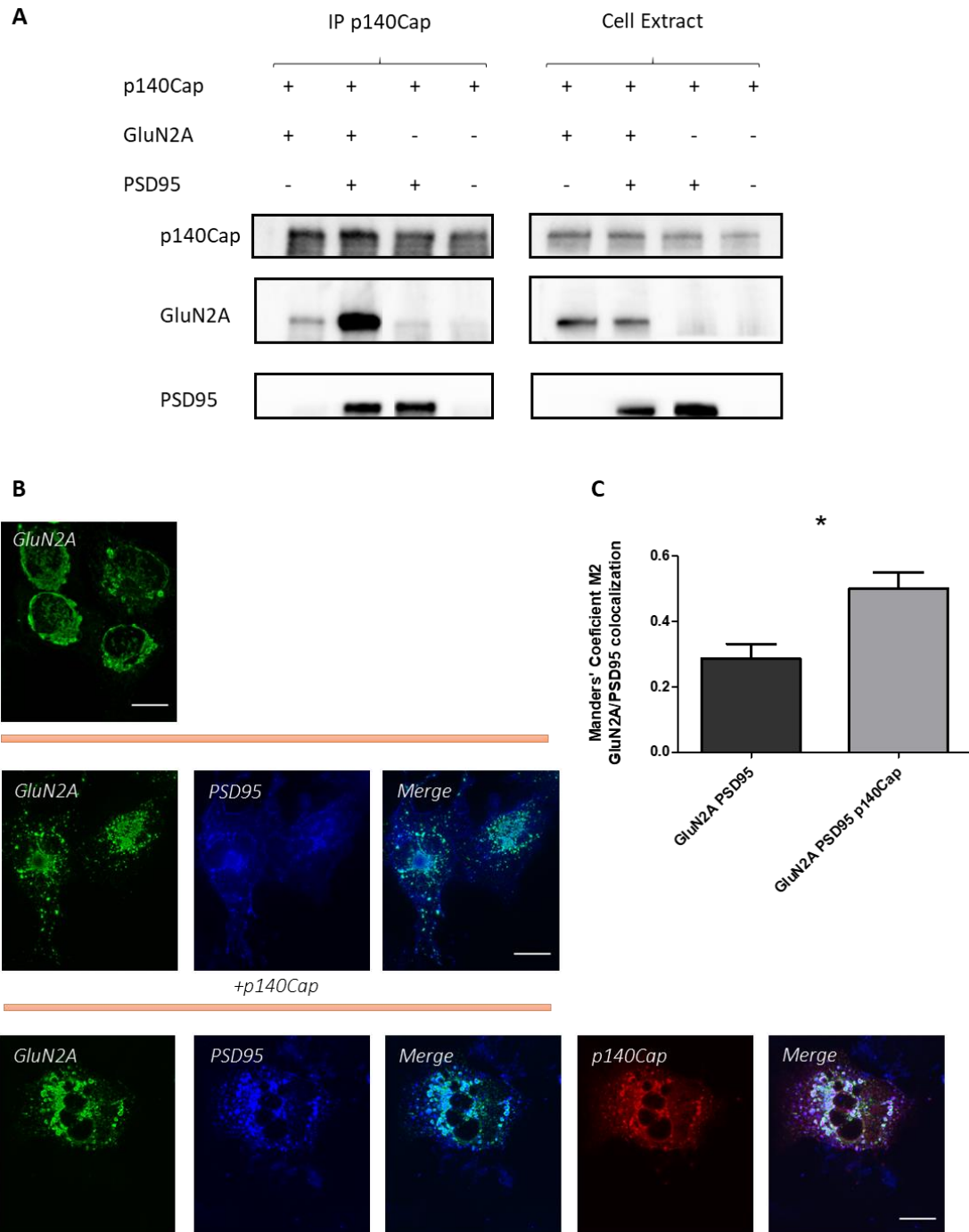
Figure 16: *A*: *GluN2A immunostaining was performed in combination PSD95 in primary WT and p140Cap KO hippocampal neurons at DIV16 Scale bar 12µm.* *B*: *representative segments (30µm) considered for the analysis of co-localization. 15 dendritic segments were analysed for each experimental group.* *C*: *percentage of co-localization between GluN2A and PSD95 (p=4,53738E-05).* *D*: *DIV 14 p140Cap KO hippocampal neurons were transfected with control cDNA (emty myc vector), or with p140Cap aa1-770. 48 hours after transfection cells were labelled with anti-GluN2A and phalloidin to analyse the rescue of GluN2A localization.*
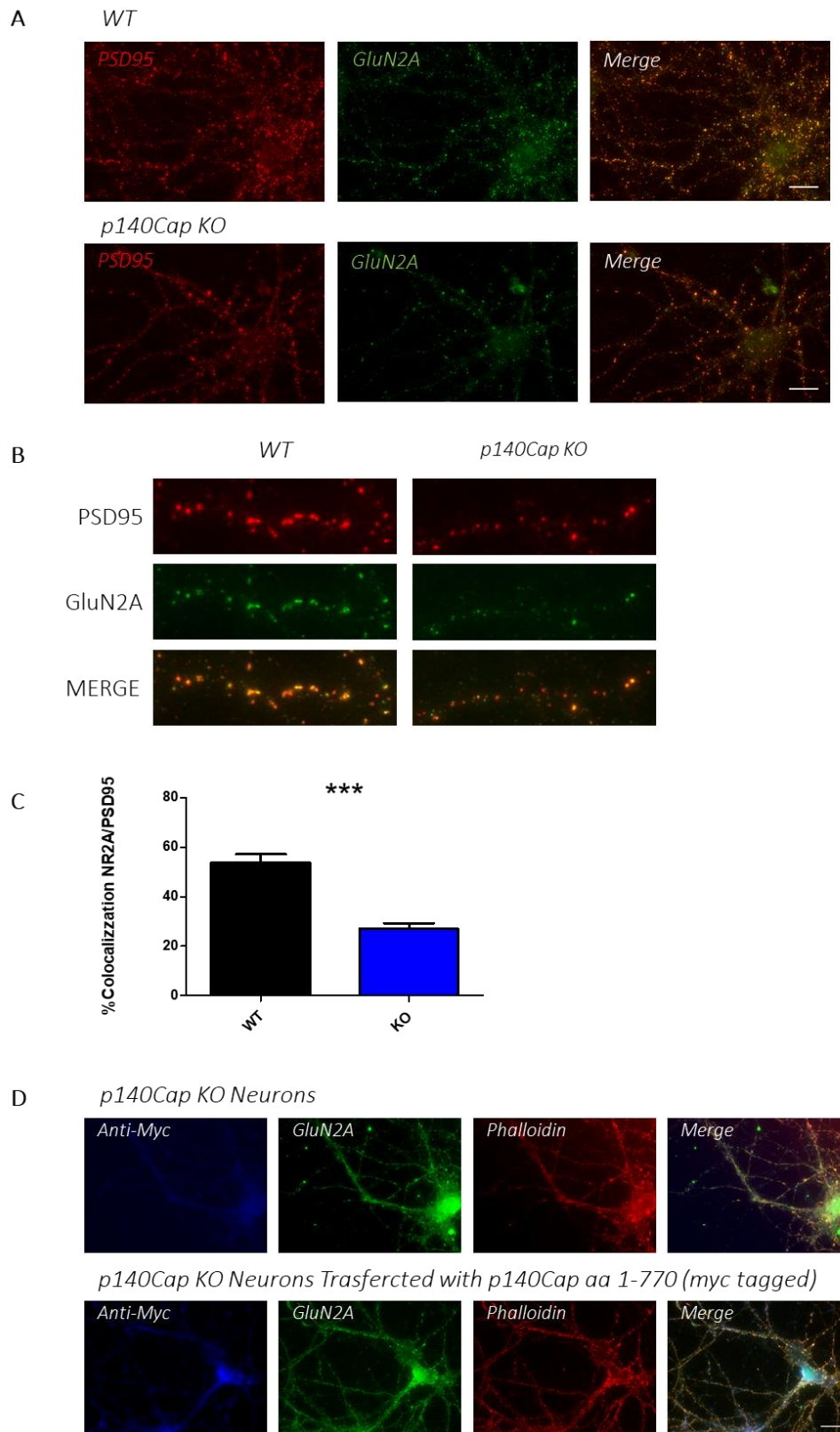
5.7 P140CAP IS REQUIRED FOR THE RECRUITMENT AND ACTIVATION OF ACTIN REGULATOR RAC1 GTPASE AT THE EXCITATORY PSD

As shown above, decreased association of GluN2A with PSD95 in p140Cap KO synaptosomes, was also accompanied by a concomitant decrease in Rac1 GTPase association to GluN2A in comparison to WT synaptosomes (Figure 14A and C).

It is already known that when NMDAR complex is activated, it can recruit Rac1 to form part of the receptor complex (Tejada-Simon et al., 2006). NMDAR activation in hippocampal slices causes Rac1 to translocate from the cytosol to the membrane and to become activated (Rac1-GTP) (Tejada-Simon et al., 2006). Moreover, Rac-1 activation is fundamental for actin-dependent reorganization of dendritic spine morphology (Schubert & Dotti, 2007). Rac1 involvement in transmission of cellular signals depends not only on its membrane association, but also by shifting from an inactive GDP-bound state to an active GTP-bound state. Therefore, to assess whether reduced association of Rac1 with GluN2A in KO synaptosomes could correlate with Rac1 activation, a Rac1 GST-PAK pull-down assay was performed on synaptosomes of adult mice. As shown in figure 17, we found a significant decrease of Rac1 activity in p140Cap KO synaptosomes compared to WT. These data underline the relevance of p140Cap for Rac1 recruitment to NMDAR molecular complex and for its activation.

Figure 17: GST-PAK pull-down assay to evaluate Rac1 activity in WT and p140Cap KO synaptosomes.
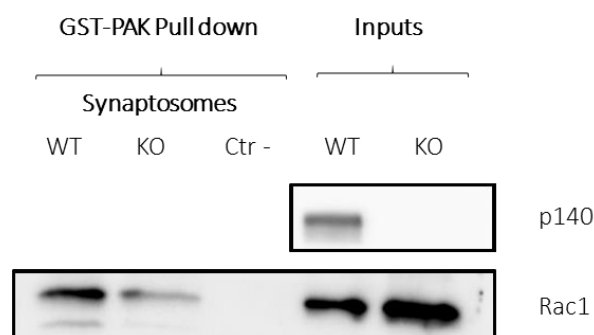
5.8 SYNAPTIC LIPID RAFTS FROM P140CAP KO MICE CONTAIN REDUCED AMOUNTS OF GLUN2A AND PSD95

The data shown above revealed that p140Cap may influence the composition of the molecular complex associated to GluN2A subunit-containing NMDA receptor, indicating that p140Cap is required for stabilizing the association between GluN2A and PSD95.

Furthermore, here we show that p140Cap may modulate Rac1 recruitment to the NMDAR complex.

To assess the mechanism through which p140Cap could regulate the composition of GluN2A-associated molecular complex, we focused our attention on the ability of p140Cap to associate with membrane lipid rafts. Indeed, p140Cap is a putative membrane associated protein, due to the presence of a myristylation sequence. Moreover, it has been predicted to be a membrane lipid raft-associated protein by two different proteomic analysis performed on rat brain (Jia et al., 2006; Suzuki et al., 2011). Membrane lipid rafts are signaling platforms enriched of cholesterol and sphingolipids, which are essential for the organization and compartmentalization of membrane receptor signaling components. Recent studies describe that NMDARs trafficking to lipid rafts, is dynamically enhanced during synaptic plasticity process such as memory formation (Delint-Ramirez et al., 2008). Moreover, also Rac1 GTPase has been shown to segregate to cholesterol-rich, liquid-ordered domains (lipid rafts), where it has been shown to stabilize these microdomains in a process associated with actin polymerization (Tsai & Philips, 2012).

Based on these evidence, we hypothesized that p140Cap could influence the composition of the molecular complex associated to NMDARs, increasing the recruitment of the NMDAR and of its associated molecules to lipid rafts. In turn, the localization of NMDAR into lipid rafts could "reinforce" downstream signal transduction, facilitating the assembly of molecular complexes required for the activation of a specific signaling pathway. This hypothesis was further supported by the reduced association of GluN2A with lipid raft marker Flotillin-1 observed in p140Cap KO synaptosomes (Figure 14A and D).

We experimentally confirmed that p140Cap associates with lipid rafts. Indeed, immunofluorescence experiments revealed that p140Cap co-localized with the lipid raft marker protein Flotillin-1 in primary hippocampal neurons at DIV 16 (Figure 18A). In addition, the presence of p140Cap was detected also in lipid rafts purified from mouse brain. Detergent resistant membrane (DRM) were isolated from adult mouse brain based on their insolubility in Triton X-100 at 4°C and on their ability to float in density gradients (Figure 18B). Lipid raft-containing fraction was tracked by the enrichment of the lipid raft associated protein Flotillin-1. Flotillin-1 showed highest enrichment in low density fraction 2. In contrast, the transferrin receptor, which is excluded from lipid raft, deposited

at the bottom of the gradient (phase 4 and 5). The results showed that p140Cap was highly enriched in the lipid raft fraction, although it was also present at the bottom of the gradient (Figure 18C).

Figure 18: A: p140Cap and Flotillin-1 immunofluorescence in WT primary hippocampal neurons (DIV16). B: representative image of brain lipid raft separation in a sucrose density gradient. C: detergent resistant membrane (DRM) were isolated from adult mice brain. Lipid raft-containing fraction was tracked by the enrichment of the lipid raft associated protein Flotillin-1. In contrast, transferrin receptor CD71 was used as negative control since it is a raft excluded protein.
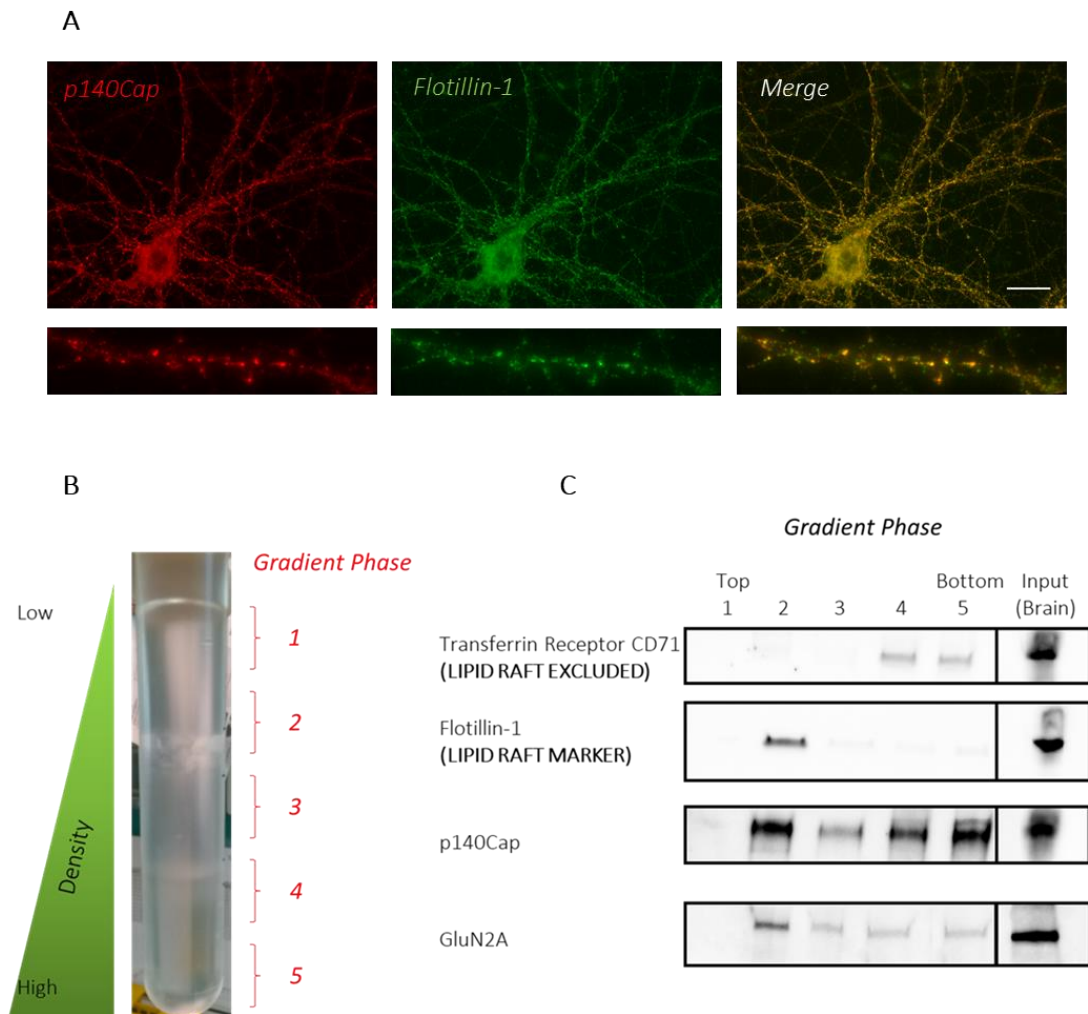
We moved further to quantify the amount of GluN2A recruited to synaptic lipid rafts in WT and p140Cap KO mice. Synaptic lipid rafts were purified under a discontinuous sucrose gradient from WT and p140Cap KO P2 crude synaptosomes. Nine fractions were collected from the top to the bottom of the gradient. Equal volumes of each fraction were analysed by western blot to detect and quantify the presence of Flotillin-1, as a marker of the lipid raft-enriched fractions. Flotillin-1 showed the higher enrichment in phase 4, while transferrin receptor was only present in high density fractions (7, 8 and 9) (Figure

19A). When the amount of GluN2A and PSD95 in fraction 4 of WT and p140Cap KO mice was compared, we found a significant and selective decrease of the percentage of GluN2A and PSD95 present in lipid raft domains of p140Cap KO mice. A slight decrease was also observed for GluN2B and GluN1 subunits of NMDAR. In contrast, we did not detect significant reduction in the lipid raft recruitment of other molecules such as the AMPA receptor subunit 2 (Gria2), the kinases Src and CamK-β, and of Rac1 (Figure 19B and C), suggesting that the composition of synaptic lipid rafts in p140CapKO is not markedly altered, excepting for the levels of GluN2A and PSD95.

These data show that p140Cap facilitates the functional association of GluN2A with PSD95 and their enrichment into lipid rafts. Such increase in these specific membrane domains enriched in signaling molecules, could results in improved efficiency of signal transduction.

Figure 19: A: Synaptic lipid raft isolated from WT and p140Cap KO synaptosomes. 30 µl of each phase was analysed by western blot. Flotillin-1 showed the higher enrichment in phase 4, negative control instead, represented by transferrin receptor, was localized in high density phases. B: Lipid raft enriched phase was analysed (30 µl) and immunoblotted with the indicated antibodies. Images are representative of n=5 mice per experimental group. C: protein quantification normalized on Flotillin-1.
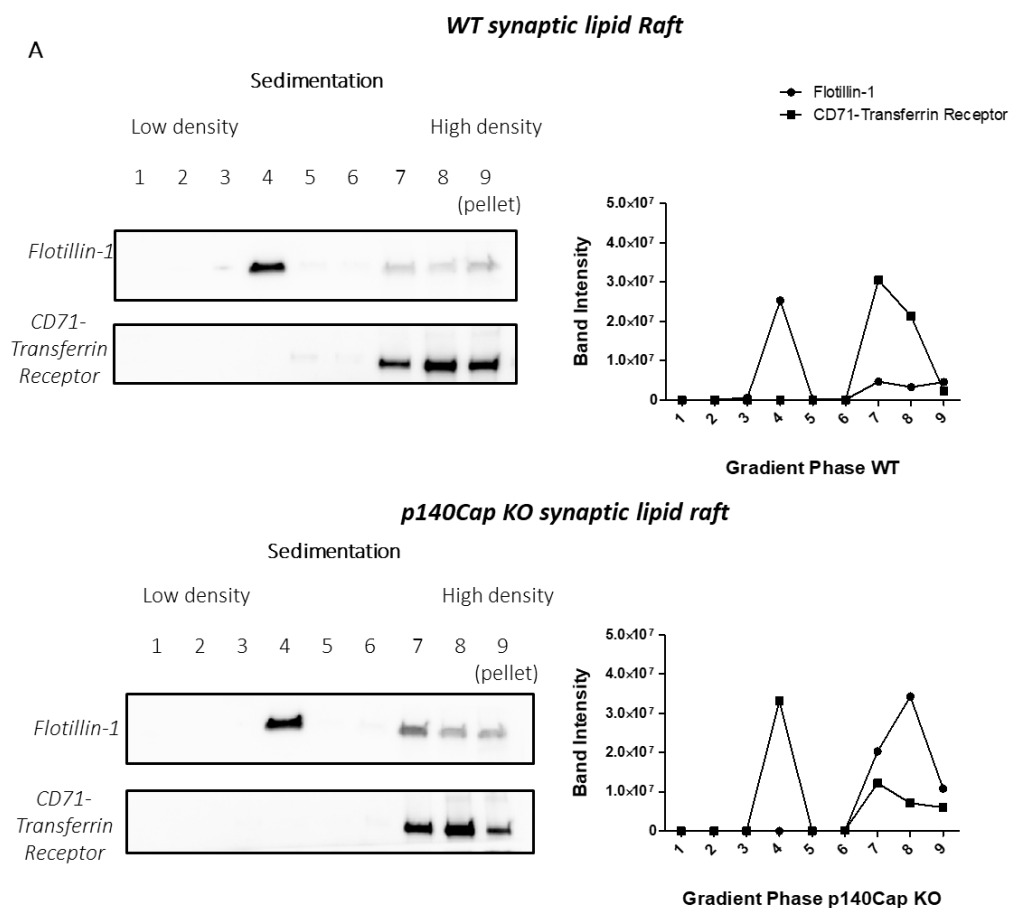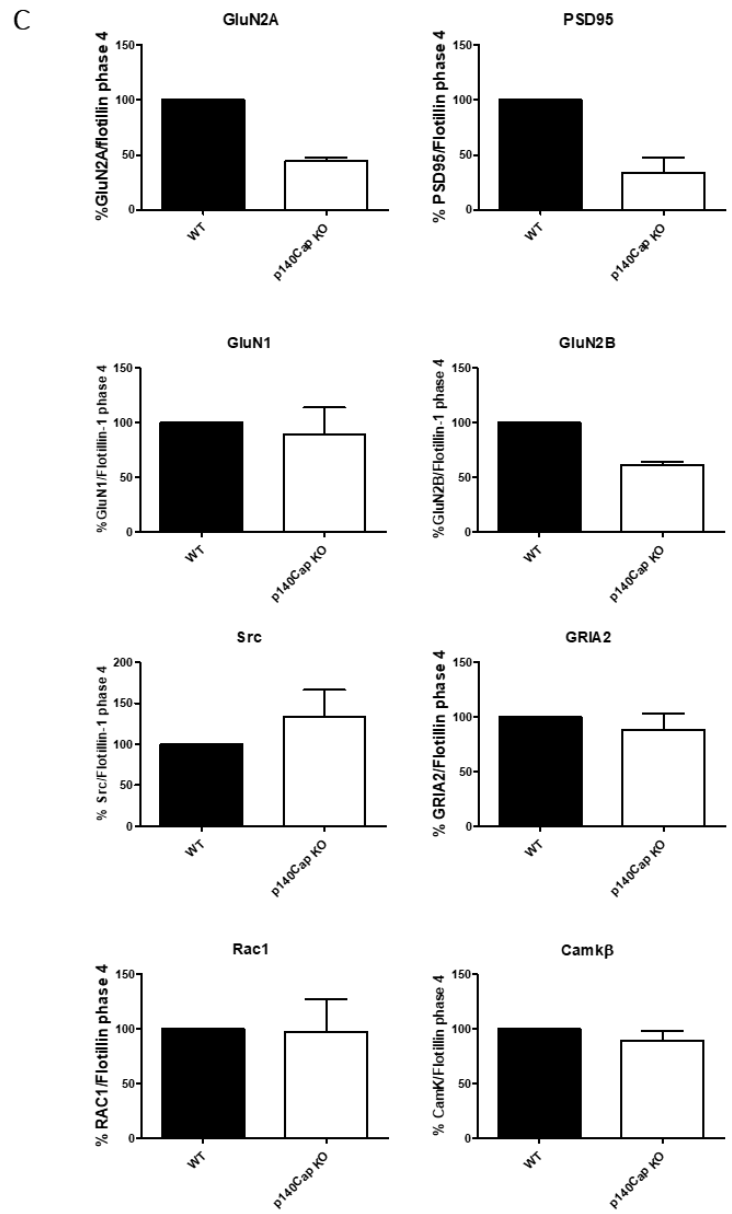
6 DISCUSSION

The present study investigates the involvement of p140Cap in the molecular complexes essential for glutamatergic transmission across synapses. By biochemical protein-protein interaction assays, we demonstrated that p140Cap is a new interactor of the NMDA receptor subunit GluN2A. This result confirms the data obtained from proteomic study focused on the identification of the p140Cap interactors in synaptosomes (Alfieri et al., 2017). Indeed, the interactome analysis revealed that p140Cap was found as a high-fidelity interactor of both NMDA receptor subunits type 2 GluN2A and GluN2B. Co-immunoprecipitation of endogenous p140Cap from mouse crude synaptosomes or exogenous p140Cap in transfected HEK293 cells revealed that p140Cap specifically co-immunoprecipitates with the GluN2A subunit, while very low association was detected with GluN2B. Moreover, the association occurs through p140Cap proline-rich region 1 (aa 351-691) and C-terminal tail domain of GluN2A (aa1349-1464). This region of GluN2A includes an SH3-like domain (aa 1382-1420) (Ladepeche et al., 2014), already identified as a putative binding domain for the interaction of GluN2A with the PSD-95 family proteins. The presence of this SH3-domain in GluN2A tail leads us to hypothesize that the association with p140Cap could be based on a classical proline rich -SH3 domain association. Further experiments will be performed to validate this model of interaction. To address the physiological relevance of p140Cap/GluN2A interaction, we analysed GluN2B to GluN2A expression switch during neuron development in vitro cultures. However, this analysis revealed no significant differences in the kinetics of GluN2A expression between WT and p140Cap KO neurons. Since this result demonstrated that p140Cap does not influence GluN2A expression, we focus our attention in dissecting the interaction of p140Cap and GluN2A at synapse.

NMDAR physically associates a huge number of different molecules, which include scaffold, adhesion and signalling proteins which execute their functions within complexes and higher-order molecular machines (Frank & Grant, 2017). We found that p140Cap may modulate the composition of the molecular complex associated to GluN2A-containing NMDARs. Indeed, in p140Cap KO synaptosomes, GluN2A was significantly less associated with three components of the molecular complex, namely the scaffold protein PSD95, the Rho-GTPase Rac1 and the lipid raft associated protein Flotillin-1. This is an important evidence considering that NMDA receptor dysfunction may arise

from disorganized biochemical signaling pathways downstream of the channel. For instance, NMDAR complex trafficking, localization, and down-stream signaling are described to be abnormal in schizophrenia (Funk, Rumbaugh, Harotunian, McCullumsmith, & Meador-Woodruff, 2009).

Additional relevant finding is the reduced association and co-localization between PSD95 and GluN2A observed in p140Cap KO neurons, suggesting a possible receptor delocalization. This idea is also supported by the rescue of GluN2A synaptic localization in KO hippocampal neurons expressing p140Cap domains involved in the association with GluN2A. Further experiments will be performed to validate the rescue in terms of co-localization with PSD95 in KO neurons. Moreover, electrophysiological recordings of GluN2A containing NMDARs in WT and p140Cap KO neurons will be performed to assess differences in basal state currents. Similar experiments will be also done in KO hippocampal neurons expressing p140Cap domains involved in the association with GluN2A, to assess an electrophysiological rescue.

Besides the reduced association of GluN2A with PSD95 in p140Cap KO synaptosomes, also Rac1 emerged to be significantly less associated to GluN2A receptor complex. This reduced recruitment of Rac1 is consistent with its reduced activation. Rac1 is an important mediator of actin-remodelling of the "spinoskeleton", playing a fundamental role downstream NMDARs activation. Moreover, Rac1 is necessary for LTP (Simons & Sampaio, 2011).

These evidences suggest a role for p140Cap in promoting Rac1 recruitment to NMDAR complex and in allowing its activation. Interestingly, previous works of our group demonstrated that p140Cap may control the activation of another Rho-GTPase protein, RhoA, by decreasing Src-dependent tyrosine phosphorylation of the RhoA-specific GTPase-activating protein p190RhoGAP (Repetto et al., 2014). In the model here proposed instead, p140Cap does not influence directly Rac1 activation, but somehow allows its accurate localization in the NMDAR complex and therefore its proper activation. In this model, p140Cap modulates the composition of the molecular complex associated to GluN2A containing NMDAR by increasing its recruitment in specific membrane subdomain (lipid rafts) which act as a membrane hub to optimize signal transduction (Figure 20). Receptor activation and downstream signalling occurring in lipid rafts is protected from non-raft enzymes such as membrane phosphatases that otherwise could affect the signaling process (Simons & Toomre, 2000). Moreover, also

activated Rac1 segregates to cholesterol-rich, liquid-ordered domains (lipid rafts) in the plasma membrane and stabilizes these microdomains in a process associated with actin polymerization (Moissoglu et al., 2014; Tsai & Philips, 2012).

Recent studies describe that physiological and pathological events such as spatial learning and ischemia can induce the dynamic shift of NMDA receptors signaling complexes between the non-raft membrane and lipid-rafts (Besshoh et al., 2005; Delint-Ramirez et al., 2008).

Figure 20: p140Cap potentiate the association between GluN2A and PSD-95 forming a ternary complex. Moreover, p140Cap mediates GluN2A/PSD95 recruitment to synaptic lipid raft to increase the efficiency of signal transduction.
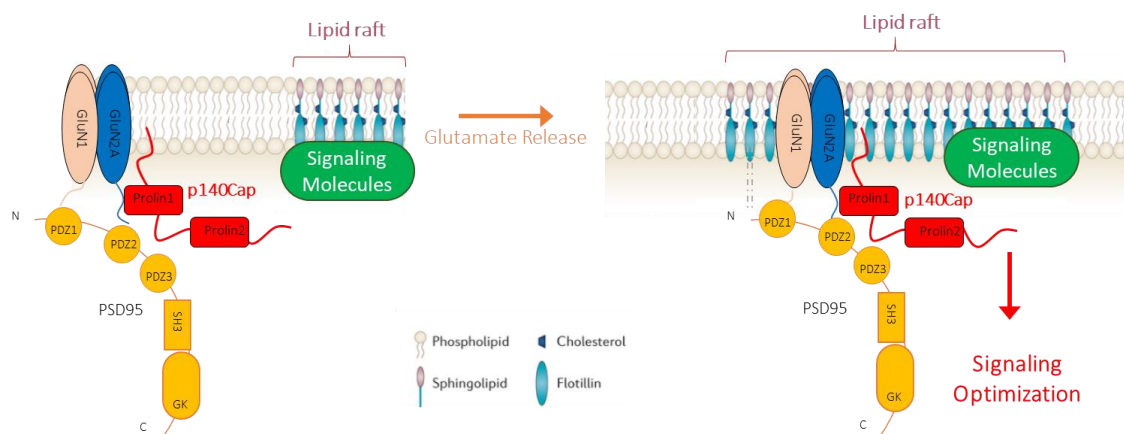
We show that p140Cap is present in brain lipid rafts and co-localizes with lipid raft marker Flotillin-1. Interestingly, p140Cap is also present in the high density phases of the gradient, suggesting that it may have different functions in these non-raft regions. Indeed, we will perform further experiment to assess whether p140Cap presence in lipid rafts correlates with its increased phosphorylation.

We also demonstrate that synaptic lipid rafts of p140Cap KO mice have a reduced level of GluN2A and PSD95, while the amount of other receptors or enzymes involved in NMDARs signaling do not change. Thus, p140Cap may mediates the selective enrichment of GluN2A/PSD95 in synaptic lipid rafts, thus improving the efficiency of signal transduction. This result is consistent with previous works in which the recruitment of NMDARs to lipid rafts was studied in the hippocampus during spatial memory formation (Delint-Ramirez et al., 2008), showing that spatial learning experience, induced with water maze training, causes a rapid recruitment of NMDAR subunits (GluN1, GluN2A, GluN2B) and PSD-95 to synaptic lipid rafts. Further experiments will be performed to assess GluN2A and PSD95 recruitment in synaptic lipid raft of WT and

p140Cap KO animals subject to spatial memory formation behavioural test (i.e. novel object recognition).

The data here presented suggest that p140Cap may influence GluN2A-containing NMDARs recruitment in lipid rafts. The impaired LTP and LTD and the defects in memory and learning observed in p140Cap KO mice could be explained by the reduced localization of NMDARs in the synaptic lipid rafts. Interestingly, diminished levels of NMDAR in lipid rafts were found in the hippocampus of the 3xTg-AD mouse model of Alzheimer's disease without affecting the amount of NMDARs in post-synaptic density (Morin, Diaz-Cintra, Bermudez-Rattoni, & Delint-Ramirez, 2016), suggesting a possible role of p140Cap in neurodegenerative diseases.

p140Cap is also a key regulator of dendritic spine morphology by regulating actin dynamics through the regulation of cortactin (Jaworski et al., 2009; Repetto et al., 2014). In this perspective, p140Cap may act as a linker protein coordinating receptors dynamic between membrane and lipid rafts with dendritic spine cytoskeleton remodelling.

7 ATTIVITÀ FORMATIVE

DOCUMENTAZIONE RELATIVA ALLA PARTECIPAZIONE AD ATTIVITA' FORMATIVE NELL'ANNO 2014

Seminari/Congressi:

13 March 2014, MBC, Via NIzza 52, Torino. "Molecular Imaging of Enzymatic Activity in Inflammation and Cancer", Dr. Alexei Bogdanov (Ospite: S. Aime).

22 May 2014 MBC, Via NIzza 52, Torino. "Reciprocal metabolic deregulation of tumors and their stroma: a new druggable synergy " Prof.ssa Paola Chiarugi (Ospite: V. Poli).

6 and 13 June 2014 Microbiologia, via Santena 9, Torino."Seminari di Immunoterapia dei tumori" Dr.ssa Federica Marchesi, Dr.ssa Paola Nistico'.

12 June 2014 MBC, Via NIzza 52, Torino."Microenvironmental regulation of breast cancer metastasis" Dr. Antoine E. Karboub (Ospite: D. Taverna).

27 June 2014 MBC, Via NIzza 52, Torino. "Targeted Therapy of Cancer: where we are heading" (M. Giovarelli, M. Macagno).

2 July 2014 Torino Esposizioni, C.so Massimo d'Azeglio 15, Torino "Essere giovani protagonisti in H2020: il CV e opportunità di finanziamento attraverso la mobilità internazionale".

29 October 2014 MBC, Via NIzza 52, Torino. "Unmet clinical needs: Basic Scientists meet Clinicians to fill the gap", Seminari del Dipartimento Biotecnologie Molecolari e Scienze della Salute".

19 December 2014 Aula CeRMS, AUO Città della Salute e della Scienza, Via Cherasco 15 Torino "T cells and autoimmunity afternoon" (F.Novelli).

Poster Presentation

28-31 May 2014 XI National Conference of the Italian Society of Immunology, Clinical Immunology and Allergology" SIICA, Florence (Italy).

"TLR8 stimulation of intestinal epithelial cells affects the differentiation /functions of human monocytes" *C. Angelini, B. Varano, P. Puddu, L. Conti, S.Gessani*.

28-31 May 2014 XI National Conference of the Italian Society of Immunology, Clinical Immunology and Allergology" SIICA, Florence (Italy).

"HER2 vaccine induce regulatory mechanisms in patients with HER2-overexpressing tumor: considerations for designing tumor vaccines".

S.Occhipinti, L.Sponton, C.Angelini, A.Amici, C.Marchini, M.A.Satolli, M.Donadio, F.Novelli, M.Giovarelli

Corsi:

" Introduzione alla ricerca Bibliografica, Scuola di Dottorato in Scienze della Vita e della Salute" 17/09/2012 e 24/09/2014

DOCUMENTAZIONE RELATIVA ALLA PARTECIPAZIONE AD ATTIVITA' FORMATIVE NELL'ANNO 2015

Seminari/Congressi:

18-20 February 2015, MBC Via Nizza 52, Torino. Convegno "Frontiers in Regenerative Medicine".

16 April 2015, MBC Via Nizza 52, Torino. "Molecular networks regulating neuronal and non-neuronal cell motility" Prof. Ivan De Curtis.

6 May 2015, MBC Via Nizza 52, Torino. "Circular and linear Non-Coding RNAs in tumorigenesis" Prof. Pier Paolo Pandolfi.

1-3 Juli 2015, MBC Via Nizza 52, Torino. Congresso "SIBBM frontiers in molecular biology".

15 September 2015, "MBC Via Nizza 52, Torino. "New perspectives for prevention of cognitive disability in Down syndrome" Prof.ssa Renata Bartesaghi.

23-24 September 2015, MBC Via Nizza 52, Torino. NEURINOX Symposium: Innovative concepts for treating Neurodegenerative diseases.

6 October 2015, MBC Via Nizza 52, Torino. "Towards unraveling the importance of cell adhesion and cytoskeletal remodeling during brain development" Dott.ssa Silvia Cappello

Poster Presentation:

18-20 February 2015 Congress FRONTIERS IN REGENERATIVE MEDICINE Turin.

"Human mesenchymal stem cells and mesenchymal stem cell-derived microvesicles impair maturation and function of myeloid dendritic cells: induction of a regulatory phenotype in type 1 diabetci patients. Peptides". Abstract book 138.

A. Carpanetto, E. Favaro, C. Caorsi, C. Angelini, M. Giovarelli, G. Camussi, M.M. Zanone.

17-19 September ABCD 2015. Bologna.

"Uncover p140Cap role in synaptic plasticity through the analysis of its interactome".

A.Alfieri, A. Morellato, C. Angelini, I. Russo, Y. Coutè, O. Sorokina, D. Armstrong, M. Matteoli, E. Menna,E. Boeri Erba, E. Turco, P. Defilippi

 Corsi:

"Corso di Biostatistica (4CFU)" prof. Provero. 15, 23, 30 Giugno 2015.

"Corso di Inglese Scientifico" da Novembre 2015 a Marzo 2016

DOCUMENTAZIONE RELATIVA ALLA PARTECIPAZIONE AD ATTIVITA' FORMATIVE NELL'ANNO 2016

Seminari/Congressi:

April 4, 2016 MBC Via Nizza 52, Torino "Encoding synaptic GluN2A-containing NMDA receptor activation: the role of Ring Finger Protein 10". Fabrizio Gardoni, Ph.D. Dept. Pharmacological Sciences UNIMI, Milano.

May 27, 2016 MBC Via Nizza 52, Torino "Endosomal lipids in trafficking and signaling" Jean Gruenberg (Geneva, Switzerland).

June 23, 2016 MBC Via Nizza 52, Torino "Huntington's Disease: from evolutionary biology to pathogenesis" Prof. Chiara Zuccato (Dip. di Bioscienze Università degli Studi di Milano).

June 28, 2016 MBC Via Nizza 52, Torino "Optical nanoscopy 2.0" Prof. Alberto Diaspro (Istituto Italiano di Tecnologia, Genoa).

July 14, 2016 MBC Via Nizza 52, Torino "Nanoprobes for functional neuroimaging" Angelo Bifone (Director of the Center for Neuroscience and Cognitive Systems and Tenured Senior Scientist of the Istituto Italiano di Tecnologia).

September 29, 2016 MBC Via Nizza 52, Torino "IMARIS ANALISI QUANTITATIVA DELLE IMMAGINI in 3D", Workshop applicativo, Maurizio Abbate.

November 17, 2016 MBC Via Nizza 52, Torino "Developing molecular therapies for Rett Syndrome", Stuart Cobb (Institute of Neuroscience and Psychology, College of Medical, Veterinary and Life Science, University of Glasgow UK).

November 24, 2016 MBC Via Nizza 52, Torino "Unravelling the genetics of autism and related disorders" Silvia De Rubeis, Ph.D. (Icahn School of Medicine at Mount Sinai Department of Psychiatry, New York).

Poster presentation

April 7-9, 2016 ABCD National Ph.D. Meeting Salerno

July 2-6, 2016 FENS Forum of Neuroscience Copenhagen

"p140Cap and Synaptic Plasticity through the interaction with NMDA receptor"

C. Angelini, A. Alfieri, I. Russo, A. Morellato, L. Pavinato, S. Marchi, P. Pinton, E. Turco, P. Defilippi

Corsi

"Corso di Inglese Scientifico Livello B1/B2" tenuto presso l'MBC dalla Prof.ssa Justina Walus nel periodo novembre 2015 – marzo 2016 (lezione 50 ore, esame finale 8CFU).

"Corso di microscopia di base Nikon Instruments" tenuto martedì 21Giugno 2016 presso l'MBC dal Dott. Cristiano Rumio.

DOCUMENTAZIONE RELATIVA ALLA PARTECIPAZIONE AD ATTIVITA' FORMATIVE NELL'ANNO 2017

Seminari/Congressi:

February 3, 2017 MBC Via Nizza 52, Torino Angelo Poletti DiSFeB/CEND Università degli Studi di Milano "The protective role of protein quality control system in neurodegenerative diseases".

February 14, 2017 MBC Via Nizza 52, Torino Dr. Carlo Sala "eEF2K/eEF2 pathway in regulating neuronal network plasticity"

March 7, 2017 MBC Via Nizza 52, Torino Dr Gaia Novarino PhD (Institute of Science and Technology Austria) "Whole sequencing and functional analysis identify novel pathways and treatments for cognitive disorders"

April 11, 2017   MBC Via Nizza 52, Torino Dr. Stephan Wilmes University of Dundee "Dimerization dynamics of cytokine receptors probed by single molecule imaging".

May 22, 2017 GIORNATA DI STUDIO GUIDO TARONE MBC Aula Darwin, Via Nizza 52, Torino

September 11, 2017 MBC Via Nizza 52, Torino Dr.ssa Loriana Vitillo "A journey into pluripotency: from integrin signaling to cell-based therapies"

September 19, 2017, MBC Via Nizza 52, Torino Aula Darwin "D-day 2017".

November 23, 2017 SIBBM LECTURE "A tale of proteomics, disease mechanisms & data mountains" Angus Lamond Centre for Gene Regulation and Expression, University of Dundee, UK

Poster presentation:
June 25 to 28, 2017 7th International Conference on Tumor-Host Interaction and Angiogenesis, Monte Verità, Ascona, Southern Switzerland.
"p140Cap expression in syngeneic ERBB2+ breast tumors modulates tumor microenvironment towards a less favorable "milieu" to tumor progression"
Vincenzo Salemme, Jennifer Chapelle, Mauro Vedelago, Federica Cavallo, Laura Conti, Stefania Lanzardo, Costanza Angelini, Daniela Delli Castelli, Enzo Terreno, Alessia Lamolinara, Enrico Moiso, Manuela Iezzi, Emilia Turco and Paola Defilippi.

October 1-4, "XVII Congresso Nazionale SINS Lacco Ameno Ischia".
"p140Cap controls synaptic plasticity through its interaction with NMDA receptor"
Angelini C, Alfieri A, Morellato A, Pavinato L, Cravero T, Turco E, Defilippi P.

"Synaptic intercatome mining reveals p140Cap as a new hub for PSD proteins involved in psychiatric and neurological disorders"
Alfieri A, Sorokina O, Adriat A, Angelini C, Russo I, Morellato A, Matteoli M, Menna E, Boeri Erba E, McLean C, Armstrong J, Ala U, Buxbam J, Brusco A, De Rubeis S, Turco E, Defilippi P.
December 4-6, "6thEuropean Synapse Meeting, Milano".
"p140Cap controls synaptic plasticity through its interaction with NMDA receptor"
Angelini C, Alfieri A, Morellato A, Pavinato L, Cravero T, Turco E, Defilippi P.

"Characterization of the Skt gene in the synapse behavioural studies and analysis of synaptic complexes"

Morellato A, Alfieri A, Angelini C, Pavinato P, Mele P, Gavello P, El-Assawi P, Mauro A, Carbone E, Eva C, Turco E, Defilippi P.

Corsi:

May 29, 30, 31 2017 Mini course "Highlights on Neuroscience" Giornate di Approfondimento in Neuroscienze con la visiting professor Michelle Studer (4CFU).

8 ACKNOWLEDGMENTS

Questi quattro anni di dottorato sono stati come un viaggio "zaino in spalla": lungo, difficile ma allo stesso tempo unico ed emozionante. Ringrazio la professoressa Mirella Giovarelli per avermi dato la possibilità di iniziare questo viaggio. Ringrazio la professoressa Paola Defilippi e la professoressa Emilia Turco per avermi accolto nel loro gruppo di ricerca e per aver creduto in me. Le ringrazio perché grazie a loro ho imparato molto e fatto tante esperienze importanti per la mia crescita professionale.

Ringrazio Annalisa per il supporto, per i consigli, per il suo spirito critico e per la sua risolutezza. Ringrazio Tiziana per la sua infinità disponibilità e per condividere con noi la sua esperienza. Ringrazio Lisa e Henri per la loro curiosità, per la loro voglia di imparare e perché ogni giorno mi insegnano ad insegnare. Ringrazio Alessandro per la sua compagnia, per il suo spirito di squadra e per la passione per gli orsetti gommosi che ci accomuna.

Ringrazio la mia famiglia per il supporto che, nonostante la lontananza, non mi ha fatto mai mancare.

Ringrazio il mio compagno di viaggio Roberto per condividere con me l'ombrello quando piove e la bellezza di un cielo stellato.

Infine, ringrazio chi ancora non è arrivato ma è in viaggio per raggiungerci, per la meraviglia che ha già portato nelle nostre vite.

9 REFERENCES

Al-Hallaq, R. A., Conrads, T. P., Veenstra, T. D., & Wenthold, R. J. (2007). NMDA di-heteromeric receptor populations and associated proteins in rat hippocampus. *J Neurosci, 27*(31), 8334-8343. doi:10.1523/JNEUROSCI.2155-07.2007

Alfieri, A., Sorokina, O., Adrait, A., Angelini, C., Russo, I., Morellato, A., . . . Defilippi, P. (2017). Synaptic Interactome Mining Reveals p140Cap as a New Hub for PSD Proteins Involved in Psychiatric and Neurological Disorders. *Front Mol Neurosci, 10*, 212. doi:10.3389/fnmol.2017.00212

Asaka, Y., Jugloff, D. G., Zhang, L., Eubanks, J. H., & Fitzsimonds, R. M. (2006). Hippocampal synaptic plasticity is impaired in the Mecp2-null mouse model of Rett syndrome. *Neurobiol Dis, 21*(1), 217-227. doi:10.1016/j.nbd.2005.07.005

Astro, V., de Curtis, I. (2015). Plasma membrane-associated platforms: dynamic scaffolds that organize membrane-associated events. *Sci Signal* Mar 10;8(367):re1. doi: 10.1126/scisignal.aaa3312

Besshoh, S., Bawa, D., Teves, L., Wallace, M. C., & Gurd, J. W. (2005). Increased phosphorylation and redistribution of NMDA receptors between synaptic lipid rafts and post-synaptic densities following transient global ischemia in the rat brain. *J Neurochem, 93*(1), 186-194. doi:10.1111/j.1471-4159.2004.03009.x

Besshoh, S., Chen, S., Brown, I. R., & Gurd, J. W. (2007). Developmental changes in the association of NMDA receptors with lipid rafts. *J Neurosci Res, 85*(9), 1876-1883. doi:10.1002/jnr.21336

Blanke, M. L., & VanDongen, A. M. J. (2009). Activation Mechanisms of the NMDA Receptor. In A. M. Van Dongen (Ed.), *Biology of the NMDA Receptor*. Boca Raton (FL).

Browman, D. T., Hoegg, M. B., & Robbins, S. M. (2007). The SPFH domain-containing proteins: more than lipid raft markers. *Trends Cell Biol, 17*(8), 394-402. doi:10.1016/j.tcb.2007.06.005

Brown, R. E., & Milner, P. M. (2003). The legacy of Donald O. Hebb: more than the Hebb synapse. *Nat Rev Neurosci, 4*(12), 1013-1019. doi:10.1038/nrn1257

Chen, B. S., & Roche, K. W. (2007). Regulation of NMDA receptors by phosphorylation. *Neuropharmacology, 53*(3), 362-368. doi:10.1016/j.neuropharm.2007.05.018

Chin, L. S., Nugent, R. D., Raynor, M. C., Vavalle, J. P., & Li, L. (2000). SNIP, a novel SNAP-25-interacting protein implicated in regulated exocytosis. *J Biol Chem, 275*(2), 1191-1200.

Cortese, M. S., Uversky, V. N., & Dunker, A. K. (2008). Intrinsic disorder in scaffold proteins: getting more from less. *Prog Biophys Mol Biol, 98*(1), 85-106. doi:10.1016/j.pbiomolbio.2008.05.007

Cull-Candy, S., Brickley, S., & Farrant, M. (2001). NMDA receptor subunits: diversity, development and disease. *Curr Opin Neurobiol, 11*(3), 327-335.

Damiano, L., Le Devedec, S. E., Di Stefano, P., Repetto, D., Lalai, R., Truong, H., . . . Defilippi, P. (2012). p140Cap suppresses the invasive properties of highly metastatic MTLn3-EGFR cells via impaired cortactin phosphorylation. *Oncogene, 31*(5), 624-633. doi:10.1038/onc.2011.257

Delint-Ramirez, I., Fernandez, E., Bayes, A., Kicsi, E., Komiyama, N. H., & Grant, S. G. (2010). In vivo composition of NMDA receptor signaling complexes differs between membrane subdomains and is modulated by PSD-95 and PSD-93. *J Neurosci, 30*(24), 8162-8170. doi:10.1523/JNEUROSCI.1792-10.2010

Delint-Ramirez, I., Salcedo-Tello, P., & Bermudez-Rattoni, F. (2008). Spatial memory formation induces recruitment of NMDA receptor and PSD-95 to synaptic lipid rafts. *J Neurochem, 106*(4), 1658-1668.

Di Stefano, P., Cabodi, S., Boeri Erba, E., Margaria, V., Bergatto, E., Giuffrida, M. G., . . . Defilippi, P. (2004). P130Cas-associated protein (p140Cap) as a new tyrosine-phosphorylated protein involved in cell spreading. *Mol Biol Cell, 15*(2), 787-800. doi:10.1091/mbc.E03-09-0689

Di Stefano, P., Damiano, L., Cabodi, S., Aramu, S., Tordella, L., Praduroux, A., . . . Defilippi, P. (2007). p140Cap protein suppresses tumour cell properties, regulating Csk and Src kinase activity. *EMBO J, 26*(12), 2843-2855. doi:10.1038/sj.emboj.7601724

Di Stefano, P., Leal, M. P., Tornillo, G., Bisaro, B., Repetto, D., Pincini, A., . . . Defilippi, P. (2011). The adaptor proteins p140CAP and p130CAS as molecular hubs in cell migration and invasion of cancer cells. *Am J Cancer Res, 1*(5), 663-673.

Dosemeci, A., Makusky, A. J., Jankowska-Stephens, E., Yang, X., Slotta, D. J., & Markey, S. P. (2007). Composition of the synaptic PSD-95 complex. *Mol Cell Proteomics, 6*(10), 1749-1760. doi:10.1074/mcp.M700040-MCP200

Dosemeci, A., Weinberg, R. J., Reese, T. S., & Tao-Cheng, J. H. (2016). The Postsynaptic Density: There Is More than Meets the Eye. *Front Synaptic Neurosci, 8*, 23. doi:10.3389/fnsyn.2016.00023

Ewald, R. C., & Cline, H. T. (2009). NMDA Receptors and Brain Development. In A. M. Van Dongen (Ed.), *Biology of the NMDA Receptor*. Boca Raton (FL).

Fan, X., Jin, W. Y., & Wang, Y. T. (2014). The NMDA receptor complex: a multifunctional machine at the glutamatergic synapse. *Front Cell Neurosci, 8*, 160. doi:10.3389/fncel.2014.00160

Farr, C. D., Gafken, P. R., Norbeck, A. D., Doneanu, C. E., Stapels, M. D., Barofsky, D. F., . . . Saugstad, J. A. (2004). Proteomic analysis of native metabotropic glutamate receptor 5 protein complexes reveals novel molecular constituents. *J Neurochem, 91*(2), 438-450. doi:10.1111/j.1471-4159.2004.02735.x

Fetterolf, F., & Foster, K. A. (2011). Regulation of long-term plasticity induction by the channel and C-terminal domains of GluN2 subunits. *Mol Neurobiol, 44*(1), 71-82. doi:10.1007/s12035-011-8190-4

Frank, R. A., & Grant, S. G. (2017). Supramolecular organization of NMDA receptors and the postsynaptic density. *Curr Opin Neurobiol, 45*, 139-147. doi:10.1016/j.conb.2017.05.019

Funk, A. J., Rumbaugh, G., Harotunian, V., McCullumsmith, R. E., & Meador-Woodruff, J. H. (2009). Decreased expression of NMDA receptor-associated proteins in frontal cortex of elderly patients with schizophrenia. *Neuroreport, 20*(11), 1019-1022. doi:10.1097/WNR.0b013e32832d30d9

Gardoni, F., Caputi, A., Cimino, M., Pastorino, L., Cattabeni, F., & Di Luca, M. (1998). Calcium/calmodulin-dependent protein kinase II is associated with NR2A/B subunits of NMDA receptor in postsynaptic densities. *J Neurochem, 71*(4), 1733-1741.

Gardoni, F., Polli, F., Cattabeni, F., & Di Luca, M. (2006). Calcium-calmodulin-dependent protein kinase II phosphorylation modulates PSD-95 binding to NMDA receptors. *Eur J Neurosci, 24*(10), 2694-2704. doi:10.1111/j.1460-9568.2006.05140.x

Gardoni, F., Schrama, L. H., van Dalen, J. J., Gispen, W. H., Cattabeni, F., & Di Luca, M. (1999). AlphaCaMKII binding to the C-terminal tail of NMDA receptor

subunit NR2A and its modulation by autophosphorylation. *FEBS Lett, 456*(3), 394-398.

Gold, M. G. (2012). A frontier in the understanding of synaptic plasticity: solving the structure of the postsynaptic density. *Bioessays, 34*(7), 599-608. doi:10.1002/bies.201200009

Hayashi, K., Suzuki, A., Hirai, S., Kurihara, Y., Hoogenraad, C. C., & Ohno, S. (2011). Maintenance of dendritic spine morphology by partitioning-defective 1b through regulation of microtubule growth. *J Neurosci, 31*(34), 12094-12103. doi:10.1523/JNEUROSCI.0751-11.2011

Henson, M. A., Roberts, A. C., Perez-Otano, I., & Philpot, B. D. (2010). Influence of the NR3A subunit on NMDA receptor functions. *Prog Neurobiol, 91*(1), 23-37. doi:10.1016/j.pneurobio.2010.01.004

Hering, H., Lin, C. C., & Sheng, M. (2003). Lipid rafts in the maintenance of synapses, dendritic spines, and surface AMPA receptor stability. *J Neurosci, 23*(8), 3262-3271.

Hotulainen, P., & Hoogenraad, C. C. (2010). Actin in dendritic spines: connecting dynamics to function. *J Cell Biol, 189*(4), 619-629. doi:10.1083/jcb.201003008

Husi, H., & Grant, S. G. (2001). Proteomics of the nervous system. *Trends Neurosci, 24*(5), 259-266.

Ito, H., Atsuzawa, K., Sudo, K., Di Stefano, P., Iwamoto, I., Morishita, R., . . . Nagata, K. (2008). Characterization of a multidomain adaptor protein, p140Cap, as part of a pre-synaptic complex. *J Neurochem, 107*(1), 61-72. doi:10.1111/j.1471-4159.2008.05585.x

Jaworski, J., Kapitein, L. C., Gouveia, S. M., Dortland, B. R., Wulf, P. S., Grigoriev, I., . . . Hoogenraad, C. C. (2009). Dynamic microtubules regulate dendritic spine morphology and synaptic plasticity. *Neuron, 61*(1), 85-100. doi:10.1016/j.neuron.2008.11.013

Jia, J. Y., Lamer, S., Schumann, M., Schmidt, M. R., Krause, E., & Haucke, V. (2006). Quantitative proteomics analysis of detergent-resistant membranes from chemical synapses: evidence for cholesterol as spatial organizer of synaptic vesicle cycling. *Mol Cell Proteomics, 5*(11), 2060-2071. doi:10.1074/mcp.M600161-MCP200

Kim, E., Cho, K. O., Rothschild, A., & Sheng, M. (1996). Heteromultimerization and NMDA receptor-clustering activity of Chapsyn-110, a member of the PSD-95 family of proteins. *Neuron, 17*(1), 103-113.

Kim, E., Naisbitt, S., Hsueh, Y. P., Rao, A., Rothschild, A., Craig, A. M., & Sheng, M. (1997). GKAP, a novel synaptic protein that interacts with the guanylate kinase-like domain of the PSD-95/SAP90 family of channel clustering molecules. *J Cell Biol, 136*(3), 669-678.

Ladepeche, L., Dupuis, J. P., & Groc, L. (2014). Surface trafficking of NMDA receptors: gathering from a partner to another. *Semin Cell Dev Biol, 27*, 3-13. doi:10.1016/j.semcdb.2013.10.005

Lavezzari, G., McCallum, J., Dewey, C. M., & Roche, K. W. (2004). Subunit-specific regulation of NMDA receptor endocytosis. *J Neurosci, 24*(28), 6383-6391. doi:10.1523/JNEUROSCI.1890-04.2004

Lin, Y., Skeberdis, V. A., Francesconi, A., Bennett, M. V., & Zukin, R. S. (2004). Postsynaptic density protein-95 regulates NMDA channel gating and surface expression. *J Neurosci, 24*(45), 10138-10148. doi:10.1523/JNEUROSCI.3159-04.2004

Lisman, J., Yasuda, R., & Raghavachari, S. (2012). Mechanisms of CaMKII action in long-term potentiation. *Nat Rev Neurosci, 13*(3), 169-182. doi:10.1038/nrn3192

Martin, D. D., Beauchamp, E., & Berthiaume, L. G. (2011). Post-translational myristoylation: Fat matters in cellular life and death. *Biochimie, 93*(1), 18-31. doi:10.1016/j.biochi.2010.10.018

Merrill, M. A., Chen, Y., Strack, S., & Hell, J. W. (2005). Activity-driven postsynaptic translocation of CaMKII. *Trends Pharmacol Sci, 26*(12), 645-653. doi:10.1016/j.tips.2005.10.003

Moissoglu, K., Kiessling, V., Wan, C., Hoffman, B. D., Norambuena, A., Tamm, L. K., & Schwartz, M. A. (2014). Regulation of Rac1 translocation and activation by membrane domains and their boundaries. *J Cell Sci, 127*(Pt 11), 2565-2576. doi:10.1242/jcs.149088

Morin, J. P., Diaz-Cintra, S., Bermudez-Rattoni, F., & Delint-Ramirez, I. (2016). Decreased levels of NMDA but not AMPA receptors in the lipid-raft fraction of 3xTg-AD model of Alzheimer's disease: Relation to Arc/Arg3.1 protein expression. *Neurochem Int, 100*, 159-163. doi:10.1016/j.neuint.2016.09.013

Niethammer, M., Kim, E., & Sheng, M. (1996). Interaction between the C terminus of NMDA receptor subunits and multiple members of the PSD-95 family of membrane-associated guanylate kinases. *J Neurosci, 16*(7), 2157-2163.

Nimchinsky, E. A., Sabatini, B. L., & Svoboda, K. (2002). Structure and function of dendritic spines. *Annu Rev Physiol, 64*, 313-353. doi:10.1146/annurev.physiol.64.081501.160008

Otto, G. P., & Nichols, B. J. (2011). The roles of flotillin microdomains--endocytosis and beyond. *J Cell Sci, 124*(Pt 23), 3933-3940. doi:10.1242/jcs.092015

Paoletti, P. (2011). Molecular basis of NMDA receptor functional diversity. *Eur J Neurosci, 33*(8), 1351-1365. doi:10.1111/j.1460-9568.2011.07628.x

Paoletti, P., Bellone, C., & Zhou, Q. (2013). NMDA receptor subunit diversity: impact on receptor properties, synaptic plasticity and disease. *Nat Rev Neurosci, 14*(6), 383-400. doi:10.1038/nrn3504

Paoletti, P., & Neyton, J. (2007). NMDA receptor subunits: function and pharmacology. *Curr Opin Pharmacol, 7*(1), 39-47. doi:10.1016/j.coph.2006.08.011

Papouin, T., & Oliet, S. H. (2014). Organization, control and function of extrasynaptic NMDA receptors. *Philos Trans R Soc Lond B Biol Sci, 369*(1654), 20130601. doi:10.1098/rstb.2013.0601

Prybylowski, K., Chang, K., Sans, N., Kan, L., Vicini, S., & Wenthold, R. J. (2005). The synaptic localization of NR2B-containing NMDA receptors is controlled by interactions with PDZ proteins and AP-2. *Neuron, 47*(6), 845-857. doi:10.1016/j.neuron.2005.08.016

Repetto, D., Aramu, S., Boeri Erba, E., Sharma, N., Grasso, S., Russo, I., . . . Defilippi, P. (2013). Mapping of p140Cap phosphorylation sites: the EPLYA and EGLYA motifs have a key role in tyrosine phosphorylation and Csk binding, and are substrates of the Abl kinase. *PLoS One, 8*(1), e54931. doi:10.1371/journal.pone.0054931

Repetto, D., Camera, P., Melani, R., Morello, N., Russo, I., Calcagno, E., . . . Defilippi, P. (2014). p140Cap regulates memory and synaptic plasticity through Src-mediated and citron-N-mediated actin reorganization. *J Neurosci, 34*(4), 1542-1553. doi:10.1523/JNEUROSCI.2341-13.2014

Sala, C., & Segal, M. (2014). Dendritic spines: the locus of structural and functional plasticity. *Physiol Rev, 94*(1), 141-188. doi:10.1152/physrev.00012.2013

Sanders, E. M., Nguyen, M. A., Zhou, K. C., Hanks, M. E., Yusuf, K. A., Cox, D. N., & Dumas, T. C. (2013). Developmental modification of synaptic NMDAR composition and maturation of glutamatergic synapses: matching postsynaptic slots with receptor pegs. *Biol Bull, 224*(1), 1-13. doi:10.1086/BBLv224n1p1

Sans, N., Prybylowski, K., Petralia, R. S., Chang, K., Wang, Y. X., Racca, C., . . . Wenthold, R. J. (2003). NMDA receptor trafficking through an interaction between PDZ proteins and the exocyst complex. *Nat Cell Biol, 5*(6), 520-530. doi:10.1038/ncb990

Sanz-Clemente, A., Nicoll, R. A., & Roche, K. W. (2013). Diversity in NMDA receptor composition: many regulators, many consequences. *Neuroscientist, 19*(1), 62-75. doi:10.1177/1073858411435129

Schubert, V., & Dotti, C. G. (2007). Transmitting on actin: synaptic control of dendritic architecture. *J Cell Sci, 120*(Pt 2), 205-212. doi:10.1242/jcs.03337

Sheng, M. (2001). The postsynaptic NMDA-receptor--PSD-95 signaling complex in excitatory synapses of the brain. *J Cell Sci, 114*(Pt 7), 1251.

Sheng, M., & Hoogenraad, C. C. (2007). The postsynaptic architecture of excitatory synapses: a more quantitative view. *Annu Rev Biochem, 76*, 823-847. doi:10.1146/annurev.biochem.76.060805.160029

Sheng, M., & Kim, E. (2011). The postsynaptic organization of synapses. *Cold Spring Harb Perspect Biol, 3*(12). doi:10.1101/cshperspect.a005678

Simons, K., & Sampaio, J. L. (2011). Membrane organization and lipid rafts. *Cold Spring Harb Perspect Biol, 3*(10), a004697. doi:10.1101/cshperspect.a004697

Simons, K., & Toomre, D. (2000). Lipid rafts and signal transduction. *Nat Rev Mol Cell Biol, 1*(1), 31-39. doi:10.1038/35036052

Suzuki, T., Zhang, J., Miyazawa, S., Liu, Q., Farzan, M. R., & Yao, W. D. (2011). Association of membrane rafts and postsynaptic density: proteomics, biochemical, and ultrastructural analyses. *J Neurochem, 119*(1), 64-77. doi:10.1111/j.1471-4159.2011.07404.x

Swanwick, C. C., Shapiro, M. E., Vicini, S., & Wenthold, R. J. (2010). Flotillin-1 promotes formation of glutamatergic synapses in hippocampal neurons. *Dev Neurobiol, 70*(13), 875-883. doi:10.1002/dneu.20828

Swanwick, C. C., Shapiro, M. E., Yi, Z., Chang, K., & Wenthold, R. J. (2009). NMDA receptors interact with flotillin-1 and -2, lipid raft-associated proteins. *FEBS Lett, 583*(8), 1226-1230. doi:10.1016/j.febslet.2009.03.017

Tada, T., & Sheng, M. (2006). Molecular mechanisms of dendritic spine morphogenesis. *Curr Opin Neurobiol, 16*(1), 95-101. doi:10.1016/j.conb.2005.12.001

Tejada-Simon, M. V., Villasana, L. E., Serrano, F., & Klann, E. (2006). NMDA receptor activation induces translocation and activation of Rac in mouse hippocampal area CA1. *Biochem Biophys Res Commun, 343*(2), 504-512. doi:10.1016/j.bbrc.2006.02.183

Tomasoni, R., Repetto, D., Morini, R., Elia, C., Gardoni, F., Di Luca, M., . . . Matteoli, M. (2013). SNAP-25 regulates spine formation through postsynaptic binding to p140Cap. *Nat Commun, 4*, 2136. doi:10.1038/ncomms3136

Tsai, F. D., & Philips, M. R. (2012). Rac1 gets fattier. *EMBO J, 31*(3), 517-518. doi:10.1038/emboj.2011.481

Ulbrich, M. H., & Isacoff, E. Y. (2008). Rules of engagement for NMDA receptor subunits. *Proc Natl Acad Sci U S A, 105*(37), 14163-14168. doi:10.1073/pnas.0802075105

Uversky, V. N. (2015). Intrinsically disordered proteins and their (disordered) proteomes in neurodegenerative disorders. *Front Aging Neurosci, 7*, 18. doi:10.3389/fnagi.2015.00018

Zhou, Q., & Sheng, M. (2013). NMDA receptors in nervous system diseases. *Neuropharmacology, 74*, 69-75. doi:10.1016/j.neuropharm.2013.03.030

10 PUBLISHED PAPERS

- ✓ "Direct and Intestinal Epithelial Cell-mediated Effects of TLR8 Triggering on Human Dendritic Cells, CD14+CD16+ Monocytes and γδ T Lymphocytes". **Costanza Angelini**, Barbara Varano, Patrizia Puddu, Maurizio Fiori, Sandra Gessani, Lucia Conti. Front Immunol. 2017 Dec 22;8:1813. doi: 10.3389/fimmu.2017.01813. PMID: 29312324

- ✓ "p140Cap Regulates GABAergic Synaptogenesis and Development of Hippocampal Inhibitory Circuits". Isabella Russo, Daniela Gavello, Elisabetta Menna, David Vandael, Carola Veglia, Noemi Morello, Irene Corradini, Elisa Focchi, Annalisa Alfieri, **Costanza Angelini**, Federico Tommaso Bianchi, Alessandro Morellato, Andrea Marcantoni, Marco Sassoè-Pognetto, Matteo Maria Ottaviani, Latefa Yekhlef, Maurizio Giustetto, Stefano Taverna, Valentina Carabelli, Michela Matteoli, Emilio Carbone, Emilia Turco, Paola Defilippi. Cereb Cortex. 2017 Nov 17:1-15. doi: 10.1093/cercor/bhx306. PMID:29161354.

- ✓ "Synaptic Interactome Mining Reveals p140Cap as a New Hub for PSD Proteins Involved in Psychiatric and Neurological Disorders." Alfieri A, Sorokina O, Adrait A, **Angelini C**, Russo I, Morellato A, Matteoli M, Menna E, Boeri Erba E, McLean C, Armstrong JD, Ala U, Buxbaum JD, Brusco A, Couté Y, De Rubeis S, Turco E and Defilippi P. Front. Mol. Neurosci.10:212.doi: 10.3389/fnmol.2017.00212. PMID: 28713243.

- ✓ "Human mesenchymal stem cells and derived extracellular vesicles induce regulatory dendritic cells in type 1 diabetic patients." Favaro E, Carpanetto A, Caorsi C, Giovarelli M, **Angelini C**, Cavallo-Perin P, Tetta C, Camussi G, Zanone MM. Diabetologia. 2016 Feb;59(2):325-33. doi: 10.1007/s00125-015-3808-0. PMID:26592240.

Direct and Intestinal Epithelial Cell-Mediated Effects of TLR8 Triggering on Human Dendritic Cells, CD14+CD16+ Monocytes and γδ T Lymphocytes

Costanza Angelini[1], Barbara Varano[1,2], Patrizia Puddu[1], Maurizio Fiori[3], Antonella Baldassarre[4], Andrea Masotti[4], Sandra Gessani[1,2] and Lucia Conti[1,2]*

[1] *Department of Hematology, Oncology and Molecular Medicine, Istituto Superiore di Sanità, Rome, Italy, [2] Center for Gender-Specific Medicine, Istituto Superiore di Sanità, Rome, Italy, [3] Department of Food Safety, Nutrition and Veterinary Public Health, Istituto Superiore di Sanità, Rome, Italy, [4] Bambino Gesù Children's Hospital-IRCCS, Research Laboratories, Rome, Italy*

Toll-like receptor (TLR)7/8 plays a crucial role in host recognition/response to viruses and its mucosal expression directly correlates with intestinal inflammation. The aim of this study was to investigate the role of TLR7/8 stimulation of intestinal epithelium in shaping the phenotype and functions of innate immunity cell subsets, and to define direct and/or epithelial cell-mediated mechanisms of the TLR7/8 agonist R848 immunomodulatory activity. We describe novel, TLR8-mediated, pro- and anti-inflammatory effects of R848 on *ex vivo* cultured human blood monocytes and γδ T lymphocytes, either induced by direct immune cell stimulation or mediated by intestinal epithelial cells (IEC). Apical stimulation with R848 led to its transport across normal polarized epithelial cell monolayer and resulted in the inhibition of monocyte differentiation toward immunostimulatory dendritic cells and Th1 type response. Furthermore, γδ T lymphocyte activation was promoted following direct exposure of these cells to the agonist. Conversely, a selective enrichment of the CD14+CD16+ monocyte subpopulation was observed, which required a CCL2-mediated inflammatory response of normal epithelial cells to R848. Of note, a TLR-mediated activation of control γδ T lymphocytes was promoted by inflamed intestinal epithelium from active Crohn's disease patients. This study unravels a novel regulatory mechanism linking the activation of the TLR8 pathway in IEC to the monocyte-mediated inflammatory response, and highlights the capacity of the TLR7/8 agonist R848 to directly enhance the activation of γδ T lymphocytes. Overall these results expand the range of cell targets and immune responses controlled by TLR8 triggering that may contribute to the antiviral response, to chronic inflammation, as well as to the adjuvant activity of TLR8 agonists, highlighting the role of intestinal epithelium microenvironment in shaping TLR agonist-induced responses.

Keywords: cell activation, pathogen recognition, inflammation, microenvironment, adjuvant

Abbreviations: AS, apical side; BS, basolateral side; CD, Crohn's disease; CDEIS, Crohn's Disease Endoscopic Index of Severity; CM, conditioned medium; DC, dendritic cell; IBD, inflammatory bowel disease; IEC, intestinal epithelial cells; IPP, isopentenilpyrophosphate; ODN, oligonucleotides; PRR, pattern recognition receptor; TEER, transepithelial electrical resistance; TLR, toll-like receptor; TM, transport medium; ZOL, zoledronate.

INTRODUCTION

Toll-like receptors (TLR) play a fundamental role in pathogen recognition by immune cells leading to immune response activation and pathogen clearance (1). They also control intestinal homeostasis by sensing commensal microorganisms and avoiding detrimental responses.

TLR7 and TLR8 are expressed by myeloid cells, lymphocytes and intestinal epithelial cells (IEC) (2) and recognize specific moieties in viral ssRNA. Their triggering results in viral antigen presentation and generation of protective immune response (3). Conversely, their altered expression in epithelial and lamina propria immune cells may contribute to chronic intestinal inflammation. In particular, TLR7/8 expression in colonic mucosa is increased following antibiotic-induced dysbiosis in mice (4), and abnormal TLR8 expression/signaling characterizes chronic intestinal inflammation contributing to the pathogenesis of inflammatory bowel diseases (IBD) and to inflammation-associated tumorigenesis (5). This receptor is selectively activated in inflamed colonic epithelium of IBD subjects (6, 7) and its expression directly correlates with the severity of intestinal inflammation (8). Furthermore, TLR8 expression characterizes gastrointestinal tumors and correlates with metastasis and poor prognosis (9).

The evidence that different, even opposite, effects can be elicited by TLR7/8 stimulation highlights the importance of a deeper characterization of cell types and immune functions that can be targeted when TLR7/8 agonists are used as vaccine adjuvants. In this regard, the TLR7/8 agonist R848 (also known as resiquimod, S-28463), has come to light as an effective mean of enhancing both antiviral and antitumor responses. R848 is a hydrophobic, low molecular weight synthetic compound, belonging to the imidazoquinoline family and recognizing both TLR7 and TLR8 (10). This agonist has a demonstrated potential as vaccine adjuvant and cancer therapeutic by virtue of its capacity to induce immune mediators and to directly activate dendritic cells (DC), thus preferentially triggering Th1 type responses and enhancing both humoral and cellular immunity (11, 12). However, despite its strong adjuvant properties in mice following topic and oral administration (13–15), the use of R848 in humans has been hampered by their capacity, not yet understood, to rapidly reach the bloodstream and to exert strong systemic effects, mostly dependent on cytokine storm induction (16). Nevertheless, whether and how this compound is adsorbed and/or diffuses across epithelia and tissues, and the role of the delivery route and tissue microenvironment in shaping TLR agonist-induced responses have been only poorly investigated.

The aim of this study was to identify novel cell types and/or immune functions controlled by TLR7/8 triggering of the intestinal epithelium, and to define direct and/or epithelial cell-mediated mechanisms of the R848 immunomodulatory activity. We report that R848 easily diffuses across the polarized Caco-2 cell monolayer and, through TLR8 triggering, it delivers both inflammatory and regulatory signals to monocytes and γδ T lymphocytes, either directly or through epithelial cell stimulation. Specifically, this agonist, when transported across

normal epithelial cell monolayer, directly impairs the differentiation of monocytes toward immunostimulatory DC and promotes the activation of γδ T lymphocytes. Simultaneously, it drives the enrichment of the CD14+CD16+ monocyte sub-population by stimulating inflammatory chemokine production by IEC.

These results unravel a novel regulatory mechanism linking the activation of the TLR8 pathway in IEC to the monocyte-mediated inflammatory response, and highlight the capacity of R848 to directly enhance the activation of γδ T lymphocytes. This expands the range of cell targets and immune cell responses controlled by TLR8 triggering that may contribute to the antiviral response, to chronic inflammation, as well as to the adjuvant activity of TLR8 agonists.

MATERIALS AND METHODS

Culture of Polarized Caco-2 Cells

Polarized IEC monolayer was obtained by culturing Caco-2 cells (ATCC #HTB-37, 8×10^4 cell/cm^2) on polycarbonate-coated trans-well chambers (0,4 μm pore, 24 mm diameter, Corning) in high glucose DMEM plus 10% FBS and non-essential amino acids for 21 days. Medium was changed every 2 days and IEC differentiation and integrity was monitored by measuring transepithelial electrical resistance (TEER) throughout the culture period by a Volt-meter (Millicell ERS; Millipore Co., Bedford, MA, USA). At the end of the differentiation period (TEER values >800 Ω cm^2), medium was changed, DMEM was replaced by RPMI plus 10% FBS at the basolateral side (BS), and cultures were stimulated at the apical side (AS) with R848 (Resiquimod, 5 μg/ml, kindly provided by Dr. Philippe Neuner, IRBM), CL264 (5 μg/ml, InvivoGen) or β-glucan (10 μg/ml, 1 → 3 β-glucan from baker's yeast, Sigma Aldrich) for 24 h. Agonist concentration 5-fold higher with respect to that used for immune cells was chosen to stimulate epithelial cells. Conditioned medium (CM) was then collected from the BS, filtered and stored at -80°C. IEC monolayer integrity was monitored before and at different time points after treatment by measuring TEER and phenol red transport (17). TEER variations < 10% and phenol red transport ≤ 2% were considered acceptable. Six different preparations of Caco-2 trans-well cultures, leading to comparable results, were used for the study.

HPLC Analysis of R848 Transport across Intestinal Epithelium

R848 was loaded to the IEC monolayer AS and, at different time points, CM from the BS were collected and analyzed by HPLC for agonist content. HPLC analyses were performed on HPLC system 1100 series coupled to a Diode Array Detector and autosampler (Agilent Technologies, Rome, Italy). The column was a Symmetry C18 reversed-phase (150 mm × 3.0 mm, 5 μm), connected to a Sentry Guard Column Symmetry C18 5 μm (3.9 mm × 20 mm) (Waters, Milford, MA, USA). The mobile phase was constituted by solvent A (water containing glacial acetic acid 1% v/v) and solvent B (acetonitrile).

Chromatography was carried out by linear gradient at room temperature, according to the following program: 2% B for 2 min; from 2 to 100% B in 8 min, holding on for 2 min, finally to 2% B in 2 min; the equilibrium time between analyses was 5 min. The flow rate was 0.300 ml/min and 10 μl of sample was injected onto the column. Wavelength λ = 245 nm. The extent of agonist transport was calculated by dividing the cumulative amount of molecule transported, at the different time points, into the BS CM with the original loading concentration. Caco-2 IEC monolayer was also exposed to different concentrations of R848 for 5 h, BS CM was analyzed by HPLC and the apparent permeability coefficients (Papp) were calculated as previously described (18).

Monocyte-Derived DC Generation and Culture

Monocytes were isolated from the peripheral blood of healthy donors by Ficoll/Paque density gradient centrifugation followed by immunomagnetic selection using CD14+ microbeads (MACS monocyte isolation kit, Miltenyi Biotec, Auburn, CA, USA), according to the manufacturer's instructions. To obtain control immature monocyte-derived DC, monocytes were seeded at 1×10^6 cells/ml in standard medium [RPMI 1640 medium containing 10% FBS, GM-CSF (50 ng/ml, kindly provided by Schering-Plough, Dardilly, France) and IL-4 (500 U/ml, Miltenyi Biotec, Auburn, CA, USA)] and cultured for 5 days. Fresh medium plus cytokines was added at day 3 of culture. For some experiments, monocytes were cultured in standard medium and exposed to R848 (1 μg/ml), CL264 (1–2 μg/ml), or β-glucan (2 μg/ml) soon after seeding. CM-conditioned DC was generated in the same conditions by replacing standard medium with Caco-2 CM. For cytokine blocking, monocytes were seeded in CM after a 30-min pre-incubation of this latter with neutralizing Ab (2.5 μg/ml) to CCL2 (rabbit polyclonal, Sigma Aldrich) or IL-6 (mouse monoclonal, Sigma Aldrich), or with isotype control Ab (rabbit and mouse IgG, respectively). TLR blocking was performed by treating R848 CM-exposed monocytes with phosphorothioate oligonucleotides (ODN) targeting TLR7/8/9 (# 2088, TCCTGGCGGGGAAGT; 1 μM) or specific for TLR7 (# 20958, TCCTAACAAAAAAAT; 2.5 μM) soon after seeding.

γδ T Lymphocyte Isolation, Culture, and Interaction with DC

γδ T lymphocytes were isolated from cryopreserved PBMC of healthy donors by positive selection with immunomagnetic beads (Miltenyi Biotec), according to the manufacturer's instructions. Positively selected population contained >95% viable γδ T cells as assessed by flow cytometry. After an overnight culture in complete medium (RPMI plus 10% FBS), purified γδ T cells were washed, suspended in the same medium at the density of 10^6 cells/ml and exposed to R848 or CL264, or seeded, at the same density, in Caco-2 or primary IEC-derived CM. Cells were stimulated with the non-peptide phosphoantigen isopentenilpyrophosphate (IPP, 2 μg/ml, Sigma Aldrich) and cultured for 48 h.

Dendritic cell/γδ T cell co-cultures were set up by adding purified lymphocytes to autologous control or CM-generated DC (1:1

ratio) as previously described (19). Co-cultures were left untreated or stimulated with the aminobiphosphonate zoledronate (ZOL, 10 μg/ml, kindly provided by Novartis Pharma, Origgio, VA) and analyzed 48 h later.

CD4+ T Cell Activation Assay

Naive CD4+ T lymphocytes were isolated from PBMC of healthy donors by negative selection with immunomagnetic beads (Miltenyi Biotec), according to the manufacturer's instructions. The purity of isolated cells (≥98%) was checked by flow cytometry after labeling with anti-CD4-PE and anti-CD45 RA-FITC.

For T cell activation assay, 5-day cultured control or CM-generated DC were stimulated with LPS (10 ng/ml) for 24 h to obtain mature cells. Mature DC were washed twice in serum-free RPMI and co-cultured with freshly isolated allogeneic naive CD4+ T lymphocytes (1:10 ratio), in a mixed leukocyte reaction assay, for 12 days in RPMI plus 5% human AB serum. IL-2 (50 U/ml) was added to the co-cultures at day 6. Lymphocytes were then harvested, counted, seeded in fresh medium and stimulated with PMA (50 ng/ml) and Ionomycin (1 μg/ml). 18 h later, culture medium was collected for IFNγ content determination.

Ethics Statement

Healthy donor buffy coats were obtained from Centro Trasfusionale, Sapienza University of Rome. Buffy coats were not obtained specifically for this study. Informed consent was asked to blood donors according to the Italian law n. 219 (October 21, 2005), recently revised (D.L. of the Ministry of Health, November 2, 2015). Data have been treated by Centro Trasfusionale according to the Italian law on personal data management "Codice in materia di protezione dei dati personali" (Testo unico D.L. June 30, 2003 n. 196).

Investigation including IBD patients has been conducted in accordance with the Declaration of Helsinki and, according to national and international guidelines. The study was approved by the review board of Istituto Superiore di Sanità (project identification code: CE/11/299). All the subjects included were provided with complete information about the study and asked to sign an informed consent.

Patients and Biological Samples

Endoscopic biopsies, taken from colon/ileum tissue, were obtained from patients with documented Crohn's disease (CD, $n = 8$) or age and sex matched healthy controls (HC, $n = 8$, undergoing screening colonoscopy), attending to the Digestive Endoscopy Unit (Catholic University, Rome, Italy). The exclusion criteria were: clinical evidence of active infection, recent (within 14 days) use of antibiotics, pregnancy, hormone-based therapy, and treatment with corticosteroids. Endoscopic activity was assessed according to the Crohn's Disease Endoscopic Index of Severity (remission when score <3) (20). Biopsies were kept in ice-cold PBS containing penicillin, streptomycin (50 IU/ml) and gentamycin (0.5 mg/ml) (Transport Medium, TM) before enterocyte isolation.

Isolation of Primary IEC

IEC were isolated from whole biopsies as previously described (21). Briefly, biopsies were extensively washed by shaking in TM,

and then incubated in TM containing EDTA and EGTA (1 mM) for 75 min at 21°C under soft stirring. Intestinal crypts were then allowed to detach from mucosa by vigorous shaking and cultured ON in RPMI plus 10% FBS. CM was collected, filtered, and stored at −80°C.

Determination of Soluble Immune Mediators

Caco-2 CM as well as supernatants from control and CM-generated DC, γδ T lymphocytes, and DC-T cell co-cultures were analyzed by ELISA for their content of CCL2, IL-10, PGE$_2$ (R&D Systems Inc., Minneapolis, MN, USA), IL-1β, IL-6, IL-12, TNFα, and IFNγ (Biolegend, San Diego, CA, USA), according to the manufacturer's instructions.

Flow Cytometry Analysis

The expression of surface markers was analyzed by flow cytometry. Briefly, cells were pre-incubated for 30 min on ice with PBS containing 10% human AB serum to block non-specific Ig binding and then incubated with the specific Abs or control isotypes for 30 min on ice, washed, and analyzed. The following Abs were used: FITC- or APC-conjugated CD14 (BD Pharmigen or eBiosciences, respectively), PE-CD1a, PE-CD206/MR, PE-CD209/DC-SIGN (BD Pharmigen), and FITC-CD16 (eBiosciences). At least 10,000 events/sample were acquired by a FACScan cytometer (BD Biosciences). Data analysis was performed by gating on the monocyte/DC populations and excluding death cells and debris.

Immunoblotting Analysis

Whole cell extracts were prepared by lysing cells in RIPA buffer [150 mM NaCl, 50 mM Tris–Cl (pH 7.5), 1% Nonidet P-40, 0.5% sodium deoxycholate, and 0.1% sodium dodecyl sulfate (SDS)] containing a cocktail of protease (Roche) and phosphatase inhibitors (Sigma-Aldrich). Cell lysates (10 µg per lane) were fractionated on 8% SDS-PAGE, transferred to a nitrocellulose membrane, and subjected to immunoblot analysis using antibodies specific for the total or tyrosine phosphorylated forms of STAT3 (Cell Signaling Technology). Equal loading of proteins was verified by blotting the same gel with antibodies to β-actin (BD Biosciences).

Real-time PCR

Total RNA was isolated from 21-day cultured polarized Caco-2 cell monolayer or freshly isolated blood monocytes and γδ T lymphocytes with Total RNA Purification Plus Kit (Norgen Biotek, Canada). RNA quality was checked on an Agilent 2100 Bioanalyzer and reverse transcribed (SuperScript™ III, ThermoFisher). Glucuronidase beta (GUSB) was used as reference gene. Primers for TLR7 (Hs.PT.58.38778009), TLR8 (Hs.PT.58.15023918.G), and GUSB (Hs.PT.39a.22214857) were purchased from Integrated DNA technologies. mRNA levels were quantified by qPCR on a QuantStudio™ 12K Flex OpenArray® (Applied Biosystems) by using the comparative ΔΔC_t method.

Statistical Analysis

GraphPad Prism 5 software was used for statistical analysis. Statistical comparisons were performed by the one-way analysis of variance, with Newman–Keuls *post hoc* test, for multiple groups and by the two-tailed paired Student's *t*-test for independent samples, as appropriate. Differences were considered significant when *p* values were <0.05.

RESULTS

R848-Conditioned IEC Affect the Differentiation of Monocyte-Derived DC and Their Capacity to Stimulate Th1 Type Responses

To assess whether TLR7/8 triggering in intestinal epithelium may transduce signals ultimately affecting the functional properties of innate immunity cells, we analyzed the effects of polarized Caco-2 cell monolayer, stimulated with R848, on the differentiation of human monocytes toward DC. Polarized IEC monolayer was left untreated or stimulated, at the AS, with R848. Human peripheral blood monocytes were induced to differentiate toward DC in the presence of control medium or CM from unstimulated or TLR-stimulated Caco-2 cells. As shown in **Figures 1A,B**, a significant proportion of monocytes exposed to CM from R848-conditioned IEC monolayer (R848 CM) did not express the DC-specific marker CD1a and retained the expression of CD14 as compared to cultures exposed to standard medium, indicative of impaired DC differentiation. Conversely, only a slight reduction in CD1a expression was detected when DC were generated in the presence of control CM (**Figures 1A,B**). Likewise, DC differentiation was not affected when monocytes were exposed to CM from Caco-2 cells stimulated with β-glucan, an immunomodulatory compound endowed with adjuvant properties, which recognizes a different family of pattern recognition receptor (PRR) (**Figures 1A,B**).

Despite the negative effect exerted by R848 CM on monocyte to DC differentiation, cells generated under these conditions expressed levels of mannose receptor (MR) and DC-SIGN comparable, or even higher, to those of cells cultured in standard medium (**Figure 1C**; MR: 98% ± 7.3 vs. 96.7% ± 6.0; DC-SIGN: 97% ± 4.9 vs. 96% ± 6.4; *n* = 4).

By contrast, when DC cultures obtained under the different conditions were analyzed for cytokine expression, significant changes in the profile of cytokines constitutively released were observed. As shown in **Figure 2A**, cells generated in R848 CM expressed higher levels of both pro-inflammatory (IL-1β, TNFα) and regulatory (IL-6, IL-10) cytokines as compared to cultures generated in control CM and standard medium, suggesting that a heterogeneous population of cells differentiated from R848 CM-stimulated monocytes.

To further investigate the nature of these cells, we analyzed the levels of phosphorylated STAT3, whose activation is induced by both IL-6 and IL-10 and has been reported in cells with regulatory/tolerogenic features. As expected, constitutive STAT3 activation was found in R848 CM-generated cells but
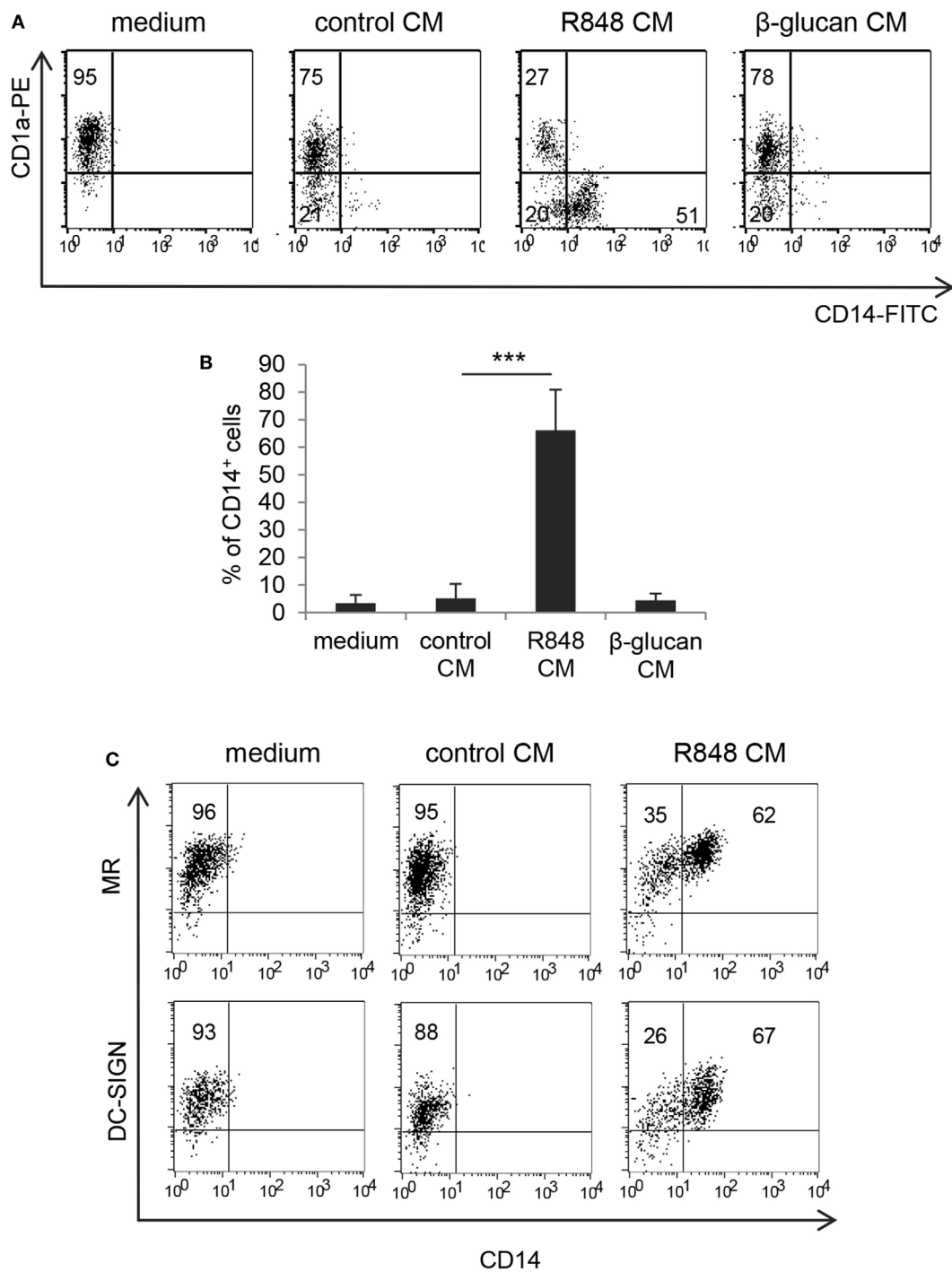
FIGURE 1 | Effects of R848-exposed intestinal epithelial cell (IEC) monolayer on dendritic cell (DC) differentiation. Peripheral blood monocytes were induced to differentiate toward DC in standard medium or in conditioned medium (CM) from Caco-2 cell-derived IEC monolayer, left untreated or stimulated with R848 **(A–C)** or β-glucan **(A,B)**. At day 5, cells were harvested and analyzed for the expression of the indicated surface markers by flow cytometry. One representative experiment out of 4 is reported in panels **(A,C)**. Numbers in quadrants indicate the percentages of positive cells. The percentage of CD14+ cells is reported in panel **(B)**, mean values ± SD from 10 independent experiments are shown. ***$p < 0.001$.

not in cells differentiated in standard medium or control CM (**Figure 2B**). Accordingly, R848 CM-generated cells were found to impair IFNγ production in co-cultured CD4+ T lymphocytes

(**Figure 2C**), whereas no effect was observed on the production of IL-17 (data not shown). In line with the effect on Th1 cytokine production, a reduced secretion of the Th1-polarizing
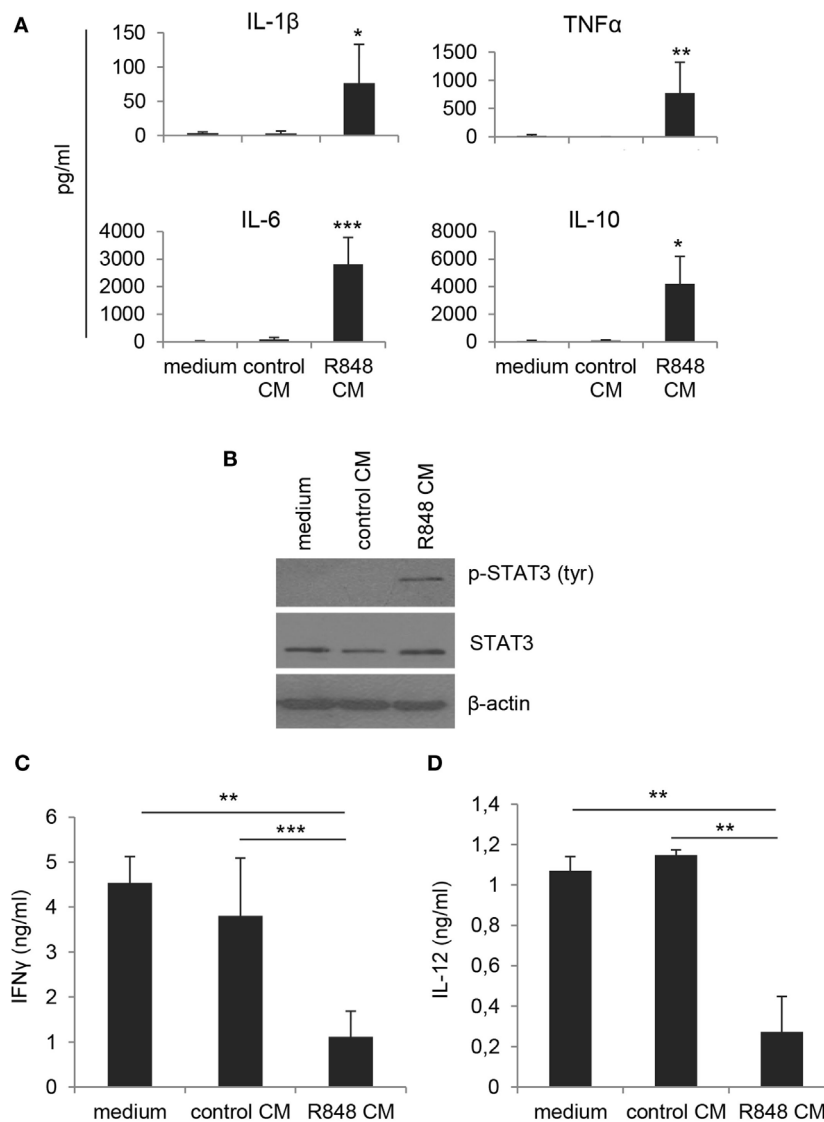
FIGURE 2 | Effects of R848-exposed IEC monolayer on DC functional properties. Monocyte-derived DC were generated as described in the legend to **Figure 1** and harvested at day 5 of culture. **(A)** Cell supernatants were analyzed for the release of the indicated cytokines by ELISA. Mean values ± SD from five independent experiments are shown. Comparisons with control CM are reported. **(B)** Western blot analysis of phospho-STAT3 (pSTAT3), total STAT3, and β-actin was performed on protein extracts. A representative blot out of four independent experiments analyzed is shown. **(C)** Cells cultured as in panels **(A,B)** were stimulated with LPS for 24 h and then co-cultured with allogeneic naive CD4+ T lymphocytes (1:10 ratio). After 18 h stimulation with PMA and ionomycin, supernatants were collected and analyzed for IFNγ content. Data are shown as mean values ± SD from four independent experiments. **(D)** LPS-stimulated DC cultures were analyzed for IL-12 production by ELISA. Mean values ± SD from three independent experiments are shown. *$p < 0.05$; **$p < 0.01$; ***$p < 0.001$.

cytokine IL-12 was also detected in R848 CM DC-T cell co-cultures (**Figure 2D**).

Apical Exposure of Polarized Caco-2 Cells to R848 Results in Agonist Transport across the Epithelial Cell Monolayer

Given the highly hydrophobic nature and the small molecular weight of R848, as well as the rapid systemic effects observed in *in vivo* studies following its oral or intracolonic delivery, we therefore investigated whether treatment of polarized Caco-2 cells could result in agonist transport across the monolayer. To this aim, Caco-2 cell monolayer was exposed, at its AS, to R848 and CM from the BS was collected at 0.5, 2, 5, and 24 h and subject to HPLC analysis. A chromatogram of CM spiked with 5 µg/ml of R848 is shown in **Figure 3A**. A significant proportion of apically loaded R848 was found to be transported to the BS chambers already after 30 min of exposure and this proportion increased overtime, reaching more than 40% of transport at
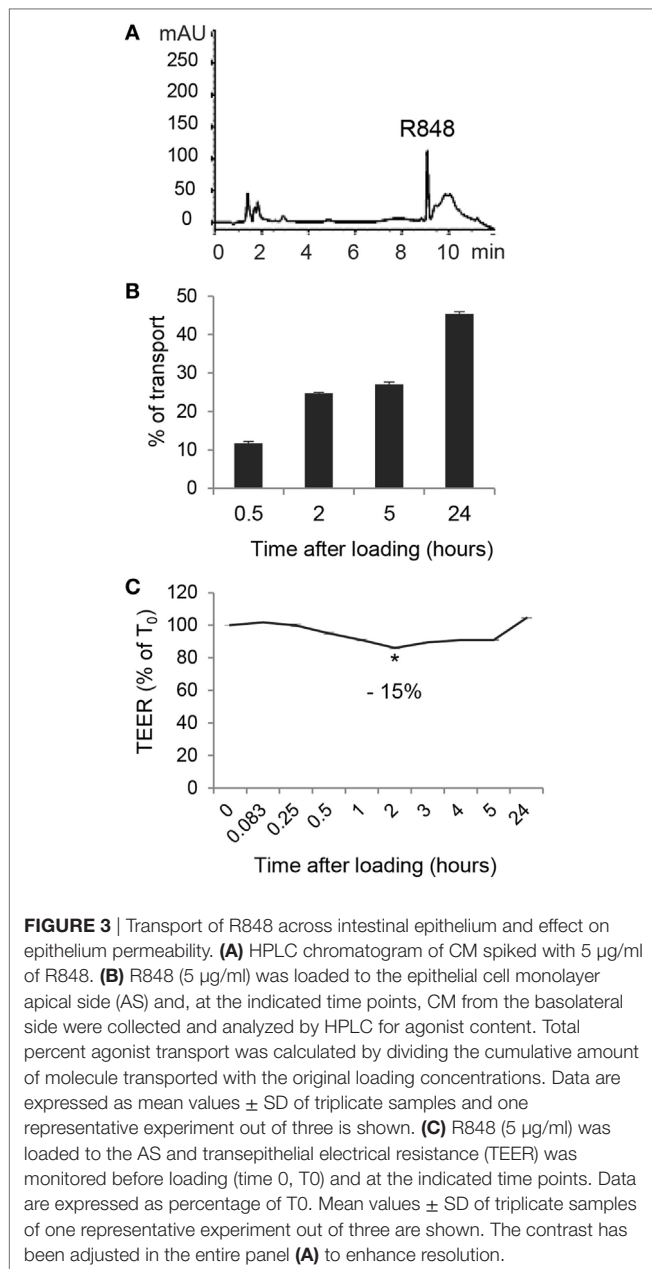
FIGURE 3 | Transport of R848 across intestinal epithelium and effect on epithelium permeability. **(A)** HPLC chromatogram of CM spiked with 5 µg/ml of R848. **(B)** R848 (5 µg/ml) was loaded to the epithelial cell monolayer apical side (AS) and, at the indicated time points, CM from the basolateral side were collected and analyzed by HPLC for agonist content. Total percent agonist transport was calculated by dividing the cumulative amount of molecule transported with the original loading concentrations. Data are expressed as mean values ± SD of triplicate samples and one representative experiment out of three is shown. **(C)** R848 (5 µg/ml) was loaded to the AS and transepithelial electrical resistance (TEER) was monitored before loading (time 0, T0) and at the indicated time points. Data are expressed as percentage of T0. Mean values ± SD of triplicate samples of one representative experiment out of three are shown. The contrast has been adjusted in the entire panel **(A)** to enhance resolution.
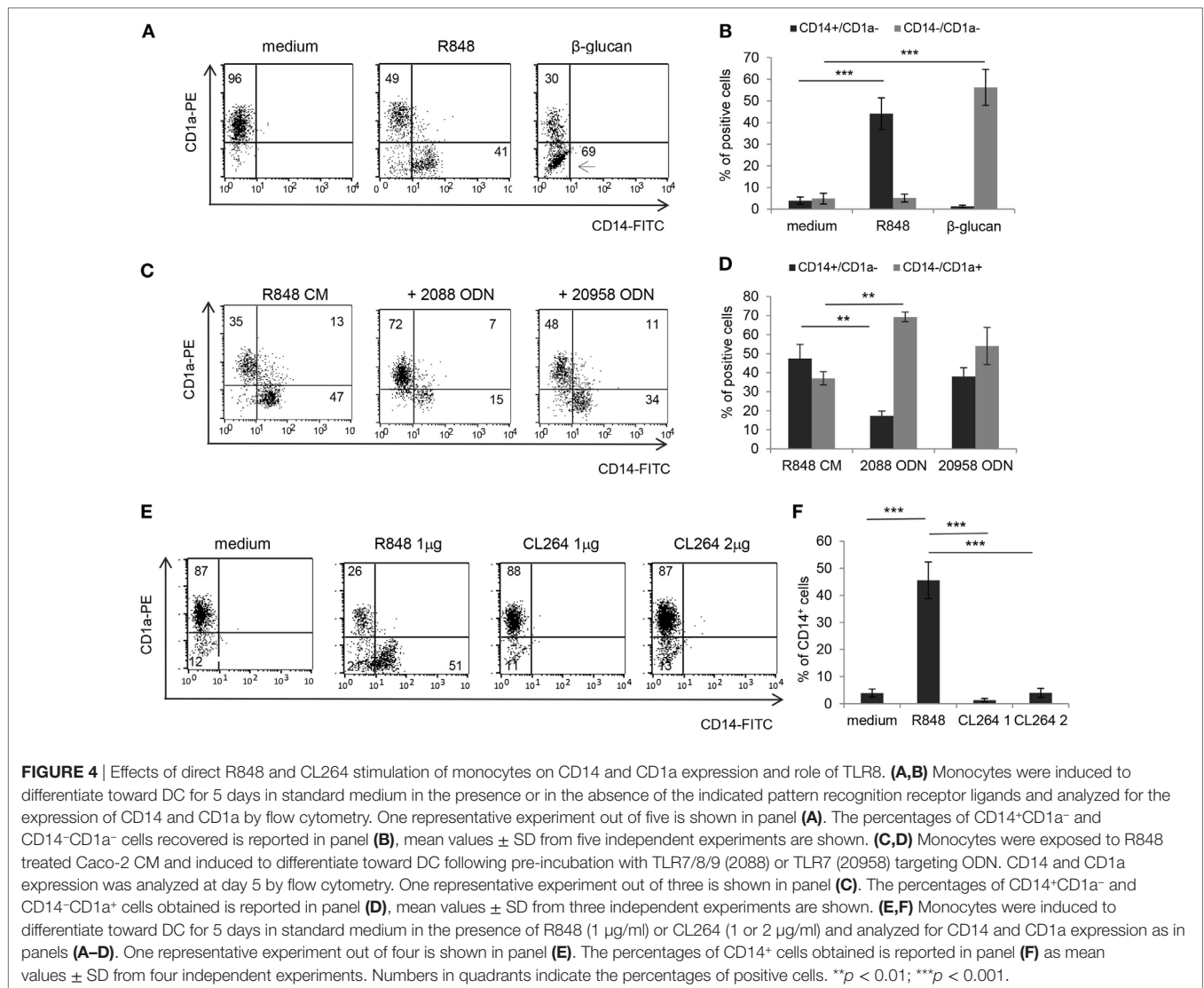
$3.5 \pm 1.7 \times 10^{-6}$, and $3.2 \pm 1.8 \times 10^{-6}$ cm/s, with 1, 2, and 5 µg/ml apical loading, respectively) were compatible with complete agonist adsorption.

R848 CM-Induced Impairment of DC Differentiation/Activation Results from TLR8-Mediated Direct Stimulation of Monocytes by the Transported Agonist

Based on the finding that R848 is transported through IEC monolayer, we then investigated whether the effects observed with IEC CM could be reproduced after direct stimulation of immune cells by R848 or whether they required epithelial cell response to the agonist. To this aim, the exact concentration of R848 released in the BS CM at the different time points was calculated. A significant effect on the percentage of CD14^{+} cells was only observed when CM from Caco-2 cells exposed for 24 h to 5 µg/ml of R848 was used (1 ± 0.15 µg/ml of agonist released), whereas only barely detectable changes were appreciated when CM derived from cells exposed for shorter times or lower concentrations were used (data not shown). Thus, monocytes were directly exposed to a comparable concentration of R848 (1 µg/ml) and induced to differentiate toward DC. As shown in **Figures 4A,B**, direct agonist treatment of monocytes resulted in reduced DC differentiation, as demonstrated by the high proportion of CD14^{+}CD1a^{−} cells found in these cultures as compared to control cultures. The effect of the direct stimulation with the agonist on DC differentiation was comparable to that of R848 CM (**Figure 1A**). Furthermore, as observed for R848 CM-generated DC, cells differentiated following direct exposure to R848 upregulated the expression of MR and DC-SIGN and exhibited constitutive cytokine expression (data not shown). Conversely, while β-glucan CM did not exert any effect on DC differentiation (**Figure 1A**), the exogenous addition of this compound to monocytes resulted in a strong enrichment of CD14/CD1a double negative cells with respect to untreated control cultures (**Figures 4A,B**), in keeping with previously reported data (23). The biochemical properties of β-glucan might influence its transport through epithelial cells thus providing an explanation for the divergent effect of this compound with respect to R848.

As a further evidence that the effect of R848-conditioned epithelial cells on DC differentiation is dependent on the agonist released in CM, and to investigate the relative contribution of TLR7 and TLR8 to this effect, monocytes were cultured in R848 CM after pre-exposure to phosphorothioate ODN targeting TLR7/8/9 (#2088) or TLR7 (#20958). An almost complete recovery of CD14^{−}CD1a^{+} DC was obtained only in the presence of the TLR7/8/9 targeting ODN, whereas the TLR7-specific ODN did not exert any significant effect (**Figures 4C,D**), thus suggesting a selective role of TLR8. In keeping with these results, monocytes were found to express significantly higher levels of TLR8 with respect to TLR7 (Figure S1 in Supplementary Material). The selective requirement of TLR8 stimulation was also confirmed in experiments in which DC differentiation was induced following monocyte exposure to the TLR7 specific ligand CL264 (**Figures 4E,F**).

24 h (**Figure 3B**). To evaluate whether R848 transport could be somehow related to agonist-induced alteration of epithelial permeability, TEER was monitored before agonist loading and at different time points during treatment. As shown in **Figure 3C**, a 15% drop in TEER values was observed at 2 h post-treatment, but recovered soon after, suggesting that some reversible R848-induced perturbation of monolayer permeability could also contribute to its transport. Dose-response experiments were then performed in which Caco-2 cell monolayer was apically exposed to different R848 concentrations for 5 h and the apparent permeability was calculated (18, 22). The permeability coefficients obtained ($P_{app} = 4.52 \pm 0.8 \times 10^{-6}$,

FIGURE 4 | Effects of direct R848 and CL264 stimulation of monocytes on CD14 and CD1a expression and role of TLR8. (A,B) Monocytes were induced to differentiate toward DC for 5 days in standard medium in the presence or in the absence of the indicated pattern recognition receptor ligands and analyzed for the expression of CD14 and CD1a by flow cytometry. One representative experiment out of five is shown in panel (A). The percentages of CD14+CD1a− and CD14−CD1a− cells recovered is reported in panel (B), mean values ± SD from five independent experiments are shown. (C,D) Monocytes were exposed to R848 treated Caco-2 CM and induced to differentiate toward DC following pre-incubation with TLR7/8/9 (2088) or TLR7 (20958) targeting ODN. CD14 and CD1a expression was analyzed at day 5 by flow cytometry. One representative experiment out of three is shown in panel (C). The percentages of CD14+CD1a− and CD14−CD1a+ cells obtained is reported in panel (D), mean values ± SD from three independent experiments are shown. (E,F) Monocytes were induced to differentiate toward DC for 5 days in standard medium in the presence of R848 (1 µg/ml) or CL264 (1 or 2 µg/ml) and analyzed for CD14 and CD1a expression as in panels (A–D). One representative experiment out of four is shown in panel (E). The percentages of CD14+ cells obtained is reported in panel (F) as mean values ± SD from four independent experiments. Numbers in quadrants indicate the percentages of positive cells. **p < 0.01; ***p < 0.001.
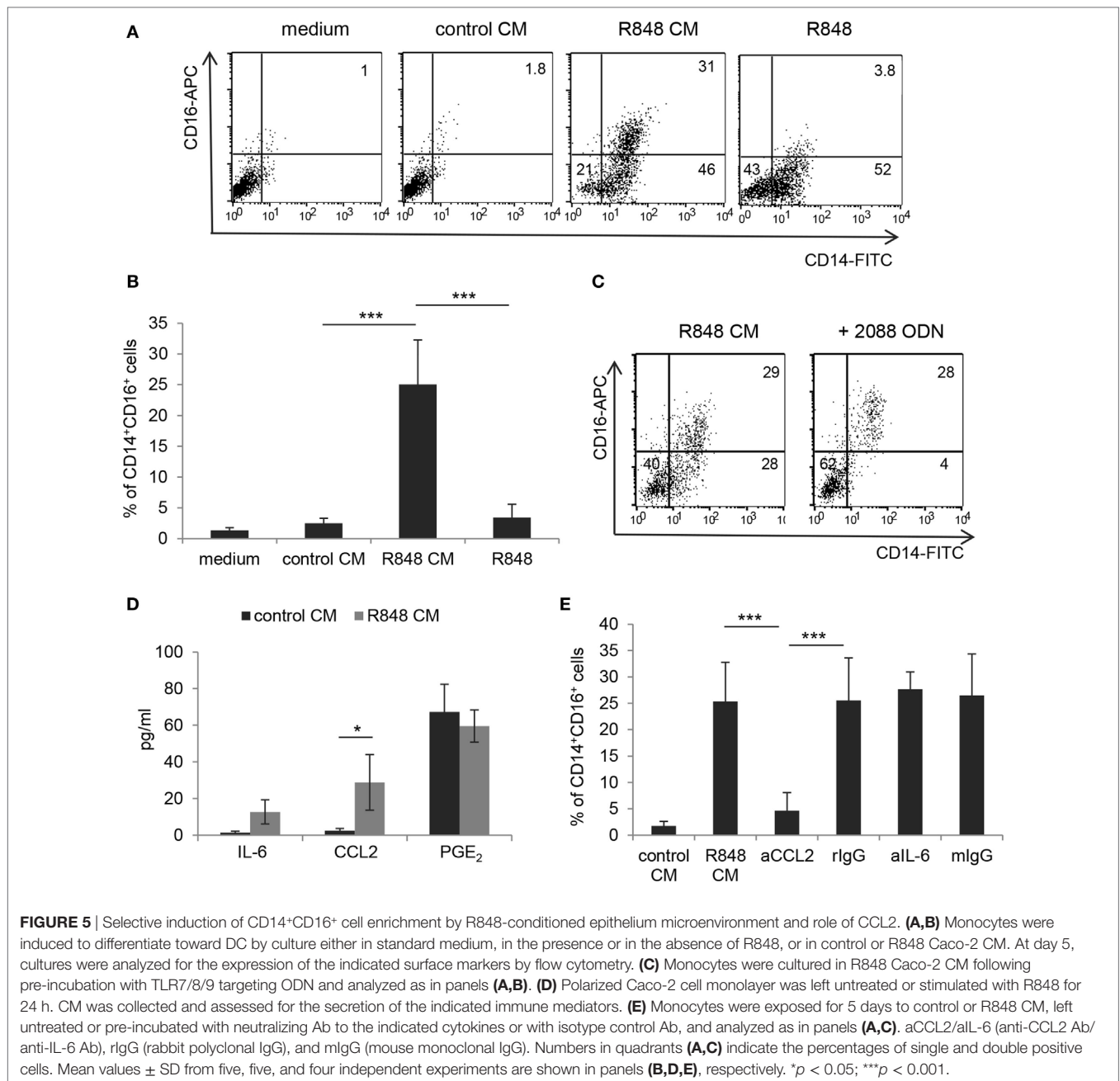
R848-Conditioned Epithelial Cell Monolayer, but Not Direct R848 Exposure of Monocytes, Drives the Accumulation of the CD14+CD16+ Subpopulation: Role of Epithelial Cell-Derived CCL2

It has been reported that R848 injection in non-human primates results in a decrease of blood myeloid DC and concomitant enrichment of the CD14+CD16+ monocyte subpopulation, known to be associated with several inflammatory conditions (24, 25). To investigate whether R848 conditioning of IEC monolayer could affect the monocyte subset distribution, monocyte cultures exposed for 5 days to control or R848 CM were analyzed for the expression of CD14 and CD16. **Figures 5A,B** show that a proportion of the CD14+ cells obtained upon monocyte exposure to R848 CM (see **Figure 1A**) indeed co-expressed CD16. As expected, cells cultured in control CM or standard medium neither expressed CD14 nor CD16 (**Figures 5A,B**).

A donor-dependent variable percentage (3.1–9.8%) of CD14/CD16 double positive cells was present in the starting population of freshly isolated CD14+ monocytes.

To analyze whether direct agonist exposure of monocytes could be responsible for the induction of CD14+CD16+ cells, parallel monocyte cultures were exogenously stimulated with R848 and checked for the appearance of double positive cells. In contrast to what observed with R848 CM, when monocytes were directly exposed to a comparable (1 µg/ml, **Figures 5A,B**) or even higher (up to 4 µg/ml, data not shown) concentration of the agonist, the population of CD14/CD16 double positive cells was no longer identified. Experiments with the TLR7/8 targeting ODN further confirmed that R848 CM-induced enrichment of this subset was driven by the epithelium microenvironment and not by direct stimulation of monocytes with the agonist transported across the epithelial cell monolayer (**Figure 5C**). Specifically, the addition of TLR7/8/9 ODN to monocytes completely reduced the proportion of CD14+CD16− cells recovered (**Figure 5C**; 2.5 ± 1.7 vs.

FIGURE 5 | Selective induction of CD14+CD16+ cell enrichment by R848-conditioned epithelium microenvironment and role of CCL2. **(A,B)** Monocytes were induced to differentiate toward DC by culture either in standard medium, in the presence or in the absence of R848, or in control or R848 Caco-2 CM. At day 5, cultures were analyzed for the expression of the indicated surface markers by flow cytometry. **(C)** Monocytes were cultured in R848 Caco-2 CM following pre-incubation with TLR7/8/9 targeting ODN and analyzed as in panels **(A,B)**. **(D)** Polarized Caco-2 cell monolayer was left untreated or stimulated with R848 for 24 h. CM was collected and assessed for the secretion of the indicated immune mediators. **(E)** Monocytes were exposed for 5 days to control or R848 CM, left untreated or pre-incubated with neutralizing Ab to the indicated cytokines or with isotype control Ab, and analyzed as in panels **(A,C)**. aCCL2/aIL-6 (anti-CCL2 Ab/anti-IL-6 Ab), rIgG (rabbit polyclonal IgG), and mIgG (mouse monoclonal IgG). Numbers in quadrants **(A,C)** indicate the percentages of single and double positive cells. Mean values ± SD from five, five, and four independent experiments are shown in panels **(B,D,E)**, respectively. *$p < 0.05$; ***$p < 0.001$.

$35 \pm 9.5\%$, $n = 3$, $p < 0.001$) without affecting that of the CD14/CD16 double positive cells (**Figure 5C**; 25 ± 8.7 vs. $28 \pm 7.53\%$, $n = 3$, $p < 0.001$). No effect was exerted on this latter cell population by the TLR7-specific ODN as well (data not shown).

Notably, when monocytes were exposed to CM from Caco-2 cells stimulated with the TLR7 selective agonist CL264, the CD14+CD16+ cell enrichment was no longer observed [$1.83 \pm 0.9\%$ (CL264 CM) vs. $28 \pm 7.53\%$ (R848 CM), $n = 3$, $p < 0.001$]. This suggested that the accumulation of this monocyte subpopulation induced by R848 CM requires TLR8 recognition on IEC. Accordingly, TLR8 was found to be expressed at higher

levels with respect to TLR7 in Caco-2 cell monolayer (Figure S1 in Supplementary Material).

To the aim of identifying the soluble factor(s) released by R848-stimulated Caco-2 cell monolayer that could be responsible for CD14+CD16+ cell enrichment, we focused on proinflammatory mediators relevant for intestinal inflammation, such as IL-6, CCL2, and PGE$_2$. As shown in **Figure 5D**, the expression of CCL2, but not of IL-6, was significantly induced in R848-stimulated Caco-2 cell cultures as compared to unstimulated cultures. Conversely, comparable levels of PGE$_2$ were found in both untreated and R848-exposed epithelial cells (**Figure 5D**).

Based on this evidence, monocytes were then induced to differentiate into DC in the presence of R848 CM previously incubated with neutralizing antibodies to CCL2 or IL-6. The results of this analysis showed that CCL2 but not IL-6 blocking almost completely abolished the appearance of the CD14^{+}CD16^{+} cell population (**Figure 5E**). The possible role of type I IFN was also investigated, but neutralizing Ab to these cytokines failed to affect monocyte phenotype (data not shown).
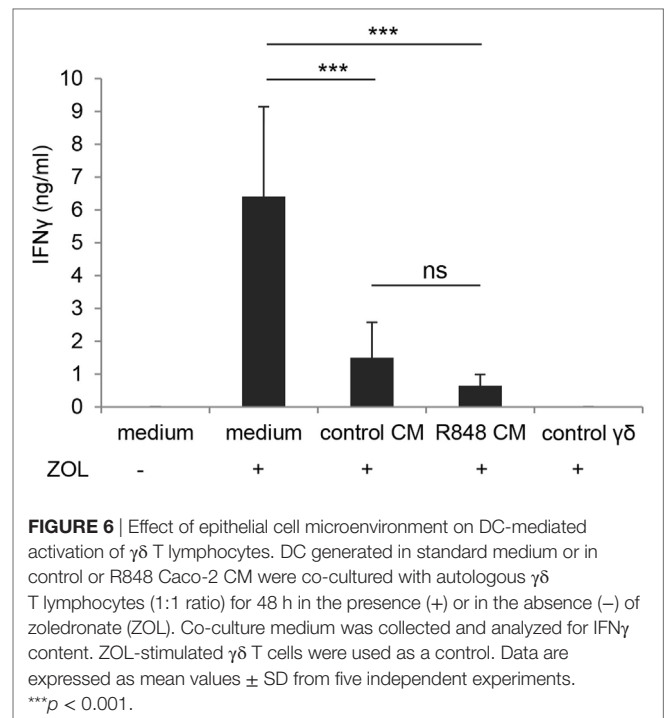
Epithelial Cell Microenvironment Impairs DC-γδ T Cell Crosstalk Independently of R848 Conditioning

In light of the negative effect on CD4^{+} T cell-mediated IFNγ production exerted by DC generated in R848 CM (**Figure 2C**), we further analyzed the impact of these cells on the activation of γδ T lymphocytes. We previously reported that aminobiphosphonate-induced activation of γδ T cells requires the presence of DC (19). Thus, DC generated in the presence of control or R848 Caco-2 CM were co-cultured with ZOL-stimulated autologous γδ T lymphocytes, and lymphocyte activation was assessed by measuring IFNγ secretion. As shown in **Figure 6**, DC generated in Caco-2 CM, regardless of R848 stimulation, exhibited a significantly reduced capacity to activate γδ T lymphocytes, as assessed by the lower levels of IFNγ released in the co-culture medium with respect to that of control DC generated in standard medium. This suggests that signals delivered by intestinal epithelium in homeostatic conditions may negatively regulate the DC/γδ T cell cross-talk and that R848 exposure neither potentiates nor counteracts this immunosuppressive microenvironment.

R848 CM and Direct R848 Exposure Potentiate Phosphoantigen-Induced Activation of γδ T Lymphocytes *via* TLR8

In order to evaluate the effect of R848-conditioned epithelial cells on the direct, DC-independent activation of γδ T cells, purified γδ T lymphocytes were stimulated with the non-peptide phosphoantigen IPP in the presence of control or R848 CM and analyzed for IFNγ secretion. As shown in **Figure 7A**, direct γδ T cell activation was not affected by their exposure to CM from unstimulated epithelial cell monolayer as comparable levels of IFNγ were released by cells cultured in control CM and standard medium. In contrast, lymphocytes cultured in R848 CM expressed significantly higher levels of this cytokine (**Figure 7A**), indicating that agonist stimulation may provide a suitable microenvironment sustaining their activation.

Based on previously reported data (26) as well as on our results (Figure S1 in Supplementary Material), showing that human circulating γδ T lymphocytes express both TLR7 and TLR8, we then assessed whether the effect of R848 CM on γδ T cell activation was due to their direct exposure to the released agonist. Thus, purified blood γδ T cell cultures were kept in standard medium and simultaneously stimulated with IPP and R848. As shown in **Figure 7B**, the agonist was *per se* able to significantly increase TCR-mediated IFNγ production at concentrations comparable to those found in Caco-2 CM, thus demonstrating that R848

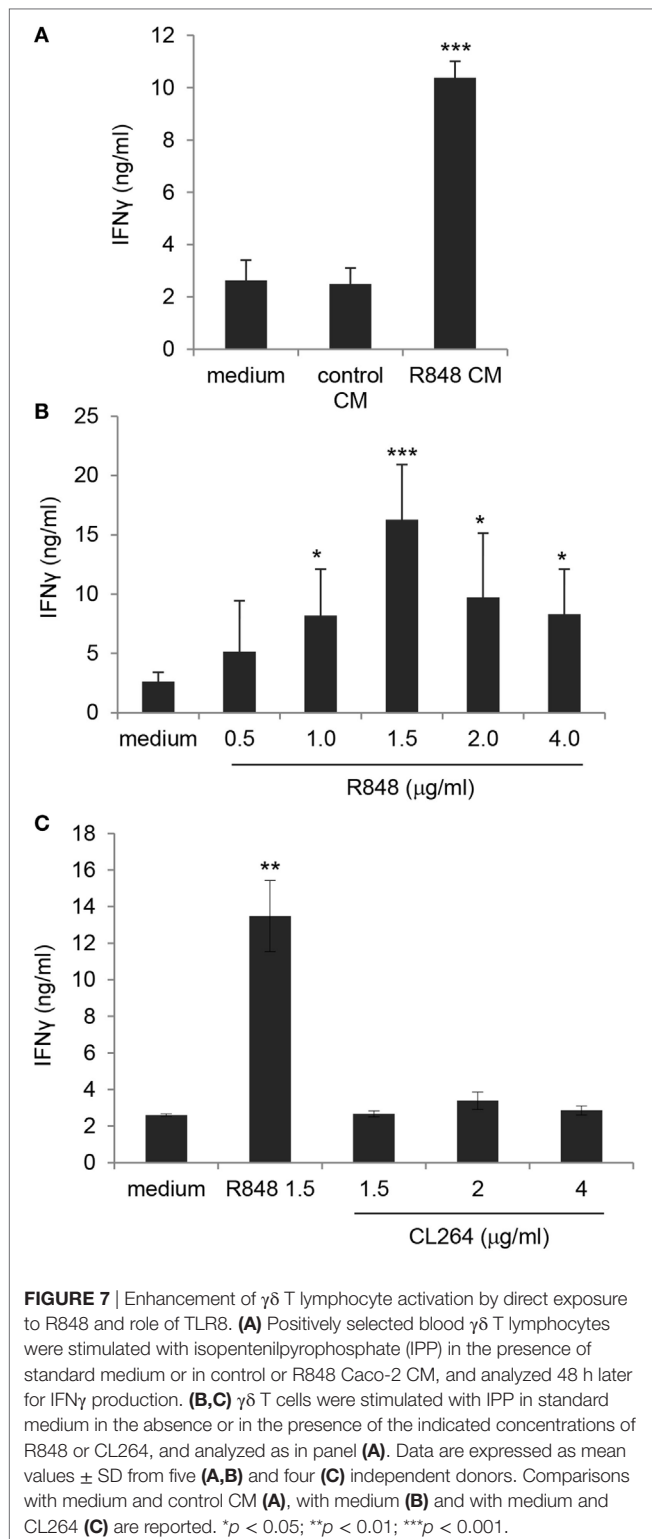**FIGURE 6** | Effect of epithelial cell microenvironment on DC-mediated activation of γδ T lymphocytes. DC generated in standard medium or in control or R848 Caco-2 CM were co-cultured with autologous γδ T lymphocytes (1:1 ratio) for 48 h in the presence (+) or in the absence (−) of zoledronate (ZOL). Co-culture medium was collected and analyzed for IFNγ content. ZOL-stimulated γδ T cells were used as a control. Data are expressed as mean values ± SD from five independent experiments. ***p < 0.001.

transported across Caco-2 cell monolayer is responsible for γδ T lymphocyte hyper-activation. According to the higher IFNγ release, an increased proportion of CD25-positive cells was observed in γδ T cell cultures exposed to both R848 and R848 CM (data not shown).
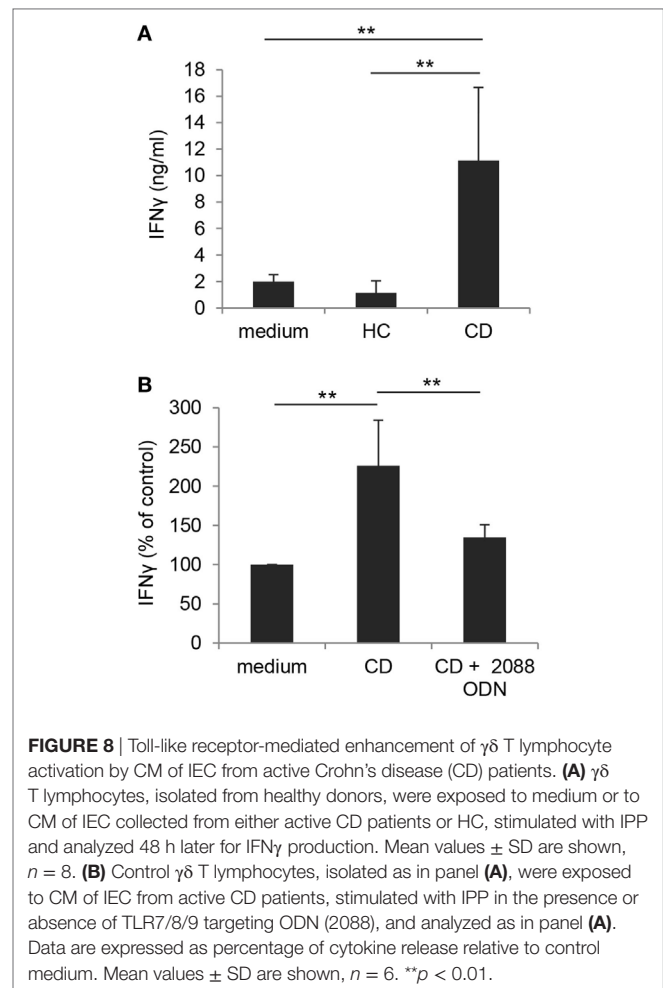
To further investigate the relative contribution of TLR7 and TLR8 to the R848-mediated effect on γδ T lymphocytes, these cells were exposed to comparable concentrations of the TLR7 specific ligand CL264. As shown in **Figure 7C**, stimulation of lymphocytes with the TLR7 agonist did not increase IPP-induced IFNγ production, thus pointing to TLR8 as the main mediator of R848 effect. Accordingly, TLR8 was expressed at higher levels with respect to TLR7 in these cells (Figure S1 in Supplementary Material).

TLR-Mediated Activation of γδ T Lymphocytes Is Promoted by Inflamed Intestinal Epithelium from Active CD Patients

Based on our findings and data from the literature showing an increased number of activated Vδ2 T cells in intestinal mucosa from CD patients (27), we sought to investigate whether TLR/PRR activating structures likely present in inflamed intestinal microenvironment could affect the activation potential of γδ T cells. To this aim, blood γδ T lymphocytes from healthy donors were stimulated with IPP in the presence of CM of IEC, isolated from colonic biopsies of either subjects with endoscopically active CD or sex/age matched HC. As shown in **Figure 8A**, IPP-induced activation, as assessed by IFNγ production, was significantly enhanced when γδ T lymphocytes were exposed to CM of IEC from active CD patients as compared to control

FIGURE 7 | Enhancement of γδ T lymphocyte activation by direct exposure to R848 and role of TLR8. **(A)** Positively selected blood γδ T lymphocytes were stimulated with isopentenilpyrophosphate (IPP) in the presence of standard medium or in control or R848 Caco-2 CM, and analyzed 48 h later for IFNγ production. **(B,C)** γδ T cells were stimulated with IPP in standard medium in the absence or in the presence of the indicated concentrations of R848 or CL264, and analyzed as in panel **(A)**. Data are expressed as mean values ± SD from five **(A,B)** and four **(C)** independent donors. Comparisons with medium and control CM **(A)**, with medium **(B)** and with medium and CL264 **(C)** are reported. *$p < 0.05$; **$p < 0.01$; ***$p < 0.001$.

FIGURE 8 | Toll-like receptor-mediated enhancement of γδ T lymphocyte activation by CM of IEC from active Crohn's disease (CD) patients. **(A)** γδ T lymphocytes, isolated from healthy donors, were exposed to medium or to CM of IEC collected from either active CD patients or HC, stimulated with IPP and analyzed 48 h later for IFNγ production. Mean values ± SD are shown, $n = 8$. **(B)** Control γδ T lymphocytes, isolated as in panel **(A)**, were exposed to CM of IEC from active CD patients, stimulated with IPP in the presence or absence of TLR7/8/9 targeting ODN (2088), and analyzed as in panel **(A)**. Data are expressed as percentage of cytokine release relative to control medium. Mean values ± SD are shown, $n = 6$. **$p < 0.01$.

medium. Conversely, CM of IEC from HC did not significantly affect IFNγ release (**Figure 8A**). Interestingly, a significant reduction in CD CM-induced γδ T cell activation was observed when these cells were stimulated with IPP in the presence of TLR7/8/9 targeting ODN (**Figure 8B**), thus suggesting the presence of TLR targeting T cell co-activating structures in the microenvironment of patient inflamed epithelium.

DISCUSSION

The TLR7/8 agonist R848 has been extensively studied for its adjuvant activity and its effects on immune responses following either topic or oral administration. The main adjuvant activity has been so far attributed to its capacity to induce the production of immune mediators and the activation of DC, thereby leading to the enhancement of both humoral and cellular immune responses. Moreover, data from the literature suggest that most of the responses induced by oral or topic R848 delivery likely result from agonist diffusion within tissues and in the circulation thus leading to direct immune cell stimulation. The results of this study not only expand the range of cellular targets and immune responses influenced by R848 but also provide novel evidence that some of these responses might require the cooperation of agonist-conditioned tissues, such as the intestinal epithelium, thus highlighting the importance of local microenvironment in shaping immune responses.

Specifically, we demonstrate herein that R848 is easily transported across the Caco-2 cell-derived polarized IEC monolayer, showing permeability coefficients typical of completely adsorbed drugs. Consistent with our finding, previous studies performed in mice orally injected with the agonist had suggested that this molecule could easily cross the gut mucosa (14, 15). Furthermore, it was reported that, following intracolonic administration of R848 in mice, a systemic inflammatory response was induced in the absence of epithelium disruption, consistent with a rapid penetration of R848 across the intestinal wall into the draining lymphatic system (28). As a further evidence, topical R848 application was found to confer robust resistance to mice against intravenous challenge with virulent *Leishmania* strains, in keeping with a rapid and efficient transfer of the agonist into the underlying tissues and into the circulation, responsible for systemic immunization (29).

Our results also unravel the effects of TLR8 stimulation of IEC on the phenotype/function of innate immunity cells. Specifically, we report for the first time that apical exposure of polarized Caco-2 cell monolayer to R848 drives the enrichment of the inflammatory CD14+CD16+ monocyte subpopulation by inducing the production of CCL2 by epithelial cells. In keeping with this finding, data previously obtained *in vivo* in non-human primates (25) highlighted that R848 injection leads to a decrease of myeloid DC number in the blood and a concomitant enrichment of CD14+CD16+ cells, likely due to the induction of pro-inflammatory cytokines/chemokines. Interestingly, it has been shown that *in vitro* exposure of human monocytes to CCL2 results in the enrichment of the CD14+CD16+ cell subset and that this chemokine is responsible for inflammatory monocyte accumulation induced by breast cancer cell microenvironment (30). Accordingly, we demonstrate that R848-induced CCL2 in polarized Caco-2 cell monolayer strongly contributes to the accumulation of CD14/CD16 double positive cells, whereas no effect is exerted by IL-6 or type I IFN. As a further evidence that the induction of this cell population is dependent on IEC response to R848, we show that it does not occur following direct exposure of monocytes to the agonist. In this regard, although R848 was shown to regulate the expression and function of different Fcγ receptor members, with both activating and inhibitory functions, no direct effect was reported on the expression of CD16/FcγRIII (31). The enrichment of the CD14+CD16+ cell population, previously associated with chronic inflammatory conditions (32), at mucosa level might contribute to the strong inflammatory reactions that characterize R848 activity in exposed animals.

We also report that R848, either transported through the IEC monolayer or directly administered to freshly isolated γδ T cells, enhances the phosphoantigen-induced activation of these innate lymphocytes. Specifically, significantly higher levels of IFNγ are produced when the γδ TCR is triggered in the presence of R848. Although it has been shown that human γδ T lymphocytes express different TLR, including TLR7 and TLR8, to the best of our knowledge this is the first demonstration that TLR7/8 ligands can potentiate their activation. Furthermore, the selective requirement of TLR8 for this effect was also shown. Additionally, our results indicate that, at tissue level, the mechanisms of γδ T cell activation can be more complex and finely regulated. In fact we

show that, although R848 transported across the IEC monolayer exerts a promoting effect on phosphoantigen-induced direct activation of γδ T lymphocytes, it does not counteract the negative control exerted by IEC microenvironment on the DC-dependent activation of these cells. This suggests that tissue microenvironment may regulate the balance between activating and inhibitory factors and ultimately dictate the type of response. In keeping with this hypothesis, and with results from other groups (33, 34), we report that this compound exerts immunosuppressive activities such as the inhibition of DC differentiation and of Th1 type response generation.

Overall, the enhancing effect of R848 on γδ T lymphocyte activation would be particularly relevant considering the key role of these cells in the first-line defense against infections and tumors (35). Notably, these unconventional T cells represent attractive effectors for cancer immunotherapy (36). On the other hand, the generation of DC characterized by a reduced capacity to induce both conventional and γδ T lymphocyte-mediated responses, would limit the inflammatory response and/or contribute to immunosuppression. The opposite, pro-inflammatory vs. regulatory, effects are consistent with the dual role of TLR7/8 agonists in driving either protective immunity or chronic inflammation/autoimmunity (3, 37). The induction of anti-inflammatory/regulatory pathways (IL-10 production and Treg cell expansion) has also been reported to limit the adjuvant activity of other TLR agonists (38). These findings highlight the complexity of effects that can be elicited by TLR agonists, depending on the target cell type, and the importance of the administration route in regulating the intensity of response and in balancing apparently opposite effects.

In addition to their relevance in the mechanism of action of R848, our data argue for an involvement of γδ T and CD14+CD16+ cell-mediated responses during natural viral infections, when TLR8 ligands are produced. In particular, expansion of these cell populations has been described in some viral infections (32, 39, 40) where they play either protective or pathogenic roles, as well as in chronic inflammatory conditions characterized by break of gut homeostasis and microbial translocation (27, 41). Notably, we show that the CM of IEC isolated from subjects with active CD strongly enhances the activation of phosphoantigen responsive control γδ T lymphocytes with respect to IEC from healthy donors. Accordingly, it has been recently reported that an increased number of activated Vδ2 T cells is detected in intestinal mucosa from CD patients (27). Although different mechanisms can be responsible for this effect, we demonstrate that TLR-activating structures released at the level of inflamed epithelium strongly contribute to γδ T lymphocyte activation induced by intestinal microenvironment of active CD patients. The response of epithelium itself to TLR stimulation might in turn potentiate, through the release of pro-inflammatory mediators, the effects of microbial products on immune cells thus enhancing/perpetuating inflammation. In this regard, TLR8 expression has been reported to be selectively activated in inflamed colonic epithelium of IBD-affected subjects (6, 7) and its mucosal expression directly correlates with the severity of intestinal inflammation (8).

Altogether, the results of this study increase our knowledge on the molecular mechanisms and cellular responses that might be

triggered by TLR8 stimulation. They also add novel information on the mechanism(s) through which R848 exerts its adjuvant activity as well as on the role that the delivery route can play in regulating TLR agonist-induced responses. A better knowledge of the mechanisms and pathways regulated through TLR stimulation as well as of the role of TLR agonist administration route in shaping immune responses might contribute to the design of more effective strategies for microbial and cancer vaccines, as well as to better understand the role of microbial molecular patterns in infectious diseases and in chronic inflammation.

ETHICS STATEMENT

This study has been conducted in accordance with the Declaration of Helsinki and, according to national and international guidelines, it was approved by the review board of Istituto Superiore di Sanità (project identification code: CE/11/299). All the subjects included were provided with complete information about the study and asked to sign an informed consent.

AUTHOR CONTRIBUTIONS

CA designed and performed the experiments; BV performed the experiments; MF performed the biochemical analyses; PP analyzed the data and provided intellectual input; AB and AM performed TLR gene expression profiles; SG provided intellectual input throughout the study; LC conceived the study, supervised work, analyzed data, and wrote the manuscript.

ACKNOWLEDGMENTS

FUNDING

SUPPLEMENTARY MATERIAL

The Supplementary Material for this article can be found online at http://www.frontiersin.org/articles/10.3389/fimmu.2017.01813/full#supplementary-material.

REFERENCES

1. Kawai T, Akira S. The role of pattern-recognition receptors in innate immunity: update on toll-like receptors. *Nat Immunol* (2010) 11(5):373–84. doi:10.1038/ni.1863

2. Ohto U, Tanji H, Shimizu T. Structure and function of toll-like receptor 8. *Microbes Infect* (2014) 16(4):273–82. doi:10.1016/j.micinf.2014.01.007

3. Diebold SS. Recognition of viral single-stranded RNA by toll-like receptors. *Adv Drug Deliv Rev* (2008) 60(7):813–23. doi:10.1016/j.addr.2007.11.004

4. Grasa L, Abecia L, Forcen R, Castro M, de Jalon JA, Latorre E, et al. Antibiotic-induced depletion of murine microbiota induces mild inflammation and changes in toll-like receptor patterns and intestinal motility. *Microb Ecol* (2015) 70(3):835–48. doi:10.1007/s00248-015-0613-8

5. Fukata M, Arditi M. The role of pattern recognition receptors in intestinal inflammation. *Mucosal Immunol* (2013) 6(3):451–63. doi:10.1038/mi.2013.13

6. Steenholdt C, Andresen L, Pedersen G, Hansen A, Brynskov J. Expression and function of toll-like receptor 8 and Tollip in colonic epithelial cells from patients with inflammatory bowel disease. *Scand J Gastroenterol* (2009) 44(2):195–204. doi:10.1080/00365520802495529

7. Abreu MT. Toll-like receptor signalling in the intestinal epithelium: how bacterial recognition shapes intestinal function. *Nat Rev Immunol* (2010) 10(2):131–44. doi:10.1038/nri2707

8. Sanchez-Munoz F, Fonseca-Camarillo G, Villeda-Ramirez MA, Miranda-Perez E, Mendivil EJ, Barreto-Zuniga R, et al. Transcript levels of toll-like receptors 5, 8 and 9 correlate with inflammatory activity in Ulcerative Colitis. *BMC Gastroenterol* (2011) 11:138. doi:10.1186/1471-230X-11-138

9. Helminen O, Huhta H, Lehenkari PP, Saarnio J, Karttunen TJ, Kauppila JH. Nucleic acid-sensing toll-like receptors 3, 7 and 8 in esophageal epithelium, Barrett's esophagus, dysplasia and adenocarcinoma. *Oncoimmunology* (2016) 5(5):e1127495. doi:10.1080/2162402X.2015.1127495

10. Hemmi H, Kaisho T, Takeuchi O, Sato S, Sanjo H, Hoshino K, et al. Small anti-viral compounds activate immune cells via the TLR7 MyD88-dependent signaling pathway. *Nat Immunol* (2002) 3(2):196–200. doi:10.1038/ni758

11. Ahonen CL, Gibson SJ, Smith RM, Pederson LK, Lindh JM, Tomai MA, et al. Dendritic cell maturation and subsequent enhanced T-cell stimulation induced with the novel synthetic immune response modifier R-848. *Cell Immunol* (1999) 197(1):62–72. doi:10.1006/cimm.1999.1555

12. Wagner TL, Ahonen CL, Couture AM, Gibson SJ, Miller RL, Smith RM, et al. Modulation of TH1 and TH2 cytokine production with the immune response modifiers, R-848 and imiquimod. *Cell Immunol* (1999) 191(1):10–9. doi:10.1006/cimm.1998.1406

13. Vasilakos JP, Smith RM, Gibson SJ, Lindh JM, Pederson LK, Reiter MJ, et al. Adjuvant activities of immune response modifier R-848: comparison with CpG ODN. *Cell Immunol* (2000) 204(1):64–74. doi:10.1006/cimm.2000.1689

14. Yrlid U, Cerovic V, Milling S, Jenkins CD, Klavinskis LS, MacPherson GG. A distinct subset of intestinal dendritic cells responds selectively to oral TLR7/8 stimulation. *Eur J Immunol* (2006) 36(10):2639–48. doi:10.1002/eji.200636426

15. Yrlid U, Milling SW, Miller JL, Cartland S, Jenkins CD, MacPherson GG. Regulation of intestinal dendritic cell migration and activation by plasmacytoid dendritic cells, TNF-alpha and type 1 IFNs after feeding a TLR7/8 ligand. *J Immunol* (2006) 176(9):5205–12. doi:10.4049/jimmunol.176.9.5205

16. Vasilakos JP, Tomai MA. The use of toll-like receptor 7/8 agonists as vaccine adjuvants. *Expert Rev Vaccines* (2013) 12(7):809–19. doi:10.1586/14760584.2013.811208

17. Zhang J, Lu Y, Wei J, Li L, Han L. Protective effect of carboxymethylpachymaran on TNF-alpha-induced damage in Caco-2 cell monolayers. *Int J Biol Macromol* (2016) 93(Pt A):506–11. doi:10.1016/j.ijbiomac.2016.07.095

18. Gupta V, Doshi N, Mitragotri S. Permeation of insulin, calcitonin and exenatide across Caco-2 monolayers: measurement using a rapid, 3-day system. *PLoS One* (2013) 8(2):e57136. doi:10.1371/journal.pone.0057136

19. Conti L, Casetti R, Cardone M, Varano B, Martino A, Belardelli F, et al. Reciprocal activating interaction between dendritic cells and pamidronate-stimulated gammadelta T cells: role of CD86 and inflammatory cytokines. *J Immunol* (2005) 174(1):252–60. doi:10.4049/jimmunol.174.1.252

20. Mary JY, Modigliani R. Development and validation of an endoscopic index of the severity for Crohn's disease: a prospective multicentre study. Groupe d'Etudes Therapeutiques des Affections Inflammatoires du Tube Digestif (GETAID). *Gut* (1989) 30(7):983–9. doi:10.1136/gut.30.7.983

21. Seidelin JB, Horn T, Nielsen OH. Simple and efficient method for isolation and cultivation of endoscopically obtained human colonocytes. *Am J Physiol Gastrointest Liver Physiol* (2003) 285(6):G1122–8. doi:10.1152/ajpgi.00533.2002

22. Artursson P, Palm K, Luthman K. Caco-2 monolayers in experimental and theoretical predictions of drug transport. *Adv Drug Deliv Rev* (2001) 46(1–3):27–43. doi:10.1016/S0169-409X(00)00128-9

23. Nisini R, Torosantucci A, Romagnoli G, Chiani P, Donati S, Gagliardi MC, et al. beta-Glucan of *Candida albicans* cell wall causes the subversion of human monocyte differentiation into dendritic cells. *J Leukoc Biol* (2007) 82(5):1136–42. doi:10.1189/jlb.0307160

24. Ziegler-Heitbrock L. The CD14+ CD16+ blood monocytes: their role in infection and inflammation. *J Leukoc Biol* (2007) 81(3):584–92. doi:10.1189/jlb.0806510

25. Kwissa M, Nakaya HI, Oluoch H, Pulendran B. Distinct TLR adjuvants differentially stimulate systemic and local innate immune responses in nonhuman primates. *Blood* (2012) 119(9):2044–55. doi:10.1182/blood-2011-10-388579

26. Pietschmann K, Beetz S, Welte S, Martens I, Gruen J, Oberg HH, et al. Toll-like receptor expression and function in subsets of human gammadelta T lymphocytes. *Scand J Immunol* (2009) 70(3):245–55. doi:10.1111/j.1365-3083.2009.02290.x

27. McCarthy NE, Hedin CR, Sanders TJ, Amon P, Hoti I, Ayada I, et al. Azathioprine therapy selectively ablates human Vdelta2(+) T cells in Crohn's disease. *J Clin Invest* (2015) 125(8):3215–25. doi:10.1172/JCI80840

28. Karlsson A, Jagervall K, Utkovic H, Karlsson L, Rehnstrom E, Fredin MF, et al. Intra-colonic administration of the TLR7 agonist R-848 induces an acute local and systemic inflammation in mice. *Biochem Biophys Res Commun* (2008) 367(2):242–8. doi:10.1016/j.bbrc.2007.12.046

29. Craft N, Birnbaum R, Quanquin N, Erfe MC, Quant C, Haskell J, et al. Topical resiquimod protects against visceral infection with *Leishmania infantum* chagasi in mice. *Clin Vaccine Immunol* (2014) 21(9):1314–22. doi:10.1128/CVI.00338-14

30. Feng AL, Zhu JK, Sun JT, Yang MX, Neckenig MR, Wang XW, et al. CD16+ monocytes in breast cancer patients: expanded by monocyte chemoattractant protein-1 and may be useful for early diagnosis. *Clin Exp Immunol* (2011) 164(1):57–65. doi:10.1111/j.1365-2249.2011.04321.x

31. Butchar JP, Mehta P, Justiniano SE, Guenterberg KD, Kondadasula SV, Mo X, et al. Reciprocal regulation of activating and inhibitory Fc{gamma} receptors by TLR7/8 activation: implications for tumor immunotherapy. *Clin Cancer Res* (2010) 16(7):2065–75. doi:10.1158/1078-0432.CCR-09-2591

32. Wong KL, Yeap WH, Tai JJ, Ong SM, Dang TM, Wong SC. The three human monocyte subsets: implications for health and disease. *Immunol Res* (2012) 53(1–3):41–57. doi:10.1007/s12026-012-8297-3

33. Assier E, Marin-Esteban V, Haziot A, Maggi E, Charron D, Mooney N. TLR7/8 agonists impair monocyte-derived dendritic cell differentiation and maturation. *J Leukoc Biol* (2007) 81(1):221–8. doi:10.1189/jlb.0705385

34. Hackstein H, Knoche A, Nockher A, Poeling J, Kubin T, Jurk M, et al. The TLR7/8 ligand resiquimod targets monocyte-derived dendritic cell differentiation via TLR8 and augments functional dendritic cell generation. *Cell Immunol* (2011) 271(2):401–12. doi:10.1016/j.cellimm.2011.08.008

35. Poggi A, Zocchi MR. gammadelta T lymphocytes as a first line of immune defense: old and new ways of antigen recognition and implications for cancer immunotherapy. *Front Immunol* (2014) 5:575. doi:10.3389/fimmu.2014.00575

36. Hannani D, Ma Y, Yamazaki T, Dechanet-Merville J, Kroemer G, Zitvogel L. Harnessing gammadelta T cells in anticancer immunotherapy. *Trends Immunol* (2012) 33(5):199–206. doi:10.1016/j.it.2012.01.006

37. Yokogawa M, Takaishi M, Nakajima K, Kamijima R, Fujimoto C, Kataoka S, et al. Epicutaneous application of toll-like receptor 7 agonists leads to systemic autoimmunity in wild-type mice: a new model of systemic *Lupus erythematosus*. *Arthritis Rheumatol* (2014) 66(3):694–706. doi:10.1002/art.38298

38. Engel AL, Holt GE, Lu H. The pharmacokinetics of toll-like receptor agonists and the impact on the immune system. *Expert Rev Clin Pharmacol* (2011) 4(2):275–89. doi:10.1586/ecp.11.5

39. Latha TS, Reddy MC, Durbaka PV, Rachamallu A, Pallu R, Lomada D. gammadelta T cell-mediated immune responses in disease and therapy. *Front Immunol* (2014) 5:571. doi:10.3389/fimmu.2014.00571

40. Ahout IM, Jans J, Haroutiounian L, Simonetti ER, van der Gaast-de Jongh C, Diavatopoulos DA, et al. Reduced expression of HLA-DR on monocytes during severe respiratory syncytial virus infections. *Pediatr Infect Dis J* (2016) 35(3):e89–96. doi:10.1097/INF.0000000000001007

41. Koch S, Kucharzik T, Heidemann J, Nusrat A, Luegering A. Investigating the role of proinflammatory CD16+ monocytes in the pathogenesis of inflammatory bowel disease. *Clin Exp Immunol* (2010) 161(2):332–41. doi:10.1111/j.1365-2249.2010.04177.x

ORIGINAL ARTICLE

p140Cap Regulates GABAergic Synaptogenesis and Development of Hippocampal Inhibitory Circuits

Isabella Russo[1], Daniela Gavello[2,3], Elisabetta Menna[4,5], David Vandael[2,3], Carola Veglia[1], Noemi Morello[6], Irene Corradini[4,5], Elisa Focchi[4], Annalisa Alfieri[1], Costanza Angelini[1], Federico Tommaso Bianchi[1,7], Alessandro Morellato[1], Andrea Marcantoni[2,3], Marco Sassoè-Pognetto[6,8], Matteo Maria Ottaviani[6], Latefa Yekhlef[9], Maurizio Giustetto[6,8], Stefano Taverna[9], Valentina Carabelli[2,3], Michela Matteoli[4,5], Emilio Carbone[2,3], Emilia Turco[1] and Paola Defilippi[1]

[1]Department of Molecular Biotechnology and Health Sciences, University of Torino, 10126 Torino, Italy, [2]Department of Drug Science, University of Torino, 10126 Torino, Italy, [3]NIS Centre of Excellence, 10126 Torino, Italy, [4]Institute of Neuroscience, CNR, 20129 Milano, Italy, [5]Istituto Clinico Humanitas, IRCCS, 20089 Rozzano, Italy, [6]Department of Neuroscience, University of Torino, 10126 Torino, Italy, [7]Neuroscience Institute Cavalieri Ottolenghi, University of Torino, 10043 Orbassano, Italy, [8]National Institute of Neuroscience—Italy, 10126 Torino, Italy and [9]Division of Neuroscience, San Raffaele Scientific Institute, 20132 Milano, Italy

Address correspondence to Emilio Carbone. Email: emilio.carbone@unito.it; Paola Defilippi. Email: paola.defilippi@unito.it.

Abstract

The neuronal scaffold protein p140Cap was investigated during hippocampal network formation. p140Cap is present in presynaptic GABAergic terminals and its genetic depletion results in a marked alteration of inhibitory synaptic activity. p140Cap$^{-/-}$ cultured neurons display higher frequency of miniature inhibitory postsynaptic currents (mIPSCs) with no changes of their mean amplitude. Consistent with a potential presynaptic alteration of basal GABA release, p140Cap$^{-/-}$ neurons exhibit a larger synaptic vesicle readily releasable pool, without any variation of single GABA$_A$ receptor unitary currents and number of postsynaptic channels. Furthermore, p140Cap$^{-/-}$ neurons show a premature and enhanced network synchronization and appear more susceptible to 4-aminopyridine-induced seizures in vitro and to kainate-induced seizures in vivo. The hippocampus of p140Cap$^{-/-}$ mice showed a significant increase in the number of both inhibitory synapses and of parvalbumin- and somatostatin-expressing interneurons. Specific deletion of p140Cap in forebrain interneurons resulted in increased susceptibility to in vitro epileptic events and increased inhibitory synaptogenesis, comparable to those observed in p140Cap$^{-/-}$ mice. Altogether, our data demonstrate that p140Cap finely tunes inhibitory synaptogenesis and GABAergic neurotransmission, thus regulating the establishment and maintenance of the proper hippocampal excitatory/inhibitory balance.

Key words: p140Cap, GABAergic synaptogenesis, GABAergic neuron development, GABAergic neurotransmission

Introduction

Synaptic excitation/inhibition (E/I) balance is crucial for brain function (Hensch 2005; Maffei et al. 2006; Yizhar et al. 2011) and its alteration underlies several neurological conditions. The comprehension of the cellular mechanisms that regulate E/I balance is therefore crucial to understand brain development and functioning in order to discover new molecular bases of brain diseases. A wide range of developmental and physiological mechanisms has been identified that maintain the E/I equilibrium (Englot et al. 2009; Tatti et al. 2017). Inhibitory interneurons (INs) are key participants in the generation of normal neural activity in the cerebral cortex and hippocampus. By innervating selectively different domains of pyramidal cells, they are the main source of "feedback" and "feed-forward" inhibition (Kullmann 2011). GABAergic INs critically pace and synchronize populations of excitatory principal cells to coordinate neuronal information processing (McBain and Fisahn 2001; Klausberger and Somogyi 2008).

In line with INs playing a central role in the control of neural activity, GABAergic deficits lead to pathological conditions and contribute to cognitive deficits associated with several psychiatric and neurological diseases. Recent studies have highlighted that alterations in the inhibitory network are involved in dysfunctions associated with schizophrenia, autism and intellectual disabilities (Coghlan et al. 2012; Marín 2012). In addition, selective enhancement of GABAergic synaptogenesis has been found to induce a permanent increase in the inhibitory tone throughout the brain, reduced synaptic plasticity in the hippocampus, and severe forms of intellectual disability (Papale et al. 2017).

p140Cap is an adapter protein highly expressed in neurons, encoded by the SRCIN1 gene, initially identified as a SNAP25-binding protein (Chin et al. 2000) and as a key element of the postsynaptic density (Ito et al. 2008). Indeed, p140Cap localizes to dendritic spines and its down-regulation in hippocampal excitatory neurons negatively affects their morphology and synaptic plasticity via regulation of the microtubule cytoskeleton (Jaworski et al. 2009). In agreement, p140Cap$^{-/-}$ mice show defects in learning and memory, a decreased long-term potentiation (LTP) and long-term depression (LTD), and extensive remodeling of the actin cytoskeletal architecture of synapses (Repetto et al. 2014). In addition, p140Cap interacts with proteins essential for transmission across chemical synapses (both excitatory and inhibitory synapses) and cell-cell junctions (Alfieri et al. 2017), enlightening a key role in synaptogenesis, synaptic transmission and synaptic plasticity.

In this work, we show that p140Cap is present in the inhibitory presynaptic compartment. Genetic ablation of p140Cap from neurons leads to enhanced frequency of miniature inhibitory postsynaptic currents (mIPSCs), increased size of electrically evoked inhibitory postsynaptic currents (eIPSCs) and early synchronization of hippocampal network, with significantly higher firing activity. Surprisingly, p140Cap$^{-/-}$ mice display an enhanced susceptibility to the pharmacological induction of epileptic seizures combined with an increased density of INS and inhibitory GABAergic synapses. Conditional mice lacking p140Cap specifically in forebrain INs display an increase of both susceptibility to in vitro epileptic events and density of inhibitory synapses, comparable with null mice. Together, these data highlight a crucial role of p140Cap in inhibitory network development and maturation.

Materials and Methods

Mice and Treatments

p140Cap$^{-/-}$ mice were previously described (Repetto et al. 2014). Mice were maintained in the transgenic unit of the Molecular Biotechnology Center (University of Turin, Turin, Italy) and provided with food and water ad libitum. Genetic screening was performed by PCR as previously described (Repetto et al. 2014). To obtain a p140Cap floxed allele, we designed the targeting construct as follows: both the fifth exon and the 11th exon of p140Cap gene were flanked with loxP sites, the second one bearing also the neomycin resistance gene, flanked with Flippase Recognition Target (FRT) sites to permit its excision (See Supplementary Fig. S2). This construct was introduced by electroporation into mouse ES cells and homologous recombination was confirmed by Southern blot. ES cells carrying p140Cap-fl-neo allele were injected into C57 blastocysts to generate germ-line chimeras. The neomycin resistance cassette in the targeting construct was removed by crossing heterozygous p140Cap + /fl-neo mice with mice carrying the FLP recombinase under the control of the actin promoter (from The Jackson Laboratory) to produce mice carrying the p140Cap floxed allele. To generate interneuron specific p140Cap knockout mice, p140Cap fl/fl mice were crossed to mice expressing the Cre recombinase under the control of the Dlx5/6 promoter (from The Jackson Laboratory) to obtain p140Cap fl/fl;Dlx5/6-Cre mice. Animal care and handling throughout the experimental procedures were conducted in accordance with European Community Council Directive 2010/63/UE for care and use of experimental animals and were approved by the Italian Ministry of Health (Authorization 49/2014-PR) and by the Bioethical Committee of the University of Turin. All efforts were made to minimize animal suffering and to reduce the number of animals used.

Cultured Neurons on MEAs

Hippocampal neurons were obtained from WT and p140Cap$^{-/-}$ 18-day embryos. Hippocampus was rapidly dissected under sterile conditions, kept in cold HBSS (4 °C) with high glucose, and then digested with papain (0,5 mg/ml) dissolved in HBSS plus DNAse (0,1 mg/ml) (Trygve et al. 2007; Gavello et al. 2012). Isolated cells were then plated at the final density of 1200 cells/mm^2 onto the MEA (previously coated with poly-DL-lysine and laminin) and allowed to adhere on the center of the chip by using a ring made of Sylgard 184 (Dow Corning), 4.5 mm internal diameter (11 mm external diameter), which was removed after 4 h. The cells were incubated with 1% penicillin/streptomycin, 1% glutamax, 2.5% fetal bovine serum, 2% B-27 supplemented neurobasal medium in a humidified 5% CO2 atmosphere at 37 °C. Each MEA dish was covered with a fluorinated ethylene-propylene membrane (ALA scientific, Westbury, NY, USA) to reduce medium evaporation and maintain sterility, thus allowing repeated recordings from the same chip. Recordings were carried out since 11 Days in Vitro (DIV) until DIV 18. Culture medium was partially (1/3) changed once a week, depending on the age of the culture (young cultures did not need weekly change of medium). Following experiments, MEA dishes were re-used by cleaning overnight in 1% Tergazyme (Sigma-Aldrich, St. Louis, MO), rinsing in distilled water and then sterilizing overnight under UV ray.

MEA Recordings

Multisite extracellular recordings were performed using the MEA-system, purchased from Multi-Channel Systems (Reutlingen, Germany). The 60 electrodes array (TiN/SiN) is composed by a 8×8 square grid with $200\,\mu m$ inter-electrode spacing and $30\,\mu m$ electrode diameter. Data acquisition was controlled through MC_Rack software (Multi-Channel Systems Reutlingen, Germany), setting the threshold for spike detection at $-15\,\mu V$ and sampling at $10\,kHz$. Experiments were performed in a non-humidified incubator at $37\,°C$ and with 5% CO2, without replacing the culture medium. Before starting the experiments, cells were allowed to stabilize in the non-humidified incubator for $90\,s$; recording of the spontaneous activity was then carried out for $90\,s$.

Analysis of MEA Activity

Burst analysis was performed using Neuroexplorer software (Nex Technologies, Littleton, MA, USA) after spike sorting operations. Because a burst consists of a group of spikes with decreasing amplitude (Vaghi et al., 2014), we set a threshold of at least 3 spikes and a minimum burst duration of $10\,ms$. We set interval algorithm specifications such as maximum interval to start burst ($0.17\,s$) and maximum interval to end burst ($0.3\,s$) recorded in $0.02\,s$ bins. Burst analysis has been performed by monitoring the following parameters: number of spikes, frequency, number of bursts and burst duration. Cross-correlation probability versus time diagrams were constructed by means of Neuroexplorer software (Nex Technologies, Littleton, MA, USA), using $\pm0.5\,s$ and $\pm3.5\,s$ and $5\,ms$ bin size. Data are expressed as means $\pm$ S.E.M and statistical significance was calculated by using Student's unpaired t-test. Values of $P < 0.05$ were considered significant.

Electrophysiological Recordings and Data Analysis in Cultured Neurons

Patch electrodes, fabricated from thick borosilicate glasses (Hilgenberg, Mansfield, Germany), were pulled and fire-polished to a final resistance of $2–4\,M\Omega$. Patch clamp recordings were performed in whole-cell configuration using a Multiclamp 700-B amplifier connected to a Digidata 1440 and governed by the pClamp10 software (Axon Instruments, Molecular Devices Ltd., USA) (Marcantoni et al. 2009, 2014). mIPSCs and eIPSCs were acquired at $1–10\,kHz$ sample frequency and filtered at one-half the acquisition rate with an 8-pole low-pass Bessel filter (Baldelli et al. 2005). Recordings with leak currents of $>100\,pA$ or a series resistance of $>20\,M\Omega$ were discarded. All the experiments were performed at room temperature ($22–24\,°C$).

Peak-scaled variance analysis - Analysis of mIPSCs was performed as described by (Baldelli et al. 2005), using MiniAnalysis programs (version 6.0.3, Synaptosoft, Leonia, NJ) and following the signal analysis requirements discussed in (Traynelis et al. 1993). The variance analysis of mIPSCs was used to determine the number of GABA receptor channels (N_{Ch}) and their mean unitary current (i) (Fig. 2A). Briefly, 60 to 130 mIPSCs were selected and averaged. The mean waveform obtained from the average of N trace was scaled to the peak of each individual mIPSC and subtracted. The mean variance $\sigma^2(t)$ was then calculated by summing the squares of the difference traces divided by N-1 and plotted versus the decaying phase of mean current I(t) (gray area in Fig. 2A).

Evoked IPSCs (eIPSCs)—Monosynaptic GABAergic eIPSCs were recorded following the approach described in (Baldelli et al. 2005). Current pulses of $0.1\,ms$ and variable amplitude ($8–30\,\mu A$) were generated by an isolated pulse stimulator (model 2100; A-M-System, Carlsburg, WA) and delivered through a glass pipette of $1\,\mu m$ tip diameter filled with Tyrode's solution placed in contact with the cell body of the GABAergic IN in a loose-seal configuration (Baldelli et al. 2005). The postsynaptic neuron was voltage-clamped and maintained at a holding potential of $-70\,mV$. The current artifact produced by the presynaptic extracellular stimulation was subtracted in the eIPSCs shown.

Solutions and Drugs

mIPSCs were recorded by superfusing the whole-cell-clamped postsynaptic neuron with Tyrode's solution containing (in mM): 2 CaCl$_2$, 150 NaCl, 1 MgCl$_2$, 10 HEPES, 4 KCl, and 10 glucose, pH 7.4 (Baldelli et al. 2005). When required, solutions with higher Ca^{2+} concentrations ($5–10\,mM$) were prepared by lowering the NaCl content. The unselective glutamate receptor antagonist, kynurenic acid ($1\,mM$) (Sigma), was added to the Tyrode's solution to block excitatory transmission. Tetrodotoxin ($0.3\,\mu M$) was added to block spontaneous action potential propagation. The neuron was constantly superfused through a gravity system, as previously described (Baldelli et al. 2005). The perfusion solution was changed rapidly ($50–60\,ms$) and applied for variable periods of time. The tip of the perfusion pipette ($100–200\,\mu m$) was placed $40–80\,\mu m$ to the cell body. The standard internal solution was (in mM): 90 CsCl, 20 TEA-Cl, 10 EGTA, 10 glucose, 1 MgCl$_2$, 4 ATP, 0.5 GTP, and 15 phosphocreatine, pH 7.4. K+ was substituted for Cs+ and TEA+ in the pipette solution to block outward potassium currents. N-(2,6-dimethylphenylcarbamoyl-methyl) triethylammonium bromide ($10\,mM$) was added to block Na^+ currents activated during an eIPSC (Baldelli et al. 2005). The hypertonic sucrose containing solution was prepared by adding $500\,mM$ sucrose to the Tyrode.

Slice Electrophysiology

Mice of both sexes (34–40 days of age) were anesthetized with an intraperitoneal injection of a mixture of ketamine/xylazine ($100\,mg/kg$ and $10\,mg/kg$, respectively) and perfused transcardially with ice-cold artificial cerebrospinal fluid (ACF) containing (in mM): 125 NaCl, 3.5 KCl, 1.25 NaH$_2$PO$_4$, 2 CaCl$_2$, 25 NaHCO$_3$, 1 MgCl$_2$, and 11 D-glucose, saturated with 95% O$_2$ 5% CO$_2$ (pH 7.3). After decapitation, brains were removed from the skull and $300\,\mu m$-thick horizontal slices containing the entorhinal cortex and the hippocampus were cut in ACF at $4\,°C$ using a VT1000S vibratome (Leica Microsystems, Wetzlar, Germany). Individual slices were then submerged in a recording chamber mounted on the stage of an upright BX51WI microscope (Olympus, Japan). Slices were perfused with ACF continuously flowing at a rate of $2–3\,ml/min$ at $32\,°C$. Glass electrodes (tip resistance $1–2\,M\Omega$) were filled with ACF and positioned in the CA1 area of the hippocampus and layer II–III of the medial entorhinal cortex (mEC), $~250\,\mu m$ below the pial surface. Local field potentials (LFP) were acquired at a frequency of $10\,kHz$ and band-passed within a $1\,Hz–1\,kHz$ frequency range. All recordings were performed using a MultiClamp 700B amplifier interfaced with a PC through a Digidata 1440 A (Molecular Devices, Sunnyvale, CA, USA). Data were acquired using pClamp10 software (Molecular Devices) and analyzed with Origin 9.1 (Origin Lab, Northampton, MA, USA).

Kainate-induced Seizures

Susceptibility to kainate-induced seizures was determined as previously described (Bozzi et al. 2000; Corradini et al. 2014). Briefly, p140Cap$^{+/+}$, p140Cap$^{-/-}$, Flox-p140Cap and C-p140Cap mice received 25–35 mg/kg body weight intraperitoneal (i.p.) kainic acid (KA, Sigma Aldrich, St. Louis, MO) dissolved in saline solution. Following injection, animals were returned to cages where seizure severity was scored every 10 min for a maximum of 3 h, according to a modified Racine scale (Bozzi et al. 2000; Corradini et al. 2014): stage 0, normal behavior; stage 1, immobility; stage 2, forelimb and/or tail extension, rigid posture; stage 3, repetitive movements, head bobbing; stage 4, rearing and falling; stage 5, continuous rearing and falling; stage 6, severe whole-body convulsions; stage 7, death. Saline-injected animals of both genotypes were used as controls. Observers were blind to treatment and genotype of each animal and scores were assigned based on the maximum stage reached during the observational period. Data collected were used to calculate the time course of seizure severity for each genotype.

Immunofluorescence on Primary Hippocampal Cultures

Primary hippocampal cultures were fixed at 16 DIV with 4% formaldehyde 4% sucrose, and immunofluorescence staining was performed using the following antibodies: p140Cap monoclonal antibody (generated in our lab and used 1:500) and VGAT Rabbit polyclonal (affinity purified from Synaptic System 131 003, 1:500). After 3 washings in phosphate-buffer saline (PBS), cultured neurons were rinsed in a PBS—0.1% Triton solution for 5 min followed by 30 min of saturation with PBS—5% BSA at room temperature. The primary antibody was diluted in a PBS—1% BSA solution and incubated for 2–3 h at 4 °C. After 3 washes, secondary antibodies were incubated at 1:1000 for 1 h at R.T. Coverslips were mounted with Prolong. Images were acquired at LSM 510 META confocal microscope (Leica Microsystems, Germany), using a 63×-oil objective and analyzed with Fiji ImageJ software.

Immunohistochemistry and Immunofluorescence

For immunohistochemistry experiments, animals were anesthetized with an intraperitoneal injection of a mixture of Zoletil (fixed-ratio combination 1:1 of zolazepam and tiletamine) (Zoletil: 80 mg/Kg. Alcyon, Italy) and Xilazine (Nerfasin: 10 mg/Kg. Alcyon, Italy) and transcardially perfused with PBS followed by 4% ice-cold formaldehyde in 0.1 M phosphate buffer (PB, pH 7.4). After perfusion, brains were dissected and postfixed in the same fixative solution overnight at 4 °C. After several washes in 0.1 M PB, brains were cryoprotected by immersion in 10, 20, and 30% sucrose solutions. Coronal sections (30 μm) were cut with a cryostat and stored at 20 °C in a solution containing 30% ethylene glycol and 25% glycerol in 0.1 M PB (pH 7.2) until processing. Immunohistochemistry was carried out according to a protocol for free-floating sections as previously described (Morello et al. 2017). After being rinsed in PBS (3 × 10 min), sections were immersed in 1% H_2O_2 in PBS for 20 min to block endogenous peroxidase activity. After a blocking step in PBS containing 0.05% Triton X-100 and 10% normal goat serum (NGS), sections were incubated overnight at RT with the following primary antibodies diluted in PBS with 3% NGS and 0.05% Triton X-100: rat anti-somatostatin (SOM, MAB354, 1:250; Millipore Corporation), rabbit anti-calretinin (CR, 214 102, 1:500; SYSY, Goettingen, Germany), mouse anti-parvalbumin (PV, 235, 1:10 000; Swant, Marly, Switzerland). The following day, after several PBS rinses, the sections were incubated for 1 h with the appropriate biotinylated secondary antibodies (1:250, Vector Labs; Burlingame, CA) diluted in PBS with 3% NGS and 0.05% Triton X-100, followed by 1 h incubation in a solution containing a biotin-avidin complex (1:100, Vector Labs). Finally, sections were immersed in a solution containing 3,3'-diaminobenzidine (DAB) (0.05% in TRIS-HCl, pH 7.6) with 0.01% H_2O_2 as chromogen for the peroxidase reaction.

For immunofluorescence experiments, following 3 rinses in PBS and the blocking step, sections were incubated overnight at 4 °C with the following primary antibodies: rabbit polyclonal anti-VGAT (VGAT, 131 003, 1:1000 SYSY) and mouse monoclonal anti-neuron-specific nuclear protein (NeuN, MAB377 clone A60, 1:500, Merck Millipore). On the following day, after 3 washing in PBS, sections were immersed for 2 h at RT in secondary fluorescent antibodies (Alexa Fluor Secondary Antibodies 1:200, Invitrogen). After several PBS rinses, the sections were mounted on glass slides and observed with a bright-field microscope (Eclipse 800, Nikon, Japan) equipped with a CCD camera (Axiocam HRc, Zeiss, Germany) or a 510 META laser-scanning confocal microscope (Zeiss, Germany).

Quantitative Analysis of Immunohistochemical Signals

The numbers of INs were estimated in coronal sections. For each animal, 4 sections along the rostro-caudal axis of the dorsal hippocampus were analyzed. Digital micrographs were processed with the software ImageJ, and the number of immunolabeled cells was calculated manually. All data are reported as mean ± SEM. Statistical analysis was done by Student's t-test, using GraphPad Prism software (La Jolla, CA, USA). For the quantification of inhibitory synapses, images were acquired in stratum pyramidale of the CA1 hippocampal subfield using a 40× oil immersion lens with an additional confocal zoom of up to 3 (voxel sizes of 0.10 × 0.10 × 1 μm). The parameters of acquisition (laser power, pinhole, gain, offset) were maintained constant between the 2 groups. Images were analyzed with the ImageJ software.

Electron Microscopy

Mice were perfused with 1% formaldehyde/1% glutaraldehyde in phosphate buffer (0.1 M PB, pH 7.4). Their brains were postfixed in the same fixative overnight, and small specimens taken from the dorsal hippocampus were postfixed in 1% OsO_4 in 0.1 M cacodylate buffer, dehydrated, and embedded in epoxy resin. Ultrathin sections were stained with uranyl acetate and lead citrate and observed in a JEM-1010 transmission electron microscope (Jeol) equipped with a side-mounted CCD camera (Mega View III, Soft Imaging System). The density of perisomatic GABAergic synapses was assessed by analyzing 381 digitized images from 3 p140Cap$^{-/-}$ and 3 control mice. Images were captured in CA1 stratum pyramidale. Type 2 synapses surrounding the cell body of pyramidal neurons were identified by the presence of numerous presynaptic vesicles, a visible synaptic cleft and symmetric pre- and postsynaptic specializations. The perimeter of pyramidal cells was measured with the Mega View software. Image acquisition and morphometric analysis were performed by an experimenter blind to the genotype of the mice.

Real-time PCR

Total RNA was extracted from dissected Median Ganglionic Eminence (MGE), Caudal Ganglionic Eminence (CGE) and

Lateral Ganglionic Eminence (LGE) samples from E15.15 p140Cap$^{+/+}$ embryos using Trizol Reagent (Ambion, Life Technologies Italia, Torino, Italy) and its concentration was determined with a NanoDrop™ 1100 (NanoDrop Technologies, Wilmington, DE, USA). Total RNA was reverse-transcribed with a high capacity cDNA reverse transcription kit (#4 368 813, Applied BioSystem) according to manufacturer's instruction and amplified with specific primers. RT-PCR analysis was carried out in 96-well plates in the ABI Prism 7300 real-time PCR system using Power SYBR® Green PCR Master Mix (#4 367 659, Invitrogen), specific primers and 10 ng total RNA converted into cDNA in 10 μl final volume.

Primers sequences:

p140Cap FW 5′CGGGATCCTGCAGCGGCAGCGCAC3′
p140Cap REV 5′GCGAATTCCACATACCCTCATCCACTTGCC3′
GAPDH FW 5′AGAAGGTGGTGAAGCAGGCATC3′
GAPDH REV 5′CGGCATCGAAGGTGGAAGAGTG3′

Immunostaining of Mouse Embryonic Cortex

Embryonic brains were dissected at E12.5 and fixed for 12–16 h at 4 °C in 4% formaldehyde. To evaluate proliferation, pregnant females were injected at E12.5 with 35 mg/kg 5-ethynyl-2 deoxyuridine (EdU). Fixed brains were equilibrated in 30% sucrose in PBS for 12–24 h at 4 °C, embedded with Tissue-TEK (O.C.T., Sakura Finetek), snap-frozen in liquid nitrogen, and stored at −20 °C. Sectioning was performed at 20 μm with a cryostat. Cryosections were rehydrated 5 times in PBS before further processing. For Nkx2.1 staining, monoclonal antibodies 8G7G3/1 from Thermo fisher were used at 1:100 dilution. Cryosections were subjected to antigen retrieval by heating in 0.01 M citrate buffer pH 6.0 at 70 °C for 1 h. Sections were permeabilized using 0.3% Triton X-100 in PBS for 30 min and quenched with 0.1 M glycine for 30 min, and incubated with primary antibodies overnight at 4 °C, followed by secondary antibody for 1 h at room temperature in a solution of 0.2% gelatin, 300 mM NaCl, and 0.3% Triton X-100 in PBS. DNA was stained in the last wash using DAPI. For EdU detection, the Click-iT EdU Alexa Fluor 488 Imaging Kit (Invitrogen, Carlsbad, CA) was used, according to the supplier's instructions. Apoptosis was measured by the TUNEL assay using "In Situ cell death detection kit, TMD red" (Roche, Basel; Switzerland) according to manufacturer's protocol. Following TUNEL staining, sections were counterstained with DAPI. The slides were mounted using ProLong anti-fade reagent (Thermo Fisher Scientific, Waltham, MA, USA). Imaging was performed using a Leica TCS SP5-AOBS 5-channel confocal system (Leica Microsystems) equipped with a 405-nm diode, an argon ion, and a 561-nm DPSS laser. Fixed cells were imaged using a HCX PL APO 20X/ DRY objective. Edu+ cells were counted on DAPI+ cells, from a cropped MGE image of known area, processed with ImageJ software.

Results

p140Cap Localizes at Inhibitory Synapses and its Loss Leads to Presynaptic GABAergic Alterations

We have previously demonstrated that p140Cap is part of the excitatory postsynaptic compartment (Jaworski et al. 2009; Repetto et al. 2014). To investigate if p140Cap localizes at inhibitory synapses, we performed double labeling immunofluorescence of primary hippocampal neurons using an antibody that recognizes the vesicular GABA transporter VGAT, a specific marker of inhibitory presynaptic terminals. The colocalization of p140Cap (green labeling) with VGAT (red labeling) was evident in 16 DIV cultures (Fig. 1A), suggesting presynaptic localization. This is consistent with previous electron microscopic observations in the rat brain (Ito et al. 2008).

To investigate the functional relevance of p140Cap at inhibitory synapses, we tested whether removal of p140Cap altered the synaptic activity of inhibitory INs. Miniature GABAergic post synaptic currents (mIPSCs) were recorded from 16-18 DIV hippocampal p140Cap$^{+/+}$ or p140Cap$^{-/-}$ neurons. Cells were held at −70 mV (V$_h$), and perfused locally with a Tyrode solution containing 300 nM TTX and 1 mM kynurenic acid to block both spontaneous action potentials and glutamatergic postsynaptic activity. Data were collected from 3 independent experiments for each genotype (Fig. 1B) (Baldelli et al. 2002, 2005; Allio et al. 2015). p140Cap ablation increased mIPSCs frequency by approximately 4-fold compared to controls. Mean inter-event intervals decreased from 1.74 ± 1.2 s in control (n = 1371 from 16 cells) to 0.33 ± 0.02 s in p140Cap$^{-/-}$ neurons (n = 1775 from 13 cells; p < 0.001) (Fig. 1C, left panel), with no difference in the average amplitude (−38.5 ± 0.9 pA in control vs. −40.1 ± 0.6 pA in p140Cap$^{-/-}$ neurons; p = 0.135) (Fig. 1D, left panel). The corresponding cumulative probability functions of the inter-event intervals and amplitudes are shown in Fig. 1C,D (right panels). These data are consistent with a potential presynaptic alteration of basal GABA release in the absence of p140Cap.

We then investigated whether p140Cap ablation altered the electrically evoked inhibitory postsynaptic currents (eIPSCs) induced by presynaptic action potential stimulation. The absence of the adapter protein caused a marked increase of eIPSCs (0.78 ± 0.12 nA in control (n = 14 cells) versus 1.32 ± 0.33 nA in p140Cap$^{-/-}$ neurons (n = 8 cells); p = 0.033) (Fig. 1E). To test if p140Cap$^{-/-}$ neurons exhibit a larger synaptic vesicle readily releasable pool (RRP), neurons were stimulated with a 500 mM hypertonic sucrose modified Tyrode's solution. The integral of the area under the current evoked by the stimulus that represents the RRP (Pyle et al. 2000) was significantly larger in p140Cap$^{-/-}$ neurons as compared to controls (p = 0.023, unpaired t-test) (Fig. 1F). The same occurred to the current amplitude that increased from −0.80 ± 0.09 nA in control (n = 14 cells) to −1.34 ± 0.28 nA in p140Cap$^{-/-}$ neurons (n = 8 cells) (p = 0.018, unpaired t-test). Conversely, the postsynaptic response of primary hippocampal neurons to saturating GABA concentrations (10 μM) was comparable in control and p140Cap$^{-/-}$ neurons (p = 0.527) (Fig. 1G).

Given that ablation of p140Cap does not alter the mean amplitude of miniature events in 16-18 DIV hippocampal neurons, it is likely that the absence of p140Cap preserves the unitary conductance and the density of postsynaptic GABA$_A$ receptors. To examine this, we measured the unitary conductance of GABA$_A$ channels by using the peak-scaled variance analysis (PSVA) of mIPSCs, which allows an estimate of the unitary current i carried by single postsynaptic GABA$_A$ channels (Traynelis et al. 1993). Figure 2A summarizes the procedure followed to determine the variance, $\sigma^2(t)$, from a group of mIPSCs, with data collected from 3 independent experiments for each genotype (see Materials and Methods). In 16-18 DIV neurons, loss of p140Cap caused almost no changes to the $\sigma^2(t)$ versus mean current (I(t)) relationship (Fig. 2B,C). The plot was clearly parabolic in both cases. The initial slope of the parabola yielded an estimate of the weighted single-channel current. On average, we obtained similar mean unitary currents of −2.2 ± 0.1 pA (n = 13 cells) and −2.0 ± 0.1 pA (n = 9 cells) in control and p140Cap$^{-/-}$ neurons (P = 0.469), respectively (Fig. 2D),
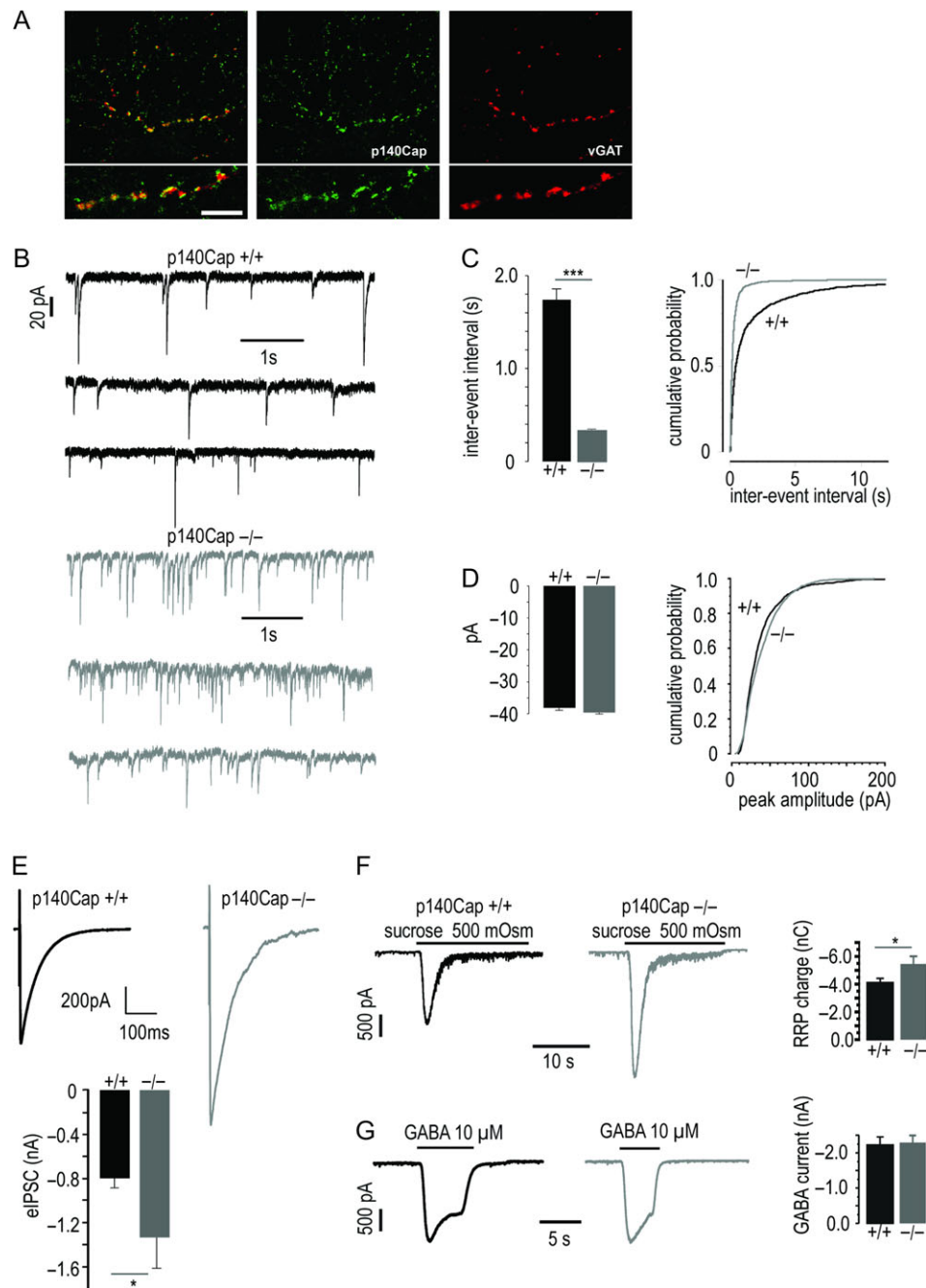
Figure 1. Localization of p140Cap in the VGAT-positive presynaptic compartment and presynaptic electrophysiological GABAergic alterations in p140Cap$^{-/-}$ mice. (A) p140Cap localizes with the inhibitory synaptic marker VGAT// Immunofluorescence staining on 16 DIV hippocampal primary interneurons. Cells were stained for p140Cap in green and VGAT in red; scale bar: 10 μm. (B) Representative mIPSCs recorded from p140Cap$^{+/+}$ (black traces); and p140Cap$^{-/-}$ (gray traces) primary hippocampal cultures at 16–18 DIV. (C) Cumulative probability functions of the inter-event intervals for p140Cap$^{+/+}$ (black trace) and p140Cap$^{-/-}$ (gray trace). The inset to the left shows the mean frequency of events that results 4-fold higher for p140Cap$^{-/-}$ as compared to p140Cap$^{+/+}$. (D) Same as for (C) but concerning the mIPSC amplitude. (E) Top. Representative eIPSCs recorded during presynaptic stimulation of a control (black trace) and p140Cap$^{-/-}$ (gray trace) neurons; Vh = −70 mV. Bottom. The mean peak amplitude of eIPSCs from control and p140Cap$^{-/-}$ neurons. (F) Response of neurons to 500 mM hypertonic sucrose containing Tyrode's solution. (G) Representative postsynaptic responses of hippocampal neurons to 10 μM GABA. Black trace is from p140Cap$^{+/+}$ neurons while gray trace is from p140Cap$^{-/-}$ cells.

corresponding to a mean single-channel conductance of 31.0 and 28.6 pS. Because the mean amplitude of mIPSCs was not altered by the absence of p140Cap (Fig. 1D, left panel), we concluded that in 16–18 DIV hippocampal neurons the density of GABA$_A$ receptors was unaffected by the loss of p140 Cap (Fig. 1D, right panel).

Taken together, these data indicate that loss of p140Cap has specific potentiating presynaptic effects, consisting in enhanced RRP that result in increased mIPSC frequency and higher eIPSCs, without effects on the conductance and density of functional postsynaptic GABA$_A$ receptors. Interestingly, confocal analysis revealed a significant increase of the density of
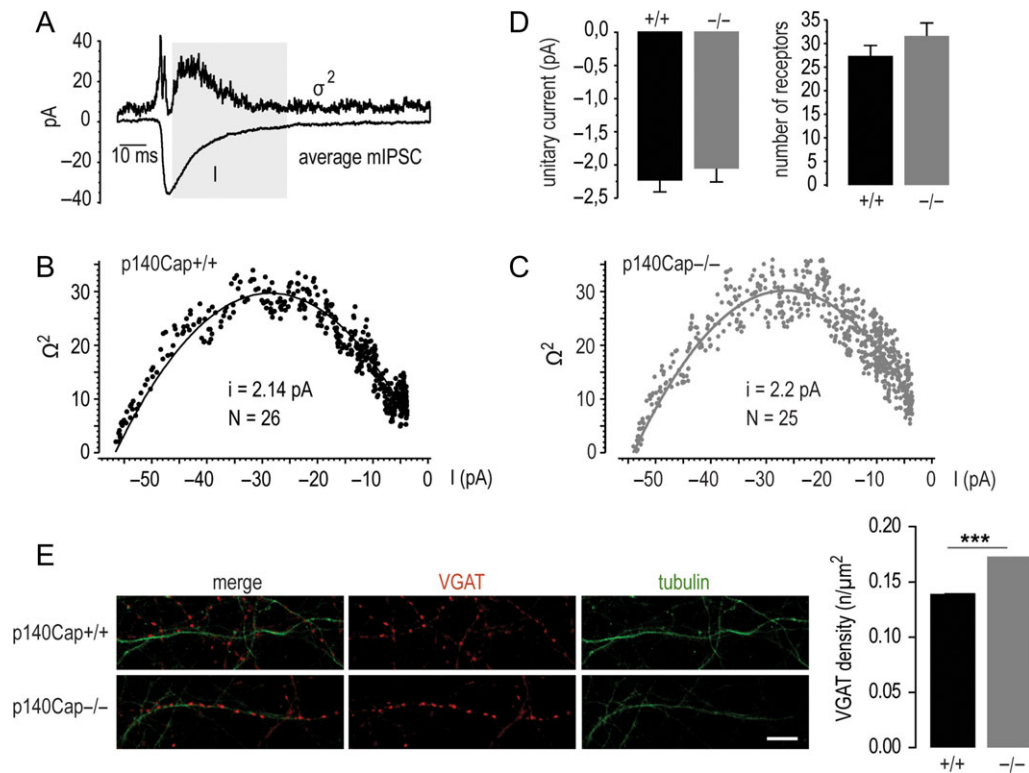
Figure 2. Peak-scaled variance analysis of mIPSCs and overall density of VGAT punctae. (A–D) Peak-scaled variance analysis of mIPSCs. (A) Time course of the mean variance $\sigma^2(t)$ (top) and mean current I(t) (bottom), obtained by averaging mIPSCs of nearly the same amplitude. The gray rectangle indicates the temporal window where the σ^2 vs. I plots of panel (B) and (C) were derived (see Materials and Methods for details). (B,C) σ^2 vs. I plots obtained from mIPSCs recorded in p140Cap$^{+/+}$ (B) and p140Cap$^{-/-}$ neurons (C). (E) Representative images of 16-18 DIV p140Cap$^{+/+}$ and p140Cap$^{-/-}$ hippocampal primary neurons stained for the inhibitory presynaptic marker vGAT (red) and the microtubule protein Tubulin (green), and relative quantification of the density of VGAT puncta per unit length. Scale bar value = 10 μm.

VGAT puncta formed on target dendrites by individual axons in p140Cap$^{-/-}$ neurons, with respect to age-matched control neurons (Fig. 2E) (number of VGAT/μm, p140Cap$^{+/+}$ = 0.139 ± 0.006; p140Cap$^{-/-}$ = 0.173 ± 0.006; number of examined dendrites: 36 p140Cap$^{+/+}$, 43 p140Cap$^{-/-}$; 3 independent experiments, data are presented as mean ± SEM. Unpaired t-test, p = 0.0003), indicating that not only the release properties at inhibitory terminals but also the ability to form inhibitory synapses on target neurons is changed in neurons lacking p140Cap.

p140Cap$^{-/-}$ Cultures Display Abnormal Spontaneous Firing Properties and Enhanced Network Synchronization During Neuronal Maturation

To investigate whether the increased number of functional inhibitory synapses affects network activity during neuronal maturation in p140Cap$^{-/-}$ neurons, we compared the electrical properties of p140Cap$^{+/+}$ and p140Cap$^{-/-}$ hippocampal networks using micro-electrode arrays (MEAs). Spontaneous firing of hippocampal neurons was monitored at 2 developmental stages (9 and 18 DIV) in order to assess the maturation of the network. As shown previously (Gavello et al. 2012), the firing properties of hippocampal neurons vary significantly with time in these conditions. Spontaneous activity is mainly characterized by an asynchronous spike train activity with limited number of bursts in immature cultures, that switches to a burst activity characterized by a higher degree of synchronization in mature cultures.

The firing frequency at 9 DIV was significantly lower in p140Cap$^{-/-}$ (0.50 ± 0.05 Hz, n = 11 MEA, 277 channels, 3 independent experiments) with respect to controls (0.74 ± 0.11 Hz, n = 5 MEA; 400 channels, 3 independent experiments, P = 0.022 unpaired t-test) (Fig. 3A,B). On the contrary, at 18 DIV the absence of p140Cap induced a 3-fold increase in firing frequency compared to controls (2.55 ± 0.13 Hz vs. 0.87 ± 0.05 Hz, respectively; P < 0.0001, unpaired t-test) (Fig. 3C,D). In addition, the number of bursts (12.3 ± 0.5 vs. 6.2 ± 0.4, P < 0.0001, unpaired t-test) and the burst duration (0.36 ± 0.04 vs. 0.09 ± 0.004 s, P < 0.0001, unpaired t-test) were significantly larger in p140Cap$^{-/-}$ neurons with respect to controls (Fig. 3E,F).

Besides monitoring simultaneously the activity of many neurons (60 or more), MEA recordings allow to evaluate the degree of synchronization of neuronal networks during culture maturation (Gavello et al. 2012). We found that p140Cap$^{-/-}$ neurons exhibited synchronized activity at earlier stages than the control. p140Cap$^{-/-}$ neurons displayed an increased synchronism at 9 DIV that was absent in control neurons of the same age. This effect was clearly visible when comparing the raster plots, where action potentials (AP) monitored by each active recording channel are converted in a sequence of vertical lines versus time, and by the relative cross-correlation peak. In 9 DIV control neurons, AP activity is distributed randomly over time (Fig. 3G, left plot), becoming more synchronized at 18 DIV, when nearly all recording channels display synchronous AP bursts for tens of seconds (Fig. 3I, left plot). Conversely, p140Cap$^{-/-}$ neurons displayed, already at 9 DIV, robust synchronous firing (Fig. 3G, right plot), that increased at 18 DIV
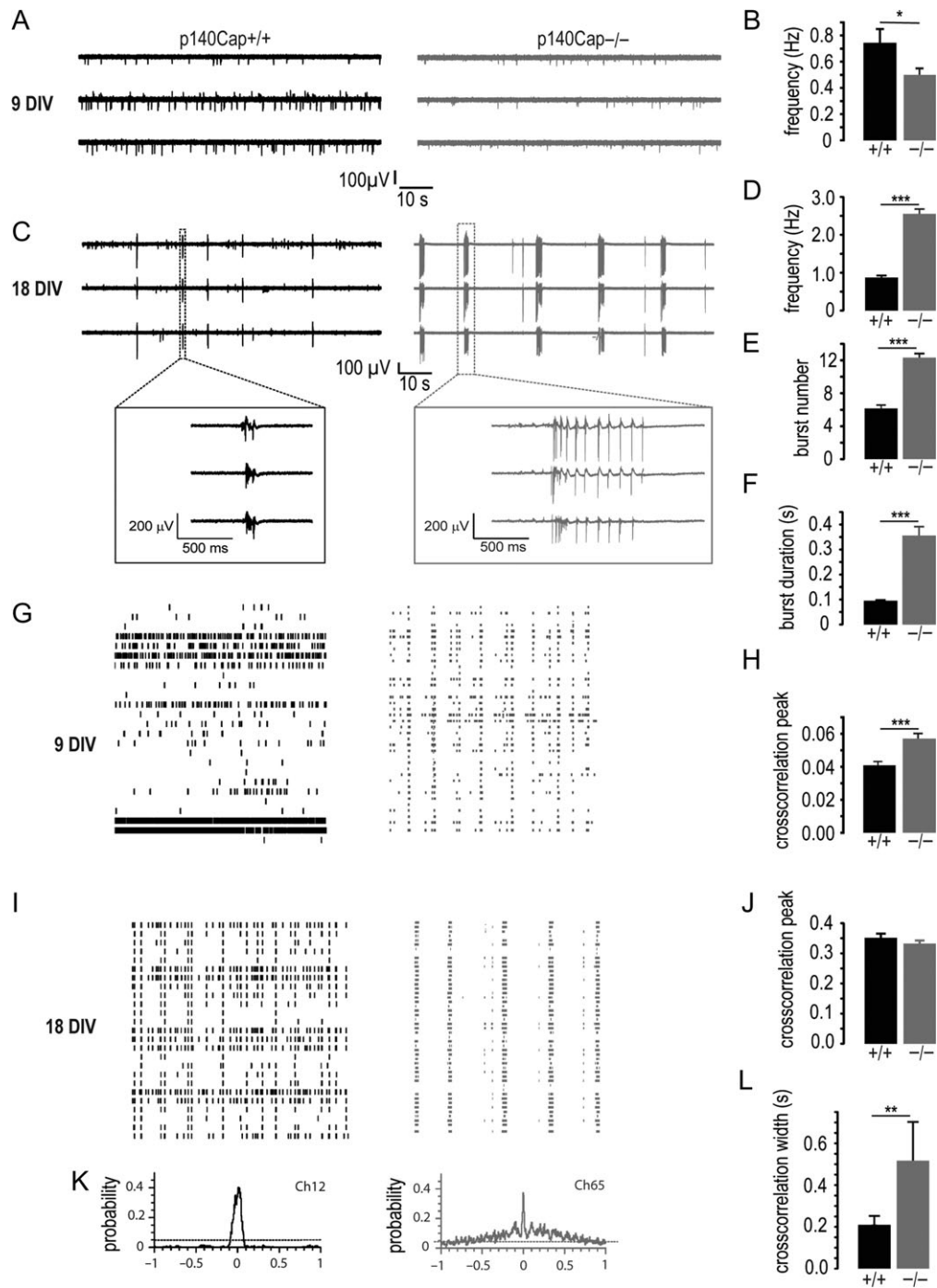
Figure 3. MEAs analysis on 9 and 18 DIV hippocampal neurons from p140Cap^{+/+} and p140Cap^{−/−} mice. (A) Representative traces of spontaneous firing from primary hippocampal neurons at 9 DIV measured with conventional micro-electrode arrays (MEAs). p140Cap^{+/+} traces are shown in black (left) while p140Cap^{−/−} traces are in gray (right). (B) Firing frequency (phasic) was significantly smaller in p140Cap^{−/−} (as compared to control neurons at 9 DIV). (C) At 18 DIV spikes were principally grouped in bursts. This was the case for p140Cap^{+/+} as well as for p140Cap^{−/−} neurons. The insets at the bottom are a representation of the events indicated by the rectangle at an enlarged timescale. (D) Quantification of firing frequency at 18 DIV. (E, F) Burst number and burst duration. (G) Representative raster plots from MEA recordings of primary hippocampal networks at 9 DIV from p140Cap^{+/+} (black traces) and p140Cap^{−/−} neurons (gray traces). (H) Mean cross-correlation peaks at 9 DIV in p140Cap^{−/−} neurons compared to controls. (I, J) Same as for panel (G) and (H) but for 18 DIV neurons. (K) Representative time course of the cross-correlation function recorded for p140Cap^{+/+} from channel 12 and p140Cap^{−/−} neurons from channel 65. (L) Mean width of the cross-correlation function obtained from p140Cap^{+/+} and p140Cap^{−/−} neuronal networks.

(Fig. 3I, right plot), as shown by the relative correlation peak (Fig. 3H). Firing activity was evident in a large number of recording channels (80 ± 5% vs. 81 ± 8%, respectively) and was highly synchronous in both p140Cap^{+/+} and p140Cap^{−/−}

neuronal networks, suggesting that at 18 DIV comparable areas of both networks were effectively interconnected. The mean cross-correlation peak estimated from the recording channels were high in both cases (0.35 ± 0.2 vs. 0.32 ± 0.2, respectively)

(Fig. 3J), but exhibited a significantly different shape (Fig. 3K). In control neurons the cross-correlation function was significantly narrow (mean width at 0.05 was 197 ± 57 ms; n = 7 MEA), while in p140Cap$^{-/-}$ neurons the cross-correlation function after peaking at a maximal value at t = 0 persisted for longer times (mean width at 0.05 was 520 ± 185 ms, n = 13 MEA; P = 0.0001, unpaired t-test) (Fig. 3L). This time-extended strong correlation results most likely from the prolonged bursting activity of neurons in the absence of p140Cap, and ensures a more effective synchronous activity within the network.

p140Cap$^{-/-}$ Mice are more Susceptible to 4-Aminopyridine-induced Seizures In Vitro and to Kainate-induced Seizures In Vivo

The finding that knocking out p140Cap leads to higher hippocampal network synchronization at early times in cultured hippocampal neurons prompted us to test the ability of p140Cap$^{-/-}$ mice to develop seizure-like events (SLEs). We first induced SLEs in vitro using brain horizontal slices containing the hippocampus and the entorhinal cortex (EC), extracellularly perfused with the pro-convulsive compound 4-aminopyridine (4-AP). Local field potential (LFP) recordings (Fig. 4A and inset below) were performed by placing the tip of artificial cerebrospinal fluid (ACF)-filled glass pipettes in the CA1 area of the hippocampus and in layer II–III of the EC. A few minutes after starting the perfusion, tonic-clonic SLEs became detectable in 5 out of 14 p140Cap$^{+/+}$ slices (36%). Interestingly, a larger percentage of p140Cap$^{-/-}$ slices (6 out of 8, 75%) displayed 4-AP-induced SLEs as compared to p140Cap$^{+/+}$ preparations (p = 0.031, z-test for 2 population proportions) (Fig. 4B). Furthermore, the average number of SLEs per minute was significantly higher in p140Cap$^{-/-}$ than in control slices (0.34 ± 0.04 vs. 0.19 ± 0.03, respectively, N = 6 slices from 3 p140Cap$^{-/-}$ mice and N = 5 slices from 3 p140Cap$^{+/+}$ mice, p = 0.038, unpaired t-test) (Fig. 4C). Conversely, the average SLE duration was not different in the 2 groups (p140Cap$^{+/+}$: 31 ± 10 s, p140Cap$^{-/-}$: 39 ± 6 s, unpaired t-test, p = 0.9) (Fig. 4D). These results demonstrate that a higher hippocampal network synchronization is sufficient to make p140Cap$^{-/-}$ hippocampal slices perfused with 4-AP more prone to develop seizure-like events.

We then analyzed if seizure susceptibility is altered in p140Cap$^{-/-}$ mice in vivo after kainic acid (KA) treatment. Figure 4E shows the time course of the behavioral response of p140Cap$^{+/+}$ and p140Cap$^{-/-}$ mice to 35 mg/kg KA over a 3-h period after i.p. administration. In all mice, this dose of KA resulted in immobility and staring within the first 10 min, followed by head bobbing and stereotyped movements (stage 2 and 3 of Racine's scale) (Bozzi et al. 2000). 20 min after KA injection, p140Cap$^{-/-}$ mice rapidly progressed to stage 5 and 6 and showed continued generalized activity, while only 50% p140Cap$^{+/+}$ mice slowly reached stage 5 (genotype as between-subject factor and time within subject factor; effect of time: F = 9,67, p = 0.0001; effect of genotype: F = 12.29, p = 0.0057, 2-way repeated measure analysis of variance followed by Bonferroni post hoc test). Overall, the latency to the first stage 5 (status epilepticus) seizure differed between p140Cap$^{+/+}$ (70.3 ± 0.3 min, N = 3) and p140Cap$^{-/-}$ mice (26.6 ± 3.3 min, N = 3; p = 0.0002, unpaired t-test) (Fig. 4F). Mortality rate following KA administration was strongly different between control and p140Cap$^{-/-}$ mice (p140Cap$^{+/+}$ 0/7; p140Cap$^{-/-}$ 5/7 stats). Thus, the progression of clinical signs following KA treatment was dramatically different in control and knockout animals.
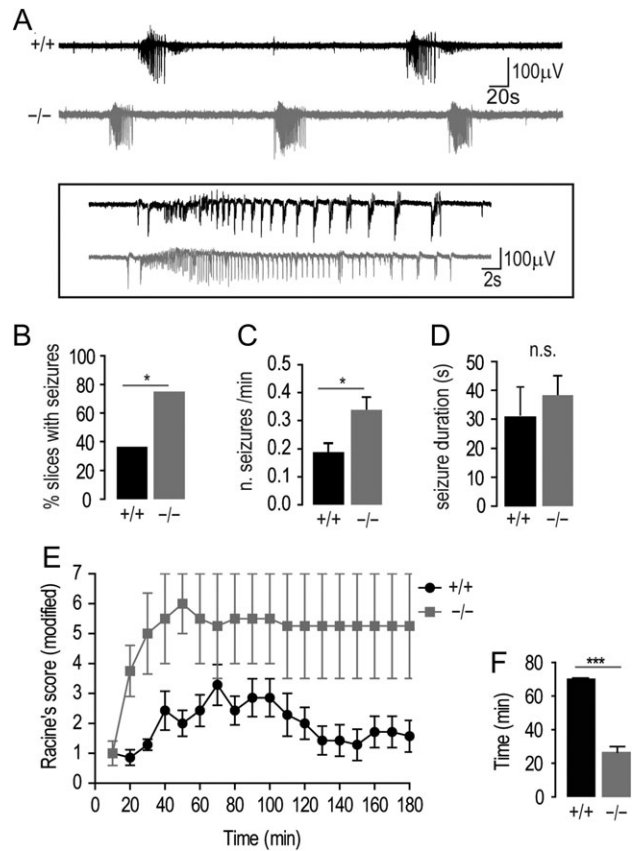

Figure 4. Seizure susceptibility in p140Cap$^{+/+}$ and p140Cap$^{-/-}$ mice. (A) Representative LFP traces recorded in the hippocampus of p140Cap$^{+/+}$ (black) and p140Cap$^{-/-}$ (gray) mice during bath perfusion with 4-AP (100 mM). The inset below shows enlarged individual ictal discharges. (B) Summary of the total percentage of slices showing detectable seizure-like activity (SLE). (C) Average SLE frequency. (D) Average SLE duration in p140Cap$^{+/+}$ and p140Cap$^{-/-}$. (E) Progression of behavioral changes after systemic KA administration (35 mg/ kg, i.p.) in p140Cap$^{+/+}$ and p140Cap$^{-/-}$ mice over a 3 h observation period. Data represent mean seizure scores ± SEM. (F) Latency to the first Stage 5: comparison between p140Cap$^{+/+}$ and p140Cap$^{-/-}$ shows that mutant animals need less time to reach status epilepticus.

p140Cap$^{-/-}$ Mice Display Higher Density of Inhibitory Synapses in the Hippocampus

To verify whether the enhanced inhibitory synapse density described in p140Cap$^{-/-}$ cultures (Fig. 2E) was also present in the intact brain, we measured the density of inhibitory VGAT-positive synapses in the CA1 region of both control and p140Cap$^{-/-}$ hippocampi by immunofluorescence and confocal microscopy (Fig. 5A, a-c). We found a significant increase of both the density and size of VGAT puncta in CA1 of mutant mice compared to controls (Number of VGAT puncta/μm2: p140Cap$^{+/+}$ = 0.059 ± 0.004, p140Cap$^{-/-}$ = 0.080 ± 0.005; area of VGAT puncta on field area: p140Cap$^{+/+}$ = 0.016 ± 0.002, p140Cap$^{-/-}$ = 0.034 ± 0.004, n = 5 p140Cap$^{+/+}$ mice, n = 5 p140Cap$^{-/-}$ mice; Mann–Whitney Rank Sum Test p = 0.019 for density; p = 0.003 for area analysis) (Fig. 5B,C). To confirm these data, we also performed an electron microscopic analysis of perisomatic synapses in the same hippocampal region (Fig. 5D). We found a significant increase of the number of symmetric synaptic appositions surrounding the cell body of CA1 pyramidal neurons in p140Cap$^{-/-}$ versus age-matched control mice (number of perisomatic symmetric synapse per 100 μm:
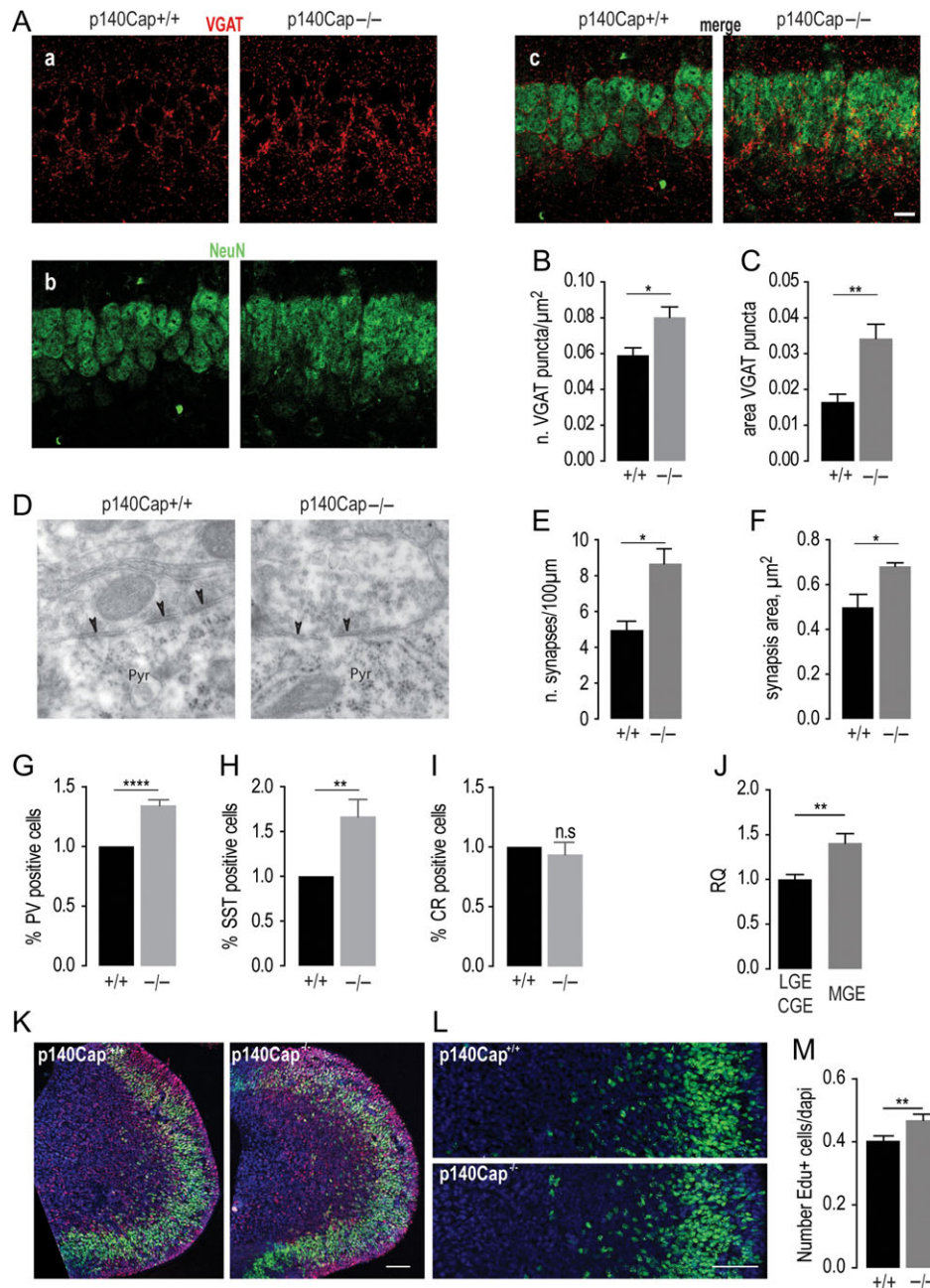
Figure 5. Quantification of VGAT inhibitory synapses and EdU analysis in p140Cap$^{+/+}$ and p140Cap$^{-/-}$ mice. (A) Representative immunofluorescence pictures of VGAT puncta in the CA1 region of 2-month-old p140Cap$^{+/+}$ and p140Cap$^{-/-}$ hippocampi (panel a). NeuN was used as marker (panel b). Merge is shown in panel c. Scale bar = 10 μm. (B) and (C) Quantification of VGAT density (B) and total area of VGAT puncta/area field (C). (D) Representative electron microscopy pictures of hippocampal CA1 region of perisomatic inhibitory synapses in 2-month-old mice. Arrows indicates symmetric synaptic appositions. (E) and (F) Quantification of density (E) and area (F) Scale bar. (G)–(I). Percentage quantification of Parvalbumin (PV) (G), Somatostatin (SST) (H) and Calretinin (CR) (I) positive cells in the CA1 region of the 2 genotypes. (J) Quantitative real-time RT-PCR analysis of p140Cap transcript in E15.5 CGE + LGE and MGE from p140Cap$^{+/+}$ embryos. (K) Representative immunofluorescence pictures of E12.5 total MGE stained for EdU (green nuclei), Nkx2.1 (red nuclei) and DAPI (blue nuclei) from p140Cap$^{+/+}$ and p140Cap$^{-/-}$ mice. Scale bar = 50 μm. (L) Cropped-Horizontal section of MGE from p140Cap$^{+/+}$ and p140Cap$^{-/-}$, with green cells representing EdU-positive cells and DAPI staining for nuclei. Scale bar = 50 μm. (M) Quantification of EdU-positive cells on DAPI-positive cells from panels L.

p140Cap$^{+/+}$ 5 ± 0.6, $N = 3$; p140Cap$^{-/-}$ 8 ± 0.76 $N = 3$; $p = 0.019$) (Fig. 5E). Moreover, the size of GABAergic terminals establishing perisomatic synapses was also increased in mouse mutants (p140Cap$^{+/+}$ 0.498 ± 0.059 μm^2 $N = 3$; p140Cap$^{-/-}$ 0.682 ± 0.016 μm^2 $N = 3$; $p = 0.039$) (Fig. 5F). These results indicate that both p140Cap-depleted neuronal cultures and p140Cap$^{-/-}$ mice display an increased number of inhibitory synapses impinging on CA1 pyramidal neurons.

To further characterize the inhibitory interneuron network in the hippocampus, we quantified 3 major classes of INs, i.e., Parvalbumin (PV), Somatostatin (SST) and Calretinin (CR) positive cells. This analysis was performed in the CA1 region of 8-week-old p140Cap$^{+/+}$ and p140Cap$^{-/-}$ mice using specific antibodies (see Supplemental Fig. 1 for representative images of the 2 genotypes). We observed a significant increase in the number of PV+ cells (≥34,1%, unpaired t-test $p < 0.0001$) (Fig. 5G), and

SST+ cells (≥66,4%, unpaired t-test $p = 0.0065$) (Fig. 5H) in p140Cap$^{-/-}$ mice with respect to p140Cap$^{+/+}$ mice, whereas the number of CR+ interneurons was unchanged (≤6,6% unpaired t-test $p = 0.543$ n.s.) ($n = 5$ p140Cap$^{+/+}$ mice, $n = 5$ p140Cap$^{-/-}$ mice) (Fig. 5I).

p140Cap$^{-/-}$ Mice Display Increased Number of Actively cycling Interneuron Progenitors in MGE

Hippocampal GABAergic interneurons originate from the ganglionic eminences (GE), which are transitory embryonic structures in the developing ventral telencephalon (Tricoire et al. 2011). It is known that interneuron diversity largely emerges from spatially segregated progenitor cells with distinct transcriptional profiles in the medial, caudal and lateral ganglionic eminence (MGE, CGE and LGE). Respectively, the MGE gives rise to the large majority of PV- and SST-expressing interneurons, while CR+ cells mostly originate from CGE (Gelman and Marín 2010; Maroof et al. 2010; Vaghi et al. 2014). For these reasons, we analyzed the expression profile of p140Cap transcript in both MGE and CGE + LGE in E15.5 p140Cap$^{+/+}$ embryos using qRT-PCR. Results indicated that the p140Cap mRNA is significantly enriched in MGE region compared to CGE + LGE (Fig. 5J). The MGE versus the CGE + LGE were further identified by the expression of the specific markers Nkx2.1 and Coup II, respectively (Supplemental Fig. 2A). Moreover, immunofluorescence and confocal analysis confirmed the presence of the p140Cap protein in the MGE already at E12.5 stage (Supplemental Fig. 2B), with a major intensity gradient in the Sub-Ventricular zone (SVZ), compared to the Ventricular zone (VZ). These observations suggest that p140Cap may play a specific role in the niche were PV+ and SST+ cells originate during development

To verify whether deletion of p140Cap affects the dynamic equilibrium between cell proliferation and cell death in Nkx2.1 progenitors, we quantified the number of actively cycling interneuron progenitors on MGE sections of E12.5 embryonic brains. This experiment revealed a small, but statistically significant increase (about 15%) in the number of BrdU-positive cells in the ventricular zone of p140Cap$^{-/-}$ mice compared to controls (p140Cap$^{+/+}$ 0.403 ± 0.016 $n = 7$; p140Cap$^{-/-}$ 0.469 ± 0.018 $n = 4$; unpaired t-test $p = 0.009$) (Fig. 5K–M). Analysis of TUNEL-positive cells in MGE at the same time point did not disclose any significant difference between the 2 genotypes, indicating that the processes of cell survival and apoptosis are not affected by the lack of p140Cap (Supplementary Fig. 2C). Indeed we found a very small percentage of TUNEL-positive cells at this stage (less than 0.1% of total number of cells), suggesting that apoptosis is not a primary event at this developmental stage. Interestingly, in p140Cap$^{-/-}$ MGE, a higher number of Nkx2.1-positive nuclei, the specific marker of MGE-interneuron progenitors, has been detected not only in the ventricular zone (VZ) but also in the sub-ventricular zone (SVZ) and in the mantle zone (MZ), 2 areas where in normal conditions, the process of cell-cycle exit and differentiation should be already started (Supplementary Fig. 2D, E).

Specific Ablation of p140Cap in Forebrain INs Leads to Higher Susceptibility to Develop Seizures In Vitro and Increased Density of Inhibitory Synapses

To investigate the relevance of p140Cap in the inhibitory network, we generated a conditional mouse model (hereafter called C-p140Cap) in which p140Cap is removed only in Dlx5/6-expressing INs by crossing p140Cap lox/lox mice with the Dlx5/

6-Cre line (Supplementary Figure 3A,B). Confocal analyses of C-p140Cap mice revealed a 42% increase in the density of VGAT puncta in the CA1 region of the hippocampus (VGAT puncta per μm^2, Flox-p140Cap: 0.166 ± 0.017 $n = 5$, C-p140Cap: 0.245 ± 0.024 $n = 4$; unpaired t-test $p = 0.0293$) as well as an increase in the size of VGAT-positive structures (VGAT puncta area on field area-normalized value, Flox-p140Cap: 0.089 ± 0.001, C-p140Cap 0.10 ± 0.003; $n = 5$ mice per genotype; unpaired t-test $p = 0.0017$) (Fig. 6A,B). C-p140Cap mice also displayed higher susceptibility to 4-aminopyridine-induced seizures in vitro, as assessed by the increased frequency of ictal events (Flox-p140Cap frequency: 0.23 ± 0.05 SLE/minute, $n = 11$ slices in 4 mice, C-p140Cap: 0.34 ± 0.04 SLE/minute, $n = 10$ slices in 4 mice, p 0.034, unpaired t-test; Flox-p140Cap SLE duration: 69 ± 11 s, $n = 11$ slices in 4 mice, C-p140Cap: 75 ± 12 s, $n = 10$ slices in 4 mice, $p = 0.728$, unpaired t-test) (Fig. 6C,D). However, seizures susceptibility after kainic acid treatment in vivo (Supplementary Fig. 4A), number of PV+ and SST+ interneurons in the hippocampus (Supplementary Fig. 4B) and number of proliferating interneuron progenitors in MGE of E12.5 embryos (Supplementary Fig. 4C) are not altered in C-p140Cap mice with respect to control Flox-p140Cap mice. These data indicate that selective removal of p140Cap from inhibitory interneurons, by using Dlx5/6-Cre line, enhances inhibitory synaptogenesis and alters E/I balance in hippocampal circuits without affecting some of the early events occurring in the IN progenitors pool, such as the number of proliferating Nkx2.1-positive cells.

Discussion

In the present study, we demonstrate that the adapter protein p140Cap plays a fundamental role in the development and refinement of the inhibitory network by regulating both the number and the activity of GABAergic synapses.

We and others have previously demonstrated that p140Cap is involved in the organization of the excitatory postsynaptic density (Sheng and Hoogenraad 2007; Tomasoni et al. 2013; Repetto et al. 2014; Fossati et al. 2015; Alfieri et al. 2017) and eventually plays a central role in learning and memory processes (Jaworski et al. 2009; Repetto et al. 2014). Indeed p140Cap$^{-/-}$ mice display impaired LTP and defective establishment and consolidation of new declarative memories (Repetto et al. 2014). At the cellular and molecular level the lack of p140Cap leads to the disruption of dendritic spine integrity (Jaworski et al. 2009; Tomasoni et al. 2013) which may be responsible for the LTP defect in hippocampal slices (Repetto et al. 2014). These studies pointed to a role for this protein in the molecular organization of excitatory synapses and indicated that p140Cap acts as a hub for postsynaptic complexes relevant to psychiatric and neurological disorders (Alfieri et al. 2017).

We here report that p140Cap is present in GABAergic presynaptic structures and its ablation results in altered GABAergic inhibitory neurotransmission (increased mIPSC frequency and GABA release) and increased number of inhibitory synapses impinging on pyramidal neurons. Therefore p140Cap regulates the developmental assembly of inhibitory circuits. Of note, some of the proteins localized in the inhibitory compartment were identified in the p140Cap synaptic interactome (Alfieri et al. 2017).

Interneurons are local circuit cells mainly responsible for inhibitory activity in the adult hippocampus, thereby controlling the activity of the principal excitatory cells (Trygve et al. 2007) and regulating the proper E/I balance (Freund and Buzsáki
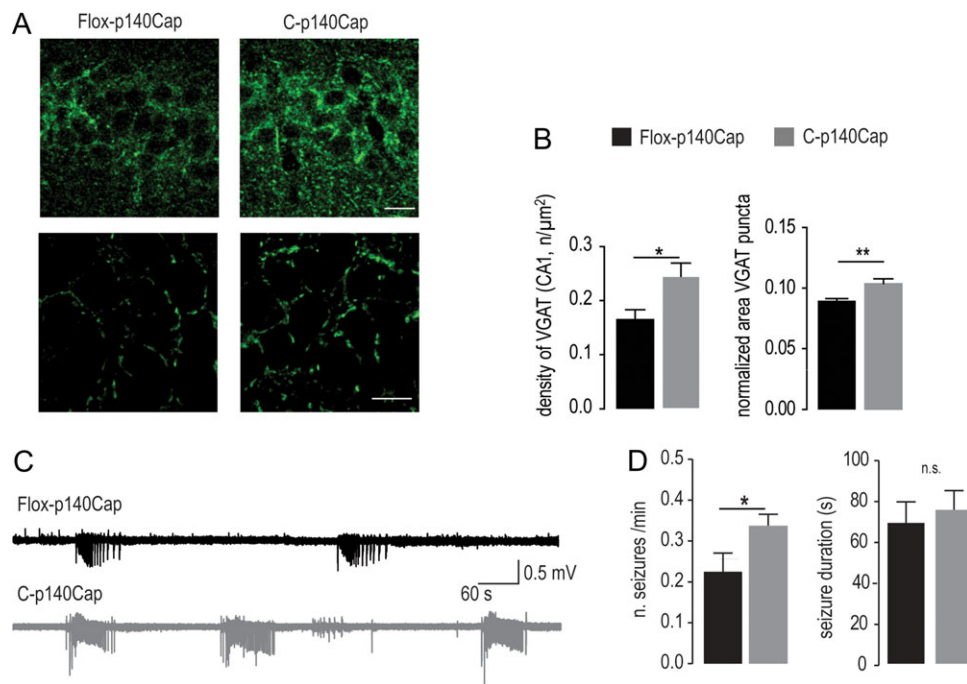
Figure 6. Selective removal of p140Cap from inhibitory interneurons affects the inhibitory compartment. (A) Representative VGAT immunofluorescence in CA1 hippocampal region of control (Flox-p140Cap) (left panels) and p140Cap conditional (C-p140Cap) (right panels) brain slices. Lower panels are a high magnification of the inset. Scale bar value = 10 μm. (B) VGAT-positive puncta density in Dlx5/6-Cre slices compared to controls and total area of VGAT puncta/area field. (C) Representative LFP traces recorded in the hippocampus of Flox-p140Cap and C-p140Cap mice during bath perfusion with 4-AP (100 μM). Calibration: 500 μV, 60 s. (D) The average SLE frequency, but not duration, was found significantly increased in p140Cap conditional brain slices compared to their controls.

1996; Somogyi and Klausberger 2005). In addition, they strongly regulate neocortical development by modulating several cellular processes such as neuronal proliferation, migration, differentiation and connectivity. Notably, altered inhibition results in pathological rearrangements which are responsible, in general, for impaired neuronal development (Tyzio et al. 2006, 2014; Gogolla et al. 2009), altered circuitry formation (Antonucci et al. 2012; Berryer et al. 2016) and abnormal neuronal plasticity (Hensch 2005; Harauzov et al. 2010; Succol et al. 2012; Deidda et al. 2015). In agreement, several developmental brain disorders such as autism, intellectual disability and schizophrenia result from an imbalanced E/I tone and are associated with alterations in GABAergic neurotransmission (Hashimoto et al. 2005; Tabuchi et al. 2007; Coghlan et al. 2012).

Several recent studies have demonstrated that fast synaptic inhibition mediated by different types of GABA releasing interneurons is also important for the generation of network oscillations, i.e., the neuronal activity generating network synchrony. This optimal brain status is essential to strengthen information processing and cognitive functions and to prevent a wide range of neurological diseases including epilepsy, schizophrenia, and autism spectrum disorders (ASDs) (for review see Coghlan et al. 2012; Marín 2012; Rapanelli et al. 2017). Synchronicity is one of the requisites of a functional neuronal network and GABAergic interneurons are the key players of this phenomenon through multiple mechanisms, including the depolarizing action of GABA during brain development, transient synaptic connections, extrasynaptic transmission, gap junction coupling, and the presence of pacemaker-like neurons (Blankenship et al. 2009; Bonifazi et al. 2009). Dysfunctions concerning some of those molecular mechanisms could be at the basis of the aberrant phenotype that we observe in p140Cap$^{-/-}$ models such as the cognitive and memory defects (Repetto et al. 2014).

Our results indicate that the absence of p140Cap results in a significant increase in neuronal network firing and synchronization, which are crucial for neuronal information processing and storage in the hippocampus (Chen et al. 2005; Li et al. 2007). Of note, spontaneous synchronized bursts were detected in p140Cap$^{-/-}$ neuronal networks both in vivo and in vitro. Indeed, differently from p140Cap$^{+/+}$ neuronal networks, which produce spontaneous synchronized bursts mostly after 2 weeks of cell seeding, p140Cap$^{-/-}$ cells exhibited synchronized activity already at 9 DIV, a time window where control neurons fire mostly in single-spike fashion. In line with the higher hippocampal network synchronization, both the global deletion of p140Cap or the selective removal of the protein from forebrain interneurons resulted in increased susceptibility to pharmacological-induced protocols of epilepsy.

Besides resulting in increased ability to form inhibitory synapses, the genetic ablation of p140Cap during brain development results in increased number of inhibitory interneurons—in particular the PV$^+$ and SST$^+$ cells—in CA1 hippocampal region, suggesting that the process of interneuron generation during development may be controlled by this protein. Of note, both p140Cap transcript and protein are already present at E12.5 in the MGE, the embryonic region where PV$^+$ and SST$^+$ interneurons originate (see also Supplementary Fig. 2A), thus opening the possibility that p140Cap may regulate neural progenitor proliferation as well as the process of interneuron migration out of MGE. The adapter protein p140Cap has been recently demonstrated to interfere with growth factor-dependent signaling in breast cancer cells, by inhibiting proliferative signals, such as the EGF-dependent Ras/Erk1/2 signaling (Damiano et al. 2010). In particular, in transformed cells, p140Cap expression limits tumor growth and confers the ability to activate the apoptotic program restoring mammary gland

tissue morphogenesis (Mailleux et al. 2007; Grasso et al. 2017). Therefore, in neuron precursors, p140Cap deficiency might affect the dynamic equilibrium between cell proliferation and cell differentiation in Nkx2.1 progenitor cells. The higher number of EdU-positive cells, which is not accompanied by a decreased cellular apoptosis, in the ventricular zone of p140Cap$^{-/-}$ mice may thus account for the increased number in MGE-derived parvalbumin and somatostatin interneurons in the hippocampus of p140Cap$^{-/-}$ mice. This is also consistent with the presence of Nkx2.1-positive nuclei of MGE-interneuron progenitors in the p140Cap$^{-/-}$ SVZ, where in normal conditions, the process of cell-cycle exit and differentiation should be already started (see Supplementary Fig. 2D,E). As an alternative mechanism, p140Cap has been recently found to stabilize E-cadherin at the cell membrane (Damiano et al. 2010). On neurons, the same E-cadherin is crucial for interneuron differentiation and correct guidance towards the cortex. Finally, the p140Cap-dependent inhibition of EGFR and Erk1/2 signaling observed in tumor cells (Damiano et al. 2010) may also account for the aberrant inhibitory synaptogenesis in GABAergic interneurons in p140Cap KO hippocampi. In recent times, different factors have been implicated in the control of inhibitory synaptogenesis, including Neuregulin 2 (Lee et al. 2015), FGF7 (Dabrowski et al. 2015), Semaphorin 4D (Kuzirian et al. 2013), SYNGAP1 (Berryer et al. 2016), and most notably BDNF (Bath et al. 2012). Of note, all these factors may require, for their action, KRAS-ERK1/2 mediated signaling and indeed an up-regulation of ERK signaling during early phases of postnatal development leads to a selective enhancement of synaptogenesis in GABAergic interneurons (Papale et al. 2017).

As already mentioned, interneuron defects are known to represent one of the main causes of brain development disorders and are also involved in neurodegenerative or injury-based disorders (Hunt and Baraban 2015). In epilepsy, the synchronization of neuronal firing involves the interaction of GABAergic inhibitory and glutamatergic excitatory mechanisms (Wu et al. 2015). In this pathological situation, fundamental disturbance in the E/I balance may result in abnormal activity of forebrain-neuronal circuits, which over time leads to epileptogenesis. Even if the role of interneurons in epilepsy is still discussed, the results of recent studies have stressed the importance of GABAergic neurons in triggering this phenomenon (Yekhlef et al. 2015; Avoli et al. 2016). In fact, activation of PV$^+$ interneurons appears to generate sustained epileptic events (Shiri et al. 2015; Yekhlef et al. 2015) and contribute to their maintainance (Ellender et al. 2014); (Khoshkhoo et al. 2017). Since these cells largely mediate synaptic inhibition, their proepileptic effect may sound counterintuitive. However, synchronous activation of groups of PV$^+$ and SST$^+$ interneurons results in a transient increase in extracellular potassium concentration ([K+]^o), which mediates membrane potential depolarization (Yekhlef et al. 2015). Such depolarization at times reaches a critical threshold for action potential firing in a relatively large number of surrounding cells (including principal glutamatergic neurons), inducing a massive activation and a further increase in [K+]^o. This phenomenon marks the initial stage of a seizure, which continues as the network keeps firing in a synchronous fashion and possibly propagates by recruiting further neighboring areas. In addition to their ability to start seizures using a non-synaptic effect (i.e., the [K+]^o increase), GABAergic interneurons may contribute to seizure maintenance as their continuous release of GABA eventually leads to an increase in chloride concentration in postsynaptic cells, resulting in a depolarizing shift in Cl$^-$ reversal potential and consequently in an excitatory, rather than inhibitory, effect of GABA (Huberfeld et al. 2007; Kaila et al. 2014). These evidences are in line with the increased susceptibility of p140Cap$^{-/-}$ mice to epileptogenic agents, even though their hippocampal network is enriched in the inhibitory component.

Notably selective removal of p140Cap in the Dlx5/6-expressing interneurons does not affect the number of interneuron progenitors in MGE and of mature PV$^+$ and SST$^+$ interneurons in the hippocampus, as well the susceptibility to kainic acid-induced seizures in vivo, suggesting that either p140Cap may contribute to some molecular events occurring in the progenitor pool before Dlx5/6-driven Cre expression, in particular the mitotic competence of the progenitors, or that the presence of p140Cap in populations other than INs is relevant for a correct INs function. The use of additional models (Taniguchi et al. 2011) may help to elucidate the role of p140Cap expression in early phases of INs development.

This work puts therefore the basis to further investigating the role of p140Cap in defining the E/I balance during hippocampal circuitry definition and the synaptopathies associated with its absence.

Supplementary Material

Supplementary data is available at *Cerebral Cortex* online.

Funding

Notes

References

Alfieri A, Sorokina O, Adrait A, Angelini C, Russo I, Morellato A, Matteoli M, Menna E, Boeri Erba E, McLean C, et al. 2017. Synaptic interactome mining reveals p140Cap as a new hub for PSD proteins involved in psychiatric and neurological disorders. Front Mol Neurosci. 10:212.

Allio A, Calorio C, Franchino C, Gavello D, Carbone E. 2015. Bud extracts from Tilia tomentosa Moench inhibit hippocampal neu- ronal fi ring through GABA A and benzodiazepine receptors activation. J Ethnopharmacol. 172:288–296.

Antonucci F, Turola E, Caleo M, Gabrielli M, Perrotta C, Novellino L, Clementi E, Giussani P, Viani P, Matteoli M, et al. 2012. Microvesicles released from microglia stimulate synaptic activity via enhanced sphingolipid metabolism. EMBO J. 31:1231–1240.

Avoli M, de Curtis M, Gnatkovsky V, Gotman J, Kohling R, Levesque M, Manseau F, Shiri Z, Williams S. 2016. Specific imbalance of excitatory/inhibitory signaling establishes seizure onset pattern in temporal lobe epilepsy. J Neurophysiol. 115:3229–3237.

Baldelli P, Hernandez-Guijo JM, Carabelli V, Carbone E. 2005. Brain-derived neurotrophic factor enhances GABA release probability and nonuniform distribution of N- and P/Q-type channels on release sites of hippocampal inhibitory synapses. J Neurosci. 25:3358–3368.

Baldelli P, Novara M, Carabelli V, Hernandez-Guijo JM, Carbone E. 2002. BDNF up-regulates evoked GABAergic transmission in developing hippocampus by potentiating presynaptic N- and P/Q-type Ca^{2+} channels signalling. Eur J Neurosci. 16:2297–2310.

Bath KG, Akins MR, Lee FS. 2012. BDNF control of adult SVZ neurogenesis. Dev Psychobiol. 54:578–589.

Berryer MH, Chattopadhyaya B, Xing P, Riebe I, Bosoi C, Sanon N, Antoine-Bertrand J, Levesque M, Avoli M, Hamdan FF, et al. 2016. Decrease of SYNGAP1 in GABAergic cells impairs inhibitory synapse connectivity, synaptic inhibition and cognitive function. Nat Commun. 7:13340.

Blankenship AG, Blankenship AG, Feller MB, Feller MB. 2009. Mechanisms underlying spontaneous patterned activity in developing neural circuits. Nat Rev Neurosci. 11:18–29.

Bonifazi P, Goldin M, Picardo MA, Jorquera I, Cattani A, Bianconi G, Represa A, Ben-Ari Y, Cossart R. 2009. GABAergic hub neurons orchestrate synchrony in developing hippocampal networks. Science. 326:1419–1424.

Bozzi Y, Vallone D, Borrelli E. 2000. Neuroprotective role of dopamine against hippocampal cell death. J Neurosci. 20: 8643–8649.

Chen S, Yue C, Yaari Y. 2005. A transitional period of Ca^{2+}-dependent spike afterdepolarization and bursting in developing rat CA1 pyramidal cells. J Physiol. 567:79–93.

Chin LS, Nugent RD, Raynor MC, Vavalle JP, Li L. 2000. SNIP, a novel SNAP-25-interacting protein implicated in regulated exocytosis. J Biol Chem. 275:1191–1200.

Coghlan S, Horder J, Inkster B, Mendez MA, Murphy DG, Nutt DJ. 2012. GABA system dysfunction in autism and related disorders: from synapse to symptoms. Neurosci Biobehav Rev. 36:2044–2055.

Corradini I, Donzelli A, Antonucci F, Welzl H, Loos M, Martucci R, De Astis S, Pattini L, Inverardi F, Wolfer D, et al. 2014. Epileptiform activity and cognitive deficits in SNAP-25(+/-) mice are normalized by antiepileptic drugs. Cereb Cortex. 24:364–376.

Dabrowski A, Terauchi A, Strong C, Umemori H. 2015. Distinct sets of FGF receptors sculpt excitatory and inhibitory synaptogenesis. Development. 142:1818–1830.

Damiano L, Di Stefano P, Camacho Leal MP, Barba M, Mainiero F, Cabodi S, Tordella L, Sapino A, Castellano I, Canel M, et al. 2010. p140Cap dual regulation of E-cadherin/EGFR cross-talk and Ras signalling in tumour cell scatter and proliferation. Oncogene. 29:3677–3690.

Deidda G, Parrini M, Naskar S, Bozarth IF, Contestabile A, Cancedda L. 2015. Reversing excitatory GABAAR signaling restores synaptic plasticity and memory in a mouse model of Down syndrome. Nat Med. 21:318–326.

Ellender TJ, Raimondo JV, Irkle A, Lamsa KP, Akerman CJ. 2014. Excitatory effects of parvalbumin-expressing interneurons maintain hippocampal epileptiform activity via synchronous afterdischarges. J Neurosci. 34:15208–15222.

Englot DJ, Modi B, Mishra AM, DeSalvo M, Hyder F, Blumenfeld H. 2009. Cortical deactivation induced by subcortical network dysfunction in limbic seizures. J Neurosci. 29: 13006–13018.

Fossati G, Morini R, Corradini I, Antonucci F, Trepte P, Edry E, Sharma V, Papale A, Pozzi D, Defilippi P, et al. 2015. Reduced SNAP-25 increases PSD-95 mobility and impairs spine morphogenesis. Cell Death and Differ. 22:1425–1436.

Freund TF, Buzsáki G. 1996. Interneurons of the hippocampus. Hippocampus. 6:347–470.

Gavello D, Rojo-Ruiz J, Marcantoni A, Franchino C, Carbone E, Carabelli V. 2012. Leptin counteracts the hypoxia-induced inhibition of spontaneously firing hippocampal neurons: a microelectrode array study. PLoS One. 7:e41530.

Gelman DM, Marín O. 2010. Generation of interneuron diversity in the mouse cerebral cortex. Eur J Neurosci. 31:2136–2141.

Gogolla N, LeBlanc JJ, Quast KB, Südhof TC, Fagiolini M, Hensch TK. 2009. Common circuit defect of excitatory-inhibitory balance in mouse models of autism. J Neurodev Disord. 1: 172–181.

Grasso S, Chapelle J, Salemme V, Aramu S, Russo I, Vitale N, Verdun L, Dallaglio K, Castellano I, Amici A, et al. 2017. The scaffold protein p140Cap limits ERBB2-mediated breast cancer progression interfering with Rac GTPase-controlled circuitries. Nat Commun. 8:1–16.

Harauzov A, Spolidoro M, DiCristo G, De Pasquale R, Cancedda L, Pizzorusso T, Viegi A, Berardi N, Maffei L. 2010. Reducing intracortical inhibition in the adult visual cortex promotes ocular dominance plasticity. J Neurosci. 30:361–371.

Hashimoto T, Bergen SE, Nguyen QL, Xu B, Monteggia LM, Pierri JN, Sun Z, Sampson AR, Lewis DA. 2005. Relationship of brain-derived neurotrophic factor and its receptor TrkB to altered inhibitory prefrontal circuitry in schizophrenia. J Neurosci. 25:372–383.

Hensch TK. 2005. Critical period plasticity in local cortical circuits. Nat Rev Neurosci. 6:877–888.

Huberfeld G, Wittner L, Clemenceau S, Baulac M, Kaila K, Miles R, Rivera C. 2007. Perturbed chloride homeostasis and GABAergic signaling in human temporal lobe epilepsy. J Neurosci. 27:9866–9873.

Hunt RF, Baraban SC. 2015. Interneuron transplantation as a treatment for epilepsy. Cold Spring Harbor Perspect Med. 5:a022376.

Ito H, Atsuzawa K, Sudo K, Di Stefano P, Iwamoto I, Morishita R, Takei S, Semba R, Defilippi P, Asano T, et al. 2008. Characterization of a multidomain adaptor protein, p140Cap, as part of a pre-synaptic complex. J Neurochem. 107:61–72.

Jaworski J, Kapitein LC, Gouveia SM, Dortland BR, Wulf PS, Grigoriev I, Camera P, Spangler SA, Di Stefano P, Demmers J, et al. 2009. Dynamic microtubules regulate dendritic spine morphology and synaptic plasticity. Neuron. 61:85–100.

Kaila K, Ruusuvuori E, Seja P, Voipio J, Puskarjov M. 2014. GABA actions and ionic plasticity in epilepsy. Curr Opin Neurobiol. 26:34–41.

Khoshkhoo S, Vogt D, Sohal VS. 2017. Dynamic, cell-type-specific roles for GABAergic interneurons in a mouse model of optogenetically inducible seizures. Neuron. 93: 291–298.

Klausberger T, Somogyi P. 2008. Neuronal diversity and temporal dynamics: the unity of hippocampal circuit operations. Science. 321:53–57.

Kullmann DM. 2011. Interneuron networks in the hippocampus. Curr Opin Neurobiol. 21:709–716.

Kuzirian MS, Moore AR, Staudenmaier EK, Friedel RH, Paradis S. 2013. The class 4 semaphorin Sema4D promotes the rapid assembly of GABAergic synapses in rodent hippocampus. J Neurosci. 33:8961–8973.

Lee KH, Lee H, Yang CH, Ko JS, Park CH, Woo RS, Kim JY, Sun W, Kim JH, Ho WK, et al. 2015. Bidirectional signaling of neuregulin-2 mediates formation of GABAergic synapses and maturation of glutamatergic synapses in newborn granule cells of postnatal hippocampus. J Neurosci. 35:16479–16493.

Li Y, Zhou W, Li X, Zeng S, Liu M, Luo Q. 2007. Characterization of synchronized bursts in cultured hippocampal neuronal networks with learning training on microelectrode arrays. Biosens Bioelectron. 22:2976–2982.

Maffei A, Nataraj K, Nelson SB, Turrigiano GG. 2006. Potentiation of cortical inhibition by visual deprivation. Nature. 443:81–84.

Mailleux AA, Overholtzer M, Schmelzle T, Bouillet P, Strasser A, Brugge JS. 2007. BIM regulates apoptosis during mammary ductal morphogenesis, and its absence reveals alternative cell death mechanisms. Dev Cell. 12:221–234.

Marcantoni A, Carabelli V, Vandael DH, Comunanza V, Carbone E. 2009. PDE type-4 inhibition increases L-type Ca(2+) currents, action potential firing, and quantal size of exocytosis in mouse chromaffin cells. Pflugers Arch. 457:1093–1110.

Marcantoni A, Raymond EF, Carbone E, Marie H. 2014. Firing properties of entorhinal cortex neurons and early alterations in an Alzheimer's disease transgenic model. Pflugers Arch. 466:1437–1450.

Marín O. 2012. Interneuron dysfunction in psychiatric disorders. Nat Rev Neurosci. 13:107–120.

Maroof AM, Brown K, Shi SH, Studer L, Anderson SA. 2010. Prospective isolation of cortical interneuron precursors from mouse embryonic stem cells. J Neurosci. 30:4667–4675.

McBain CJ, Fisahn A. 2001. Interneurons unbound. Nat Rev Neurosci. 2:11–23.

Morello N, Plicato O, Piludu MA, Poddighe L, Serra MP, Quartu M, Corda MG, Giorgi O, Giustetto M. 2017. Effects of forced swimming stress on ERK and histone H3 phosphorylation in limbic areas of roman high- and low-avoidance rats. PLoS One. 12:e0170093.

Papale A, d'Isa R, Menna E, Cerovic M, Solari N, Hardingham N, Cambiaghi M, Cursi M, Barbacid M, Leocani L, et al. 2017. Severe intellectual disability and enhanced gamma-aminobutyric acidergic synaptogenesis in a novel model of rare RASopathies. Biol Psychiatry. 81:179–192.

Pyle JL, Kavalali ET, Piedras-Renteria ES, Tsien RW. 2000. Rapid reuse of readily releasable pool vesicles at hippocampal synapses. Neuron. 28:221–231.

Rapanelli M, Frick LR, Pittenger C. 2017. The role of interneurons in autism and tourette syndrome. Trends Neurosci. 40:397–407.

Repetto D, Camera P, Melani R, Morello N, Russo I, Calcagno E, Tomasoni R, Bianchi F, Berto G, Giustetto M, et al. 2014. p140Cap regulates memory and synaptic plasticity through Src-mediated and citron-N-mediated actin reorganization. J Neurosci. 34:1542–1553.

Sheng M, Hoogenraad CC. 2007. The postsynaptic architecture of excitatory synapses: a more quantitative view. Annu Rev Biochem. 76:823–847.

Shiri Z, Manseau F, Levesque M, Williams S, Avoli M. 2015. Interneuron activity leads to initiation of low-voltage fast-onset seizures. Ann Neurol. 77:541–546.

Somogyi P, Klausberger T. 2005. Defined types of cortical interneurone structure space and spike timing in the hippocampus. J Physiol. 562:9–26.

Succol F, Fiumelli H, Benfenati F, Cancedda L, Barberis A. 2012. Intracellular chloride concentration influences the GABA A receptor subunit composition. Nat Commun. 3: 710–738.

Tabuchi K, Blundell J, Etherton MR, Hammer RE, Liu X, Powell CM, Sudhof TC. 2007. A neuroligin-3 mutation implicated in autism increases inhibitory synaptic transmission in mice. Science. 318:71–76.

Taniguchi H, He M, Wu P, Kim S, Paik R, Sugino K, Kvitsiani D, Fu Y, Lu J, Lin Y, et al. 2011. A resource of Cre driver lines for genetic targeting of GABAergic neurons in cerebral cortex. Neuron. 71:995–1013.

Tatti R, Haley MS, Swanson OK, Tselha T, Maffei A. 2017. Review neurophysiology and regulation of the balance between excitation and inhibition in neocortical circuits. Biol Psychiatry. 81:821–831.

Tomasoni R, Repetto D, Morini R, Elia C, Gardoni F, Di Luca M, Turco E, Defilippi P, Matteoli M. 2013. SNAP-25 regulates spine formation through postsynaptic binding to p140Cap. Nat Commun. 4:2136.

Traynelis SF, Silver RA, Cull-Candy SG. 1993. Estimated conductance of glutamate receptor channels activated during EPSCs at the cerebellar mossy fiber-granule cell synapse. Neuron. 11:279–289.

Tricoire L, Pelkey KA, Erkkila BE, Jeffries BW, Yuan X, McBain CJ. 2011. A blueprint for the spatiotemporal origins of mouse hippocampal interneuron diversity. J Neurosci. 31: 10948–10970.

Trygve S, Moser EI, Gaute TE. 2007. From grid cells to place cells: a mathematical model. Hippocampus. 17:801–812.

Tyzio R, Cossart R, Khalilov I, Minlebaev M, Hubner CA, Represa A, Ben-Ari Y, Khazipov R. 2006. Maternal oxytocin triggers a transient inhibitory switch in GABA signaling in the fetal brain during delivery. Science. 314:1788–1792.

Tyzio R, Nardou R, Ferrari DC, Tsintsadze T, Shahrokhi A, Eftekhari S, Khalilov I, Tsintsadze V, Brouchoud C, Chazal G, et al. 2014. Oxytocin-mediated GABA inhibition during delivery attenuates autism pathogenesis in rodent offspring. Science. 343:675–679.

Vaghi V, Pennucci R, Talpo F, Corbetta S, Montinaro V, Barone C, Croci L, Spaiardi P, Consalez GG, Biella G, et al. 2014. Rac1 and Rac3 GTPases control synergistically the development of cortical and hippocampal GABAergic interneurons. Cereb Cortex. 24:1247–1258.

Wu Y, Liu D, Song Z. 2015. Neuronal networks and energy bursts in epilepsy. Neuroscience. 287:175–186.

Yekhlef L, Breschi GL, Lagostena L, Russo G, Taverna S. 2015. Selective activation of parvalbumin- or somatostatin-expressing interneurons triggers epileptic seizurelike activity in mouse medial entorhinal cortex. J Neurophysiol. 113: 1616–1630.

Yizhar O, Fenno LE, Prigge M, Schneider F, Davidson TJ, O'Shea DJ, Sohal VS, Goshen I, Finkelstein J, Paz JT, et al. 2011. Neocortical excitation/inhibition balance in information processing and social dysfunction. Nature. 477: 171–178.

Synaptic Interactome Mining Reveals p140Cap as a New Hub for PSD Proteins Involved in Psychiatric and Neurological Disorders

Annalisa Alfieri[1†], Oksana Sorokina[2,4,5], Annie Adrait[3,4,5], Costanza Angelini[1], Isabella Russo[1], Alessandro Morellato[1], Michela Matteoli[6,7], Elisabetta Menna[6,7], Elisabetta Boeri Erba[8,9,10], Colin McLean[2], J. Douglas Armstrong[2], Ugo Ala[1,11], Joseph D. Buxbaum[12,13,14,15,16,17], Alfredo Brusco[18,19], Yohann Couté[3,4,5], Silvia De Rubeis[12,13], Emilia Turco[1*] and Paola Defilippi[1*]

[1] Department of Molecular Biotechnology and Health Sciences, Molecular Biotechnology Center, Università di Torino, Torino, Italy, [2] The Institute for Adaptive and Neural Computation, School of Informatics, University of Edinburgh, Edinburgh, United Kingdom, [3] Université Grenoble Alpes, iRTSV-BGE, Grenoble, France, [4] CEA, iRTSV-BGE, Grenoble, France, [5] Institut National de la Santé et de la Recherche Médicale, BGE, Grenoble, France, [6] Institute of Neuroscience, Consiglio Nazionale delle Ricerche (CNR), Milan, Italy, [7] Humanitas Clinical and Research Center, IRCCS, Rozzano, Italy, [8] Institut de Biologie Structurale, Université Grenoble Alpes, Grenoble, France, [9] CEA, DSV, IBS, Grenoble, France, [10] Centre National de la Recherche Scientifique, IBS, Grenoble, France, [11] GenoBiToUS-Genomics and Bioinformatics, Università di Torino, Turin, Italy, [12] Seaver Autism Center for Research and Treatment, Department of Psychiatry, Icahn School of Medicine at Mount Sinai, New York, NY, United States, [13] Department of Psychiatry, Icahn School of Medicine at Mount Sinai, New York, NY, United States, [14] Department of Neuroscience, Icahn School of Medicine at Mount Sinai, New York, NY, United States, [15] Friedman Brain Institute, Icahn School of Medicine at Mount Sinai, New York, NY, United States, [16] Department of Genetics and Genomic Sciences, Icahn School of Medicine at Mount Sinai, New York, NY, United States, [17] Mindich Child Health and Development Institute, Icahn School of Medicine at Mount Sinai, New York, NY, United States, [18] Department of Medical Sciences, Università di Torino, Turin, Italy, [19] Medical Genetics Unit, Azienda Ospedaliera Città della Salute e della Scienza di Torino, Turin, Italy

Altered synaptic function has been associated with neurological and psychiatric conditions including intellectual disability, schizophrenia and autism spectrum disorder (ASD). Amongst the recently discovered synaptic proteins is p140Cap, an adaptor that localizes at dendritic spines and regulates their maturation and physiology. We recently showed that p140Cap knockout mice have cognitive deficits, impaired long-term potentiation (LTP) and long-term depression (LTD), and immature, filopodia-like dendritic spines. Only a few p140Cap interacting proteins have been identified in the brain and the molecular complexes and pathways underlying p140Cap synaptic function are largely unknown. Here, we isolated and characterized the p140Cap synaptic interactome by co-immunoprecipitation from crude mouse synaptosomes, followed by mass spectrometry-based proteomics. We identified 351 p140Cap interactors and found that they cluster to sub complexes mostly located in the postsynaptic density (PSD). p140Cap interactors converge on key synaptic processes, including transmission across chemical synapses, actin cytoskeleton remodeling and cell-cell junction organization. Gene co-expression data further support convergent functions: the p140Cap interactors are tightly co-expressed with each other and with p140Cap. Importantly, the p140Cap interactome and its co-expression network show strong enrichment in genes associated with schizophrenia, autism, bipolar disorder, intellectual disability and epilepsy, supporting

synaptic dysfunction as a shared biological feature in brain diseases. Overall, our data provide novel insights into the molecular organization of the synapse and indicate that p140Cap acts as a hub for postsynaptic complexes relevant to psychiatric and neurological disorders.

INTRODUCTION

Mutations in genes encoding synaptic proteins have been associated with several brain disorders, including schizophrenia, autism spectrum disorder (ASD) and developmental delay/intellectual disability (DD/ID) (De Rubeis et al., 2014; Fromer et al., 2014; Deciphering Developmental Disorders, 2015). The term "synaptopathies" has in fact been proposed to cover a broad range of clinical manifestations having synaptic dysfunction as common etiology (Grant, 2012). The synaptic genes implicated in brain diseases span several functional classes, including adhesion molecules (e.g., *NRXN1*; Kim et al., 2008), neurotransmitter receptors (e.g., *GRIN2B* ; Endele et al., 2010), voltage-gated ion channels (e.g., *SCN2A*; Rauch et al., 2012), scaffolding proteins of the postsynaptic density (PSD) (e.g., *SHANK3*; Betancur and Buxbaum, 2013) and signaling proteins (e.g., *SYNGAP1* ; Hamdan et al., 2009).

Enormous progress has been made in the characterization of the synaptic proteome (Bayes et al., 2014), and the molecular and functional dissection of specific subsynaptic complexes is likely to reveal novel genes relevant to brain pathophysiology. Amongst the recently discovered synaptic proteins is p140Cap/SNIP (Chin et al., 2000; Di Stefano et al., 2004), a scaffolding protein localized in dendritic spines (Jaworski et al., 2009) and encoded by the *SRCIN1* gene. Previous work from our laboratory and others indicates that p140Cap is key in regulating synaptogenesis, synaptic transmission and synaptic plasticity (Jaworski et al., 2009; Tomasoni et al., 2013; Repetto et al., 2014). Acute down-regulation of p140Cap in primary hippocampal neurons reduces the number of mushroom spines and proportionally increases the number of dendritic filopodia (Jaworski et al., 2009; Tomasoni et al., 2013), a defect in synaptic maturation that can also be observed in p140Cap knockout (KO) mice (Repetto et al., 2014). Notably, dendritic spine dysgenesis is a consistent neuroanatomical finding in several psychiatric disorders, including ID, ASD and schizophrenia (Penzes et al., 2011). Further, p140Cap KO mice display defective long-term potentiation (LTP) and reduced long-term depression (LTD), two forms of synaptic plasticity necessary for learning and memory. Consistently, p140Cap KO mice show impairments in object recognition, suggestive of defects in memory consolidation and retrieval cognitive defects (Repetto et al., 2014).

The molecular complexes and pathways underlying p140Cap function are largely unknown. p140Cap was originally identified as an interactor of SNAP-25 in a two-hybrid screen (Chin et al., 2000) and subsequent studies have shown that this interaction takes place in the PSD, involving also PSD95, and is required for spine morphogenesis (Tomasoni et al., 2013;

Fossati et al., 2015). p140Cap had been also shown to interact with other components of the pre-synaptic compartment, such as vinexin and synaptophysin (Ito et al., 2008). Other interactions necessary for p140Cap-mediated control of spine formation and/or maturation are those with the EB3 (Jaworski et al., 2009), Endophilin A1 (Yang et al., 2015), and Src kinase (Di Stefano et al., 2007; Repetto et al., 2013, 2014). EB3 binds the plus-end of growing microtubules that can enter dendritic spines and influence their morphology (Jaworski et al., 2009). Endophilin A1 is localized both presynaptically, where it regulates synaptic vesicle endocytosis, and postsynaptically, where it controls spine morphogenesis (Yang et al., 2015). The correct functioning of both EB3 and Endophilin A1 requires p140Cap and its downstream effector cortactin, an F-actin-binding protein, that regulates the actin cytoskeleton organization (Uruno et al., 2001). The p140Cap-dependent regulation of cortactin activity might require a direct interaction as well as the suppression of the Src kinase pathway. In fact, cortactin is inhibited by Src phosphorylation (Martinez-Quiles et al., 2004), and p140Cap directly binds Src (Di Stefano et al., 2007) and suppresses its activation through binding to the C-terminal Src kinase (Csk) (Di Stefano et al., 2007; Repetto et al., 2013). Consistently, synapses isolated from p140Cap KO mice have increased phosphorylation on Src kinase Tyrosine 416 (Repetto et al., 2014) and treatment with a specific Src inhibitor ameliorates the spine defects observed in p140Cap KO neurons (Repetto et al., 2014). Beyond its role in spine morphology, p140Cap-mediated suppression of Src has been recently implicated in the homeostatic brake that restrains cocaine reward in the nucleus accumbens (Damez-Werno et al., 2016).

Given the role of p140Cap in synaptogenesis and the repercussions on cognition in its absence, we sought to capture the p140Cap molecular complexes at synapses and investigate their relevance for brain disorders. By using biochemical, proteomic, gene co-expression, and genetic data, we provide a comprehensive analysis of the p140Cap synaptic interactome. Our results reveal that p140Cap acts as a hub for synaptic proteins implicated in psychiatric and neurological disorders.

MATERIALS AND METHODS

Animals

Mixed 129Sv × C57BL/6J p140Cap heterozygous mice were generated as described in (Repetto et al., 2014). All experiments were approved and performed in accordance with the Italian law (authorization D.M. n°279/95B 27/11/1995) and dispositions of "D.L. n°116, 27/1/1992 in relation to animal use and protection in scientific research." Male, 3-month old wild-type (WT) and

p140Cap knockout (KO) littermates were used for synaptosomes preparations. Animals were sacrificed by cervical dislocation.

Synaptosomes Preparation

Synaptosomes were prepared from the telencephalon. The tissue was homogenized with a Dounce glass homogenizer and glass pestle in 8 ml ice-cold synaptosome buffer (4 mM Hepes pH = 7.3, 320 mM sucrose, 1 mM EGTA, Roche protease inhibitors 25X, 1 mM Sodium Orthovanadate, 1 mM DTT, phenylmethylsulphonyl fluoride, 1 mM sodium fluoride). The homogenate was centrifuged at 1,000 g for 10 min at 4°C. After discarding the nuclear pellet, the supernatant was centrifuged at 12,500 g for 20 min at 4°C. The pellet containing the synaptosomal fraction was resuspended in the synaptosome buffer and further centrifuged at 12,500 g for 20 min at 4°C. The final pellet (crude synaptosome fraction) was resuspended in 2 ml of ice-cold lysis buffer (150 mM NaCl, 50 mM Tris pH = 7, 5% Glycerol, 1% NP-40, 1 mM $MgCl_2$, Roche protease inhibitors 25X, 1 mM Sodium Orthovanadate, 1 mM DTT, phenylmethylsulphonyl fluoride, 1 mM sodium fluoride) and immediately processed for immunoprecipitation (Figure S1).

Western Blot

Western blots were performed with Mini-PROTEAN® TGX™ Precast Gels from Bio-Rad (California 94547 USA).gradient 4–15% Gels were transferred on Nitrocellulose blotting membrane (GE Healthcare Life Sciences) using Towbin buffer (25 mM Tris, 192 mM Glycine, 20% Methanol). Membranes were blocked with Tris-buffered saline TBS (50 mM Tris p < h 7–150 mM NaCl) with 5% Milk for 1 h at room temperature, incubated with primary and secondary antibodies as indicated below, and then developed with Bio-Rad's Clarity ECL on ChemiDoc Touch Imaging System (Biorad). For western blot of crude synaptosomal proteins, 30 ug of proteins was used.

Antibodies

Specific mouse monoclonal antibody (Mab) against p140Cap *(clone 2A8)* was produced at the MBC, University of Torino, as previously described (Di Stefano et al., 2007; Repetto et al., 2013). The antibodies used are as follows: Dlg4 (Mab, Abcam), Citron-N (rabbit polyclonal, Abcam), Grin2A (rMab from Millipore; rabbit polyclonal from Thermo Scientific), Grin2b (mouse monoclonal antibody, Neuromab), Grin1 rabbit polyclonal (Thermo Scientific), Shank2 (rabbit polyclonal, Synaptic System), Shank3 (rabbit polyclonal, Synaptic System), Snap25 (Mab, Synaptic System), Actin I-19 (rabbit polyclonal, Santa Cruz Biotechnology), Trio (rabbit polyclonal, Santa Cruz Biotechnology), rabbit polyclonal Camk2 (Cell Signaling), Homer-1 (rabbit polyclonal, Thermo Scientific), Cadherin-11 (Mab, Thermo Scientific), Syncam (rabbit polyclonal, Thermo Scientific), Ttc3 (rabbit polyclonal, as described in Berto et al., 2007), and Gfap (Mab, Dako-Agilent Technologies), Bassoon (rabbit polyclonal, Synaptic System). Mouse and rabbit IgGs were purchased from Santa Cruz Biotechnology. Secondary antibodies anti-mouse and anti-rabbit were purchased from Sigma Aldrich.

p140Cap Immunoprecipitation

1.25 mg of Dynabeads protein G (30 mg Dynabeads®/mL Invitrogen, Carlsbad, CA, USA) were initially washed using a Sodium Acetate buffer (100 mM Sodium acetate pH = 5, 0.1% NP-40) and incubated with 6 µg of p140Cap antibody diluted in the same buffer for 1 h at room temperature under gentle rotation. Beads were then washed twice withSodium acetate buffer and with Sodium Borate buffer (0.2 M Sodium borate pH = 9, 0.1% NP-40) Crosslinking was performed with 25 mM Dymethil Pimelimidate in 1 ml of Sodium Borate buffer for 45 min at room temperature on a wheel. Beads were washed again with Sodium Borate buffer and then with 0.2 M Ethanolamine pH = 8, 0.1% NP-40, incubated for 1 h at RT on a wheel to block the N-reactive groups and washed twice in PBS 0.1% NP-40. To remove the non-cross-linked antibody, beads were suspended in 100 mM Glycine pH = 2.5 and rapidly washed in 50 mM Tris pH = 7.4 0.1% NP-40. p140Cap-coupled Dynabeads were then washed twice with PBS 1X 0.05% Tween and then incubated with 6 mg of crude synaptosomal extracted for 2 h at 4°C. Beads were washed five times with cold lysis buffer, then resuspended in 60 µl of 2% SDS-PAGE sample buffer in reducing conditions and incubated at 70°C for 10 min. From this 1 mg was tested for Coomassie staining, 1 mg for Western blot for p140Cap to control the quality of the samples and 4 mg was used for mass spectrometry (Figure S2).

Primary Hippocampal Cultures

Primary cultures were established from the hippocampus of 17.5–18.5 embryos derived from breeding of p140Cap ± mice. The dissociated cells were plated on 20 mm coverslip coated with poly-lysine at the density of 80,000 cells/coverslip and cultured in Neurobasal medium (Invitrogen) added with B27 (Invitrogen), supplemented with antibiotics, 2 mM glutamine and glutamate for 17–18 days at 37°C. Neurons were then fixed in paraformaldehyde 4% and sucrose 4% (Sigma Aldrich) for 8 min at room temperature.

Immunofluorescence and Microscopy

Immunofluorescence staining was performed using antibodies against PSD95 (1:500 mouse monoclonal Abcam) and p140Cap homemade monoclonal antibody conjugated with Alexa Fluor 647 Antibody labeling kit (Thermo Fisher) diluted 1:500. Coverslips were first incubated with anti-PSD95 and then with Alexa fluor 488 goat anti mouse (Invitrogen); after several washes of the secondary antibody, conjugated anti-p140Cap Mab was added for 1h at room temperature and then washed away. Images were acquired using a Leica SPE confocal microscope.

Mass Spectrometry

(1) *Preparation and in-gel digestion of proteins*: proteins from co-IP eluates were stacked in the top of a 4–12% NuPAGE gel (Invitrogen) and stained with R-250 Coomassie blue. Gel bands were manually excised and cut in pieces before being washed six times with 25 mM NH_4HCO_3 for 15 min, followed by six washes in 25 mM NH_4HCO_3 containing 50% (v/v) acetonitrile. Gel pieces were then dehydrated with 100% acetonitrile and incubated with 10 mM DTT in 25 mM

NH_4HCO_3 for 45 min at 53°C and with 55 mM iodoacetamide in 25 mM NH_4HCO_3 for 35 min in the dark. Alkylation was stopped by adding 10 mM DTT in 25 mM NH_4HCO_3 (incubation for 10 min). Gel pieces were then washed again by incubation in 25 mM NH_4HCO_3 followed by dehydration with 100% acetonitrile. Modified trypsin (Promega, sequencing grade) in 25 mM NH_4HCO_3 was added to the dehydrated gel pieces before overnight incubation at 37°C. Peptides were extracted from gel pieces in three sequential extraction steps (each 15 min) using 30 μl of 50% acetonitrile, 30 μl of 5% formic acid, and finally 30 μl of 100% acetonitrile. The pooled supernatants were dried under vacuum. (2) *Nano-LC-MS/MS analyses*: the dried extracted peptides were resuspended in 5% acetonitrile and 0.1% trifluoroacetic acid and analyzed by online nanoLC-MS/MS (UltiMate 3000 RSLCnano and Q-Exactive Plus, Thermo Scientific) with 2 replicates per sample. Peptides were sampled on a 300 μm x 5 mm PepMap C18 precolumn and separated on a 75 μm × 250 mm C18 column (PepMap, Dionex). The nanoLC method consisted of a 120-min gradient at a flow rate of 300 nl/min, ranging from 5 to 37% acetonitrile in 0.1% formic acid for 114 min, before reaching 72% acetonitrile in 0.1% formic acid for the last 6 min. Spray voltage was set at 1.6 kV; heated capillary was adjusted to 270°C. Survey full-scan MS spectra (m/z = 400–1,600) were acquired with a resolution of 70,000 after accumulation of 10^6 ions (maximum filling time 200 ms). The 10 most intense ions were fragmented by higher-energy collisional dissociation after accumulation of 10^5 ions (maximum filling time 50 ms). MS and MS/MS data were acquired using the software Xcalibur (Thermo Scientific). (3) *Data analyses*: RAW files were processed using MaxQuant, version 1.5.1.2 (Cox and Mann, 2008). Spectra were searched against the Uniprot database (*Mus musculus* taxonomy, March 2015 version) and the frequently observed contaminants database embedded in MaxQuant. The I = L option was activated. Trypsin was chosen as the enzyme and 2 missed cleavages were allowed. Peptide modifications allowed during the search were: carbamidomethylation (C, fixed), acetyl (Protein N-ter, variable) and oxidation (M, variable). Minimum number of unique peptides was set to 1. The matching between runs option was activated. The mass spectrometry proteomics data have been deposited to the ProteomeXchange Consortium via the PRIDEpartner repository (Vizcaino et al., 2016) with the dataset identifier PXD004215. (4) *Statistical analyses*: The following steps were mainly performed using the Perseus toolbox (version 1.5.1.6) available in the MaxQuant environment. Proteins identified in the reverse and contaminant databases, identified with less than 2 razor + unique peptides, or exhibiting less than 6 iBAQ values in one condition (3 biological replicates with 2 analytical replicates each for control and p140Cap co-IPs) were discarded from the list. iBAQ values of the 1952 remaining proteins. After log2 transformation, iBAQ values were normalized by condition-wise centering, missing data imputation was realized (replacing missing values by a constant weak value calculated independently for each injected sample as the 2.5-percentile value of the column) and statistical testing of differential abundances between control and p140Cap conditions were conducted using welch *t*-testing. To consider

a protein as a potential binding partner of p140Cap, it must has passed our significance criteria: FDR threshold of 1% on *p*-values using the Benjamini-Hochberg method and a minimum 4-times enrichment in p140Cap WT samples compared to the KO controls.

Bioinformatic Analyses of MS Data

Throughout the study, over-representation of annotation terms (disease, function etc.) was estimated by use of the hypergeometric distribution to test whether the number of selected proteins is larger than would be expected by chance;

$$p = 1 - \sum_{i=0}^{k-1} \frac{\binom{M}{i}\binom{N-M}{n-i}}{\binom{N}{n}}$$

where N is a total number of proteins in the background distribution, M is the number of genes within distribution that are annotated to the node of interest, n is the size of the list of genes of interest and k is the number of genes within the list, which are annotated to the node. Obtained *p*-values were adjusted for multiple testing by Bonferroni correction at 0.05 or 0.01 significance levels as indicated.

For literature comparison, a list of 6,688 proteins was selected as a synaptic *universe* based on combined results from 35 published synapse proteome studies (in preparation; Supplementary Table S2). Protein lists from those studies were curated, mapped to stable IDs (Entrez, Uniprot, MGI) for human and mouse and combined into single list containing only unique protein/gene name, IDs and publication source (PMID). Summary data for the 35 publications with associated metadata (PMID, year, method, species and number of proteins found) are presented in Supplementary Table S2.

Enrichment analysis of annotation in the interactome was performed in R, specifically using the Bioconductor package ClusterProfiler for Gene Ontology (GO) and KEGG enrichment analysis (Yu et al., 2012) and Bioconductor ReactomePA package for pathway over-representation analysis (http://bioconductor. org/packages/release/bioc/html/ReactomePA.html). For each enrichment type (GO, KEGG, Reactome), two background sets of proteins were used: (1) the default mouse genome list from Bioconductor and (2) our list of 6688 published synaptic proteins-to reveal the consistency in enriched terms. *p*-values, adjusted for multiple comparison p.adjust and *q*-values for false discovery rates (FDR) are provided in Supplementary Table S3.

For disease enrichment the annotation data were standardized using MetaMap (Aronson and Lang, 2010) and NCBO Annotator (Whetzel et al., 2011; Musen et al., 2012) to recognize terms found in the Human Disease Ontology (HDO) (Schriml et al., 2012) Recognized enriched disease ontology terms were then associated with gene identifiers and stored locally. Disease term enrichment', for the p140Cap dataset', could then be calculated using the Topology-based Elimination Fisher method (Alexa et al., 2006) found in the topGO package (http://topgo.bioinf-mpi-inf.mpg.de/), together with the standardized OMIM and Ensembl variation gene-disease annotation data (14111 gene-disease associations), mapped onto the full HDO tree.

A PSD network was constructed from a list of 1,443 proteins obtained from a study of the PSD in the human brain (Bayes et al., 2011). Protein-protein interactions were obtained by mining publicly available databases: HIPPIE (Schaefer et al., 2012), BioGRID (Chatr-Aryamontri et al., 2015), IntAct (Kerrien et al., 2012), and performing an InterologWalk over different species using Bio::Homology::InterologWalk (Gallone et al., 2011). The connected PSD network consists of 1,312 proteins and 8,031 protein interactions (i.e., 131 proteins could not be connected into the network). This PSD network was clustered making use of the spectral properties of the network; the network being expressed in terms of its eigenvectors and eigenvalues, and partitioned recursively (using a fine-tuning step) into communities based on maximizing the Modularity clustering measure (Newman, 2006; Simpson et al., 2010). Where first we found the node which, when moved from one community to the other, gave the maximum change in Modularity. This node's community was then fixed and we repeat the process until all nodes had been moved. The whole process was repeated from this new state until the change in the Modularity, between the new and old state, was less than the predefined tolerance. The modularity of the full PSD network was found to be 0.36.

Robustness of the full PSD network communities was assessed by running the algorithm 500 times, randomly selecting 80% of the network node set and related interactions each time. The package clusterCons (Simpson et al., 2010) was used to build a consensus matrix from which to test the robustness of the communities, and proteins found inside the communities. Community and protein robustness values range from 0, indicating no confidence in existing through to 1, indicating absolute confidence in the cluster existing. Community robustness values range from 0.1 to 0.7, and from 0.01 to 0.9 for protein robustness. Clusters C7, C17, C22, and C23 showed evidence of being robust, with community robustness values 0.2, 0.4, 0.3, and 0.3 respectively.

We also tested the significance of annotation enrichment in each cluster using the Hypergeometric distribution formula. $P \leq 10^{-2}$, were tested for their strength of significance by recording the percentage of P-values found from every community/annotation combination, lower than or equal to the observed P-value, when 1,000 random permutations of the annotation labels were made. P-values found with a strength of significance $< 1\%$ were considered statistically significant. P-values values were also tested against a more stringent Bonferroni correction at the 0.05 (*), 0.01 (**), and 0.001 (***) significant levels, and highlighted throughout the enrichment tables.

Gene Co-expression Analysis

Gene co-expression was evaluated on 18 human-mouse conserved co-expression networks (CCNs) (Piro et al., 2011), where a link of co-expression reflects the human and mouse independent gene co-expression in the corresponding single-species networks. Statistical significance of p140Cap interactors co-expressed with p140Cap was assessed by hypergeometric distribution. Statistical significance of the co-expression between p140Cap interactors was assessed by evaluating the p-value of the z-score corresponding to the number of links found in the single CCNs, based on 100 randomization of the same CCNs.

RESULTS

Quantitative Proteomic Analysis of p140Cap Synaptic Interactome

To identify the p140Cap protein complexes and the related functional pathways at synapses, we performed a quantitative proteomic analysis of p140Cap immunoprecipitates from mouse crude synaptosomes preparations, using p140Cap KO mice (Repetto et al., 2014) as negative control (Figure S1). The quality of the preparations was verified by testing the enrichment of synaptic proteins in the crude synaptosome fraction compared to total brain extracts. PSD-95, SNAP-25, and Bassoon, as well as p140Cap, were enriched in synaptosomes (**Figure 1A**).

Three distinct crude synaptosomes were prepared from 3 month-old WT and p140Cap KO male mice and synaptosomal extracts were immunoprecipitated using p140Cap monoclonal antibody. The specificity of the immunoprecipitates (IP) was confirmed by Coomassie staining and western blot (Figure S2). In the Coomassie-stained gel, we detected a discrete band of ~150 kDa, corresponding to the expected molecular weight for p140Cap in SDS-PAGE in the IPs from WT samples but not from p140Cap KO synaptosomes (Figure S2A). Similarly, a p140Cap immunoreactive band was observed in the p140Cap IPs from WT but not from KO synaptosomes (Figure S2B). The Coomassie-stained gel reveals that several proteins seem to selectively co-immunoprecipitate with p140Cap from WT samples as compared with the KO ones. Overall, these data indicate that the p140Cap immunoprecipitation is highly specific, thus making these samples suitable for the identification of p140Cap interactors by mass spectrometry (MS).

To identify p140Cap-binding partners, we applied label-free quantitative MS-based proteomics to the p140Cap IPs from WT and KO synaptosomes. Proteins eluted from the IPs were in-gel digested and the resulting peptides analyzed by nanoliquid chromatography coupled to tandem MS (two analytical replicates per sample). Identities and intensities of the recovered peptides and proteins in each sample were obtained using MaxQuant (Cox and Mann, 2008). After filtering and statistical analysis of iBAQ values (Schwanhausser et al., 2011), 352 (351 interactors plus p140Cap) proteins enriched in the WT samples were identified (Supplementary Table S1), as represented in the Volcano plot (**Figure 1B**).

To validate the proteomic findings, we selected eleven candidates whose alterations might underlie the dendritic spine defects, the impairments in LTP/LTD, and the learning and memory deficits we previously observed in the p140Cap KO mice (Repetto et al., 2014). We then tested the presence of the selected proteins on the p140Cap IPs. We tested and validated p140Cap interactions with Citron-N, already known to interact with p140Cap (Repetto et al., 2014); the NMDA receptor subunits Grin2a, Grin2b and Grin1, the scaffold proteins Dlg4/PSD95, Shank2, Shank3, Homer1, and Camk2a. Alterations in expression or localization of several of these interactors are known to
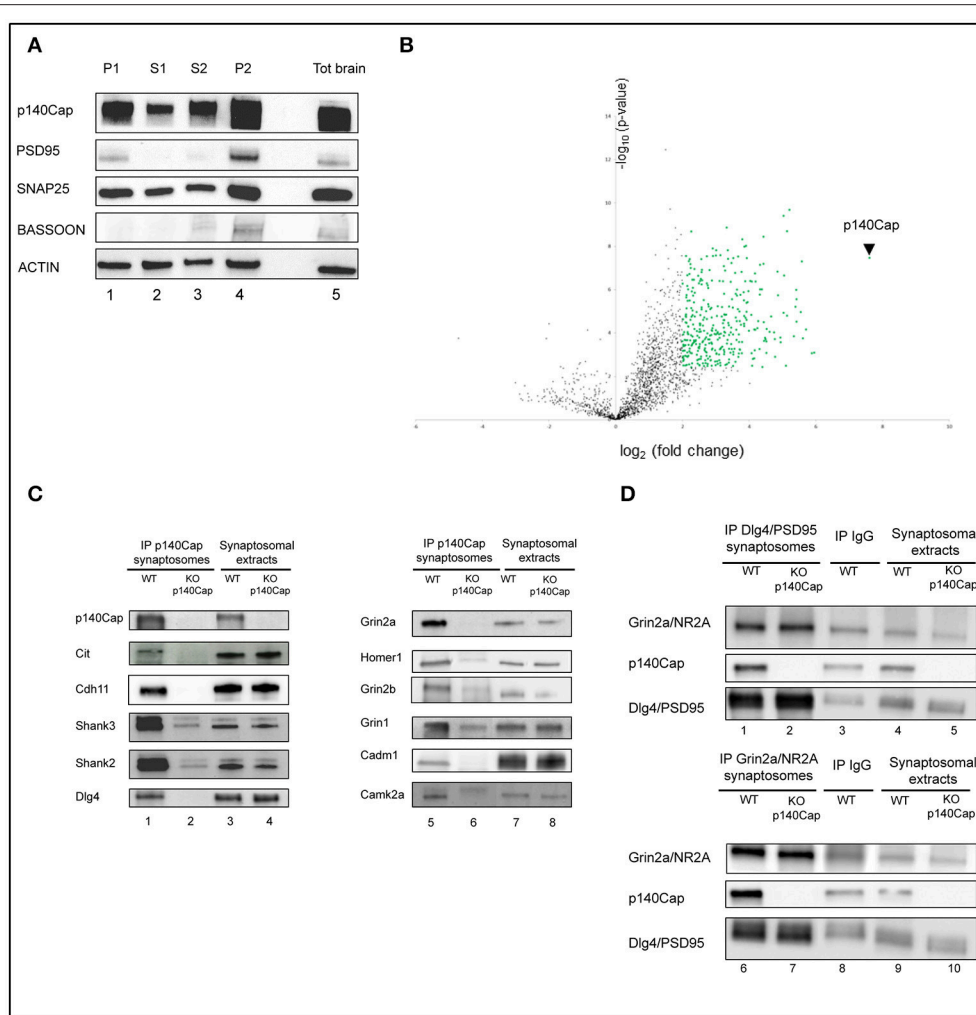
FIGURE 1 | Identification and validation of p140Cap interactors. Enrichment of synaptic markers in the synaptosomal preparation. **(A)** Validation of the synaptosomes. Western blot for p140Cap, PSD-95, Snap25, **Bassoon** and beta-actin fractions isolated during synaptosomal preparation. Lane 1, nuclear fraction (P1); lane 2, first cytosolic fraction (S1); lane 3, second cytosolic fraction (S2); lane 4, crude synaptosome (P2), lane 5, total brain extracts (see Figure S1 for details). **(B)** Statistically enriched proteins in the p140Cap IP. The Volcano plot represents the $\log_{10}(p$-value, y axis) plotted against the $\log_2$(fold change, x axis) for proteins quantified in p140Cap IPs from WT and p140Cap KO, used as negative control. 357 different proteins, including p140Cap (arrowhead) were found significantly enriched in WT samples (FDR $\leq$ 1%, $\geq$ 4-fold enrichment) are shown as green dots **(C)** Validation of synaptic p140Cap interacting proteins identified in the interactome. Lane 1 and 5, p140Cap IP in WT animals; lane 2 and 6, p140Cap IP in p140Cap KO animals; lane 3 and 7, input from WT synaptosomes; lane 4 and 8, input from KO synaptosomes. Co-immunoprecipitated proteins are shown on the left, along with their rank in MS. **(D)** Reverse validation for p140Cap interacting proteins Dlg4/PSD95 and Grin2a/NR2A. Lane 1, Dlg4/PSD95 IP in WT animals; lane 2, Dlg4/PSD95 IP in p140Cap KO animals; lane 4, input from WT synaptosomes; lane 5, input from KO synaptosomes; lane 6, Grin2a/NR2A IP in WT animals; lane 7, Grin2a/NR2A IP in p140Cap KO animals; lane 9, input from WT synaptosomes; lane 10, input from KO synaptosomes. Lane 3 and lane 8 are control IP with IgGs in WT animals.

affect LTP/LTD and cognitive functions (Grant, 2012; Luscher and Malenka, 2012; Robison, 2014; Sweatt, 2016). Further, we validated the interaction with the adhesion molecules Cadherin-11 (Cdh11) (Manabe et al., 2000) and Cadm1/Syncam (Frei and Stoeckli, 2016; **Figure 1C**). We also verified that three proteins (Ttc3, Trio, and Gfap), placed very low in the interactome, were only non specifically immunoprecipitated with anti p140Cap Mab (Figure S3). Further, we performed a reverse validation: we immunoprecipitated PSD95 and Grin2a and verified the presence of p140Cap (**Figure 1D**). The validation of the proteomic data across a range of various enrichment levels above the fixed

cut-off indicates that the p140Cap synaptic interactome we isolated contains bona fine p140Cap-containing macromolecular complexes.

Synaptic Localisation of p140CAP Complexes with Comparative Study of Reported Synaptic Datasets

To further map the p140Cap interactome, we searched published neuronal proteome datasets for p140Cap and its interactors. We found that p140Cap was reported in the majority of the

published PSD datasets (Supplementary Table S2). In a few co-IP studies, p140Cap was detected in complexes with PSD95 (Dosemeci et al., 2007), mGluR5 (Farr et al., 2004), Chmpb2 (Chassefeyre et al., 2018), and Snap25 (Fossati et al., 2015). Further, we searched for the 351 identified interactors of p140Cap across the published PSD proteomic datasets and found an exceptionally high enrichment (order of E-14 of significance in average) (Supplementary Table S2).

We also sought to verify whether p140Cap and associated proteins were found in presynaptic preparations as well, and we found that p140Cap was detected in the presynaptic compartment in several studies (Gronborg et al., 2010; Boyken et al., 2013; Weingarten et al., 2014). Specifically, it was detected in complexes with Rims1, Syn1-2-3, Git1, and Wasf1 in co-IP experiments on presynaptic protein complexes (August B Smit, personal communication). However, it was not reported in other studies focusing on synaptic vesicles (SV) or SV-recycling proteins (Morciano et al., 2005, 2009; Gorini et al., 2010; Brinkmalm et al., 2014; Wilhelm et al., 2014). p140Cap–interacting proteins, in turn, were found enriched in presynaptic datasets, although with a lower score than that found in postsynaptic studies (Supplementary Table S2). Therefore, our proteomic data, in agreement with previous studies, place p140Cap mainly, but not exclusively, in the PSD.

We then examined all the p140-interacting proteins to evaluate their distribution between pre- and postsynaptic complexes. The two lists showed a high degree of overlap, which was expected since the majority of synaptic proteins are found in both compartments. **Figure 2A** shows the distribution of the p140-interacting proteins between PSD (5023 proteins from 25 postsynaptic studies and presynaptic compartment (1215 proteins from 9 presynaptic studies). 334 of the 352 p140Cap interactors overlap with these datasets. Of these proteins, none were described as specifically presynaptic, whereas the majority was described as specifically postsynaptic (247) or found in both compartments (87). This further supports a predominantly postsynaptic localization of the p140Cap complexes.

The presence of p140Cap in the PSD has been previously shown in rat synaptic fractionation, where it is enriched in the PSD fraction together with PSD95 (Mclean Colin et al., 2016). To further validate the presence of p140Cap in the PSD, we performed a localization experiment on primary mouse hippocampal cultures. Staining of both p140Cap and PSD95 in **Figure 2B** shows a co-localization of these two proteins at synapses. All together, these results strongly indicate that the p140Cap-associated proteins share common cellular functions and fall within specific substructures of the PSD.

Functional Enrichment Analyses of the p140CAP-Containing Protein Complexes

To obtain a functional perspective of the p140Cap interactome, we tested its enrichment against KEGG, GO ontology and Reactome databases (Supplementary Table S3). We ran analysis against two reference (background) lists: (1) the default mouse genome list provided by Bioconductor and (2) a combined list of 6688 proteins from published synapse proteomics studies,

to reveal more specific p140Cap associated terms compared to the whole synaptosome. Both reference lists demonstrated a very high level of consistency in top enriched terms. However, using the synaptic as background gives more conservative (i.e., lower) significance values for enriched terms. The full lists for enrichment results are presented in Supplementary Table 3.

For the enriched terms listed here, p-values were corrected for multiple testing as described in the methods. Based on Molecular Function (MF) ontology, the 351 p140Cap-interacting proteins were significantly enriched for the "actin binding" term ($P = 2.79E-17$), which is in line with the previously described functions of p140Cap (Repetto et al., 2014). Additionally, we found that "glutamate receptor binding" ($P = 3.46E-11$), "PDZ domain binding" ($P = 1.22E-06$) and "GTPase regulator activity" ($P = 2.86E-04$) terms were also significantly increased (Supplementary Table S3). Among the top Cellular Compartment (CC) terms were "postsynaptic membrane" ($P = 3.08E-27$), "actin cytoskeleton" ($P = 2.87E-14$), and "neurotransmitter receptor complex" ($P = 8.53E-10$). This is in agreement with Biological Process (BP) GO results, where the top enriched terms were "chemical synaptic transmission" ($P = 1.81E-15$), "actin cytoskeleton organization" ($P = 4.37E-11$), "regulation of synaptic plasticity" ($P = 1.96E-09$) and "regulation of protein complex assembly" ($P = 3.63E-06$) (Supplementary Table S3). Analysis of enrichment against the Reactome pathway database revealed the overrepresentation for "Transmission across Chemical Synapses" ($P = 7.05E-15$), "Unblocking of NMDA receptor, glutamate binding and activation" ($P = 4.90E-10$), "Cell-cell junction organization" ($P = 1.44E-08$), "Ras activation upon Ca influx through NMDA receptor" ($P = 2.49E-08$), "L1CAM interactions" ($P = 1.00E-07$) (Supplementary Table S3).

To classify proteins into functionally related modules, we checked for the correlation between the experimentally measured protein abundances and Reactome pathway terms for the top 174 interacting proteins with the highest significance. Three "modules" could be detected (**Figure 3**). Module 1 (**Figure 3**, upper right) is related to "Unblocking and activating NMDA receptors," "Trafficking of AMPA receptors" and "Chemical signaling through the synapse" Reactome terms (including Gria1, Gria3, Grin2B, and Dlg4). Module 2 (**Figure 3**, center), is largely composed of cadherin-, claudin- and catenin-related proteins involved in "Cellular adhesion and junction" functions. Module 3 (**Figure 3**, bottom left) includes proteins associated in "Axon Guidance" and "Developmental Biology" function.

Taken together, the functional enrichment analysis from these three distinct sources (GO, Reactome and KEGG) indicate that the p140Cap interactors exhibit functions relevant to synaptic structure, synaptic transmission and plasticity.

The p140CAP Interactome within the Structure of the PSD

Given the enrichment in PSD (**Figure 2A**), we examined previously described PSD protein network models to assess whether the p140Cap-interacting proteins form structural composites within the PSD or are rather randomly distributed
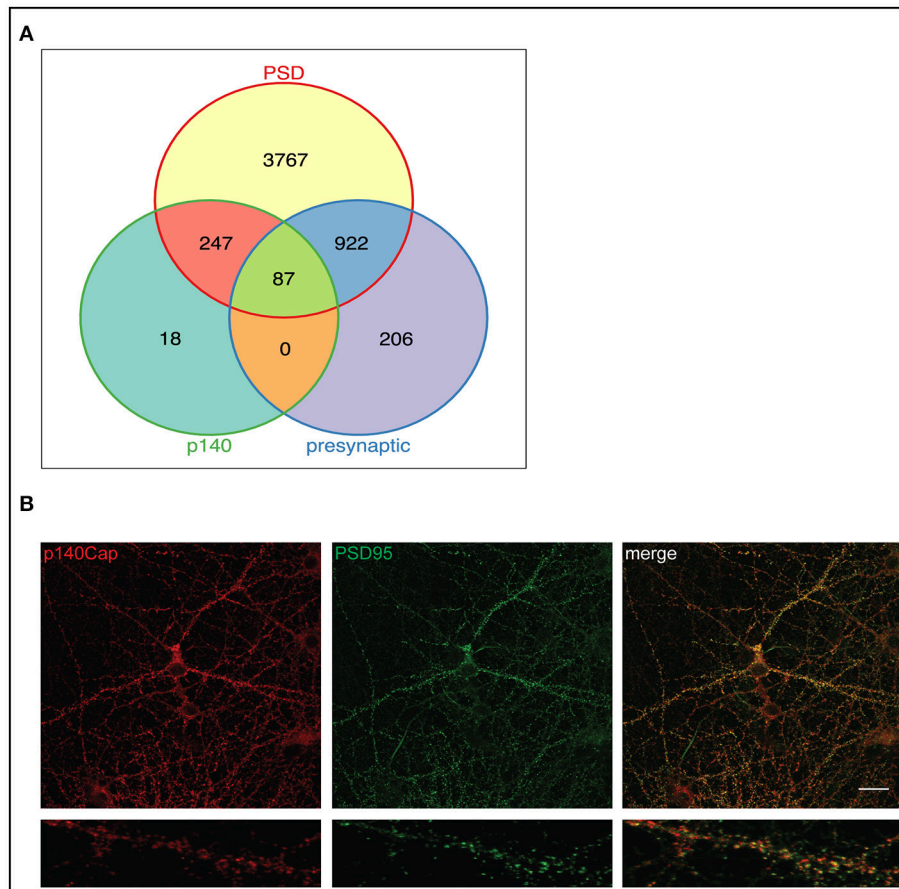
FIGURE 2 | p140Cap interacting proteins distribution in pre- and postsynaptic compartments and functional modules of the p140Cap interactome. **(A)** Venn diagram showing the overlap of 352 p140Cap interactors (green) mapped in pre- (purple) and postsynaptic (yellow) datasets. **(B)** p140Cap co-localization with PSD95 on primary hippocampal neurons. DIV 17 hippocampal neurons were stained with antibodies to p140Cap (red) and to PSD95 (green). Merge is shown on the right (Upper panels) Scale bar 20 μm. Magnification of a segment of dendrite is shown in lower panels.

throughout the network. We built a protein-protein interaction (PPI) network based on a human PSD protein dataset combined with the interaction data from several public databases (see Materials and Methods and Mclean Colin et al., 2016 for details). Spectral cluster analysis was performed on the network as described in Mclean Colin et al. (2016). Within the PSD network of 1,312 proteins, we identified 60 structural clusters based on the network topography. Essentially each cluster contains proteins that are more densely connected to other proteins within the cluster than to proteins elsewhere in the network (**Figure 4**).

Functional enrichment was tested for each of the clusters to assess structure/function relationships within the molecular network (the distribution of the proteins between the clusters and enrichment results are shown in Supplementary Table S4). We then mapped the p140Cap-interacting proteins onto the network and identified the clusters that are more strongly enriched for p140Cap-interacting proteins compared to a random distribution. We found 4 clusters with significant over-representation for p140Cap-interacting proteins: Cluster 7 (**Figure 4B**) (14/61, $P = 3.5E-02$), Cluster 17 (12/21,

$P = 3.62002E-06$), Cluster 22 (28/80, $P = 7.05E-07$), and Cluster 23 (13/39, $P = 1.4E-03$). Cluster 22 (**Figure 4D**) is overrepresented with GO BP "glutamate receptor signaling pathway," "endocytosis," "cell-cell signaling," and "synaptic transmission" terms and contains the main PSD scaffolding proteins of the MAGUK family and their interactors. This cluster was also significantly enriched with proteins from functional Module 1 (see **Figure 3**). Cluster 23 (**Figure 4E**), was found to be associated with GO BP term "cell junction assembly," and was enriched with proteins from Module 2 (see **Figure 3**). Cluster 7 (**Figure 4B**), was overrepresented with the "cytoskeleton organization," "actin cytoskeleton organization" and "cell junction assembly" terms and it contains proteins from Module 3 (**Figure 3**, Supplementary Table S4).

Co-expression Analysis of p140CAP Interactors

To assess whether the expression of p140Cap interacting proteins could also be co-regulated, we isolated the top significant 174 p140Cap-interacting proteins with an unequivocal Entrez
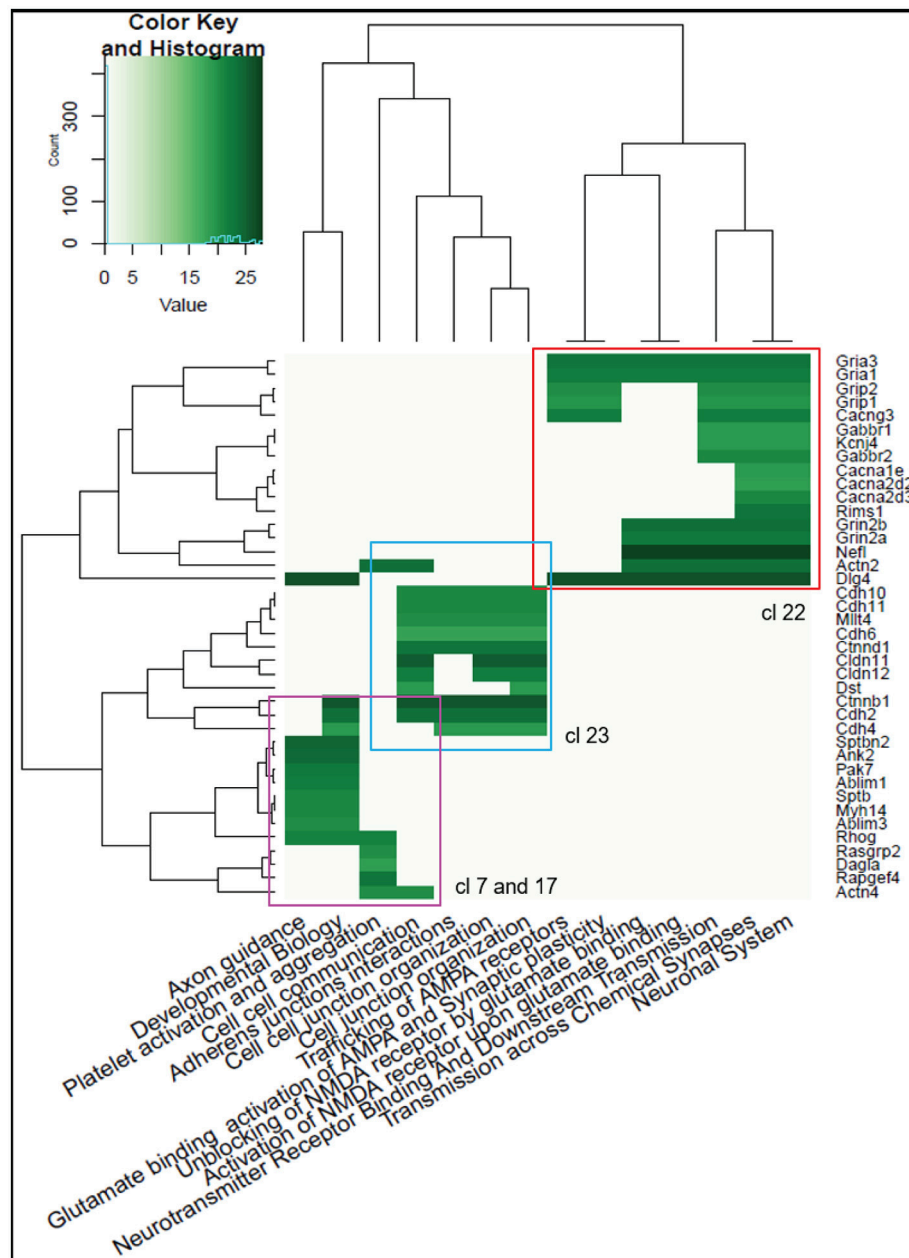
FIGURE 3 | Heatmap of the Reactome Pathway enrichment analysis clustering. Intensity is based on the average relative protein abundance in MS. Three main modules are observed: upper right, Module 1; center, Module 2; and, bottom left, Module 3.
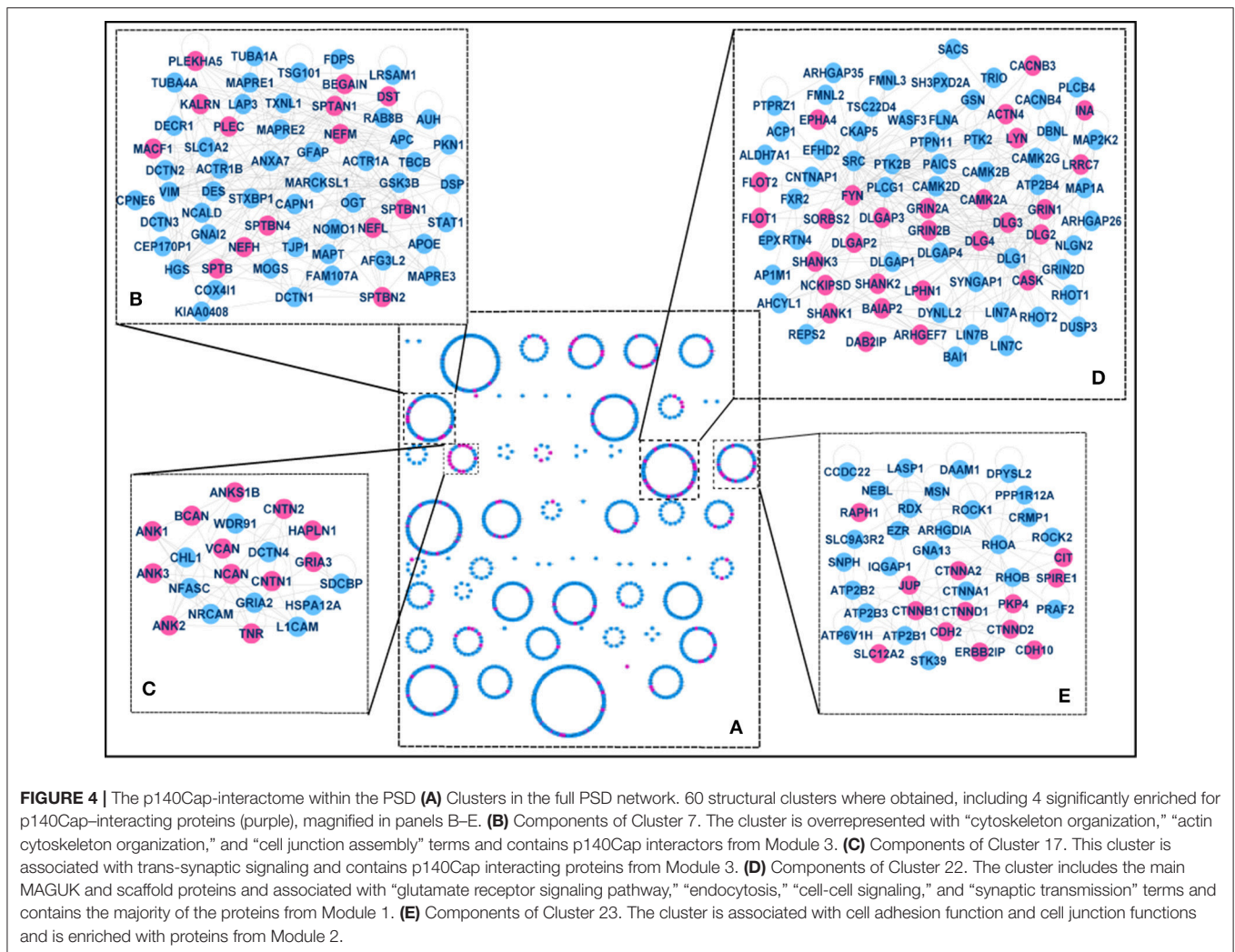
gene ID and tested their co-expression using 18 human-mouse conserved co-expression networks (CCNs) (Piro et al., 2011).

We found a statistically significant number of p140Cap interactors co-expressed with p140Cap in "All Samples," "Normal Tissues," "Brain," and "Central Nervous System" conserved co-expression networks (Supplementary Tables S5, S6). The co-expression across p140Cap interactors was also significant in six CCNs (Supplementary Table S7), including "All Samples," "Normal Tissues," "Brain," and "Central Nervous System" networks (Supplementary Table S8).

Overall, these data show that the network of p140Cap-interacting proteins also reflects a gene co-expression cluster (**Figure 5**), indicating that the components of the p140Cap interactome might undergo coordinated mechanisms of tissue-specific transcription control.

Disease Enrichment of p140Cap Related Proteins

Synaptic dysfunction has emerged as a common theme in neurological and psychiatric disorders, and recent large-scale genetic studies in ASD and schizophrenia (De Rubeis et al., 2014;

FIGURE 4 | The p140Cap-interactome within the PSD **(A)** Clusters in the full PSD network. 60 structural clusters where obtained, including 4 significantly enriched for p140Cap–interacting proteins (purple), magnified in panels B–E. **(B)** Components of Cluster 7. The cluster is overrepresented with "cytoskeleton organization," "actin cytoskeleton organization," and "cell junction assembly" terms and contains p140Cap interactors from Module 3. **(C)** Components of Cluster 17. This cluster is associated with trans-synaptic signaling and contains p140Cap interacting proteins from Module 3. **(D)** Components of Cluster 22. The cluster includes the main MAGUK and scaffold proteins and associated with "glutamate receptor signaling pathway," "endocytosis," "cell-cell signaling," and "synaptic transmission" terms and contains the majority of the proteins from Module 1. **(E)** Components of Cluster 23. The cluster is associated with cell adhesion function and cell junction functions and is enriched with proteins from Module 2.

Fromer et al., 2014) have further strengthened this hypothesis. The pathophysiological mechanisms might include abnormal expression of discrete synaptic proteins or the inability to organize into functional macromolecular complexes (Bayes et al., 2011). We investigated the disease enrichment of the genes encoding p140Cap interacting molecules (351 genes), using gene-disease annotation data collected from OMIM (http://omim.org/) and Ensembl variation (Chen et al., 2010) databases mapped onto the HDO tree using the topOnto package (https://github.com/statbio/topOnto). These analyses yielded a core background list of 14,111 gene-disease associations mapped onto 1,491 HDO terms. We also considered lists of risk genes and loci emerged from recent studies, including ASD (Sanders et al., 2015), epilepsy (EuroEPINOMIC-RES Consortium, 2014), Bipolar Disorder (Kataoka et al., 2016) and Schizophrenia (Fromer et al., 2014; Schizophrenia Working Group of the Psychiatric Genomics, 2014). The 826 gene-disease associations resulting from these analyses were then merged with the annotation set from the databases, yielding a total of 14,357 gene-disease associations mapped onto 1,491 HDO terms. Using the Topology-based Elimination Fisher method (Alexa et al., 2006),
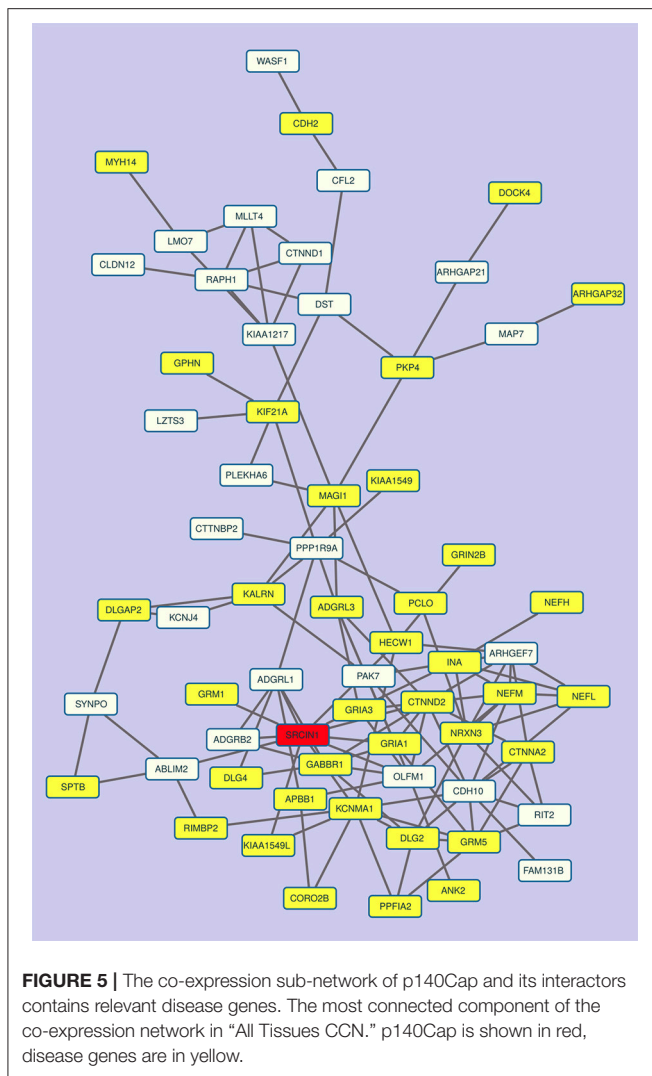
we found that the p140Cap dataset is significantly enriched for genes associated with schizophrenia ($P = 2.1E\text{-}9$), ASD ($P = 7.9E\text{-}6$), bipolar disorder ($P = 5.3E\text{-}5$), ID (1.1E-3), and epilepsy (1.7E-3) (**Table 1**, Supplementary Table S9).

Moreover, a further and independent evidence in supporting the role of p140Cap in neurological diseases came from the observation that the largest connected component of the sub-network of co-expression links of p140Cap-interactors among themselves and p140Cap in the All Tissues CCN contains several genes labeled as Disease Genes and involved in neurological diseases. These results indicate that p140Cap pathways, defined by both protein-protein interactions and gene co-expression data, are relevant to psychiatric and neurological disorders.

DISCUSSION

The structure and the combinatorial use of a handful of modulatory elements give rise to complexity at subcellular, cellular, and systems level at the synapse (Grant et al., 2016). The loss or modification of key synaptic proteins can directly

FIGURE 5 | The co-expression sub-network of p140Cap and its interactors contains relevant disease genes. The most connected component of the co-expression network in "All Tissues CCN." p140Cap is shown in red, disease genes are in yellow.

affect such network, ultimately impacting synaptic function. Our results allow to propose that the p140Cap adaptor molecule acts as a key hub of synaptic networks. Our work is the first comprehensive proteomic analysis of the synaptic interactome of p140Cap, which is indispensable for dendritic spine initiation and maturation and forms of hippocampal synaptic plasticity (Repetto et al., 2014). Our data show that the most prominent localization of p140Cap is within the PSD, with a significant enrichment for pathways related to receptors trafficking and chemical signaling through the synapse, cellular adhesion and junction, and axon guidance. We also provide evidence that the p140Cap interactome forms a gene co-expression module. Although p140Cap itself has not been implicated in brain disease yet, our results unveil a robust association of the p140Cap interactome with neurological and psychiatric disorders, including schizophrenia, ID, epilepsy and ASD.

Some of the p140Cap-interacting proteins associated to brain disorders have unknown functions in the brain. By mapping them to the synaptic p140Cap interactome, our study provides

functional cues on these disease genes, including *ROGDI, FRMD4A,* and *TRANK1.* Loss of *ROGDI,* encoding a protein with unknown function, causes Kohlschutter-Tonz syndrome (MIM 614574), which presents with psychomotor delay, early-onset intractable seizures, variable ID correlating with the severity of seizures, and amelogenesis imperfect (Schossig et al., 2012). Genetic disruption of *FRMD4A* causes a syndrome characterized by congenital microcephaly accompanied by agenesis of corpus callosum and/or partial hypoplasia of the vermis and cerebellum and ID (Fine et al., 2015) (MIM 616819). *FRMD4A* regulates cell polarity in non-neuronal cells (Ikenouchi and Umeda, 2010) and the microcephaly and brain malformations reported in carriers of *FRMD4A* mutations are compatible with defects in cell polarity in neuronal progenitors and/or newborn neurons. Beyond early brain development, our data also point to a synaptic function for *FRMD4A. TRANK1* is a GWAS-associated locus for both schizophrenia (Schizophrenia Working Group of the Psychiatric Genomics, 2014) and bipolar disorder (Chen et al., 2013; Muhleisen et al., 2014), but its functional roles in neurons are obscure. Again, our results locate it in the p140Cap synaptic network.

There is robust evidence supporting the hypothesis that synaptic dysfunction is a shared mechanism underlying a broad range of brain disorders, and our data further corroborate it. For example, alterations in glutamatergic transmission can result in a broad spectrum of psychiatric conditions. In our dataset, we detected AMPA and NMDA receptor subunits associated with schizophrenia (i.e., *GRIA1* and *GRIN2A*) and with a spectrum of DD/ID, ASD and seizures, often in co-morbidity (*GRIA3, GRIN1, GRIN2A,* and *GRIN2B*). Glutamatergic transmission is intertwined with synaptic calcium dynamics (Higley and Sabatini, 2012), and large-scale genetic studies have shown that disruption of voltage-gated calcium channels is a pathological mechanism across psychiatric disorders (Cross-Disorder Group of the Psychiatric Genomics, 2013). Notably, this pathway holds potential for rapid therapeutic intervention (Lencz and Malhotra, 2015). Seven VGCC subunits were found in the p140Cap interactome and four of them are associated to disease. *CACNA1A* haploinsufficiency can cause episodic ataxia type 2 (MIM 108500), familial hemiplegic migraine type 1 (MIM 141500) and spinocerebellar ataxia 6 (MIM 183086). More recently, *CACNA1A* mutations have been described in individuals diagnosed with ID, epilepsy, ADHD and/or ASD (Damaj et al., 2015). *CACNA2D1* and *CACNA2D2* are both associated with epilepsy and ID (Edvardson et al., 2013; Pippucci et al., 2013; Vergult et al., 2015), while *CACN2D3* has been recently implicated in ASD (De Rubeis et al., 2014). Interestingly, none of the reproducible GWAS-associated loci in schizophrenia *CACNA1C, CACNA1H,* and *CACNB2* (Schizophrenia Working Group of the Psychiatric Genomics, 2014) was detected in our dataset. However, several RIM proteins that are necessary for VGCCs regulation, including the schizophrenia-associated *RIMS1* (Schizophrenia Working Group of the Psychiatric Genomics, 2014), are detected in the p140Cap interactome.

Psychiatric manifestations are often accompanied by defects in neuronal morphogenesis, and abnormalities of dendritic spines (either the number or the shape), which are one of

TABLE 1 | Disease enrichment of p140Cap related proteins.

TERM.ID	Term	Annotated	Significant	Expected	classicFisher	elimFisher
DOID:5419	Schizophrenia	1600	65	30.54	2.1E-09	2.1E-09
DOID:12849	ASD	338	20	6.45	7.9E-06	7.9E-06
DOID:3312	Bipolar disorder	981	37	18.72	5.3E-05	5.3E-05
DOID:1059	Intellectual disability	490	20	9.35	1.18E-03	1.18E-03
DOID:1826	Epilepsy	331	15	6.32	1.78E-03	1.78E-03

The table shows the 5 top terms for the TopGo disease enrichment with results from Fisher and elimFisher tests. The agreement among the orders of magnitude for both methods indicates the strong over-representation of respective disease genes among the p140Cap interacting proteins.

the most robust neuroanatomical correlate of ID and often a finding in ASD and schizophrenia (Penzes et al., 2011). p140Cap and many of its interactors play a role in the formation, maturation and maintenance of dendritic spines. Specifically, deficiency of p140Cap results in an excess of immature filopodial-like protrusions at the expenses of mature mushroom spines (Tomasoni et al., 2013; Repetto et al., 2014). Depletion, ablation or mutations of many p140Cap interactors, including *CNKSR2* (CNK2) (Lim et al., 2014), *CTNNB1* (β-catenin) (Okuda et al., 2007), *CTNND2* (δ-catenin) (Arikkath et al., 2009), phenocopy these defects. Conversely, other p140Cap-associated proteins are needed for spine maintenance and their silencing results in reduced spine density and/or spine shrinkage, as documented for CASK (Chao et al., 2008) and ANK3 (Smith et al., 2014). All these genes are associated with psychiatric conditions, ranging from ID i.e., *CNKSR2* (Kessels and Malinow, 2009; Vaags et al., 2014), *CTNNB1* (Tucci et al., 2014), *ANK3* (Iqbal et al., 2013), *CASK* (Tarpey et al., 2009) and ASD i.e., *CTNND2* (Turner et al., 2015), *ANK3* (Iqbal et al., 2013) to schizophrenia i.e., *CNKSR2* (GWAS, PGC-SCZ 2014) and bipolar disorder ANK3 (Ferreira et al., 2008).

Similarly, the impairment in LTP and LTD and the deficits in memory and learning observed in the p140Cap KO mice (Repetto et al., 2014) could be sustained by improper functioning and/or localisation of several of these newly identified p140Cap interactors, such as the NMDARs subunits, the AMPA receptors, PSD-95, and the Shank family. *GRIN1*, *GRIN2A*, and *GRIN2B* are key in LTP induction, synaptic plasticity, learning and memory (Bliss and Collingridge, 1993; Bliss et al., 2014; Shipton and Paulsen, 2014). Synaptic trafficking of AMPARs is necessary for the induction of LTP, and GluR1-deficient mice exhibit impaired hippocampus-dependent spatial working memory and one-trial spatial memory (Kessels and Malinow, 2009). In mice lacking PSD-95, NMDA-dependent LTP and LTD frequency is shifted to enhanced LTP, consistent with severely impaired spatial learning (Migaud et al., 1998). Mice mutant for Shank proteins exhibit a large spectrum of defects in LTP and LTD (Yoo et al., 2014). Identifying the molecular complexes controlling forms of plasticity that underlie memory consolidation and retrieval has direct implications for ID and associated co-morbidities, including ASD and ADHD. It is also important for psychiatric disorders with a cognitive impairment component and/or with a premorbid cognitive deficit, as documented in schizophrenia (Reichenberg et al., 2010).

As mentioned above, *SRCIN1* has not been genetically associated with psychiatric disorders. A *de novo* missense variant resulting in a p.Glu912Asp change predicted to be probably damaging by the bioinformatic predictor Polyphen-2 and not detected in the 60,706 unrelated controls of the Exome Aggregation Database (ExAC) was found in a schizophrenia cohort (Fromer et al., 2014). Further, based on the data in ExAC, *SRCIN1* is significantly depleted in both loss-of-function and missense variants, indicating that the gene is highly intolerant to detrimental variation and so likely a source of disease risk if mutated.

In conclusion, our findings place p140Cap at the crossroad of a highly susceptible synaptic network disrupted in psychiatric and neurological disorders. These findings reinforce the current hypothesis that synaptic dysfunction is a component of all these disorders and have repercussions on our understanding of the underpinnings of psychiatric disorders and their shared comorbidity.

ETHICS STATEMENT

This study was carried out in accordance with the recommendations of Italian Ministry of Health. The protocol was approved by the Their Commitee with the number 49/2014-PR.

AUTHOR CONTRIBUTIONS

AAl, CA, IR, and AM, design, collection and assembly of data, data analysis and interpretation; AAd, YC, and EB collection and analysis of MS data; OS, JA, CM, UA, SD, JB, and AB data analysis and interpretation; AAl, OS, JA, SD, EM. MM, ET, and PD design, interpretation of the data and manuscript writing. All the authors contributed to draft the work or revise it critically for important intellectual content. All the authors gave a final approval of the version to be published. All the authors agree be accountable for all aspects of the work in ensuring that questions related to the accuracy or integrity of any part of the work are appropriately investigated and resolved.

FUNDING

ACKNOWLEDGMENTS

SUPPLEMENTARY MATERIAL

The Supplementary Material for this article can be found online at: http://journal.frontiersin.org/article/10.3389/fnmol.2017.00212/full#supplementary-material

REFERENCES

Alexa, A., Rahnenfuhrer, J., and Lengauer, T. (2006). Improved scoring of functional groups from gene expression data by decorrelating GO graph structure. *Bioinformatics* 22, 1600–1607. doi: 10.1093/bioinformatics/btl140

Arikkath, J., Peng, I. F., Ng, Y. G., Israely, I., Liu, X., Ullian, E. M., et al. (2009). Delta-catenin regulates spine and synapse morphogenesis and function in hippocampal neurons during development. *J. Neurosci.* 29, 5435–5442. doi: 10.1523/JNEUROSCI.0835-09.2009

Aronson, A. R., and Lang, F. M. (2010). An overview of MetaMap: historical perspective and recent advances. *J. Am. Med. Inform. Assoc.* 17, 229–236. doi: 10.1136/jamia.2009.002733

Bayes, A., Collins, M. O., Galtrey, C. M., Simonnet, C., Roy, M., Croning, M. D., et al. (2014). Human post-mortem synapse proteome integrity screening for proteomic studies of postsynaptic complexes. *Mol. Brain* 7:88. doi: 10.1186/s13041-014-0088-4

Bayes, A., van de Lagemaat, L. N., Collins, M. O., Croning, M. D., Whittle, I. R., Choudhary, J. S., et al. (2011). Characterization of the proteome, diseases and evolution of the human postsynaptic density. *Nat. Neurosci.* 14, 19–21. doi: 10.1038/nn.2719

Berto, G., Camera, P., Fusco, C., Imarisio, S., Ambrogio, C., Chiarle, R., et al. (2007). The Down syndrome critical region protein TTC3 inhibits neuronal differentiation via RhoA and Citron kinase. *J. Cell Sci.* 120(Pt 11), 1859–1867. doi: 10.1242/jcs.000703

Betancur, C., and Buxbaum, J. D. (2013). SHANK3 haploinsufficiency: a "common" but underdiagnosed highly penetrant monogenic cause of autism spectrum disorders. *Mol. Autism* 4:17. doi: 10.1186/2040-2392-4-17

Bliss, T. V., and Collingridge, G. L. (1993). A synaptic model of memory: long-term potentiation in the hippocampus. *Nature* 361, 31–39. doi: 10.1038/361031a0

Bliss, T. V., Collingridge, G. L., and Morris, R. G. (2014). Synaptic plasticity in health and disease: introduction and overview. *Philos. Trans. R. Soc. Lond. B Biol. Sci.* 369:20130129. doi: 10.1098/rstb.2013.0129

Boyken, J., Gronborg, M., Riedel, D., Urlaub, H., Jahn, R., and Chua, J. J. (2013). Molecular profiling of synaptic vesicle docking sites reveals novel proteins but few differences between glutamatergic and GABAergic synapses. *Neuron* 78, 285–297. doi: 10.1016/j.neuron.2013.02.027

Brinkmalm, A., Brinkmalm, G., Honer, W. G., Moreno, J. A., Jakobsson, J., Mallucci, G. R., et al. (2014). Targeting synaptic pathology with a novel affinity mass spectrometry approach. *Mol. Cell. Proteomics* 13, 2584–2592. doi: 10.1074/mcp.M114.040113

Chao, H. W., Hong, C. J., Huang, T. N., Lin, Y. L., and Hsueh, Y. P. (2008). SUMOylation of the MAGUK protein CASK regulates dendritic spinogenesis. *J. Cell Biol.* 182, 141–155. doi: 10.1083/jcb.200712094

Chassefeyre, R., Martinez-Hernandez, J., Bertaso, F., Bouquier, N., Blot, B., Laporte, M., et al. (2018). Regulation of postsynaptic function by the dementia-related ESCRT-III subunit CHMP2B. *J. Neurosci.* 35, 3155–3173. doi: 10.1523/JNEUROSCI.0586-14.2015

Chatr-Aryamontri, A., Breitkreutz, B. J., Oughtred, R., Boucher, L., Heinicke, S., Chen, D., et al. (2015). The BioGRID interaction database: 2015 update. *Nucleic Acids Res.* 43:D470-8. doi: 10.1093/nar/gku1204

Chen, D. T., Jiang, X., Akula, N., Shugart, Y. Y., Wendland, J. R., Steele, C. J., et al. (2013). Genome-wide association study meta-analysis of European and Asian-ancestry samples identifies three novel loci associated with bipolar disorder. *Mol. Psychiatry* 18, 195–205. doi: 10.1038/mp.2011.157

Chen, Y., Cunningham, F., Rios, D., McLaren, W. M., Smith, J., Pritchard, B., et al. (2010). Ensembl variation resources. *BMC Genomics* 11:293. doi: 10.1186/1471-2164-11-293

Chin, L. S., Nugent, R. D., Raynor, M. C., Vavalle, J. P., and Li, L. (2000). SNIP, a novel SNAP-25-interacting protein implicated in regulated exocytosis. *J. Biol. Chem.* 275, 1191–200. doi: 10.1074/jbc.275.2.1191

Cox, J., and Mann, M. (2008). MaxQuant enables high peptide identification rates, individualized p.p.b.-range mass accuracies and proteome-wide protein quantification. *Nat. Biotechnol.* 26, 1367–1372. doi: 10.1038/nbt.1511

Cross-Disorder Group of the Psychiatric Genomics, C. (2013). Identification of risk loci with shared effects on five major psychiatric disorders: a genome-wide analysis. *Lancet* 381, 1371–1379. doi: 10.1016/S0140-6736(12)62129-1

Damaj, L., Lupien-Meilleur, A., Lortie, A., Riou, E., Ospina, L. H., Gagnon, L., et al. (2015). CACNA1A haploinsufficiency causes cognitive impairment, autism and epileptic encephalopathy with mild cerebellar symptoms. *Eur. J. Hum. Genet.* 23, 1505–1512. doi: 10.1038/ejhg.2015.21

Damez-Werno, D. M., Sun, H., Scobie, K. N., Shao, N., Rabkin, J., Dias, C., et al. (2016). Histone arginine methylation in cocaine action in the nucleus accumbens. *Proc. Natl. Acad. Sci. U.S.A.* 113, 9623–9628. doi: 10.1073/pnas.1605045113

Deciphering Developmental Disorders, S. (2015). Large-scale discovery of novel genetic causes of developmental disorders. *Nature* 519, 223–228. doi: 10.1038/nature14135

De Rubeis, S., He, X., Goldberg, A. P., Poultney, C. S., Samocha, K., Cicek, A. E., et al. (2014). Synaptic, transcriptional and chromatin genes disrupted in autism. *Nature* 515, 209–215. doi: 10.1038/nature13772

Di Stefano, P., Cabodi, S., Boeri Erba, E., Margaria, V., Bergatto, E., Giuffrida, M. G., et al. (2004). P130Cas-associated protein (p140Cap) as a new tyrosine-phosphorylated protein involved in cell spreading. *Mol. Biol. Cell* 15, 787–800. doi: 10.1091/mbc.E03-09-0689

Di Stefano, P., Damiano, L., Cabodi, S., Aramu, S., Tordella, L., Praduroux, A., et al. (2007). p140Cap protein suppresses tumour cell properties, regulating Csk and Src kinase activity. *EMBO J.* 26, 2843–2855. doi: 10.1038/sj.emboj.7601724

Dosemeci, A., Makusky, A. J., Jankowska-Stephens, E., Yang, X., Slotta, D. J., and Markey, S. P. (2007). Composition of the synaptic PSD-95 complex. *Mol. Cell. Proteomics* 6, 1749–1760. doi: 10.1074/mcp.M700040-MCP200

Edvardson, S., Oz, S., Abulhijaa, F. A., Taher, F. B., Shaag, A., Zenvirt, S., et al. (2013). Early infantile epileptic encephalopathy associated with a high voltage gated calcium channelopathy. *J. Med. Genet.* 50, 118–123. doi: 10.1136/jmedgenet-2012-101223

Endele, S., Rosenberger, G., Geider, K., Popp, B., Tamer, C., Stefanova, I., et al. (2010). Mutations in GRIN2A and GRIN2B encoding regulatory subunits of NMDA receptors cause variable neurodevelopmental phenotypes. *Nat. Genet.* 42, 1021–1026. doi: 10.1038/ng.677

Farr, C. D., Gafken, P. R., Norbeck, A. D., Doneanu, C. E., Stapels, M. D., Barofsky, D. F., et al. (2004). Proteomic analysis of native metabotropic glutamate receptor 5 protein complexes reveals novel molecular constituents. *J. Neurochem.* 91, 438–450. doi: 10.1111/j.1471-4159.2004.02735.x

Ferreira, M. A., O'Donovan, M. C., Meng, Y. A., Jones, I. R., Ruderfer, D. M., Jones, L., et al. (2008). Collaborative genome-wide association analysis supports a role for ANK3 and CACNA1C in bipolar disorder. *Nat. Genet.* 40, 1056–1058. doi: 10.1038/ng.209

Fine, D., Flusser, H., Markus, B., Shorer, Z., Gradstein, L., Khateeb, S., et al. (2015). A syndrome of congenital microcephaly, intellectual disability and dysmorphism with a homozygous mutation in FRMD4A. *Eur. J. Hum. Genet.* 23, 1729–1734. doi: 10.1038/ejhg.2014.241

Fossati, G., Morini, R., Corradini, I., Antonucci, F., Trepte, P., Edry, E., et al. (2015). Reduced SNAP-25 increases PSD-95 mobility and impairs spine morphogenesis. *Cell Death Differ.* 22, 1425–1436. doi: 10.1038/cdd.2014.227

Frei, J. A., and Stoeckli, E. T. (2016). SynCAMs-From axon guidance to neurodevelopmental disorders. *Mol. Cell. Neurosci.* 81, 41–48. doi: 10.1016/j.mcn.2016.08.012

Fromer, M., Pocklington, A. J., Kavanagh, D. H., Williams, H. J., Dwyer, S., Gormley, P., et al. (2014). *De novo* mutations in schizophrenia implicate synaptic networks. *Nature* 506, 179–184. doi: 10.1038/nature12929

Gallone, G., Simpson, T. I., Armstrong, J. D., and Jarman, A. P. (2011). Bio::Homology::InterologWalk–a Perl module to build putative protein-protein interaction networks through interolog mapping. *BMC Bioinform.* 12:289. doi: 10.1186/1471-2105-12-289

Gorini, G., Ponomareva, O., Shores, K. S., Person, M. D., Harris, R. A., and Mayfield, R. D. (2010). Dynamin-1 co-associates with native mouse brain BKCa channels: proteomics analysis of synaptic protein complexes. *FEBS Lett.* 584, 845–851. doi: 10.1016/j.febslet.2009.12.061

Grant, S. G. (2012). Synaptopathies: diseases of the synaptome. *Curr. Opin. Neurobiol.* 22, 522–529. doi: 10.1016/j.conb.2012.02.002

Grant, S. G., Bagni, C., and O'Dell, T. J. (2016). Synaptopathy–from biology to therapy. *Neuropharmacology* 100:1. doi: 10.1016/j.neuropharm.2015.08.022

Gronborg, M., Pavlos, N. J., Brunk, I., Chua, J. J., Munster-Wandowski, A., Riedel, D., et al. (2010). Quantitative comparison of glutamatergic and GABAergic synaptic vesicles unveils selectivity for few proteins including MAL2, a novel synaptic vesicle protein. *J. Neurosci.* 30, 2–12. doi: 10.1523/JNEUROSCI.4074-09.2010

Hamdan, F. F., Gauthier, J., Spiegelman, D., Noreau, A., Yang, Y., Pellerin, S., et al. (2009). Mutations in SYNGAP1 in autosomal nonsyndromic mental retardation. *N. Engl. J. Med.* 360, 599–605. doi: 10.1056/NEJMoa0805392

Higley, M. J., and Sabatini, B. L. (2012). Calcium signaling in dendritic spines. *Cold Spring Harb. Perspect. Biol.* 4:a005686. doi: 10.1101/cshperspect.a005686

Ikenouchi, J., and Umeda, M. (2010). FRMD4A regulates epithelial polarity by connecting Arf6 activation with the PAR complex. *Proc. Natl. Acad. Sci. U.S.A.* 107, 748–753. doi: 10.1073/pnas.0908423107

Iqbal, Z., Vandeweyer, G., van der Voet, M., Waryah, A. M., Zahoor, M. Y., Besseling, J. A., et al. (2013). Homozygous and heterozygous disruptions of ANK3: at the crossroads of neurodevelopmental and psychiatric disorders. *Hum. Mol. Genet.* 22, 1960–1970. doi: 10.1093/hmg/ddt043

Ito, H., Atsuzawa, K., Sudo, K., Di Stefano, P., Iwamoto, I., Morishita, R., et al. (2008). Characterization of a multidomain adaptor protein, p140Cap, as part of a pre-synaptic complex. *J. Neurochem.* 107, 61–72. doi: 10.1111/j.1471-4159.2008.05585.x

Jaworski, J., Kapitein, L. C., Gouveia, S. M., Dortland, B. R., Wulf, P. S., Grigoriev, I., et al. (2009). Dynamic microtubules regulate dendritic spine morphology and synaptic plasticity. *Neuron* 61, 85–100. doi: 10.1016/j.neuron.2008.11.013

Kataoka, M., Matoba, N., Sawada, T., Kazuno, A. A., Ishiwata, M., Fujii, K., et al. (2016). Exome sequencing for bipolar disorder points to roles of *de novo* loss-of-function and protein-altering mutations. *Mol. Psychiatry* 21, 885–893. doi: 10.1038/mp.2016.69

Kerrien, S., Aranda, B., Breuza, L., Bridge, A., Broackes-Carter, F., Chen, C., et al. (2012). The IntAct molecular interaction database in 2012. *Nucleic Acids Res.* 40, D841-6. doi: 10.1093/nar/gkr1088

Kessels, H. W., and Malinow, R. (2009). Synaptic AMPA receptor plasticity and behavior. *Neuron* 61, 340–350. doi: 10.1016/j.neuron.2009.01.015

Kim, H. G., Kishikawa, S., Higgins, A. W., Seong, I. S., Donovan, D. J., Shen, Y., et al. (2008). Disruption of neurexin 1 associated with autism spectrum disorder. *Am. J. Hum. Genet.* 82, 199–207. doi: 10.1016/j.ajhg.2007.09.011

Lencz, T., and Malhotra, A. K. (2015). Targeting the schizophrenia genome: a fast track strategy from GWAS to clinic. *Mol. Psychiatry* 20, 820–826. doi: 10.1038/mp.2015.28

Lim, J., Ritt, D. A., Zhou, M., and Morrison, D. K. (2014). The CNK2 scaffold interacts with vilse and modulates Rac cycling during spine morphogenesis in hippocampal neurons. *Curr. Biol.* 24, 786–792. doi: 10.1016/j.cub.2014.02.036

Luscher, C., and Malenka, R. C. (2012). NMDA receptor-dependent long-term potentiation and long-term depression (LTP/LTD). *Cold Spring Harb. Perspect. Biol.* 4:a005710. doi: 10.1101/cshperspect.a005710

Manabe, T., Togashi, H., Uchida, N., Suzuki, S. C., Hayakawa, Y., Yamamoto, M., et al. (2000). Loss of cadherin-11 adhesion receptor enhances plastic changes in hippocampal synapses and modifies behavioral responses. *Mol. Cell. Neurosci.* 15, 534–546. doi: 10.1006/mcne.2000.0849

Martinez-Quiles, N., Ho, H. Y., Kirschner, M. W., Ramesh, N., and Geha, R. S. (2004). Erk/Src phosphorylation of cortactin acts as a switch on-switch off mechanism that controls its ability to activate N-WASP. *Mol. Cell. Biol.* 24, 5269–5280. doi: 10.1128/MCB.24.12.5269-5280.2004

Mclean, C., He, X., Simpson, I. T., and Armstrong, J. D. (2016). Improved functional enrichment analysis of biological networks using scalable modularity based clustering. *J. Proteomics Bioinform.* 9, 009–018. doi: 10.4172/jpb.1000383

Migaud, M., Charlesworth, P., Dempster, M., Webster, L. C., Watabe, A. M., Makhinson, M., et al. (1998). Enhanced long-term potentiation and impaired learning in mice with mutant postsynaptic density-95 protein. *Nature* 396, 433–439. doi: 10.1038/24790

Morciano, M., Beckhaus, T., Karas, M., Zimmermann, H., and Volknandt, W. (2009). The proteome of the presynaptic active zone: from docked synaptic vesicles to adhesion molecules and maxi-channels. *J. Neurochem.* 108, 662–675. doi: 10.1111/j.1471-4159.2008.05824.x

Morciano, M., Burre, J., Corvey, C., Karas, M., Zimmermann, H., and Volknandt, W. (2005). Immunoisolation of two synaptic vesicle pools from synaptosomes: a proteomics analysis. *J. Neurochem.* 95, 1732–1745. doi: 10.1111/j.1471-4159.2005.03506.x

Muhleisen, T. W., Leber, M., Schulze, T. G., Strohmaier, J., Degenhardt, F., Treutlein, J., et al. (2014). Genome-wide association study reveals two new risk loci for bipolar disorder. *Nat. Commun.* 5:3339. doi: 10.1038/ncomms4339

Musen, M. A., Noy, N. F., Shah, N. H., Whetzel, P. L., Chute, C. G., Story, M. A., et al. (2012). The national center for biomedical ontology. *J. Am. Med. Inform. Assoc.* 19, 190–195. doi: 10.1136/amiajnl-2011-000523

Newman, M. E. (2006). Finding community structure in networks using the eigenvectors of matrices. *Phys. Rev. E Stat. Nonlin. Soft Matter Phys.* 74(3 Pt 2):036104. doi: 10.1103/PhysRevE.74.036104

Okuda, T., Yu, L. M., Cingolani, L. A., Kemler, R., and Goda, Y. (2007). beta-Catenin regulates excitatory postsynaptic strength at hippocampal synapses. *Proc. Natl. Acad. Sci. U.S.A.* 104, 13479–13484. doi: 10.1073/pnas.0702334104

Penzes, P., Cahill, M. E., Jones, K. A., VanLeeuwen, J. E., and Woolfrey, K. M. (2011). Dendritic spine pathology in neuropsychiatric disorders. *Nat. Neurosci.* 14, 285–293. doi: 10.1038/nn.2741

Pippucci, T., Parmeggiani, A., Palombo, F., Maresca, A., Angius, A., Crisponi, L., et al. (2013). A novel null homozygous mutation confirms CACNA2D2 as a gene mutated in epileptic encephalopathy. *PLoS ONE* 8:e82154. doi: 10.1371/journal.pone.0082154

Piro, R. M., Ala, U., Molineris, I., Grassi, E., Bracco, C., Perego, G. P., et al. (2011). An atlas of tissue-specific conserved coexpression for functional annotation and disease gene prediction. *Eur. J. Hum. Genet.* 19, 1173–1180. doi: 10.1038/ejhg.2011.96

Rauch, A., Wieczorek, D., Graf, E., Wieland, T., Endele, S., Schwarzmayr, T., et al. (2012). Range of genetic mutations associated with severe non-syndromic sporadic intellectual disability: an exome sequencing study. *Lancet* 380, 1674–1682. doi: 10.1016/S0140-6736(12)61480-9

Reichenberg, A., Caspi, A., Harrington, H., Houts, R., Keefe, R. S., Murray, R. M., et al. (2010). Static and dynamic cognitive deficits in childhood preceding adult schizophrenia: a 30-year study. *Am. J. Psychiatry* 167, 160–169. doi: 10.1176/appi.ajp.2009.09040574

Repetto, D., Aramu, S., Boeri Erba, E., Sharma, N., Grasso, S., Russo, I., et al. (2013). Mapping of p140Cap phosphorylation sites: the EPLYA and EGLYA motifs have a key role in tyrosine phosphorylation and Csk binding, and are substrates of the Abl kinase. *PLoS ONE* 8:e54931. doi: 10.1371/journal.pone.0054931

Repetto, D., Camera, P., Melani, R., Morello, N., Russo, I., Calcagno, E., et al. (2014). p140Cap regulates memory and synaptic plasticity through Src-mediated and citron-N-mediated actin reorganization. *J. Neurosci.* 34, 1542–1553. doi: 10.1523/JNEUROSCI.2341-13.2014

Robison, A. J. (2014). Emerging role of CaMKII in neuropsychiatric disease. *Trends Neurosci.* 37, 653–662. doi: 10.1016/j.tins.2014.07.001

Sanders, S. J., He, X., Willsey, A. J., Ercan-Sencicek, A. G., Samocha, K. E., Cicek, A. E., et al. (2015). Insights into autism spectrum disorder genomic architecture and biology from 71 Risk Loci. *Neuron* 87, 1215–1233. doi: 10.1016/j.neuron.2015.09.016

Schaefer, M. H., Fontaine, J. F., Vinayagam, A., Porras, P., Wanker, E. E., and Andrade-Navarro, M. A. (2012). HIPPIE: integrating protein interaction networks with experiment based quality scores. *PLoS ONE* 7:e31826. doi: 10.1371/journal.pone.0031826

Schizophrenia Working Group of the Psychiatric Genomics, C. (2014). Biological insights from 108 schizophrenia-associated genetic loci. *Nature* 511, 421–427. doi: 10.1038/nature13595

Schossig, A., Wolf, N. I., Fischer, C., Fischer, M., Stocker, G., Pabinger, S., et al. (2012). Mutations in ROGDI cause kohlschutter-tonz syndrome. *Am. J. Hum. Genet.* 90, 701–707. doi: 10.1016/j.ajhg.2012.02.012

Schriml, L. M., Arze, C., Nadendla, S., Chang, Y. W., Mazaitis, M., Felix, V., et al. (2012). Disease Ontology: a backbone for disease semantic integration. *Nucleic Acids Res.* 40, D940-6. doi: 10.1093/nar/gkr972

Schwanhausser, B., Busse, D., Li, N., Dittmar, G., Schuchhardt, J., Wolf, J., et al. (2011). Global quantification of mammalian gene expression control. *Nature* 473, 337–342. doi: 10.1038/nature10098

Shipton, O. A., and Paulsen, O. (2014). GluN2A and GluN2B subunit-containing NMDA receptors in hippocampal plasticity. *Philos. Trans. R. Soc. Lond. B Biol. Sci.* 369, 20130163. doi: 10.1098/rstb.2013.0163

Simpson, T. I., Armstrong, J. D., and Jarman, A. P. (2010). Merged consensus clustering to assess and improve class discovery with microarray data. *BMC Bioinform.* 11:590. doi: 10.1186/1471-2105-11-590

Smith, K. R., Kopeikina, K. J., Fawcett-Patel, J. M., Leaderbrand, K., Gao, R., Schurmann, B., et al. (2014). Psychiatric risk factor ANK3/ankyrin-G nanodomains regulate the structure and function of glutamatergic synapses. *Neuron* 84, 399–415. doi: 10.1016/j.neuron.2014.10.010

Sweatt, J. D. (2016). Neural plasticity and behavior-sixty years of conceptual advances. *J. Neurochem.* 139(Suppl. 2), 179–199. doi: 10.1111/jnc.13580

Tarpey, P. S., Smith, R., Pleasance, E., Whibley, A., Edkins, S., Hardy, C., et al. (2009). A systematic, large-scale resequencing screen of X-chromosome coding exons in mental retardation. *Nat. Genet.* 41, 535–543. doi: 10.1038/ng.367

Tomasoni, R., Repetto, D., Morini, R., Elia, C., Gardoni, F., Di Luca, M., et al. (2013). SNAP-25 regulates spine formation through postsynaptic binding to p140Cap. *Nat. Commun.* 4:2136. doi: 10.1038/ncomms3136

Tucci, V., Kleefstra, T., Hardy, A., Heise, I., Maggi, S., Willemsen, M. H., et al. (2014). Dominant beta-catenin mutations cause intellectual disability with recognizable syndromic features. *J. Clin. Invest.* 124, 1468–1482. doi: 10.1172/JCI70372

Turner, T. N., Sharma, K., Oh, E. C., Liu, Y. P., Collins, R. L., Sosa, M. X., et al. (2015). Loss of delta-catenin function in severe autism. *Nature* 520, 51–56. doi: 10.1038/nature14186

Uruno, T., Liu, J., Zhang, P., Fan, Y., Egile, C., Li, R., et al. (2001). Activation of Arp2/3 complex-mediated actin polymerization by cortactin. *Nat. Cell Biol.* 3, 259–266. doi: 10.1038/35060051

Vaags, A. K., Bowdin, S., Smith, M. L., Gilbert-Dussardier, B., Brocke-Holmefjord, K. S., Sinopoli, K., et al. (2014). Absent CNKSR2 causes seizures and intellectual, attention, and language deficits. *Ann. Neurol.* 76, 758–764. doi: 10.1002/ana.24274

Vergult, S., Dheedene, A., Meurs, A., Faes, F., Isidor, B., Janssens, S., et al. (2015). Genomic aberrations of the CACNA2D1 gene in three patients with epilepsy and intellectual disability. *Eur. J. Hum. Genet.* 23, 628–632. doi: 10.1038/ejhg.2014.141

Vizcaino, J. A., Csordas, A., del-Toro, N., Dianes, J. A., Griss, J., Lavidas, I., et al. (2016). 2016 update of the PRIDE database and its related tools. *Nucleic Acids Res.* 44, D447–D456. doi: 10.1093/nar/gkv1145

Weingarten, J., Lassek, M., Mueller, B. F., Rohmer, M., Lunger, I., Baeumlisberger, D., et al. (2014). The proteome of the presynaptic active zone from mouse brain. *Mol. Cell. Neurosci.* 59, 106–118. doi: 10.1016/j.mcn.2014.02.003

Whetzel, P. L., Noy, N. F., Shah, N. H., Alexander, P. R., Nyulas, C., Tudorache, T., et al. (2011). BioPortal: enhanced functionality via new web services from the national center for biomedical ontology to access and use ontologies in software applications. *Nucleic Acids Res.* 39, W541–W545. doi: 10.1093/nar/gkr469

Wilhelm, B. G., Mandad, S., Truckenbrodt, S., Krohnert, K., Schafer, C., Rammner, B., et al. (2014). Composition of isolated synaptic boutons reveals the amounts of vesicle trafficking proteins. *Science* 344, 1023–1028. doi: 10.1126/science.1252884

Yang, Y., Wei, M., Xiong, Y., Du, X., Zhu, S., Yang, L., et al. (2015). Endophilin A1 regulates dendritic spine morphogenesis and stability through interaction with p140Cap. *Cell Res.* 25, 496–516. doi: 10.1038/cr.2015.31

Yoo, J., Bakes, J., Bradley, C., Collingridge, G. L., and Kaang, B. K. (2014). Shank mutant mice as an animal model of autism. *Philos. Trans. R. Soc. Lond. B Biol. Sci.* 369:20130143. doi: 10.1098/rstb.2013.0143

Yu, G., Wang, L. G., Han, Y., and He, Q. Y. (2012). clusterProfiler: an R package for comparing biological themes among gene clusters. *Omics* 16, 284–287. doi: 10.1089/omi.2011.0118

CrossMark

ARTICLE

Human mesenchymal stem cells and derived extracellular vesicles induce regulatory dendritic cells in type 1 diabetic patients

Enrica Favaro[1] · Andrea Carpanetto[1] · Cristiana Caorsi[2] · Mirella Giovarelli[3] ·
Costanza Angelini[3] · Paolo Cavallo-Perin[1] · Ciro Tetta[4,5] · Giovanni Camussi[1] ·
Maria M. Zanone[1]

Abstract

Aims/hypothesis Mesenchymal stem cells (MSCs) can exert an immunosuppressive effect on any component of the immune system, including dendritic cells (DCs), by direct contact, the release of soluble markers and extracellular vesicles (EVs). We evaluated whether MSCs and MSC-derived EVs have an immunomodulatory effect on monocyte-derived DCs in type 1 diabetes.

Methods Bone marrow derived MSCs were characterised and EVs were obtained by ultracentrifugation. DCs were differentiated from CD14$^+$ cells, obtained from nine type 1 diabetic patients at disease onset, pulsed with antigen GAD65 and cultured with MSCs or EVs. Levels of DC maturation and activation markers were evaluated by flow cytometry. GAD65-pulsed DCs and autologous CD14$^-$ cell were co-cultured and IFN-γ enzyme-linked immunosorbent spot responses were assayed. Secreted cytokine levels were measured and Th17 and regulatory T cells were analysed.

Results MSC- and EV-conditioned DCs acquired an immature phenotype with reduced levels of activation markers and increased IL-10 and IL-6 production. Conditioned DC plus T cell co-cultures showed significantly decreased IFN-γ spots and secretion levels. Moreover, higher levels of TGF-β, IL-10 and IL-6 were detected compared with unconditioned DC plus T cell co-cultures. Conditioned DCs decreased Th17 cell numbers and IL-17 levels, and increased FOXP3$^+$ regulatory T cell numbers. EVs were internalised by DCs and EV-conditioned DCs exhibited a similar effect.

Conclusions/interpretation In type 1 diabetes, MSCs induce immature IL-10-secreting DCs in vitro, thus potentially intercepting the priming and amplification of autoreactive T cells in tissue inflammation. These DCs can contribute to the inhibition of inflammatory T cell responses to islet antigens and the promotion of the anti-inflammatory, regulatory responses exerted by MSCs.

Keywords Cytokines · Dendritic cells · Extracellular vesicles · GAD · Mesenchymal stem cells · Prostaglandin E$_2$ · T cells · Type 1 diabetes

Electronic supplementary material The online version of this article (doi:10.1007/s00125-015-3808-0) contains peer-reviewed but unedited supplementary material, which is available to authorised users.

✉ Maria M. Zanone
  mariamaddalena.zanone@unito.it

[1] Department of Medical Sciences, University of Turin, Corso Dogliotti 14, 10126 Torino, Italy

[2] Immunogenetic and Transplant Biology Laboratory, University of Turin, Turin, Italy

[3] Department of Molecular Biotechnology and Health Sciences, University of Turin, Turin, Italy

[4] Translational Centre for Regenerative Medicine, University of Turin, Turin, Italy

[5] Medical Board, Fresenius Medical Care, Bad Homburg, Germany

Abbreviations

CCR7	C-C chemokine receptor type 7
CD	Cluster of differentiation
CFSE	Carboxyfluorescein succinimidyl ester
DC	Dendritic cell
ELISPOT	Enzyme-linked immunosorbent spot
EV	Extracellular vesicle
GAD	Glutamic acid decarboxylase
mDC	Mature dendritic cell
miRNA	MicroRNA
MSC	Mesenchymal stem cell
PBMC	Peripheral blood mononuclear cell

Springer

PGE$_2$ Prostaglandin E$_2$
PV   Pentavac
SI   Stimulation index
Th17   T helper 17
Treg   Regulatory T cell

Introduction

Dendritic cells (DCs) are a heterogeneous group of immune cells involved in the priming, differentiation and expansion of effector T cells. Activated DCs are required for priming naive T cells, and DC presentation of islet autoantigens probably occurs during the development of islet autoreactivity in type 1 diabetes. Thereafter, DCs may play a role at all disease stages [1, 2]. Recent studies indicate that DCs acquire tolerogenic properties during in vitro manipulations by supplementing culture conditions or actively silencing genes or promoting their overexpression, with therapeutic potential in the prevention and treatment of autoimmune diabetes [3–5]. In NOD mice, tolerogenic bone marrow derived DCs have been shown to delay, prevent and, in some cases, reverse diabetes [6, 7]. The inhibition of DC differentiation, maturation and function and the induction of regulatory DCs that can induce regulatory T cells (Tregs) may account for the multilevel immunomodulatory properties displayed by mesenchymal stem cells (MSCs) both in vitro and in vivo [8–10].

MSCs have emerged in recent years as a safe, promising treatment strategy for autoimmune diseases, including type 1 diabetes [11, 12]. Originally performed in animal studies, this cellular intervention has recently been translated to patients with recent-onset diabetes [13]. MSCs exhibit their immunomodulatory effects through direct contact, the production of soluble markers and the release of extracellular vesicles (EVs). EVs express MSC surface receptors and carry biologically active proteins, lipids, mRNAs, long non-coding RNAs and microRNAs (miRNAs) [14].

Several studies have suggested that direct inhibition of DC effector function is involved in the immunological tolerance state induced by MSCs [9, 10, 15]. In this context, MSCs have been shown to hinder the ability of DCs to prime antigen-specific T cells in vivo as a result of downregulating C-C chemokine receptor type 7 (CCR7) and cluster of differentiation (CD) 49dβ1, which are involved in DC homing to the draining lymph nodes [16].

So far, few studies have analysed the effects of MSCs on the profile and function of DCs in the context of type 1 diabetes, where the role of DCs has still to be fully elucidated [17, 18]. In NOD mice, MSC-released IL-6 has been reported to affect DC phenotype, differentiation and cytokine production and to divert the CD11c$^+$ subset toward a more regulatory tolerogenic phenotype [19]. Studies on the co-transplantation of allogenic islets and MSCs in streptozotocin-induced diabetic mice have shown that downregulation of the maturation, co-stimulatory and MHC class II molecules of recipient DCs contributes to graft survival by conversion to a more tolerogenic phenotype [20].

The aim of the present study was to investigate whether bone marrow derived MSCs and their EVs can alter in vitro the maturation and phenotype of monocyte-derived DCs from patients with type 1 diabetes at disease onset. The inhibition of islet antigen T cell activation by MSC- and EV-conditioned DCs and the promotion of an anti-inflammatory and Treg phenotype were also studied.

Materials and methods

Participants and DC generation Peripheral blood mononuclear cells (PBMCs) were obtained from nine white patients with recent-onset type 1 diabetes on the basis of a positive IFN-γ response to glutamic acid decarboxylase (GAD65; stimulation index [SI] ≥3; Table 1) by enzyme-linked immunosorbent spot (ELISPOT) analysis as previously described [12, 21]. CD14$^+$ monocytes were isolated by positive selection (CD14 microbeads, Miltenyi Biotec, Bergisch Gladbach, Germany) and CD14$^-$ PBMCs were stored in liquid nitrogen until needed. Immature DCs were generated by the addition of 100 ng/ml human granulocyte-macrophage colony-stimulating factor (GM-CSF) and 50 ng/ml IL-4 (both from PeproTech, Rocky Hill, NJ, USA) and induced to mature (to form mature DCs [mDCs]) on day 6 by adding 50 ng/ml TNF-α and 50 ng/ml IL-1β (both PeproTech) for 48 h and pulsed at a concentration of 1×10^6/ml with 10 μg/ml GAD65 (Diamyd, Stockholm, Sweden) or, in a limited set of control experiments ($n=3$), with 5 μg/ml Pentavac (PV) polyvalent vaccine (Sanofi Pasteur, Lyon, France). In one set of experiments, immature DCs were induced to mature with 40 ng/ml lipopolysaccharide.

All study participants gave informed consent and the study was approved by the local ethical review committee.

MSC culture, isolation of MSC-derived EVs and co-culture with DCs Heterologous MSCs were obtained from Lonza (Basel, Switzerland) and characterised. EVs were obtained by differential ultracentrifugation and quantified by nanoparticle tacking analysis, as previously described [21]. A pool of approximately 2.5×10^8/ml EV particles was labelled with 2 μl/ml Vybrant Dil (Life Technologies, OR, USA) for 15 min at 37°C and then washed, ultracentrifuged at 100,000 g and added to mDCs (2×10^5) for 24 h. After washing, EV internalisation was assessed by flow cytometry and confocal microscopy (LSM5-PASCAL, Zeiss, Oberkochen, Germany) analyses. In control experiments, Dil-labelled MSC EVs were denatured by boiling (10 min at 95°C) and then incubated with mDCs.

GAD65-pulsed mDCs (5×10^5) were seeded onto a MSC monolayer (1:1 ratio) in 24-well plates and cultured for 48 h (referred to as MSC-conditioned DCs). The optimal DC:MSC ratio (1:10, 1:1 or 10:1) and incubation time were selected on the basis of previous experiments using DCs obtained from blood donor PBMCs stimulated with 5 μg/ml recall antigen PV. Furthermore, when more DCs were recovered from a diabetic patient, mDCs were incubated with MSC-derived EVs (6.25×10^7 particles/ml) for 48 h in selected experiments (referred to as EV-conditioned DCs). Conditioned DCs were recovered by gentle aspiration and centrifugation; parallel experiments using unconditioned mDCs and MSC-or EV-conditioned DCs were performed. The levels of differentiation, co-stimulatory and maturation surface markers were analysed by flow cytometry using FITC- or phycoerythrin-conjugated monoclonal antibodies (mAbs; anti-CD14, anti-CD83, anti-CD1a, anti-CD86, anti-CCR7, anti-HLA class I and anti-HLA class II; BD Pharmingen, San Diego, CA, USA). Data were acquired using a FACSCalibur and analysed using CellQuest Software (Becton Dickinson, Franking Lakes, NJ, USA). EVs obtained from human dermal fibroblasts (i.e. fibroblast-derived EVs; Lonza) served as controls [21]. In a limited set of experiments, mDCs from diabetic patients ($n=3$) were cultured in MSC-conditioned medium or in EV-depleted conditioned medium.

Levels of *TGFB1*, *IL4*, *IL6* and *IL10* transcripts was analysed by real time PCR (primers listed in electronic supplementary material [ESM] Table 1), as previously described [21]. Levels of secreted IL-6, IL-10, TGF-β and prostaglandin E$_2$ (PGE$_2$) were measured in cell-free culture supernatant by ELISA, according to the manufacturer's instructions (R&D, Milan, Italy).

DC plus T cell co-cultures: ELISPOT, flow cytometric and ELISA analyses In parallel experiments, mDCs and MSC-conditioned DCs were co-cultured with autologous T cells (1×10^6) for 48 h (DC:T cell ratio, 1:10) and stimulated by GAD65 for 48 h. IFN-γ ELISPOT analysis was then performed, as previously described [12]. In selected experiments (four patients), T cell plus EV-conditioned DC co-cultures were also established.

T cell proliferation was detected using a carboxyfluorescein succinimidyl ester (CFSE) assay. Briefly, 2×10^7/ml CD14$^-$ cells were labelled with 500 μl CFSE (5 μmol/l; Sigma, Milan, Italy) and the reaction was stopped with RPMI medium (containing 10% FCS). CFSE-labelled CD14$^-$ cells (1.5×10^6) were co-cultured with autologous unconditioned mDCs or MSC-conditioned DCs (DC:T cell ratio, 1:10) with GAD65 stimulation for 5 days. Cell proliferation and cell-surface expression of the CD69 activation marker (anti-CD69PE mAb; BD Pharmingen) were analysed by flow cytometry.

Tregs and T helper 17 (Th17) cells were analysed in GAD65-stimulated T cells under different co-culture conditions, as previously described [21]. Levels of secreted IL-6, IL-10, TGF-β, IFN-γ and IL-17 were measured by ELISA (R&D).

Statistical analysis An SI of ≥3 was chosen as a positive response in the ELISPOT analysis [12]. Spots and levels of cytokines and PGE$_2$ were compared using the Mann–Whitney U or the Wilcoxon test for unpaired or paired data, respectively. Data were analysed using the IBM SPSS statistical package (version 9.0, Chicago, IL, USA), and p values <0.05 were considered significant.

Table 1 IFN-γ ELISPOT response to GAD65 in type 1 diabetic patients

Case no.	Sex	Age (y)	mDCs			MSC-DCs		
			Baseline count[a,b]	GAD$_{65}$[a,c]	GAD$_{65}$ SI[d]	Baseline count[a,b]	GAD$_{65}$[a,c]	GAD$_{65}$ SI[d]
1	M	45	7	77	11	5	14	2.8
2	F	28	6	94	15.6	8	11	1.3
3	M	27	7	22	3.1	6	16	2.6
4	M	28	1	5	5	2	2	1
5	F	23	34	114	3.4	23	58	2.2
6	F	21	35	117	3.9	33	61	1.8
7	M	30	8	26	3.3	7	20	2.8
8	F	30	4	24	6	5	14	1.8
9	M	28	2	28	14	4	10	2.5

Data are the mean of the triplicate wells and represent a single experiment performed in triplicate for each patient

[a] Spot number/300,000 cells

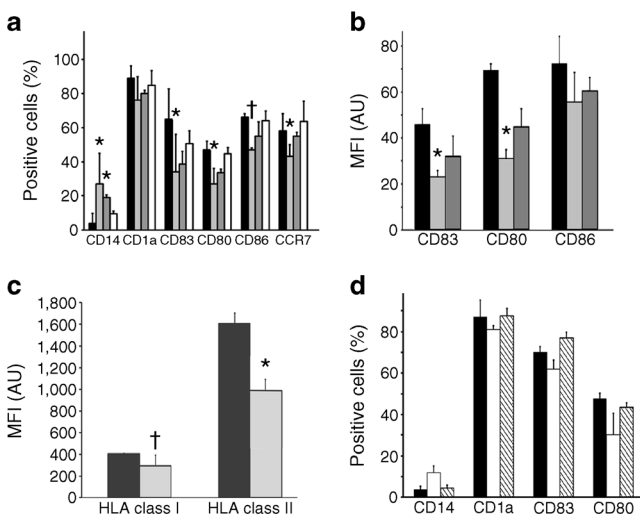[b] For co-cultured T cell+mDCs or T cell+MSC-conditioned DCs in vehicle alone

[c] For co-cultured T cells+mDCs or T cells+MSC-conditioned DCs stimulated with GAD65
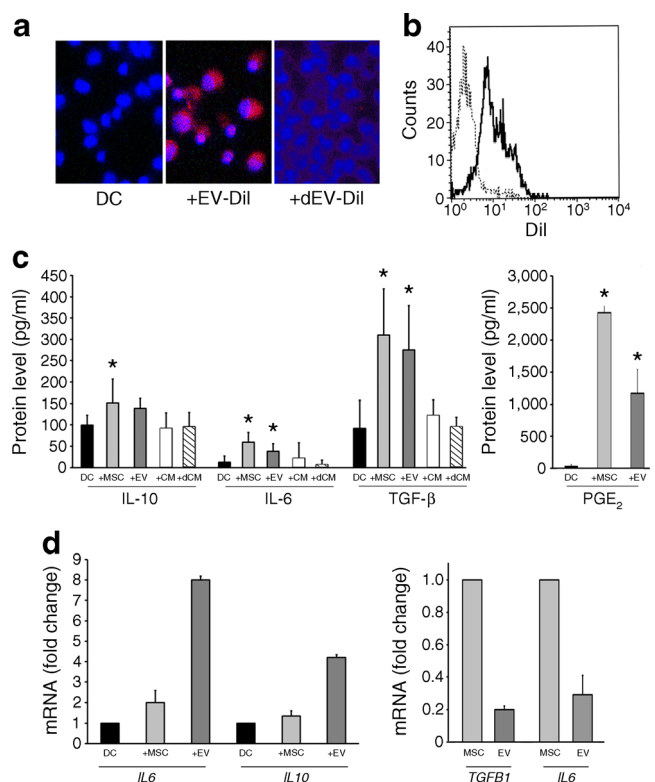
[d] SI of ≥3 indicates a positive response

Results

Effects of MSC and MSC-derived EVs on DC maturation and phenotype Phenotypic analysis of DCs generated from CD14$^+$ cells and cultured in the presence of MSCs (1:1 ratio) showed skewing toward an immature phenotype with increased expression of CD14 and a reduction of CD1a expression. Cell-surface expression of the maturation marker CD83 and the co-stimulatory molecules CD86 and CD80 was lower for MSC-conditioned DCs (Fig. 1a, b). MSCs also had significantly reduced expression of the CCR7 chemokine receptor and HLA class II molecules (Fig. 1c). Although not significantly different compared with mDCs, a similar trend was observed when EVs were used instead of MSCs in a limited number of experiments using DCs from four GAD65 responder patients (Fig. 1a). No significant modification to maturation or co-stimulation marker levels was detected in mDCs cultured with fibroblast-derived EVs, MSC-conditioned medium or EV-depleted medium (Fig. 1a, d). Furthermore, when MSCs were added at a late stage of DC differentiation and maturation, they did not significantly interfere with the lipopolysaccharide-matured DC phenotype (ESM Fig. 1).

Confocal microscopy and flow cytometric analyses indicated that MSC-derived EVs were internalised by DCs (Fig. 2a, b). In control experiments, denatured EVs were not detected in mDCs (Fig. 2a).

Secretion of IL-6, TGF-β, IL-10 and PGE$_2$ was significantly increased in MSC-conditioned DCs compared with mDCs (Fig. 2c). This cytokine pattern was also evident in EV-conditioned DCs, but not in DCs cultured in MSC-conditioned or EV-depleted medium (Fig. 2c). Upregulation of IL-6 and IL-10 in both types of conditioned DCs was confirmed by increased *IL6* and *IL10* transcript levels (Fig. 2d). Furthermore, *TGFB1* and *IL6* transcripts were detected in MSCs and in EVs, while *IL10* transcripts were only detected in MSCs (Fig. 2d), as previously reported [21].

Fig. 1 DC phenotype. (**a**) Mean±SD percentage expression of differentiation and maturation markers for GAD65-pulsed DCs generated from CD14$^+$ cells and cultured without (black) or with (light grey) MSCs, with MSC-derived EVs (dark grey) or with fibroblast-derived EVs (white). (**b**) Mean fluorescence intensity (MFI; arbitrary units [AU] of fluorescence)± SD for the surface intensity of maturation and co-stimulatory markers on DCs cultured without (black) or with (light grey) MSCs, or with MSC-derived EVs (dark grey). (**c**) MFI±SD for HLA class I and II expression on GAD65-pulsed DCs generated from CD14$^+$ cells and cultured without (black) or with (grey) MSCs. (**d**) Mean±SD percentage of expression of differentiation and maturation markers for GAD65-pulsed DCs cultured without (black) or with (white) MSC-conditioned medium or with EV-depleted medium (diagonal stripes). Data were calculated from two different experiments for each patient. In experiments using fibroblast-derived EVs or conditioned media, DCs from three patients were used. *$p<0.05$ vs DCs cultured without MSCs. $^†p=0.05$ vs DCs cultured without MSCs

Fig. 2 EV internalisation and levels of cytokine secretion. (**a**) Representative micrographs of DCs or DCs incubated with Dil-labelled EVs (+EV-Dil) or with Dil-labelled EVs denatured by boiling (+dEV-Dil). (**b**) Representative flow cytometric analysis of DCs internalising Dil-labelled EVs (solid line). Dotted line, DCs not incubated with EVs. (**c**) Mean ± SD levels of secreted IL-10, IL-6, TGF-β and PGE$_2$ under the following culture conditions: GAD65-pulsed DCs cultured without (black) or with MSCs (light grey), EVs (dark grey), MSC-conditioned medium (white) or EV-depleted medium (diagonal stripes). Data were calculated from two different experiments performed in triplicate for each patient. *$p<0.05$ vs DCs cultured without MSCs or EVs. (**d**) *IL6* and *IL10* mRNA levels measured under the following culture conditions: GAD65-pulsed DCs cultured without (black) or with MSCs (light grey) or EVs (dark grey). *TGFB1* and *IL6* mRNA levels in EVs relative to MSC levels. Results were normalised to 18S RNA and are expressed as the fold change in gene expression in DCs or MSCs ($2^{-\Delta\Delta C_t}$)

MSC- and EV-conditioned DC plus T cell co-cultures: ELISPOT and flow cytometric analyses As shown in Fig. 3a, T cells co-cultured with conditioned DCs exhibited reduced proliferation after GAD65 antigen stimulation. Levels of the early T cell activation marker CD69 were also significantly reduced (Fig. 3b, c).

ELISPOT analysis showed that GAD65-pulsed, MSC-conditioned DCs co-cultured with autologous T cells showed an inhibited IFN-γ response (mean spot number: with mDCs 56.3±43, with MSC-conditioned DCs 22.9±21; $p<0.05$ for paired data), resulting in a SI of <3, i.e. below the positive cut-off (Table 1 and Fig. 3d).

Flow cytometric analysis showed an increased proportion of CD127^{low}FOXP3$^+$ T cells (gated on CD4$^+$CD25^{high}) when co-cultured with MSC-conditioned DCs compared with mDCs ($p<0.05$), and a reduced percentage of IL-17$^+$ T cells within the CD4$^+$ population ($p<0.05$; Fig. 4a, b and ESM

Fig. 2). A similar trend in the IFN-γ response was observed in FOXP3$^+$ T cell and IL-17$^+$ T cell subsets co-cultured with EV-conditioned DCs in selected experiments, although without reaching statistical significance.

In experiments using PV to pulse mDCs, MSC-conditioned DCs co-cultured with autologous T cells showed a significant reduction in IFN-γ spots (ESM Fig. 3).

Secretion of IL-6, IL-10 and TGF-β was increased and secretion of IFN-γ and IL-17 was reduced in co-cultured MSC- and EV-conditioned DCs compared with mDCs ($p<0.05$; Fig. 4c).

Discussion

Clinical and experimental data indicate that DCs are involved in the pathogenesis of most autoimmune diseases via complex
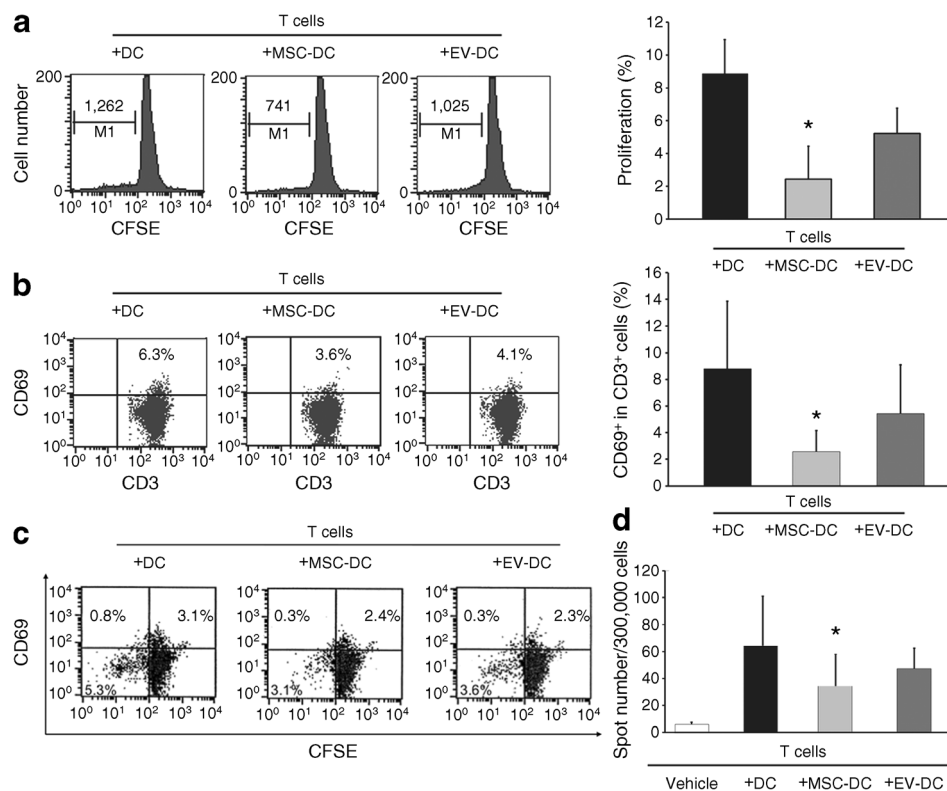

Fig. 3 T cell proliferation and activation and IFN-γ ELISPOT analysis of co-cultured DC and T cells. (**a**) Representative CFSE flow cytometric analyses of proliferating T cells obtained from a single diabetic patient, stimulated with GAD65 and primed by autologous DCs (+DC), autologous MSC-conditioned DCs (+MSC-DC) or autologous EV-conditioned DCs (+EV-DC). The number of proliferating cells is also shown. The histogram shows mean±SD percentages of proliferating CD3$^+$ cells under the following conditions: GAD65-pulsed T cells co-cultured with autologous (black), MSC-conditioned (light grey) or EV-conditioned (dark grey) DCs. (**b**) Representative flow cytometric analyses of activated CD69$^+$ T cells (upper right quadrant) of a single diabetic patient stimulated with GAD65 and primed by DCs (as described in **a**). The histogram shows mean±SD percentage of CD69$^+$ cells in the CD3$^+$ cell population under the following conditions: GAD65-pulsed T cells co-cultured with autologous (black), MSC-conditioned (light grey) or EV-conditioned (dark grey) DCs. *$p<0.05$ for paired data. (**c**) Representative flow cytometric analyses of proliferating T cells (left quadrants), as assessed by CFSE assay, and activated CD69$^+$ T cells (upper quadrants) from a single diabetic patient. These were stimulated with GAD65 and primed by DCs (as described in **a**). (**d**) Mean ± SD IFN-γ spots per well (300,000 cells) for the nine diabetic patients with a positive response to GAD65 under the following conditions: T cells challenged with vehicle alone (white) and GAD65-pulsed T cells co-cultured with autologous (black), MSC-conditioned (light grey) or EV-conditioned (dark grey) DCs. Data were calculated from experiments performed in triplicate for each patient. *$p<0.05$ vs T cells co-cultured with autologous DCs; paired data

mechanisms. DCs can bidirectionally promote either the priming and differentiation of self-reactive T cells or tolerance through the generation of Tregs or induction of effector T cell unresponsiveness [22–25]. Ex vivo manipulated tolerogenic DC-based therapies for animal models of autoimmune diseases have been reported. Tolerogenic bone marrow derived DCs can suppress collagen-induced arthritis or prevent hyperglycaemia in NOD mice without inducing generalised immunosuppression [5, 7, 26]. Intriguingly, EVs derived from in vitro generated immunosuppressive DCs can retain the effects of their parental cells [27, 28]. Recently, clinical trials using tolerogenic DC-based therapies have been designed [4, 5]. The present study of type 1 diabetes indicates that heterologous bone marrow derived MSCs in a proinflammatory

environment can skew monocyte-derived DCs toward an immature, IL-10-producing regulatory phenotype. This was associated with decreased levels of co-stimulatory marker and an altered cytokine pattern, possibly via mechanisms dependent on IL-6, TGF-β and PGE$_2$ production. In autologous co-culture experiments under islet antigen stimulation, MSC-conditioned DCs failed to trigger antigen-driven inflammatory effector T cell activation, detected as IFN-γ production, the number of Th17 cells, levels of proinflammatory IL-17 [29], and T cell proliferation and activation. DC modulation by MSCs was, at last in part, mimicked by MSC-derived EVs after internalisation by DCs.

Several lines of in vitro and in vivo research indicate that the dual ability of MSCs to suppress or promote the immune
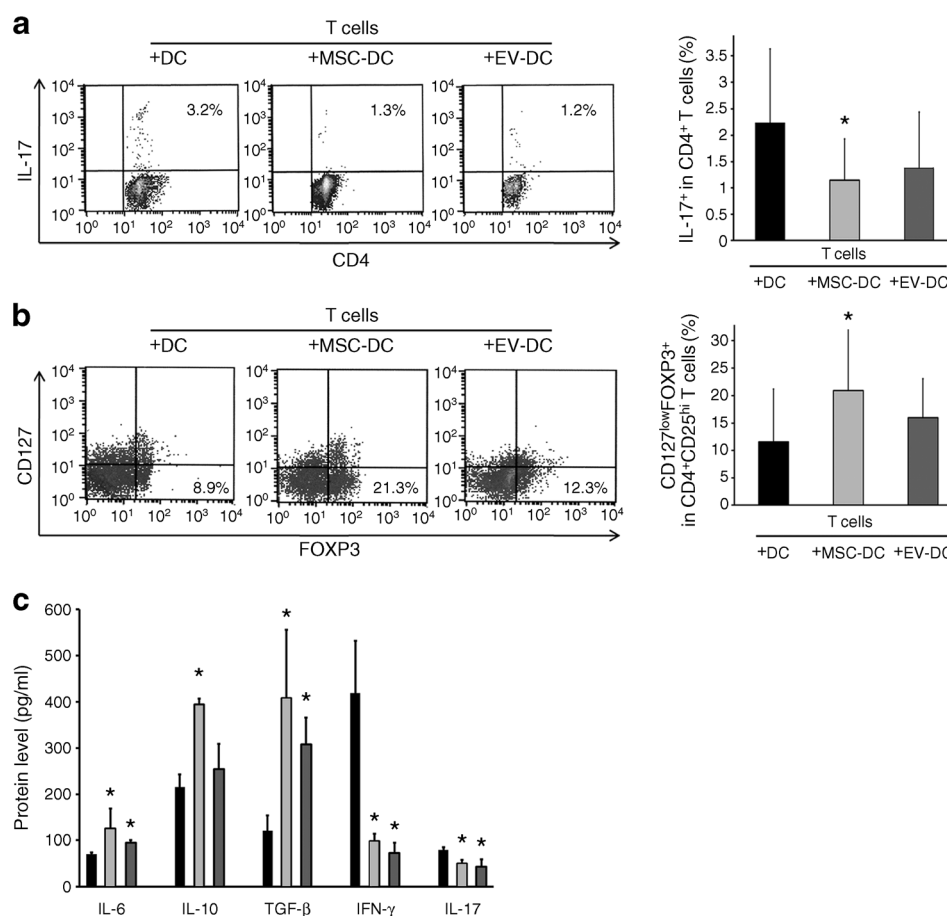
Fig. 4 Flow cytometric analysis of Th17 cells and FOXP3$^+$ Tregs and levels of cytokine secretion. (a) Representative flow cytometric analysis of IL17$^+$ CD4$^+$ T cells (upper right quadrant) obtained from a single diabetic patient, stimulated with GAD65 and primed by autologous DCs (+DC), autologous MSC-conditioned DCs (+MSC-DC) or autologous EV-conditioned DCs (+EV-DC). The histogram shows the mean± SD percentage of IL17$^+$ cells in the CD4$^+$ T cell population under the following conditions: GAD65-pulsed T cells co-cultured with autologous (black), MSC-conditioned (light grey) or EV-conditioned (dark grey) DCs. (b) Representative flow cytometric analysis of regulatory CD127^{low}FOXP3$^+$ T cells (lower right quadrant) gated on the CD4$^+$CD25^{hi} population of a single diabetic patient, stimulated with GAD65 and primed by autologous DCs (+DC), autologous MSC-conditioned DCs (+MSC-DC) or autologous EV-conditioned DCs (+EV-DC). The histogram shows the mean±SD percentage of CD127^{low}FOXP3$^+$ cells in the CD4$^+$CD25^{hi} T cell population under the following conditions: GAD65-pulsed T cells co-cultured with autologous (black), MSC-conditioned (light grey) or EV-conditioned (dark grey) DCs. *$p<0.05$ for paired data. (c) Mean ± SD levels of IL-6, IL-10, TGF-β, IFN-γ and IL-17 secreted under the following conditions: GAD65-pulsed T cells co-cultured with autologous (black), MSC-conditioned (light grey), EV-conditioned (dark grey) DCs. Data were calculated from experiments performed in duplicate for each patient. *$p<0.05$ vs co-cultures with autologous DCs

response depends on the microenvironment, and that vigorous ongoing inflammation induces the immunosuppressive function [8]. Soluble markers such as PGE_2, cytokines and released EVs contribute to the MSC effects [8, 14, 30]. However, as indicated by conditioned medium experiments in the present study, not only secreted factors but also target cell contact [8, 31] or high EV concentration [21, 32] are required to fully induce an immunomodulatory effect, at least in vitro. It has been established that after surface receptor interaction, internalisation or fusion to target cell membranes, EVs transfer proteins, lipids, functional mRNAs and miRNAs that control transcription, proliferation and immunoregulation [14, 32–35].

Although specific antigen-dependent interactions do not appear to be required to mediate DC immunoregulatory functions [36, 37], our data indicate that in vitro DC antigen specification can target diabetogenic T cells and convey tolerogenic signals. Indeed, it has been shown that antigen-primed DCs induce better protection in NOD mice and that cognate antigen–MCH class II complexes enhance IL-2 induced Treg proliferation [37–39].

Recall antigen experiments confirm at the DC level that MSCs interfere with the antigen-elicited immune response, without limiting the exploitation of their immunoregulatory properties in transplantation and several autoimmune diseases [8, 13, 30], and with the potential advantage of local action at specific inflamed anatomical sites. The key therapeutic attribute of both MSCs and DCs is related to their ability to selectively migrate to sites of tissue injury and draining lymph nodes [3, 11, 39, 40]. This may allow further local antigen provision and interaction with activated T cells in situ. In agreement with other studies [16, 41], we found that MSCs downregulate the CCR7 chemokine receptor, known to drive the mature DC homing to draining lymph nodes. This potential limiting effect could, nevertheless, inhibit an autoimmune amplification loop during the progression of type 1 diabetes. Indeed, in NOD mice, tissue inflammation augments DC maturation, CCR7 upregulation and migration to lymph nodes, where they amplify the ongoing immune response by promoting the priming of autoreactive T cells [25].

Increasing evidence indicates that DCs promote immune tolerance by the induction of Tregs [42, 43]. MSC and MSC-derived EVs induce a shift toward an anti-inflammatory Treg profile that is exploitable in immune disease settings, including diabetes [8, 11, 21, 44]. It has been suggested that direct inhibition of the DC effector function underlies the immunotolerant state induced by MSCs [9, 10, 15]. In the present study linking the immunomodulatory properties of both cell types, we show that MSC- and EV-conditioned DCs increase their IL-6 and IL-10 content and secretion. In co-culture experiments, conditioned DCs induced a higher frequency of T cells with a regulatory phenotype and increased T cell secretion of anti-inflammatory IL-10

and TGF-β and IL-6 molecules. Therefore, an amplifying loop that mediates and propagates immunomodulation while inhibiting the maturation of inflammatory DCs can be envisaged [19]. Although data regarding the effects on beta cell function and survival remain controversial [45, 46], IL-6 may also stimulate beta cell repair. Thus, in DC–MSC combination therapy, multiple layers of tolerance could be formed involving regulatory DCs, T cells and even B cells [47] that may act and accumulate in relevant tissue.

In conclusion, the present in vitro study confirms that DCs are a target of versatile, immunomodulatory MSCs in the context of type 1 diabetes. Moreover, MSC-released EVs retain this biological effect, at least in part, thus rendering them an attractive tool to exploit the benefits of MSC therapy. Their ability to induce tolerogenic DCs, together with their easy procurement, their low tumorigenicity (as shown in several clinical studies [48]) and recent promising results in new-onset diabetic patients [13] renders MSC therapy a promising therapeutic strategy to locally control autoimmune pancreas inflammation and halt the progression of type 1 diabetes.

References

1. Calderon B, Unanue ER (2012) Antigen presentation events in autoimmune diabetes. Curr Opin Immunol 24:119–128

2. Morel PA (2013) Dendritic cell subsets in type 1 diabetes: friend or foe? Front Immunol 4:1–11

3. Creusot RJ, Yaghoubi SS, Chang P et al (2009) Lymphoid-tissue-specific homing of bone-marrow-derived dendritic cells. Blood 113:6638–6647

4. Giannoukakis N, Phillips B, Finegold D, Harnaha J, Trucco M (2011) Phase I (safety) study of autologous tolerogenic dendritic cells in type 1 diabetic patients. Diabetes Care 34:2026–2032

5. Hilkens CM, Isaacs JD (2013) Tolerogenic dendritic cell therapy for rheumatoid arthritis: where are we now? Clin Exp Immunol 172:148–157

6. Creusot RJ, Giannoukakis N, Trucco M, Clare-Salzler MJ, Fathman CG (2014) It's time to bring dendritic cell therapy to type 1 diabetes. Diabetes 63:20–30

7. Tai N, Yasuda H, Xiang Y et al (2011) IL-10-conditioned dendritic cells prevent autoimmune diabetes in NOD and humanized HLA-DQ8/RIP-B7.1 mice. Clin Immunol 139:336–349

8. Wang Y, Chen X, Cao W, Shi Y (2014) Plasticity of mesenchymal stem cells in immunomodulation: pathological and therapeutic implications. Nat Immunol 15:1009–1016

9. Djouad F, Charbonnier LM, Bouffi C et al (2007) Mesenchymal stem cells inhibit the differentiation of dendritic cells through an interleukin-6-dependent mechanism. Stem Cells 25:2025–2032

10. Li YP, Paczesny S, Lauret E et al (2008) Human mesenchymal stem cells license adult CD34+ hemopoietic progenitor cells to differentiate into regulatory dendritic cells through activation of the Notch pathway. J Immunol 1:1598–1608

11. Madec AM, Mallone R, Afonso G et al (2009) Mesenchymal stem cells protect NOD mice from diabetes by inducing regulatory T cells. Diabetologia 52:1391–1399

12. Zanone MM, Favaro E, Miceli I et al (2010) Human mesenchymal stem cells modulate cellular immune response to islet antigen glutamic acid decarboxylase in type 1 diabetes. J Clin Endocrinol Metab 95:3788–3797

13. Carlsson PO, Schwarcz E, Korsgren O, Le Blanc K (2015) Preserved β-cell function in type 1 diabetes by mesenchymal stromal cells. Diabetes 64:587–592

14. Théry C, Ostrowski M, Segura E (2009) Membrane vesicles as conveyors of immune responses. Nat Rev Immunol 9:581–593

15. Aggarwal S, Pittenger MF (2005) Human mesenchymal stem cells modulate allogeneic immune cell responses. Blood 15:1815–1822

16. Chiesa S, Morbelli S, Morando S et al (2011) Mesenchymal stem cells impair in vivo T cell priming by dendritic cells. Proc Natl Acad Sci U S A 18:17384–17389

17. Allen JS, Pang K, Skowera A et al (2009) Plasmacytoid dendritic cells are proportionally expanded at diagnosis of type 1 diabetes and enhance islet autoantigen presentation to T cells through immune complex capture. Diabetes 58:138–145

18. Guerder S, Joncker N, Mahiddine K, Serre L (2013) Dendritic cells in tolerance and autoimmune diabetes. Curr Opin Immunol 25:670–675

19. Jurewicz M, Yang S, Augello A et al (2010) Congenic mesenchymal stem cell therapy reverses hyperglycemia in experimental type 1 diabetes. Diabetes 59:3139–3147

20. Li FR, Wang XG, Deng CY, Qi H, Ren LL, Zhou HX (2010) Immune modulation of co-transplantation mesenchymal stem cells with islet on T and dendritic cells. Clin Exp Immunol 161:357–363

21. Favaro E, Carpanetto A, Lamorte S et al (2014) Human mesenchymal stem cell-derived microvesicles modulate T cell response to islet antigen glutamic acid decarboxylase in patients with type 1 diabetes. Diabetologia 57:1664–1673

22. Ganguly D, Haak S, Sisirak V, Reizis B (2013) The role of dendritic cells in autoimmunity. Nat Rev Immunol 13:566–577

23. Diana J, Simoni Y, Furio L et al (2013) Crosstalk between neutrophils, B-1a cells and plasmacytoid dendritic cells initiates autoimmune diabetes. Nat Med 19:65–73

24. Wakkach A, Fournier N, Brun V, Breittmayer JP, Cottrez F, Groux H (2003) Characterization of dendritic cells that induce tolerance and T regulatory 1 cell differentiation in vivo. Immunity 18:605–617

25. Melli K, Friedman RS, Martin AE et al (2009) Amplification of autoimmune response through induction of dendritic cell maturation in inflamed tissues. J Immunol 1:2590–2600

26. Perone MJ, Bertera S, Tawadrous ZS et al (2006) Dendritic cells expressing transgenic galectin-1 delay onset of autoimmune diabetes in mice. J Immunol 177:5278–5289

27. Bianco NR, Kim SH, Ruffner MA, Robbins PD (2009) Therapeutic effect of exosomes from indoleamine 2,3-dioxygenase-positive dendritic cells in collagen-induced arthritis and delayed-type hypersensitivity disease models. Arthritis Rheum 60:380–389

28. Kim SH, Lechman ER, Bianco N et al (2005) Exosomes derived from IL-10-treated dendritic cells can suppress inflammation and collagen-induced arthritis. J Immunol 174:6440–6448

29. Arif S, Moore F, Marks K et al (2011) Peripheral and islet interleukin-17 pathway activation characterizes human autoimmune diabetes and promotes cytokine-mediated β-cell death. Diabetes 60:2112–2119

30. Koch M, Lemke A, Lange C (2015) Extracellular vesicles from MSC modulate the immune response to renal allografts in a MHC disparate rat model. Stem Cells Int 486141:1–7

31. Krampera M, Glennie S, Dyson J et al (2003) Bone marrow mesenchymal stem cells inhibit the response of naive and memory antigen-specific T cells to their cognate peptide. Blood 101:3722–3729

32. Quesenberry PJ, Aliotta J, Deregibus MC, Camussi G (2015) Role of extracellular RNA-carrying vesicles in cell differentiation and reprogramming. Stem Cell Res Ther 153:1–10

33. Cocucci E, Racchetti G, Meldolesi J (2009) Shedding microvesicles: artefacts no more. Trends Cell Biol 19:43–51

34. Akyurekli C, Le Y, Richardson RB, Fergusson D, Tay J, Allan DS (2015) A systematic review of preclinical studies on the therapeutic potential of mesenchymal stromal cell-derived microvesicles. Stem Cell Rev 11:150–160

35. Ratajczak MZ, Kucia M, Jadczyk T et al (2012) Pivotal role of paracrine effects in stem cell therapies in regenerative medicine: can we translate stem cell-secreted paracrine factors and microvesicles into better therapeutic strategies? Leukemia 26:1166–1173

36. Feili-Hariri M, Dong X, Alber SM, Watkins SC, Salter RD, Morel PAV (1999) Immunotherapy of NOD mice with bone marrow-derived dendritic cells. Diabetes 48:2300–2308

37. Zou T, Caton AJ, Koretzky GA, Kambayashi T (2010) Dendritic cells induce regulatory T cell proliferation through antigen-dependent and -independent interactions. J Immunol 1:2790–2799

38. Lo J, Peng RH, Barker T, Xia CQ, Clare-Salzler MJ (2006) Peptide-pulsed immature dendritic cells reduce response to beta cell target antigens and protect NOD recipients from type I diabetes. Ann N Y Acad Sci 1079:153–156

39. Creusot RJ, Yaghoubi SS, Kodama K (2008) Tissue-targeted therapy of autoimmune diabetes using dendritic cells transduced to express IL-4 in NOD mice. Clin Immunol 127:176–187

40. Fiorina P, Jurewicz M, Augello A et al (2009) Immunomodulatory function of bone marrow-derived mesenchymal stem cells in experimental autoimmune type 1 diabetes. J Immunol 183:993–1004

41. English K, Barry FP, Mahon BP (2008) Murine mesenchymal stem cells suppress dendritic cell migration, maturation and antigen presentation. Immunol Lett 15:50–58

42. Jonuleit H, Schmitt E, Schuler G, Knop J, Enk AH (2000) Induction of interleukin 10-producing, nonproliferating CD4(+) T cells with regulatory properties by repetitive stimulation with allogeneic immature human dendritic cells. J Exp Med 6:1213–1222

43. Dhodapkar MV, Steinman RM, Krasovsky J, Munz C, Bhardwaj N (2001) Antigen-specific inhibition of effector T cell function in humans after injection of immature dendritic cells. J Exp Med 15:233–238

44. Kordelas L, Rebmann V, Ludwig AK et al (2014) MSC-derived exosomes: a novel tool to treat therapy-refractory graft-versus-host disease. Leukemia 28:970–973

45. Kristiansen OP, Mandrup-Poulsen T (2005) Interleukin-6 and diabetes: the good, the bad, or the indifferent? Diabetes 54(Suppl 2): S114–S124

46. Boumaza I, Srinivasan S, Witt WT et al (2009) Autologous bone marrow-derived rat mesenchymal stem cells promote PDX-1 and insulin expression in the islets, alter T cell cytokine pattern and preserve regulatory T cells in the periphery and induce sustained normoglycemia. J Autoimmun 32:33–42

47. Di Caro V, Phillips B, Engman C, Harnaha J, Trucco M, Giannoukakis N (2013) Retinoic acid-producing, ex-vivo-generated human tolerogenic dendritic cells induce the proliferation of immunosuppressive B lymphocytes. Clin Exp Immunol 174:302–317

48. von Bahr L, Batsis I, Moll G et al (2012) Analysis of tissues following mesenchymal stromal cell therapy in humans indicates limited long-term engraftment and no ectopic tissue formation. Stem Cells 30:1575–1578